UNIVERISTY OF OKLAHOMA

GRADUATE COLLEGE

APPLICATIONS OF BUTTON SAMPLE HOLDERS FOR MID-INFRARED SPECTROSCOPY MEASUREMENTS

A DISSERTATION

SUBMITTED TO THE GRADUATE FACULTY

in partial fulfillment of the requirements for the

Degree of

DOCTOR OF PHILOSOPHY

BY

JASPREET SINGH
Norman, Oklahoma
2021

Downloaded from SHAREOK. Persistent Handle URL: https://hdl.handle.net/11244/332506

APPLICATIONS OF BUTTON SAMPLE HOLDERS FOR MID-INFRARED SPECTROSCOPY MEASUREMENTS

A DISSERTATION APPROVED FOR THE
DEPARTMENT OF CHEMISTRY AND BIOCHEMISTRY

BY THE COMMITTEE CONSISTING OF

Dr. Robert L. White, Chair

Dr. Mark A. Nanny

Dr. Charles V. Rice

Dr. Si Wu

Dr. Wai-Tak Yip

© Copyright by JASPREET SINGH 2021
All Rights Reserved.

This work is dedicated to my family. To my mom and sisters, I am forever grateful for your unwavering support and encouragement. To my amazing wife, your motivation and care are immeasurable.

Acknowledgements

I would like to thank Dr. Robert L. White for his guidance, support, and teaching; I am grateful to have learned from a wonderful educator and amazing chemist. Your curiosity in tackling new problems and passion for your work inspires me to be a better scientist. Thank you for creating an environment that promotes the discussion and exploration of challenges, and where all ideas could be freely conversed.

I would like to thank my graduate committee: Dr. Mark A. Nanny, Dr. Charles V. Rice, Dr. Wai-Tak Yip, and Dr. Si Wu for their encouragement, input, and guidance during my PhD study. Additionally, I would like to thank Heidi Noneman for her support and discussion on our projects.

I give my sincerest thanks to my mom Jaswinder Kaur, for all of your sacrifices, love, and support. You always put your children in front of all else, encourage us to be the best we can be, and have given us the best life possible. My achievements have only been possible because of you. To my sisters Inderpreet and Gurpreet, you are the best role models a person could ask for; thank you for always being there for me. I would like to say a special thank you to my wife Xingxiu. Going to graduate school was the best decision I made as that is where we met. Two drifters, off to see the world; thank you for joining and supporting me on this journey.

Abstract

Infrared (IR) spectroscopy is a rapid and non-destructive method for chemical analysis that is based on interactions between electromagnetic radiation and matter. Despite its widespread popularity in commercial and research environments, there have been no major developments in IR sampling methods since the 1960's. This dissertation describes applications of a new mid-IR spectroscopy sampling method that involves the use of a unique "button" sample holder. Buttons are fabricated from stainless-steel and comprise a backing to which a wire mesh is attached. This type of sample holder can accommodate thin layers of neat solid or liquid samples, eliminating the need for time-consuming and expensive sample dilution protocols. Because infrared radiation reflects from button surfaces over a wide range of angles, diffuse reflection optics are needed to collect the radiation after it interacts with the sample. The small wire diameters characteristic of the meshes used to construct buttons allow thin sample layers to be analyzed. Path lengths on the order of a few microns can be achieved, permitting analysis of high absorptivity neat samples, such as coals, that would otherwise need to be diluted in a non-absorbing sample matrix. The unique mechanism by which radiation interacts with samples produces spectra with greatly enhanced dynamic range when compared to conventional methods.

The unconventional buttons sample holder can be employed for quantitative analyses of both solids and liquids, yielding linear calibration curves. A modified button containing a sample reservoir can be utilized as a variable path length liquid cell, with path lengths determined by the sample volume. Although path lengths are not directly proportional to sample volume, quantitative liquid sample analyses can be achieved when the effective path length is constant, which requires that constant sample volumes are added to the reservoir. The

robust button design permits abrasive sampling by simply rubbing the rough button mesh over sample surfaces to remove small quantities of material. This approach was used to obtain infrared spectra of commercial pharmaceutical tablets quickly and easily. The sensitivity and reproducibility of this methodology was sufficient for product discrimination by principal component analysis (PCA).

The utility of the button sample holder was extended by constructing several unique accessories. An eight-sample carousel was built to allow multiple samples to be analyzed with minimal effort. A low-temperature thermoelectric cooling accessory was constructed to rapidly cool and heat button samples. By using this device, infrared spectra at sub-ambient temperatures were obtained. This apparatus was also useful for measuring infrared spectra of highly volatile samples. By using a temperature controller, unique temperature ramp profiles were applied to solid samples to discriminate between reversible and irreversible sample changes. A button sample holder was incorporated into a variable temperature diffuse reflectance infrared Fourier transform (VT-DRIFTS) apparatus to investigate molecular level processes occurring during zeolite dehydrations. Subtle, temperature-dependent changes in cation-exchanged Linde Type A (LTA) and NaY zeolites were identified and characterized. By using spectral subtractions, sodium-LTA dehydration was found to occur by a step-wise mechanism involving temperature-dependent changes in water-cation interactions. A VT-DRIFTS study of calcium-exchanged LTA identified a complex sequence of concurrent processes, which included the formation of carbonate species. For NaY zeolite, VT-DRIFTS difference spectroscopy was used to selectively monitor changes in the hydroxyl groups contained in water and attached to zeolite framework acid sites.

Table of Contents

Acknowledgements v

Abstract vi

Table of Contents viii

List of Figures xii

Chapter 1: Introduction 1

1.1 Spectroscopy 1

1.2 Infrared Spectroscopy 3

1.3 Mid-IR Analytical Methods 6

1.3.1 Transmission-IR 7

1.3.2 Reflectance-IR 9

1.3.3 Alternative Mid-IR Methods 11

1.4 Research Objectives 11

Chapter 2: Button-IR: Design, Theory, and Qualitative and Quantitative Analysis 13

2.1 Introduction 13

2.2 Experimental 13

2.3 Button-IR Fabrication 16

2.4 Theory of Operation 18

2.5 Analysis of Solids and Liquids 23

2.5.1 Solids 23

2.5.1.1 Analysis Using Exposed Mesh Button 23

2.5.1.2 Abrasive Button-IR 27

2.5.1.3 Quantitative Analysis 39

2.5.2 Liquids 40

2.5.2.1 Analysis using Recessed Button 40

2.5.2.2 Multiple Pathlengths in Liquids 44

2.5.2.3 Quantitative Analysis 61

2.5.3 Reproducibility and Sensitivity 62

2.6 Conclusion 64

Chapter 3: Button-IR Accessories 66

3.1 Introduction 66

3.2 Accessories 67

3.2.1 Multiple Sample Carousel 67

3.2.1.1 Conclusions 69

3.2.2 Low-Temperature Thermoelectric Cooler 70

3.2.2.1 Experimental 71

3.2.2.2 Results and Discussion 73

3.2.2.3 Conclusions 87

Chapter 4: Button-IR Variable Temperature Diffuse Reflection Infrared Spectroscopy of Ion Exchanged Linde Type A Zeolites 88

4.1 Introduction 88

4.2 Experimental 91

4.2.1 Materials. 91

4.2.2 Instrumentation. 92

4.3 Results and Discussion 94

4.3.1 Sodium-LTA (NaA) 94

4.3.2 Calcium-LTA (CaA) 103

4.4 Conclusions 126

Chapter 5: Button-IR Variable Temperature Diffuse Reflection Infrared Spectroscopy of Faujasite Y Zeolite 128

5.1 Introduction 128

5.2 Experimental 130

5.2.1 Materials. 130

5.2.2 Instrumentation. 130

5.2.3 Data Processing. 131

5.3 Results and Discussion 131

5.4 Conclusion 147

Chapter 6: Future Outlook 148

References 151

Appendix 1: Button-IR Accessories 3D Model and Images 172

Appendix 2: R Script 174

Script 1: Data conversion and baseline correction 174

Script 2: Principal Component Analysis 177

Appendix 3: Copyright 180

List of Figures

Figure 1.1 - Vibrational and rotational energy states represented for one electronic state. 2

Figure 1.2 - IR active and inactive stretches. 5

Figure 1.3 - Liquid transmission cell. 8

Figure 1.4 - Types of IR reflectance. 10

Figure 2.1 - FTIR with button, slide mechanism, and Praying Mantis diffuse reflection collection optics. 14

Figure 2.2 – Schematic of exposed mesh and recessed mesh button. 16

Figure 2.3 – Zoomed image of mesh openings. 17

Figure 2.4 – Button blank with spot welded variable mesh sizes. 18

Figure 2.5 – Specular reflection of radiation with empty, solids, or liquids in button. 19

Figure 2.6 – Emissivity of button blank and different mesh sizes in specular and diffuse modes. 20

Figure 2.7 – Schematic of button as a variable path length sample holder. 21

Figure 2.8 – Change in absorbance (left) and pathlength (right) with increasing quantities of mineral oil. 22

Figure 2.9 - Variable pathlength cell calibration curve. 23

Figure 2.10 - Silica gel spectra (a) button, (b) cup, diluted with KBr, (c) cup, neat. 24

Figure 2.11 - Variable loadings of calcium carbonate on exposed mesh button. 25

Figure 2.12 - Infrared spectra obtained for a) lignite, b) bituminous, and c) anthracite coal. 26

Figure 2.13 - Abrasive button-IR 3.5-inch floppy disk infrared spectrum. 27

Figure 2.14 – Infrared spectra of CuSCN and NH_4Cl mixtures. 29

Figure 2.15 - Tablet interior infrared spectra. 31

Figure 2.16 - Tablet coating infrared spectra. 32

Figure 2.17 - Effects of pre-processing for the A-IBP samples: (a) measured spectra; (b) after multiplicative scatter correction; (c) Kubelka-Munk format; (d) second derivative. 34

Figure 2.18 - Top: PCA results derived from Kubelka-Munk spectra. Bottom: PCA results derived from second derivative spectra. Full spectrum range (4000–700 cm^{-1}) was employed. 35

Figure 2.19 - Top: PCA results derived from Kubelka-Munk spectra. Bottom: PCA results derived from second derivative spectra. Fingerprint region (1530–1150 cm^{-1}) was employed. 36

Figure 2.20 - Standard curve for a) benzoic acid and b) liquid-to-solid deposition ammonium chloride. 39

Figure 2.21 – Paraffin oil infrared spectra measured by using (a) transmittance, (b) button specular reflectance, and (c) button diffuse reflectance. 43

Figure 2.22 - Paraffin oil infrared spectra obtained by diffuse reflection (dashed line) and by using transmission cells containing a thin film (solid lines) and incorporating a 0.17 mm spacer (dotted line). 44

Figure 2.23 – Rays passing through different thicknesses of liquid. 48

Figure 2.24 – Path length weighting functions (a) and resulting effective path length versus $a_\lambda c$ profiles calculated by using these functions (b). 49

Figure 2.25 - Effective path length versus $a_\lambda c$ plots derived from diffuse reflectance button measurements (a) and transmission cell measurements (b). The seven plots in (a) were derived from spectra obtained with paraffin oil sample volumes ranging from 1 to 4 μL in 0.5

μL intervals. The nine plots in (b) were derived from transmission cell paraffin oil measurements by using path lengths ranging from 0.04 to 0.20 mm in 0.02 mm intervals. .. 50
Figure 2.26 - Overlay of six diffuse reflectance button spectra for paraffin oil with different amounts of 10-nonadecanone. Inset plot shows ketone carbonyl band shapes and 1720 cm^{-1} calibration function. 53
Figure 2.27 - Chlorobenzene transmission cell (left ordinates) and mesh button (right ordinates) infrared spectra. Transmission cell measurements were made by using a thin film (top) and with a 0.25 mm path length (bottom). Button spectra were obtained by using a mesh with 5 μm openings (top) and with 140 μm openings (bottom). Asterisks above some 0.25 mm transmission cell peaks highlight bands with truncated intensities. 54
Figure 2.28 – Paraffin oil infrared spectra measured by (a) transmittance and (b) diffuse reflectance with the button sample holder. 56
Figure 2.29 – Variation of effective path length as a function of the volume of paraffin oil contained in the modified button reservoir. 57
Figure 2.30 – Plots of baseline absorbance as a function of the paraffin oil volume added to the button for diffuse (circles) and specular (squares) reflectance measurements. 59
Figure 2.31 – Calibration functions for 10-nonadecanone concentrations in paraffin oil obtained from diffuse reflectance button measurements. Inset plots show overlays of the 15 (3 for each of 5 concentrations) spectra from which band maxima absorbance and integrated absorbance values were obtained. 61
Figure 2.32 – (a) Button diffuse reflectance Infrared spectra for fresh (solid line) and used (dashed line) motor oil. (b) Difference spectrum calculated by subtracting a 3.5 μL paraffin

oil spectrum from the fresh oil spectrum. (c) Difference spectrum calculated by subtracting the fresh oil spectrum from the used oil spectrum. 63
Figure 3.1 – 3D printed 8-position button carousel. 66
Figure 3.2 – Carousel button single beam spectra. Numbers indicate the location of the button on the carousel in Figure 3.1. 67
Figure 3.3 – Empty button transflectance spectra. Numbers indicate the location of the button on the carousel in Figure 3.1. 68
Figure 3.4 – Overlay of paraffin oil spectra measured by using the carousel buttons. Numbers indicate the location of the button on the carousel in Figure 3.1. 69
Figure 3.5– Schematic of button heating/cooling apparatus. 71
Figure 3.6 – Button maximum heating and cooling temperature profiles beginning from different starting temperatures. 74
Figure 3.7– Overlays of three replicate infrared spectra for acetone, ethyl acetate, and chloroform measured at 10 ^{o}C. 76
Figure 3.8 – Overlay of kaolinite diffuse reflectance spectra obtained at 100, 70, 40, 10, and -20 ^{o}C. The inset plot shows an expansion of the 100 and -20 °C spectra over the O-H stretching vibration region. 78
Figure 3.9 – Top – Hydroxyl stretching vibration wavenumber changes with temperature. The solid line denotes sample temperature measurements. Peak center wavenumbers as a function of time are provided for bands nominally located at 3700 cm^{-1} (dotted line) and 3620 cm^{-1} (dashed line). (b) Adsorbed water content (3600–2500 cm^{-1} integrated area) as a function of time (dotted line). The solid line denotes sample temperatures. 79

Figure 3.10– Top - Stepped heating profile and Bottom - 15% Acetylsalicylic acid/calcium montmorillonite infrared spectra obtained initially (solid line) and during the final 20 °C isothermal period (dashed line). The 4000-1300 cm^{-1} intensities are magnified by a factor of 10..... 81

Figure 3.11 – Difference spectra characterizing changes induced by successively heating the 15% acetylsalicylic acid/montmorillonite sample to (a) 40 ^{o}C, (b) 60 ^{o}C, (c) 80 ^{o}C, and (d) 100 ^{o}C..... 84

Figure 4.1 - Diagram of the variable temperature diffuse reflection infrared spectroscopy apparatus. 93

Figure 4.2 - Mass loss curve for NaA heated at 2 °C/min in 50.0 mL/min helium 95

Figure 4.3 – VT-DRIFTS infrared spectra for NaA: (a) full spectrum and (b) water bending vibration band expansion. 96

Figure 4.4 – Integrated intensity temperature profiles for the (a) O-H stretching vibration band and (b) H-O-H bending vibration band. 97

Figure 4.5 – VT-DRIFTS difference spectrum regions representing (a) O-H stretching vibrations and (b) H-O-H bending vibrations. 98

Figure 4.6 - VT-DRIFTS difference spectrum regions representing (a) O-H stretching vibrations and (b) H-O-H bending vibrations. 99

Figure 4.7 – Mass loss versus temperature profiles for NaA (solid line) and CaA (dashed line). 104

Figure 4.8 – Overlay of VT-DRIFTS spectra obtained while heating CaA. 105

Figure 4.9 - Results of subtracting the spectra in Figure 4.8 in the O-H stretching vibration region 106

Figure 4.10 - Results of subtracting the spectra in Figure 4.8 in the fingerprint vibration region. 107
Figure 4.11 – (a) Overlay of VT-DRIFTS spectra obtained during CaA sample cooling, (b) results of subtracting the spectra in (a) in the O-H stretching vibration region, (c) results of subtracting the spectra in (a) in the fingerprint vibration region. 109
Figure 4.12 – (a) Overlay of VT-DRIFTS spectral bands associated with carbonate formation during CaA sample heating and (b) overlay of spectral bands associated with carbonate during CaA sample cooling. 112
Figure 4.13 – Band location versus elapsed time plots for the split bands representing monodentate carbonate species. The dotted line represents measured sample temperatures as a function of time. 113
Figure 4.14 – Difference spectra derived intensity changes ($\Delta T = 8$ °C) versus elapsed time for (a) O-H vibration bands and (b) carbonate and framework vibration bands. 116
Figure 4.15 - Difference spectrum peak maximum variation for bicarbonate, carbonate, and framework stretching. 117
Figure 5.1 – Ambient temperature NaY infrared spectrum. 132
Figure 5.2 – Variable temperature infrared spectra collected at 20 °C increments during sample heating in the O-H stretching (left) and H-O-H bending (right) vibration regions. . 133
Figure 5.3 – Variable temperature infrared difference spectra representing 20 °C increment changes during sample heating in the O-H stretching (left) and H-O-H bending (right) vibration regions. 134
Figure 5.4 – NaY infrared spectrum obtained at 150 °C (solid line) and component bands obtained by curve fitting (dashed lines). 135

Figure 5.5 – Variable temperature infrared spectra collected at 20 °C increments during sample cooling in the O-H stretching (left) and H-O-H bending (right) vibration regions.. 136
Figure 5.6 – Variable temperature infrared difference spectra representing 20 °C increment changes during sample cooling in the O-H stretching (left) and H-O-H bending (right) vibration regions. 137
Figure 5.7 – Infrared difference spectra representing framework vibration band changes that occurred during sample heating (solid line) and sample cooling (dashed line)..... 138
Figure 5.8 – Infrared difference spectra representing framework vibration band changes that occurred during the specified temperature increments while heating the sample. 139
Figure 5.9 – Infrared band intensity versus temperature profiles for selected framework vibration wavenumbers. 140

Chapter 1: Introduction

Spectrochemical methods are routinely used to study interactions between electromagnetic (EM) radiation and matter. These measurements involve energy state transitions in chemical species. Monitoring the EM radiation involved in specific transitions provides useful chemical information of the species being studied. Interactions between EM radiation and samples are represented by plots of radiation intensity as a function of some measure of photon energy, otherwise referred to as a spectrum[1]. A spectrum can be utilized for qualitative and quantitative analysis of chemical species, which makes spectrochemical methods powerful analytical tools.

1.1 Spectroscopy

In spectroscopic methods, the chemical species of interest is typically perturbed through some external application of energy such as heat, radiation, or via a chemical reaction. Before this external stimulus, the analyte of interest is in its ground state. After application of the stimulus, the species briefly transitions to an excited state. Spectrochemical information is obtained by measuring the light energy absorbed during excitation or released when the species returns to its ground state. The spectrochemical information gained through these measurements can be used for qualitative (i.e. identification of a chemical species) or quantitative analysis (i.e. determining analyte concentration).

In general, spectroscopy methods can be categorized into atomic and molecular spectroscopy. Atomic spectroscopy deals with analysis of free atomic species, whereas molecular spectroscopy deals with molecular species. In either case, EM radiation interacts with matter. The interaction of radiation with matter is often based on the bulk properties of

matter, such as reflection and diffraction, amongst others. EM radiation has both particle and wave characteristics, allowing photon energy to be described in terms of a quantized value or as a wavelength. Planck's equation (1.1*)* describes the relationship between energy and wavelength, where *E* is the energy in joules (J), *h* is Planck's constant ($6.63 \times 10^{-34}\ J\ s$), *c* is the speed of light ($3.00 \times 108\ m\ s^{-1}$), and λ is the wavelength (m).

$$E = \frac{hc}{\lambda} \qquad (\mathbf{1.1})$$

The EM spectrum encompasses a wide wavelength range. The most easily recognized region of the EM spectrum is the visible region, the portion visible to the naked eye, encompassing 350-770nm. Different regions of the EM spectrum can be categorized depending upon the energy transitions involved. For example, energy in the Ultraviolet (UV) region is sufficient to

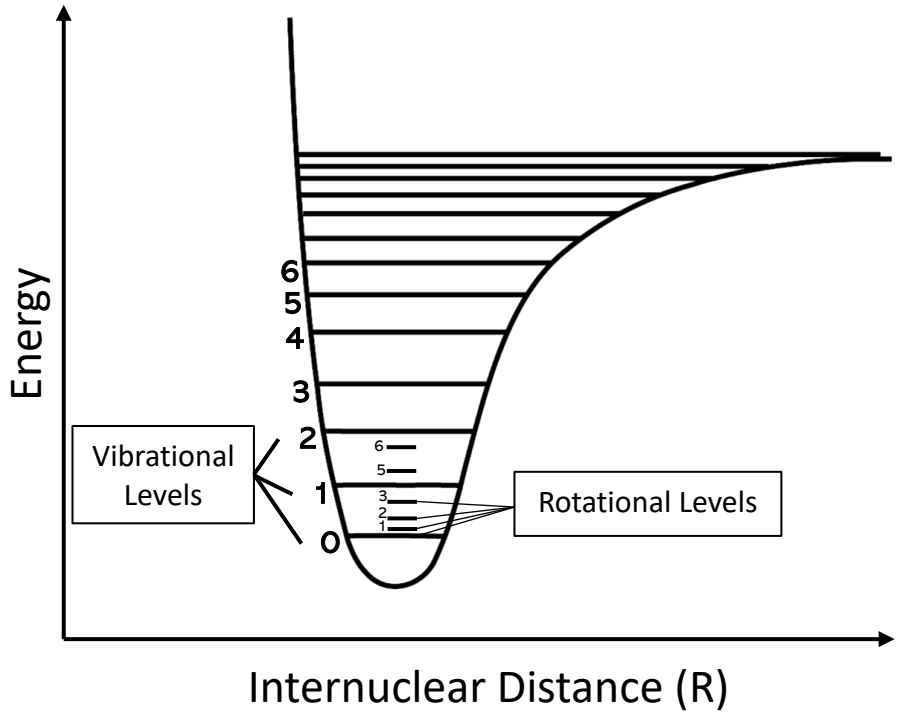

Figure 1.1 - Vibrational and rotational energy states represented for one electronic state.

promote transitions of valence and middle shell electrons and the energy in the infrared (IR)

region can excite molecular vibrations and rotations. Figure 1.1 depicts these energy levels within an electronic state. IR radiation is of sufficient energy to create excited states, therefore IR spectroscopy provides information regarding molecular structures. The IR region is a useful portion of the EM spectrum as most molecular species, except homonuclear diatomic' s, absorb IR radiation. This feature makes IR a valuable tool in chemical analyses. IR spectroscopy has been applied widely, including for food[2-5], environmental[6-8], and biological analyses[9-10]. Certain functional groups yield IR absorbance bands that are mostly independent of the rest of the molecule, allowing rapid identification of selected molecular functionalities [11-14].

1.2 Infrared Spectroscopy

Identification of the IR region traces back to the 1800's with William Herschel and his experiments using diffracted light and thermometers[15]. Herschel noted an increase in temperature for thermometers placed outside the visible light spectrum. However, this observation was largely overlooked and the application of IR radiation as an analytical tool was only realized several decades later when IR absorbance bands were correlated with specific organic groups[16-17]. Despite its analytical value, IR remained an unpopular method due to long analysis times and the requirement for unique lab instruments. The development of the interferometer [18], application of the Fourier transformation (FT), and subsequent commercialization of FTIR instruments led to IR analysis becoming a routinely used tool for scientists. The rapid analysis and non-destructive nature of IR spectroscopy has made it popular in a variety of applications, with improvements to instrumentation and development of new methodologies allowing for quantitative analyses.

The IR EM region can be divided into three sub-regions: the Near, Mid, and Far IR regions. The energy in these wavelength regions is commonly expressed by wavenumber ($\bar{\nu}$), which is inversely proportional to wavelength. Substituting into equation (1.1) and rearranging to solve for $\bar{\nu}$ yields:

$$\frac{1}{\lambda} = \bar{\nu} = \frac{E}{hc} \qquad (\mathbf{1.2})$$

Equation 1.2 shows that wavenumbers are directly proportional to photon energy. Thus, the IR regions can be expressed as 12,900-4000 cm^{-1} for Near, 4000-200 cm^{-1} for Mid, and 200-10 cm^{-1} for Far IR.

To be considered IR active, there must a change in the dipole moment during a molecular vibration. In chemical systems, the dipole is a result of the electronegativity differences of individual atoms, creating charge separations. Water, for example, has an oxygen atom with greater electronegativity that pulls electron density from its hydrogen atoms, creating a polar molecule with a permanent dipole. IR-active chemical species interact with IR radiation by absorbing radiation at resonant frequencies corresponding to the rate of change in the dipole moment for a bond or group during a vibration. Often, functional groups have unique absorption frequency ranges, allowing confirmation of their presence in a chemical species.

Molecular vibrations can be characterized by a variety of motions. Depending on the complexity of a molecule, vibrational motions can be described as stretching (symmetric and asymmetric), bending, rocking, wagging, twisting, and breathing. Each of these motions can result in a dipole moment change. However, this does not always result in distinct IR radiation absorbance due to degeneracy and low absorptivity effects. Figure 1.2 shows the examples of the linear carbon dioxide (CO_2) molecule and the bent water molecule. Water has IR active symmetric and asymmetric stretching, whereas the CO_2 symmetric stretch is IR inactive, but

the asymmetric stretch is IR active. While many different types of motions are possible, the number of fundamental vibrational modes can be calculated from the molecular formula.

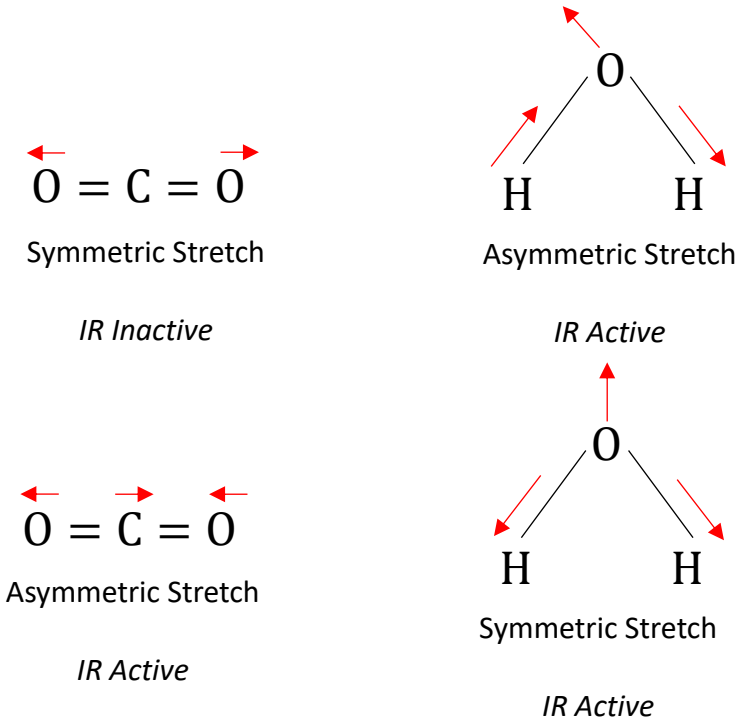

Figure 1.2 - IR active and inactive stretches.

Linear molecules have $3N - 5$ fundamental vibrational modes, and nonlinear molecules have $3N - 6$, where N is the number of atoms in the molecule. As shown by Figure 1.2, not all vibrations are necessarily IR active, but the total number of vibrations can be calculated. Because the number of vibrations depends on 3N, the more complex the molecule, the greater the number of vibrations. In addition to fundamental vibrations, molecules may exhibit weaker overtone and combination bands that contribute to the number of overall observed IR absorbance bands.

Molecular infrared spectra consist of overlapping absorbance bands that correspond to different molecular vibrations. The widths of these bands depend on various factors. When the

same functional group vibration occurs in different local environments, absorbance frequencies shift. Different local environments arise from intramolecular and intermolecular interactions that affect electron density distributions in chemical bonds (i.e. bond strength) and the spatial orientations of chemically bonded atoms (i.e. bond angles). These subtle molecular structure variations result in slight changes in vibrational frequencies, which contributes to band broadening. Additionally, vibrational coupling can result in absorbance bands that are not predicted by normal coordinate analysis. Vibrational coupling produces combination and difference bands, which appear in spectra at frequencies corresponding to linear combinations of fundamental vibrations. Although interpretations of IR spectra can be significantly complicated by band broadening, overtones, and combination and difference bands, IR spectroscopy is regarded as an important technique for substance quantifications and molecular characterizations, and thus is routinely employed. Of the three IR sub-regions, the mid-IR region includes the so-called "fingerprint" region, and is most commonly employed for molecular structure determination. The "fingerprint region" exhibits complicated absorbance band patterns that are most unique to chemical structure. Thus, mid-IR measurements are particularly useful for monitoring sample changes resulting from external perturbations (i.e. heating).

1.3 Mid-IR Analytical Methods

Since the introduction of infrared spectroscopy, several different methods of combining IR radiation with samples have been introduced. Amongst these, the most popular methods include transmission and reflectance. Each of these represents a unique approach for interacting incident radiation with samples of interest. Samples comprised of different states of matter (gas/vapor, liquid, or solid) require different optical systems to obtain spectra.

1.3.1 Transmission-IR

Transmission-IR has traditionally been the most used IR sampling method, and various spectral libraries of references exist for comparisons with unknowns. In transmission-IR, infrared radiation passes directly through the sample and then to the detector. As radiation passes through the sample, depending on the sample type, three outcomes are possible: 1) total absorption, 2) partial absorption, and 3) reflection. When radiation is totally absorbed or reflected, no information is obtained about the sample. For the portion that is partially absorbed, the radiation intensity is attenuated according to the absorbance features of the analyte, which is related to specific molecular vibrations. Samples measured in the transmission mode typically follow Beer's law, permitting quantitative analyses.

For solids, the most common approach is to press a pellet using the sample of interest diluted in an IR transparent salt such as potassium bromide (KBr). The sample/salt mixture is ground to small particle sizes, homogenized, and then pressed into a thin wafer that is inserted into the IR beam path. This technique has been widely used in a variety of applications including analysis of minerals and biological samples.[19-21] For solids, it is critical that the appropriate concentration is selected as samples that are too concentrated result in radiation being totally absorbed. Additionally, factors such as the quantity of diluted sample and the amount of pressure used to press the pellet can affect the quality of measured spectra.

Liquid samples are typically analyzed by placing them inside cells with IR transparent windows. Figure 1.3 shows an example of a liquid transmission cell. The liquid sample is placed between two IR transparent salt windows and pressed together, allowing incident radiation to pass through the sample. Sample thickness (i.e. path length) can be adjusted by using spacers of differing thicknesses. Examples of liquid transmission cell applications

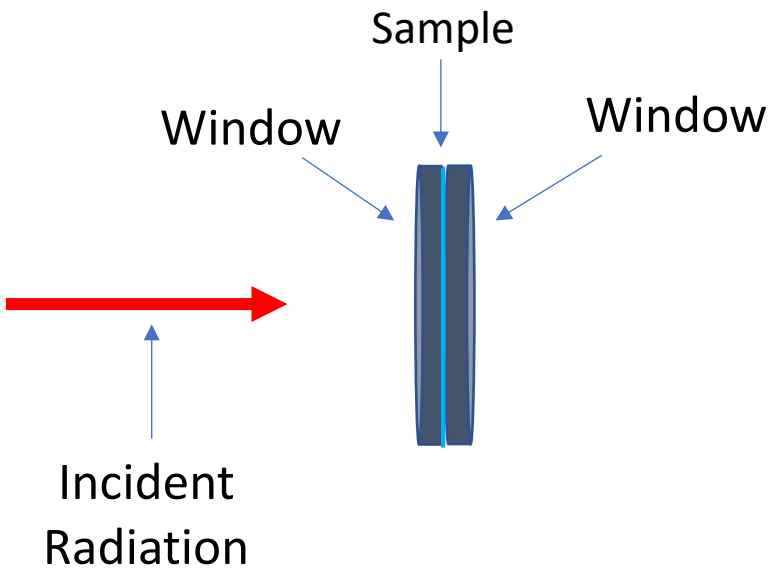

Figure 1.3 - Liquid transmission cell.

include the characterization of organic compounds, live cells, and chemical reaction monitoring.[22-24] Variable pathlength transmission cells have been designed to allow a single cell to have a variable path length without the need for spacers.[25] Care must be given when analyzing liquids because samples that are too thick can be totally absorbing. Additionally, transmission cell windows must be chosen so that they are compatible with the sample being analyzed. For example, KBr windows are not appropriate for samples containing water because this will dissolve the windows. An alternative window material for aqueous liquids is zinc selenide (ZnSe) which is less transparent when compared to KBr, but is water insoluble.

Gas samples can be analyzed with cells that are similar to the liquid cell, but the length of the cell is significantly longer to provide increased path lengths. Gas cells are sealed at both ends by IR transparent windows, allowing IR radiation to pass through the long cell and be attenuated by the gaseous analyte. Examples of gas cell applications include monitoring of environmental gases such as carbon dioxide, corrosive gases, and evolved gas analyses when solids are heated to high temperatures.[26-29] Improvements in gas cell design have led to

multi-pass cells and miniaturization for implementation in portable spectrometers.[30-31] Gas cells can be designed to retain a discrete gaseous sample, or as a flow cell through which a sample stream is passed.

1.3.2 Reflectance-IR

Whereas IR transmission cells provide a means to pass radiation through a sample, reflectance methods involve radiation that interacts with samples in a different manner. Reflectance methods can be assigned to three different categories: 1) specular reflectance, 2) diffuse reflectance, and 3) attenuated total reflection (ATR). Figure 1.4 compares these different types of reflectance. Specular reflectance involves radiation reflecting from the sample at the same angle as the angle of incidence, which is measured relative to the normal. IR reflectance measurements have been applied to studies of optically-thick samples such as polymers, art pieces, and solids.[32-35] Diffuse reflectance infrared Fourier transform spectroscopy (DRIFTS) is a technique in which radiation that interacts with a solid sample and reflected at all angles except the specular reflectance angle is detected. DRIFTS is traditionally used to analyze solid powders and rough surfaces. Examples of samples studied by DRIFTS include soils, biological samples, and inorganic solids. Both qualitative and quantitative analyses have been performed.[36-40] Samples analyzed in diffuse reflectance mode are typically represented by using Kubelka-Munk intensity units. The Kubelka-Munk function is

$$\frac{k}{s} = \frac{(1-R_\infty)^2}{2R_\infty} \qquad (\mathbf{1.3})$$

the most widely-used method to determine concentrations for heterogeneous samples. The model assumes that for a semi-infinite sample, the scattering coefficient (s) sufficiently accounts for the light propagation, and that the ratio of absorption coefficient (k) to the

scattering coefficient can be represented simply by a function of reflectance from the semi-infinite sample layer (R_∞) (eq. 1.3).

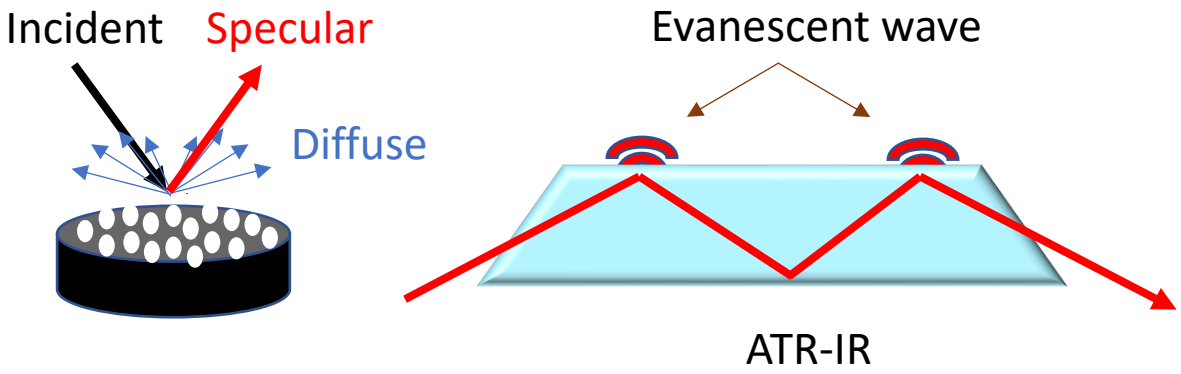

Figure 1.4 - Types of IR reflectance.

Finally, the attenuated total reflectance (ATR) technique detects IR radiation that undergoes total internal reflection through a crystal, which is in contact with a sample. In ATR, the radiation is reflected through a crystal, and an evanescent wave interacts with samples in contact with the external surface of the crystal. These sample absorbance interactions attenuate the IR radiation before it reaches the detector. ATR-IR has become the most popular method for IR analyses because of ease of use and the ability to analyze most solids and liquids. ATR-IR has been broadly used for research, including analysis of minerals, biological samples, and agricultural pollutants.[41-44] Largely due to minimal sample preparation requirements and the ability to analyze aqueous solutions, recent ATR applications have included: spectroscopic imaging of biological samples, classification of Covid-19 severity, time-resolved analyses, synchrotron radiation micro-spectrometry, and combining IR spectroscopy with machine learning.[45-49] Although ATR-IR is a particularly attractive choice, it has limitations. For example, the evanescent wave sample penetration depth is wavelength dependent, resulting in spectrum intensities that do not match transmission cell measurements because different wavenumbers have different effective pathlengths. Additional concerns include short sample

penetration depths (i.e. micron path lengths) which makes this technique better suited to highly absorbing samples. The ATR crystal must be carefully maintained and scratches and damage from abrasive samples must be avoided. Crystals must be selected based on the sample characteristics because these crystals have unique properties, making them best suited for different analyses.

1.3.3 Alternative Mid-IR Methods

In addition to transmittance and reflectance methods, other, less popular methods can be used for making mid-IR spectrum measurements. One such method is photoacoustic-IR, also referred to as photoacoustic spectroscopy (PAS), in which the absorption of IR radiation is directly measured. In PAS, samples are placed in a sealed chamber containing an inert gas and then exposed to pulsed IR radiation. The sample absorbs a portion of the incident radiation and releases the absorbed energy as heat pulses to the surrounding gas. The resulting pressure fluctuations are detected by a high-sensitivity microphone. While not commonly employed, PAS has been used for many studies, especially for highly absorbing materials, such as coals.[50-52].

IR analysis has also been coupled with other analysis methods to create hyphenated analytical techniques. For example, IR spectroscopy can be used to characterize volatiles formed while heating samples during thermogravimetric analysis (TGA). TGA-IR provides spectra for the gases released during TGA analyses.[53-54] Other hyphenated systems have incorporated IR analysis with gas and liquid chromatography.[55-59]

1.4 Research Objectives

Although the development of new IR methods continues today, most efforts have focused on addressing unique, specialized challenges. Since the introduction of ATR in the

1960's, there have been no major developments in IR sampling methods that are generally applicable for routine analyses of solids and liquids.[60-61]This dissertation describes efforts to develop a new method for IR analysis that permits routine analyses of solid powders and liquid samples. The button-IR methodology is a novel approach to IR sampling that is cheap to produce, easily incorporated into existing IR spectrometers, reusable, and can withstand harsh measurement conditions. The working principles behind the button-IR technique is described for both solid and liquid samples. The sampling device is evaluated for qualitative and quantitative applications. Specific examples of button-IR for variable temperature DRIFTS studies to monitor subtle temperature dependent changes in zeolite frameworks are described. The design and development of accessories shows that incorporation of the button sample holder extends the utility of this methodology to automated analyses and low temperature measurements.

Chapter 2: Button-IR: Design, Theory, and Qualitative and Quantitative Analysis

2.1 Introduction

Button-IR is a new method for measuring mid-infrared spectra. A button consists of a circular stainless-steel backing with a smaller diameter circle of wire mesh affixed at its center, which resembles a "button". When placed at the infrared beam focus, incident radiation strikes the round wires of the mesh and the flat backing, reflecting from these surfaces. Due to the wide range of reflected angles, the radiation is most effectively collected by using diffuse reflection optics. When powders are loaded into the button mesh, particles are trapped within small voids, providing a means to prepare thin layers of neat material that would otherwise be untenable. Infrared spectra for these thin layers can be obtained without prior dilution in a non-absorbing medium, eliminating or simplifying sample preparation procedures. Infrared radiation reflects from an empty button over a wide angular distribution. The intensity of this radiation is sufficient to provide a background single beam spectrum, therefore a non-absorbing reference material is not required.[62] Because the button mesh/backing interface provides significant infrared beam scattering, samples that do not inherently scatter can be analyzed by placing them in contact with the button surface, which is in the infrared beam path. By using this approach, the applicability of diffuse reflection infrared spectroscopy can be extended to include non-scattering materials, expanding the range of samples to include liquids.

2.2 Experimental

Paraffin oil (CAS:8042-47-5) and chlorobenzene (CAS:108-90-7) were obtained from Fisher Scientific (Waltham, MA). 10-Nonadecanone (99% purity) (CAS:504-57-4) was

obtained from Lancaster Synthesis (Pelham, MA). Davisil silica gel (grade 634, 100-200 mesh, CAS: 112926-00-8) was purchased from Sigma-Aldrich (St. Louis, MO). Aspirin, Ibuprofen (Advil and Equate brands), and Ibuprofen PM (Equate brand) were purchased over-the-counter from local retailers. Ammonium chloride (ACS reagent, >99.5%) (CAS: 21,333-0) was purchased from Aldrich Chemical Company (Milwaukee, WI). Copper (I) thiocyanate was purchased from UK Laboratory Chemicals. Standard testing sieves (No. 400 and 80) were purchased form W.S. Tyler, Incorporated (Mentor, OH) for particle sizing.

A Mattson Instruments Inc. (Madison, WI) Nova Cygni 120 Fourier transform infrared spectrophotometer (FTIR) and a Harrick Scientific Inc. (Pleasantville, NY) praying mantis diffuse reflection accessory[63] were used for infrared spectrum measurements. Figure 2.1 shows an image of the setup used for spectral measurements. The instrument sampling chamber consisted of the diffuse reflection optics (ellipsoid mirror), a sample shuttle, and the button sampling device. The components in Figure 2.1 were enclosed in a purged environment, eliminating interferences from environmental factors including CO_2 and H_2O. The button is placed at the focal point of the incident radiation, with the sample slide allowing for easy removal and placement of the button while maintaining instrument purge. Spectra were obtained over the 4000-700 cm^{-1} range at 8 cm^{-1} resolution by signal averaging 16

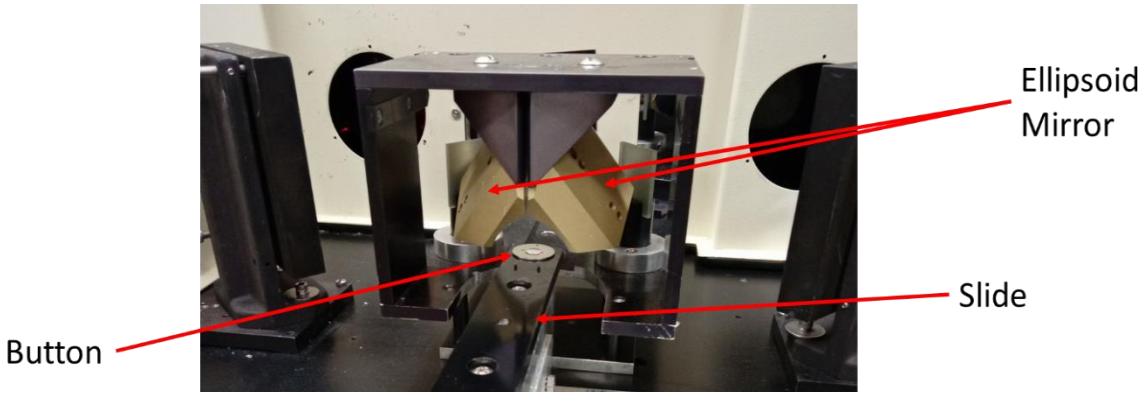

Figure 2.1 - FTIR with button, slide mechanism, and Praying Mantis diffuse reflection collection optics.

interferograms for both sample and background single beam measurements. Although all measurements were made at 8 cm^{-1} resolution, interferogram zero filling prior to processing yielded a 0.97 cm^{-1} spectrum digitization interval. This was found to provide reproducible absorbance band shapes and yielded superior signal-to-noise ratio compared to measurements made at 4 cm^{-1} resolution.[64]

The FTIR was controlled by WinFirst software (Mattson Instruments, Madison, WI). Spectragryph (version 1.2.15) was used for data conversion and pre-processing.[65] Pre-processing for abrasive sampling spectra was done with Spectragryph for multiplicative scattering correction and 2^{nd} derivative conversion and an R program was used for baseline correction by the asymmetric least squares method, and for chemometric analyses.[66] Thirty spectra were acquired for each group of pharmaceutical pills.

Thin film and fixed path length spectra were measured by using a transmission cell with NaCl windows. Thin films were created by placing a few drops of liquid between the windows. The 0.17 and 0.25 mm path lengths were established by Teflon spacers placed between the windows. Paraffin oil spectra were also obtained with path lengths ranging from 0.04 to 0.20 mm by using a Wilkes VR-6 variable path length cell with CaF_2 windows. [67] Effective optical path lengths for paraffin oil samples contained in the modified button reservoir were estimated by correlations with infrared spectra obtained by transmittance with a Wilkes VR-6 variable path length cell with CaF_2 windows. Transmittance cell path lengths were calibrated by measuring intervals between interference fringes produced when the infrared beam passed through the empty cell.[67] Baseline offsets were removed from absorbance spectra prior to calculating peak absorbances.

2.3 Button-IR Fabrication

A button (Figure 2.2) is designed entirely from durable stainless-steel, providing a cheap, reusable, and easily cleaned sample holder. There are two main components to a button, the blank, which is a flat piece of round stainless-steel sheet, and the wire mesh. The button is

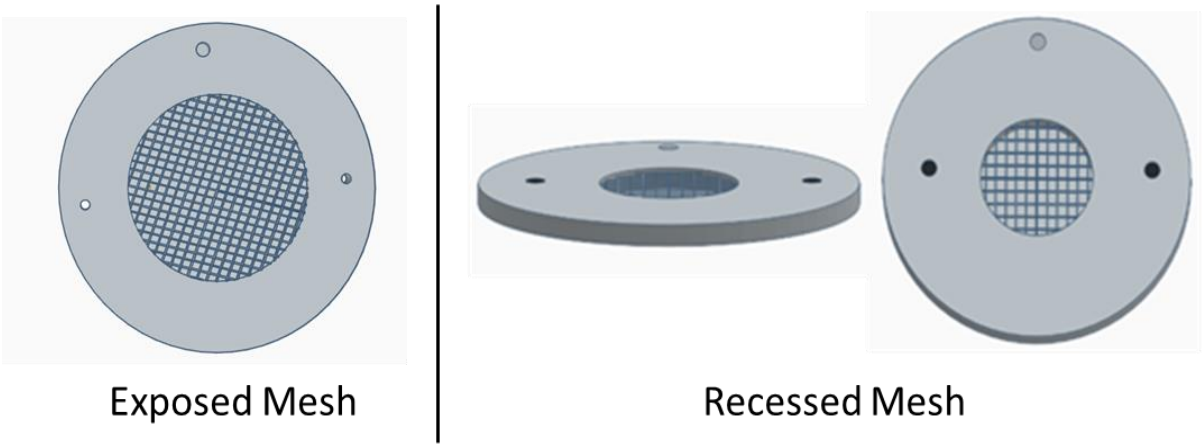

Figure 2.2 – Schematic of exposed mesh and recessed mesh button.

fabricated by spot-welding the wire mesh to the blank, which produces the exposed mesh button. This creates an all-stainless-steel design that can accommodate a variety of sample types, is easily cleaned, and reusable. The wire mesh retains samples within its cavities, making buttons easily transportable. Buttons can easily be modified. The indented blank has a 0.25-inch diameter depression that was indented into the flat base of the button. The protruding bottom is sanded away to produce a level surface. The 0.25-inch depression creates an indent within which samples can be loaded. Adding a mesh onto the indented blank creates a recessed mesh button. Different size wire mesh can be used, as indicated by the designations 100 and 200 mesh. Alignment pins eliminate rotation of the button, allowing for reproducible placement. The button blank is made from 430 grade stainless-steel, which can be attracted by a magnet. The magnets shown eliminate pitch and yaw of the button and help to keep the button in a level position. The alignment pins and magnets help buttons generate reproducible results.

Figure 2.2 depicts the exposed and recessed mesh button designs. The indentation in the recessed mesh confines liquid samples to the center. Fluid samples can be reproducibly contained within the recessed button. The exposed mesh button allows for solid samples to be easily loaded and cleaned out of the mesh cavities. Figure 2.3 shows a magnified view of an electropolished 100 mesh button. The highly reflective wires, which are about 100 µm in diameter, are woven and create openings that are about 140 µm X 140 µm in size. These void spaces can accommodate particle sizes up to 140 µm in size. Different mesh sizes can be used for button fabrication, resulting in different wire diameters and void space volumes. Figure 2.4 shows a blank alongside buttons with 3 different mesh sizes. The mesh size designation indicates the number of openings per inch. The mesh size impacts the size of the voids, allowing for different particle size ranges to be retained within the button, depending on the mesh. The ruler hatch marks reveal the small, compact size of buttons. Their small size and variable composition make buttons an easily adaptable sampling tool.

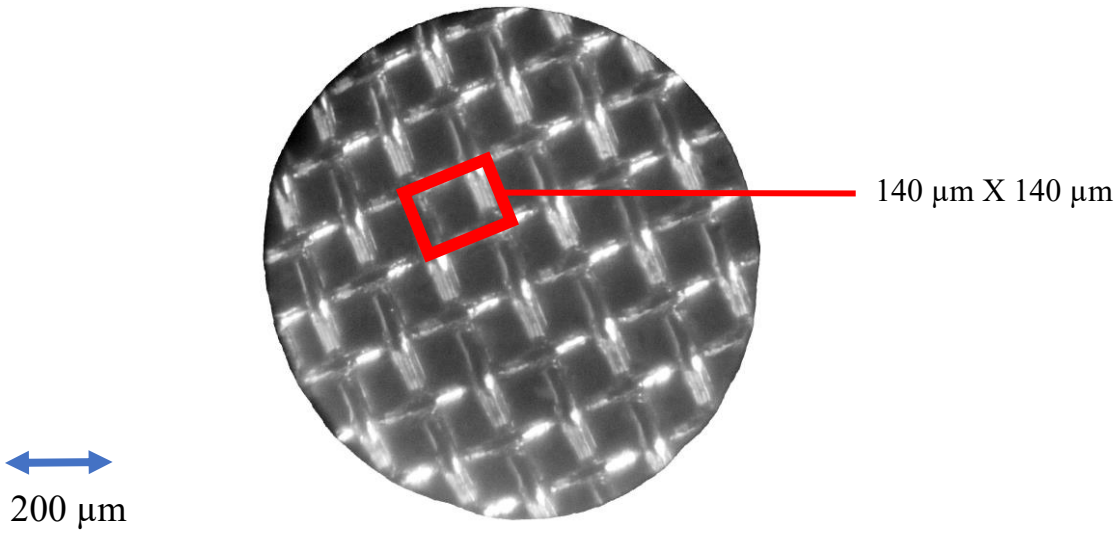

Figure 2.3 – Zoomed image of mesh openings.

2.4 Theory of Operation

Radiation reflected by buttons is impacted by both the base and the mesh. Figure 2.5 depicts simplified views of a button surfaces when radiation is striking them. The rectangular bottom represents the blank base, whereas the circles represent the wires of the mesh. For a

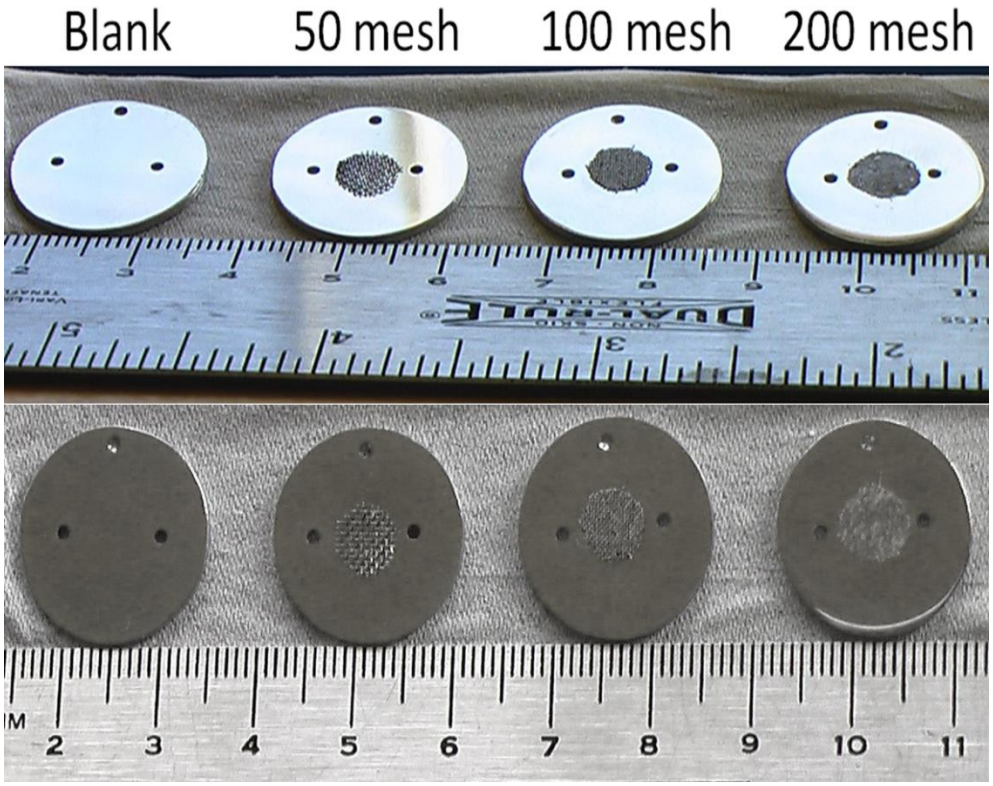

Figure 2.4 – Button blank with spot welded variable mesh sizes.

button without sample, the mesh facilitates "geometric" scattering. Exit angles are determined by the incident angle and the reflective surface shape. With an empty button, incident radiation interacts with the button in multiple ways. The reflection from an empty button can be categorized as variable angle specular reflection. When a button contains a solid sample, the presence of particles alters the exit angles and reduces the amount of specular reflection from the button backing. As Figure 2.5 shows, part of the radiation that was previously specularly reflected in the blank now interacts with a solid particle and is diffusely reflected. When a

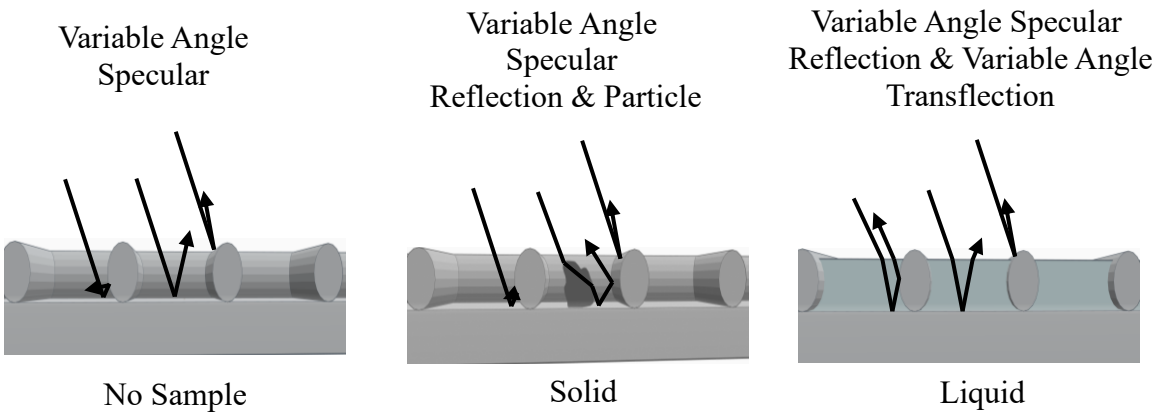

Figure 2.5 – Specular reflection of radiation with empty, solids, or liquids in button.

button contains solid particles, reflected radiation can be described as a combination of variable angle specular reflection and particle diffuse reflection. The presence of non-scattering liquids provides subtle alterations of reflected angles due to refraction. Path lengths are slightly longer than twice the sample thickness. This type of measurement is referred to as "transflectance". Figure 2.5 shows that the button base, mesh wire, and sample thickness affect the reflectivity. By changing the wire mesh size, wire diameter, and/or the sample size/thickness, reflectance from the button can be changed. This feature is highlighted in Figure 2.6,[62] which shows emissivity spectra obtained from buttons with different mesh sizes. Figure 2.6A shows specular reflectance emissivity spectra. The blank button, which has no wire mesh, results in the highest emissivity because the majority of the incident radiation specularly reflects from the backing surface. Alternatively, the 100 mesh button with a 0.10mm wire, which has the smallest open area among the buttons, has the least specular emissivity. Figure 2.6B shows diffuse reflectance emissivity spectra for the same buttons. An opposite trend to that observed in the specular mode is seen. This follows our expectations as the button that has the least amount of specular reflectance emissivity should exhibit the highest diffuse reflectance emissivity.

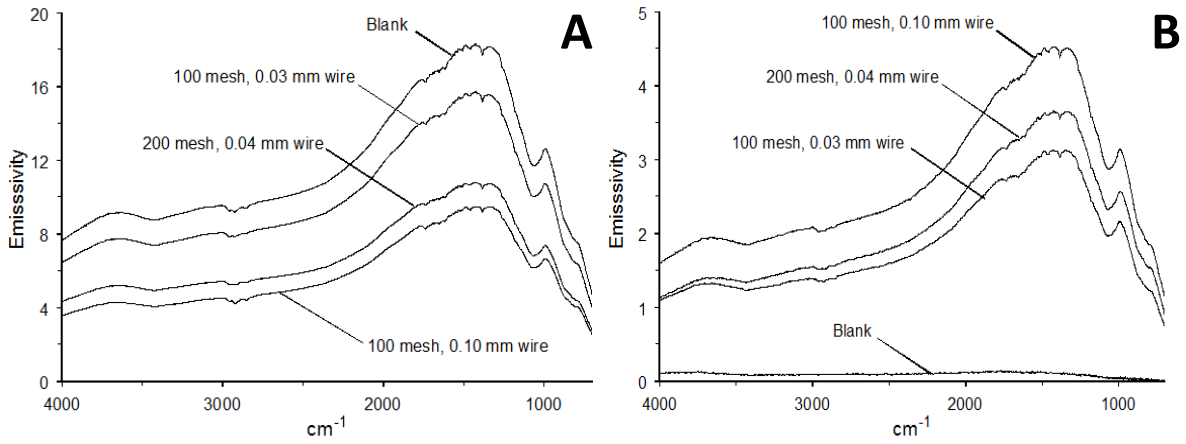

Figure 2.6 – Emissivity of button blank and different mesh sizes in specular and diffuse modes.

In order to collect radiation that is reflected both diffusely by particles and at variable angles specularly, an optical system that can collect radiation over a wide range of angles is required. The solution is to use diffuse reflection optics. Diffuse reflection optics are designed to selectively collect radiation scattered by powder samples. The ellipsoid praying mantis optical system employed for the studies described here can be configured for specular or diffuse reflectance measurements by choosing the appropriate button slide holder.[62] The diffuse reflectance slide places the button horizontally at the focal point beneath the ellipsoid mirrors. The specular reflectance slide tilts the button at an angle of 31^{o} relative to normal (i.e. vertical). Maximum detector signal was obtained when a blank button (i.e. without mesh) was placed at the specular reflectance focal point. When the same blank stainless-steel button was inserted horizontally with the diffuse reflectance slide, the detector signal dropped to less than 2% of the specular reflectance maximum. Thus, 98% of specularly reflected radiation was rejected in the diffuse reflectance measurement configuration. After spot welding wire mesh to the bottom of the button reservoir (recessed mesh button), detector signals measured by using the specular and diffuse reflectance button orientations were about 50 and 25% of

maximum, respectively. Thus, roughly 50% of specularly reflected radiation was lost due to mesh wire reflections and about half of this non-specular reflected radiation was collected by the optical system in the diffuse reflectance measurement mode.

Buttons can be utilized as a variable path length sample holder. Referring to our design of the button with an indentation, we can view the 0.25-inch depression as a cylinder (Figure 2.7). As more sample is added to the cylinder, the height of the liquid would increase. The increased sample would increase the path lengths that incident radiation would travel through the sample. By adjusting the volume of sample added, a variable path length is achieved. As liquid is added, it rises around mesh wires. Because mesh wires are round, the path length should not be a linear function of the added volume, assuming that the indentation diameter is constant from top to bottom. Figure 2.8 shows absorbance and path length changes as a function of the amount of paraffin oil added to a 100 mesh button. The oil was added in 0.2 uL quantities using a syringe. The plot on the left shows the change in absorbance for the 1260

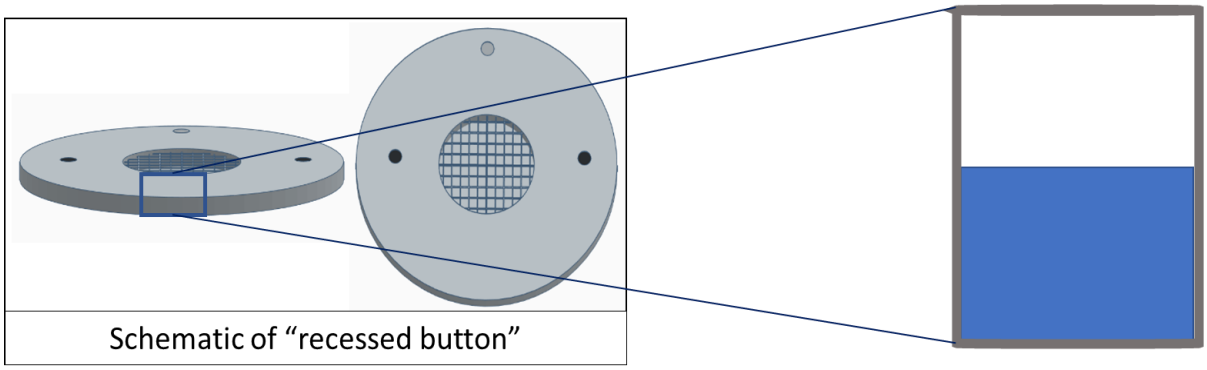

Figure 2.7 – Schematic of button as a variable path length sample holder.

cm^{-1} band as a function of volume, integrated over 1200–1290 cm^{-1}. The data shows an increase in area between 3 to 5 microliters that is not quite linear. To determine the change in path length with sample volume, the path length for each measurement was determined, as shown in the figure on the right. A variable path length transmittance cell was used to derive a

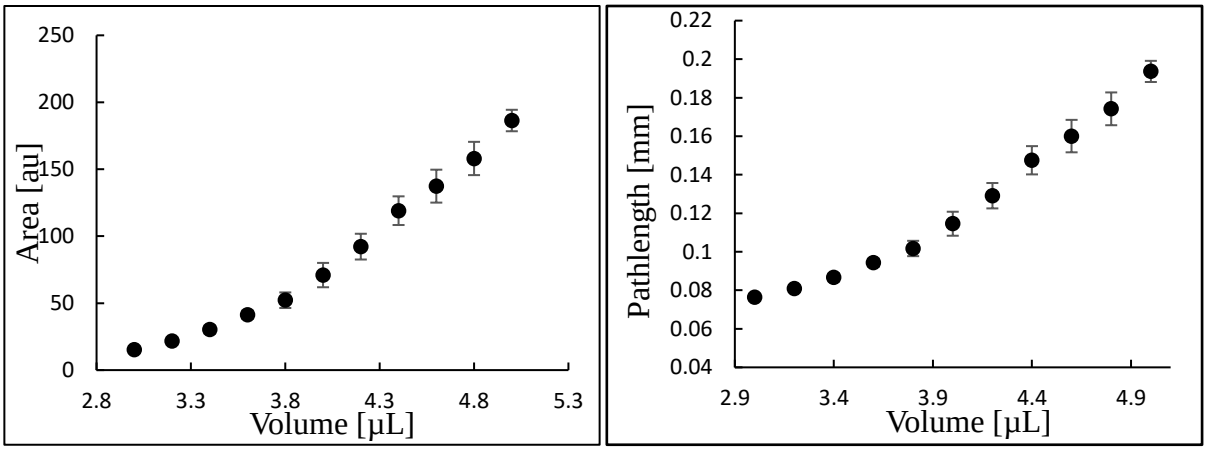

Figure 2.8 – Change in absorbance (left) and pathlength (right) with increasing quantities of mineral oil.

calibration curve by using the fringe method (Figure 2.9). The fringe method utilizes the phenomenon of constructive and destructive interference patterns when and IR beam traverses through parallel surfaces that are a finite distance apart. The interference results in a pattern on the IR spectrum consisting of peaks and valleys, from which the distance between the parallel surfaces can be determine. Equation 2.1 shows that the thickness of a sample (i.e. distance between two parallel windows) can be equated to the refractive index of the sample (n), the number of fringes between two wavenumbers (N), and the two selected wavenumbers (ν_1 and ν_2). The number of fringes can be calculated by counting the number of peaks or valleys between a starting peak or valley, respectively.

$$b = \frac{1}{2} n \times \frac{N}{(\nu_1 - \nu_2)} \quad \textbf{(2.1)}$$

The path length for each measurement was calculated from this calibration curve. Due to the variable volume displaced by the mesh wires, liquid thickness did not increase linearly with sample volume. The maximum volume tenable within the button is limited to the height within which the liquid is contained. Since the wire mesh is the limiting factor, we can expect maximum volumes to be twice the thickness of a single wire as the wire mesh is fabricated in

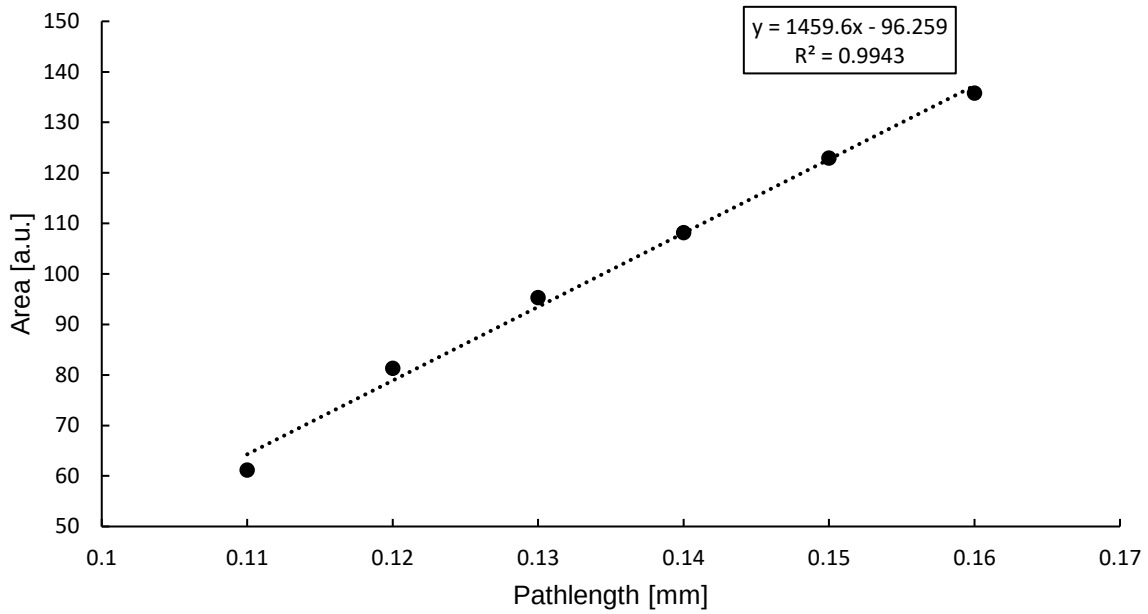

Figure 2.9 - Variable pathlength cell calibration curve.

a woven fashion. As expected, the maximum path length was about 200 µm, which was twice the wire diameter.

2.5 Analysis of Solids and Liquids

2.5.1 Solids

2.5.1.1 Analysis Using Exposed Mesh Button

One of the major advantages for buttons over traditional diffuse reflectance is the ability to analyze neat samples. For analysis, samples simply need to be placed onto the wire mesh of the button, and the particles directed into the void spaces using the flat edge of a spatula. Figure 2.10 shows an offset comparison of three measurements of silica gel. Figure 2.10A is neat silica gel measured with a button, spectrum Figure2.10B was obtained for about 7% silica gel diluted in potassium bromide, and spectrum Figure 2.10C was measured using neat silica gel. The samples employed to measure the Figure 2.10B and Figure 2.10C spectra

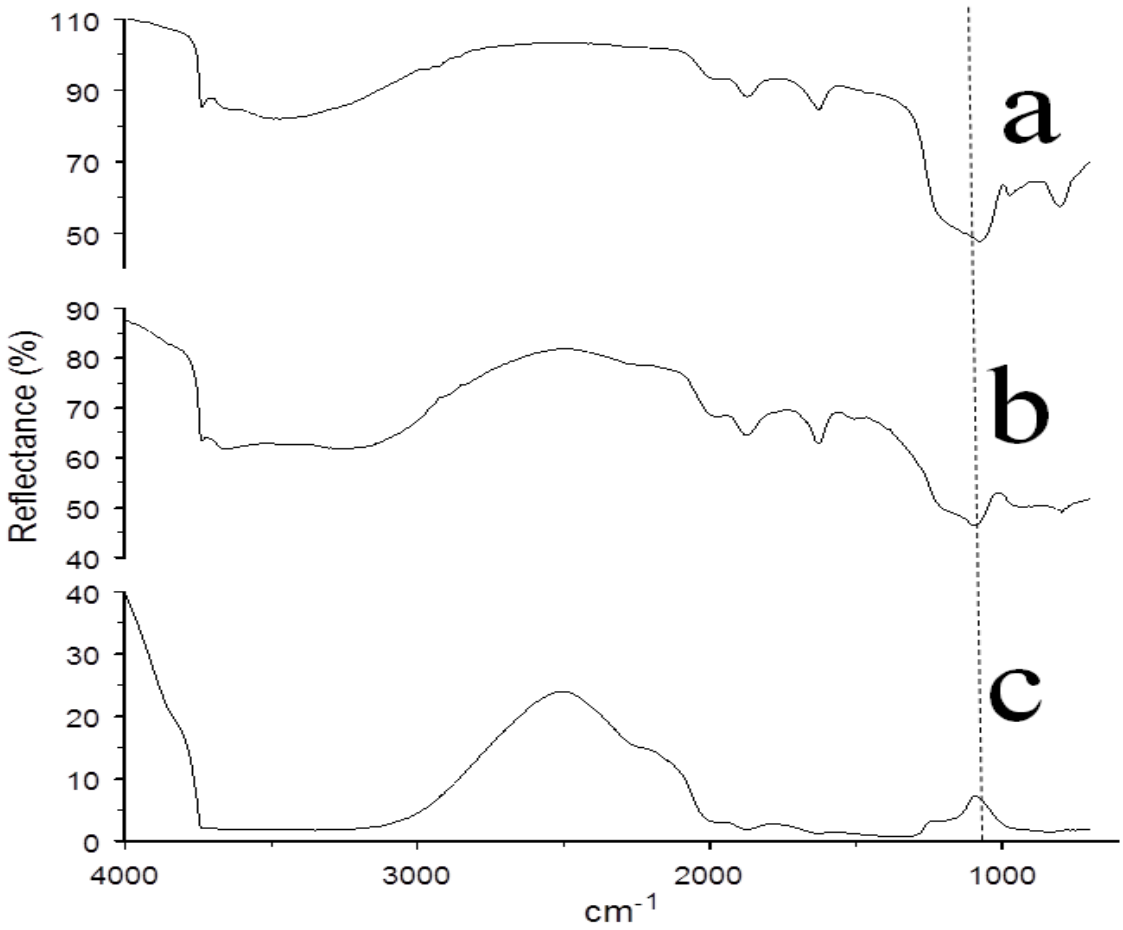

Figure 2.10 - Silica gel spectra (a) button, (b) cup, diluted with KBr, (c) cup, neat.

were placed in a traditional quarter inch dimeter, 2 mm depth diffuse reflectance cup. Figure 2.10C highlights the issues with traditional measurements of neat samples by diffuse reflectance due to excessive powder thickness, which is the bottoming out of bands and artifacts like the Reststrahlen effect. The Reststrahlen effect occurs when a band inverts. The dashed line at 1090 cm^{-1} shows the spectrum Figure 2.10C band is upside down when compared to Figure's 2.10A and B. Figure 2.10B shows an absence of the bottomed-out features and Reststrahlen effect, demonstrating the benefits of diluting samples for diffuse reflectance measurements. Figure 2.10A is similarly artifact free. While Figure's 2.10A and B are similar, distortions are still visible in the sample diluted with KBr above 3000 cm^{-1}, visible as a shoulder. This distortion arises due to electrostatic interactions between polar KBr groups

and silica gel silanol groups, causing a red shift in the OH stretching band. Thus, buttons provide artifact-free spectra that are similar to traditional spectra but without the effects of interactions between sample and diluent.

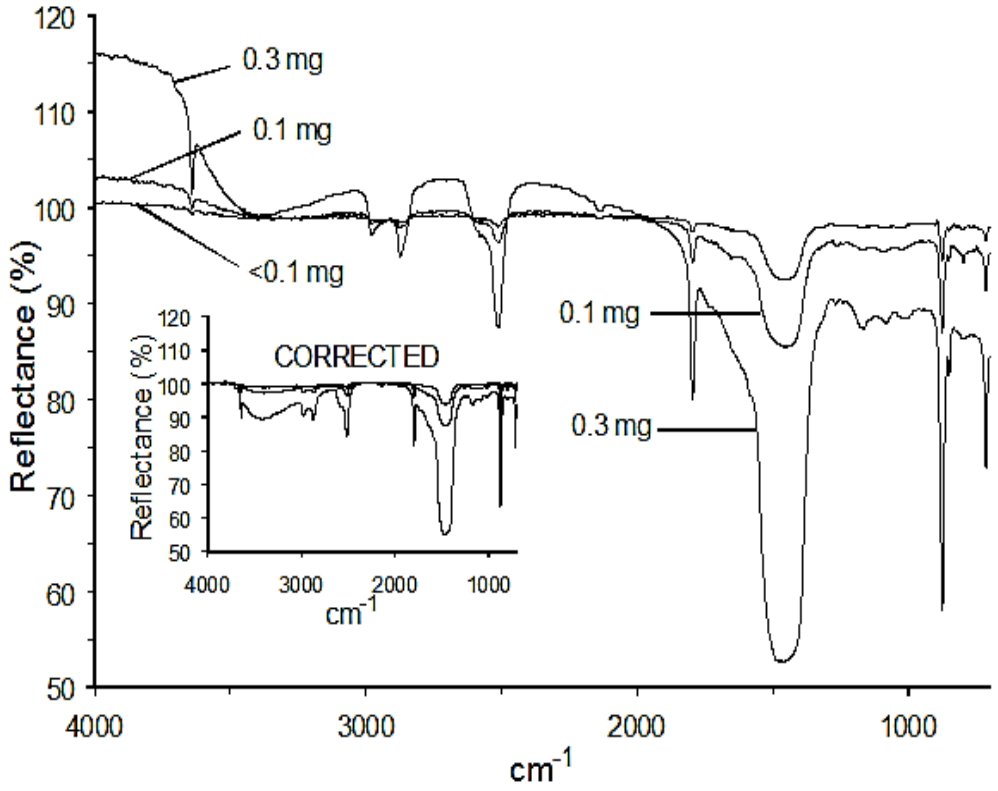

Figure 2.11 - Variable loadings of calcium carbonate on exposed mesh button.

The amount of sample added to the button impacts both the band intensity and baseline. Figure 2.11 shows the impact on spectra as increasing amounts of calcium carbonate are added to a button. As the amount of sample is increased, the baseline is affected due to increased scattering with increased quantity of powder. The spectra show that higher wavenumbers are impacted more than lower wavenumbers, as evidenced by the increasing intensities at higher wavenumber. The linear baseline slope was easily removed using correction software by subtracting a straight line going through 4000 and 2200 cm^{-1}, as demonstrated by the inset plot.

Sample thickness is dependent upon the wire mesh dimensions, being limited to a depth roughly equal to twice the wire diameter. Thin powder layers can be analyzed that are unachievable with existing diffuse reflectance sample cups. Thin sample layers permit analysis

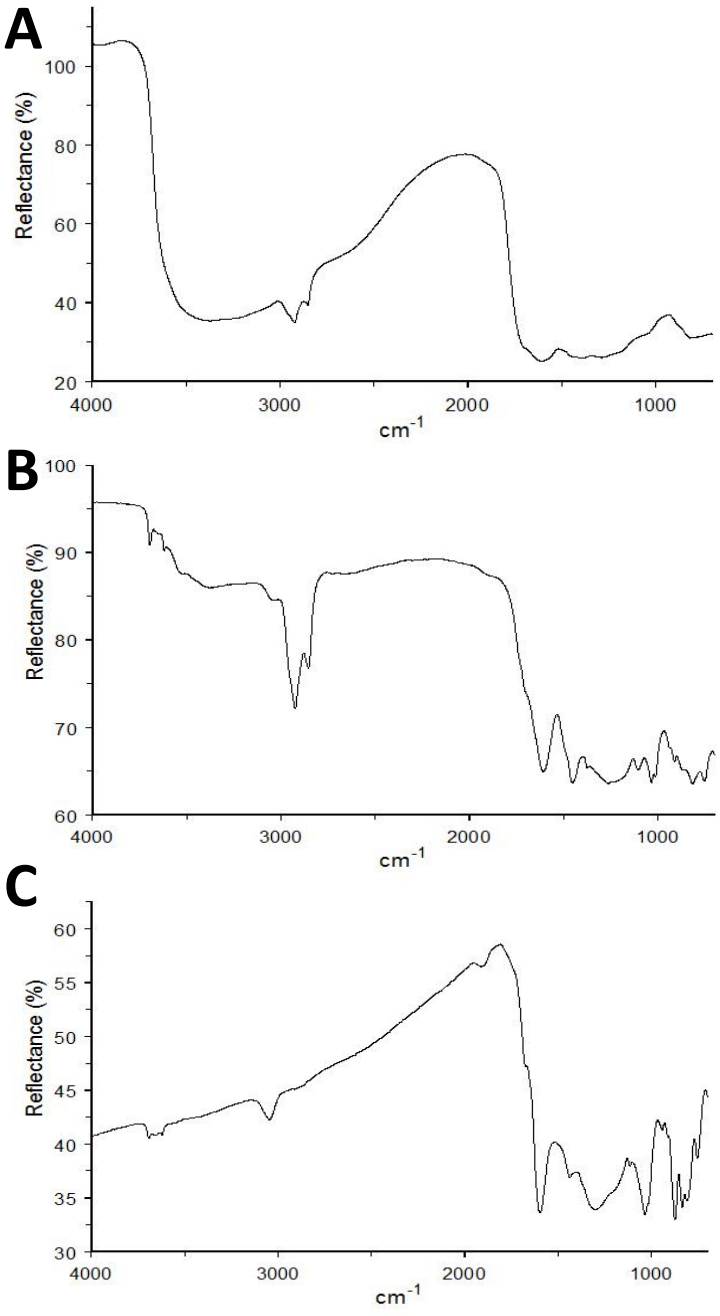

Figure 2.12 - Infrared spectra obtained for a) lignite, b) bituminous, and c) anthracite coal.

of highly absorbing samples, such as coals. Coals exhibit high absorptivity and are difficult to analyze by infrared spectroscopy. They can be analyzed by diffuse reflectance after dilution with KBr. Figure 2.12 shows coal spectra measured by using a button sample holder. Dramatic changes in these spectra show how coal structure changes with increased age, from top to bottom. The lignite spectra contains a broad OH stretching vibration band, likely arising from cellulosic oxygen. Compared to lignite, the Bituminous coal spectrum shows a decrease in OH band intensity and the presence of CH functional groups, which is consistent with increased conversion to carbon. The Anthracite spectrum reveals mostly carbon-carbon absorbance bands with little OH stretching vibration band absorbance, suggesting a high carbon content.

2.5.1.2 Abrasive Button-IR

Because button-IR can be applied to neat samples (i.e. without non-absorbing matrix dilution), removing material by rubbing a surface with the rough exposed wire mesh of a button is sufficient to prepare samples for infrared analysis. The spectrum in Figure 2.13 illustrates an example of using abrasive button sampling to obtain a representative sample from the

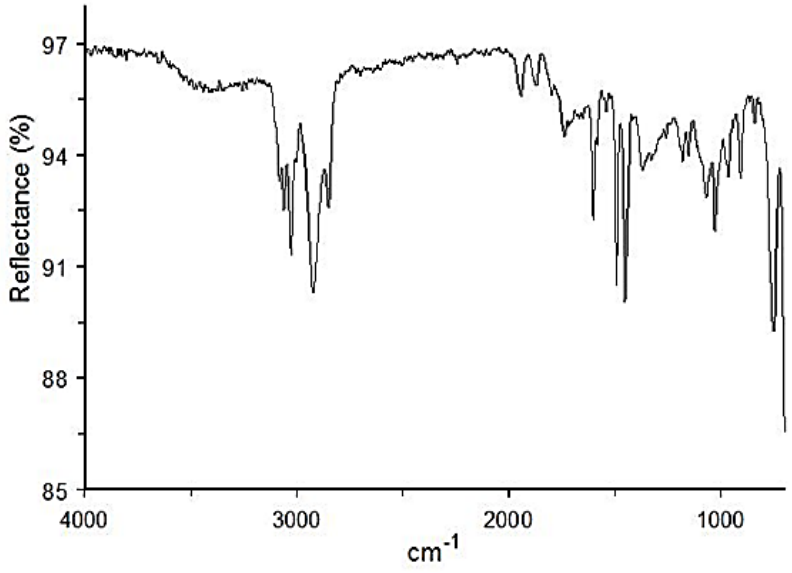

Figure 2.13 - Abrasive button-IR 3.5-inch floppy disk infrared spectrum.

surface of a 3.5-inch floppy disk. The wire mesh surface removed small pieces of the plastic surface, which were trapped within the mesh void spaces. The infrared spectrum is characteristic of polystyrene, so the floppy disk case was confirmed to consist of this polymer.[68] Abrasive button-IR was applied in the analysis of pharmaceuticals, which can be analyzed immediately after transferring material from a tablet to the button wire mesh void spaces.[62] This can be accomplished quickly and easily by rubbing the button sample holder exposed stainless-steel wire mesh across a tablet surface. The rough mesh dislodges and traps some of the tablet surface. Tablet fragments removed by abrasive sampling will be separated by size due to the sieving properties of the mesh. Smaller pieces occupy mesh void spaces whereas larger tablet fragments will remain at the mesh surface. Larger tablet fragments can be removed by brushing the mesh surface before placing the button into the infrared spectrophotometer for measurements. The sampling process is faster and simpler than conventional diffuse reflection or KBr pellet analyses because diluent is not required. Additionally, spectrum measurement signal-to-noise ratios increase by up to a factor of 20, which is typical of dilution factors employed with these infrared analysis methods. Button abrasive sampling also requires less effort than attenuated total reflectance (ATR) methods, which require tablet grinding prior to analysis and necessitate sample removal and solvent cleaning of the ATR crystal to prepare for subsequent analyses.[69] Button abrasive sampling yields small quantities (ca. µg) of solid material that is held in place by the rigid mesh structure. After loading a sample, buttons can be manipulated and transported without disturbing the trapped particles, thereby yielding reproducible measurements, and allowing samples to be stored indefinitely.

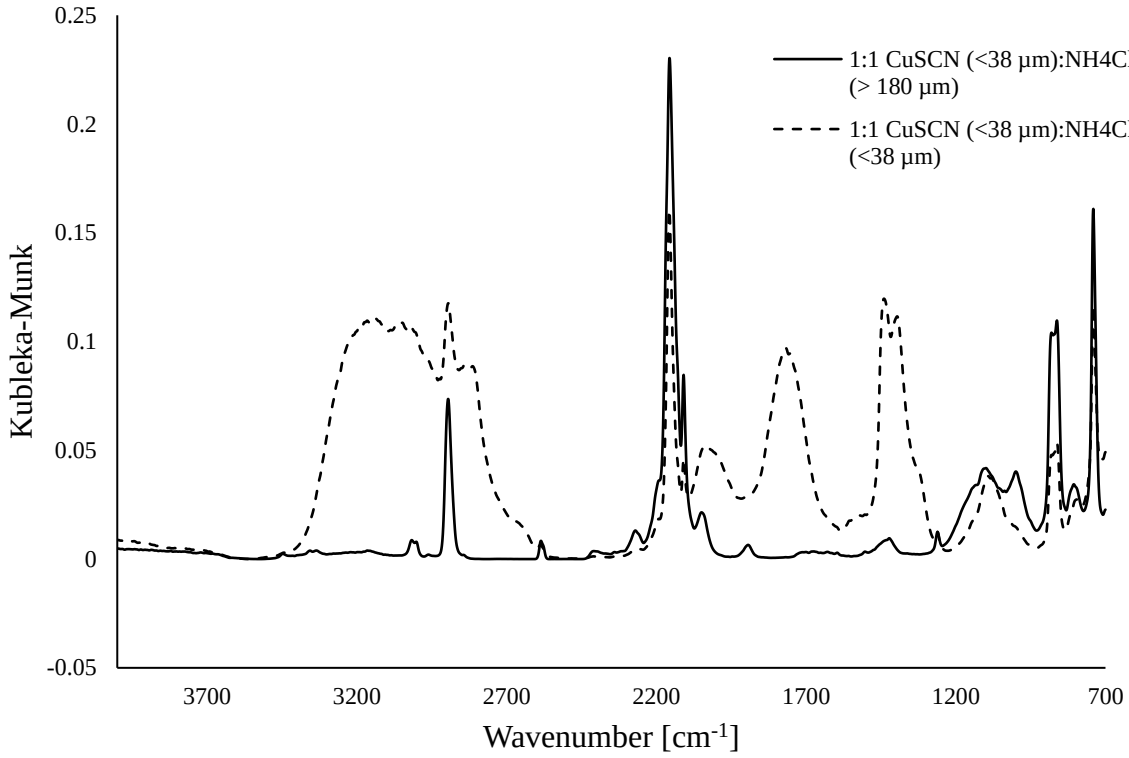

Figure 2.14 – Infrared spectra of CuSCN and NH_4Cl mixtures.

Unlike traditional abrasive sampling methodologies, for which the sampled particle size distribution is a concern, the wire mesh openings limit the sizes of particles that can be accommodated within the wire mesh. The inherent sieving properties of the exposed wire mesh button are illustrated by Figure 2.14. Mixtures (1:1 w/w) of ammonium chloride (NH_4Cl) and copper thiocyanate (CuSCN) powders having different particle size distributions were prepared. The CuSCN powder was sieved to obtain particles with sizes that were smaller than 38 µm. The NH_4Cl powder was sieved to prepare two samples, one with particle sizes that were larger than180 µm, and one containing particles that were smaller than 38 µm. Mixtures of these two substances, which exhibit significantly different infrared spectra, were used to test the sieving efficiency of a 200 mesh button. The 200 mesh button contained 86 µm square openings, so particles larger than 180 µm would be excluded from the mesh void space but particles smaller than 38 µm would be accommodated. The button-IR spectrum for the CuSCN

Table 2.1 – Commercial pharmaceutical tablet properties.

Tablet	Designation	Color/Shape	Active Ingredient(s) API(s)	API Mass (mg)	Tablet Mass (mg)
Advil Ibuprofen	A-IBP	Red/Round	Ibuprofen	200	470
Equate Ibuprofen	E-IBP	Red/Round	Ibuprofen	200	320
Equate PM	E-PM	Blue/Oval	Ibuprofen / Diphenhydramine citrate	200 / 38	500

and NH_4Cl 1:1 mixture containing <38 μm particles of each material was the sum of the infrared spectra for the pure substances. The dashed line spectrum in Figure 2.14 included a broad band over the 3300-2800 cm^{-1} range that was characteristic of NH_4Cl and a sharp peak near 2200 cm^{-1} representing CuSCN. In contrast, the button-IR spectrum obtained for the 1:1 mixture containing >180 μm NH_4Cl particles exhibited only CuSCN features. When particles for both materials were small enough to fit into mesh void spaces, infrared spectral features for both substances appeared in spectra. When the NH_4Cl mixture particles were larger than the mesh void openings, only the CuSCN powder remained after the excess material was swept from the mesh surface.

To evaluate the potential of using abrasive button sampling and mid-infrared spectroscopy to identify counterfeit pharmaceuticals, infrared spectra of commercially available ibuprofen tablets were measured. Spectra that were representative of the exterior and interior compositions of three tablets containing ibuprofen (Table 1) were compared. Ibuprofen was the sole active ingredient in the A-IBP and E-IBP formulations. E-PM tablets contained diphenhydramine citrate antihistamine in addition to ibuprofen. All three tablets had coatings to protect active ingredients from exposure to biological and chemical degradation agents.

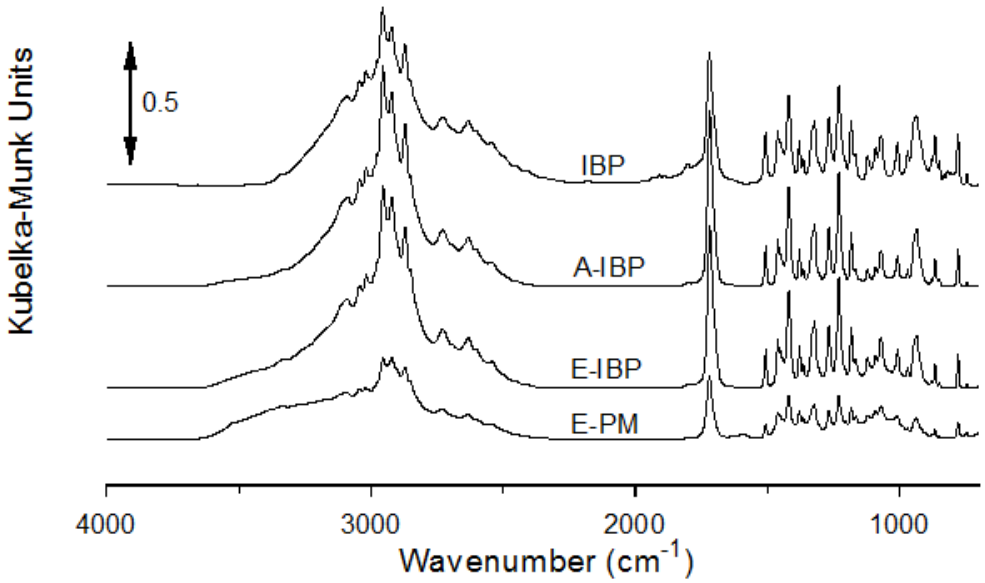

Figure 2.15 - Tablet interior infrared spectra.

The active ingredients of each tablet were sampled by cutting them open and rubbing the button sample holder mesh across the freshly exposed surface. This process was repeated for 30 different measurements for each of the three formulations. Averages of the 30 different infrared spectrum measurements obtained after sampling are shown in Figure 2.15. For reference, the top spectrum (IBP) was obtained from pure ibuprofen. As expected, the A-IBP and E-IBP interior spectra are very similar to the pure ibuprofen spectrum. Although many of the ibuprofen fingerprint region spectral features are evident in the E-PM interior spectrum, absorbance bands for other components are also visible. Based on the Figure 2.15 infrared spectra, all three formulations contained ibuprofen, but concentrations were highest in the A-IBP and E-IBP tablets. Although it is reasonable to expect that an E-PM tablet could be distinguished from the A-IBP and E-IBP tablets by infrared spectrum comparisons, differentiation between the A-IBP and E-IBP tablet compositions would be more difficult.

Figure 2.16 shows infrared spectra obtained from the three tablet coatings. Like the interior spectra (Figure 2.15), averages of 30 spectrum measurements are shown. Infrared

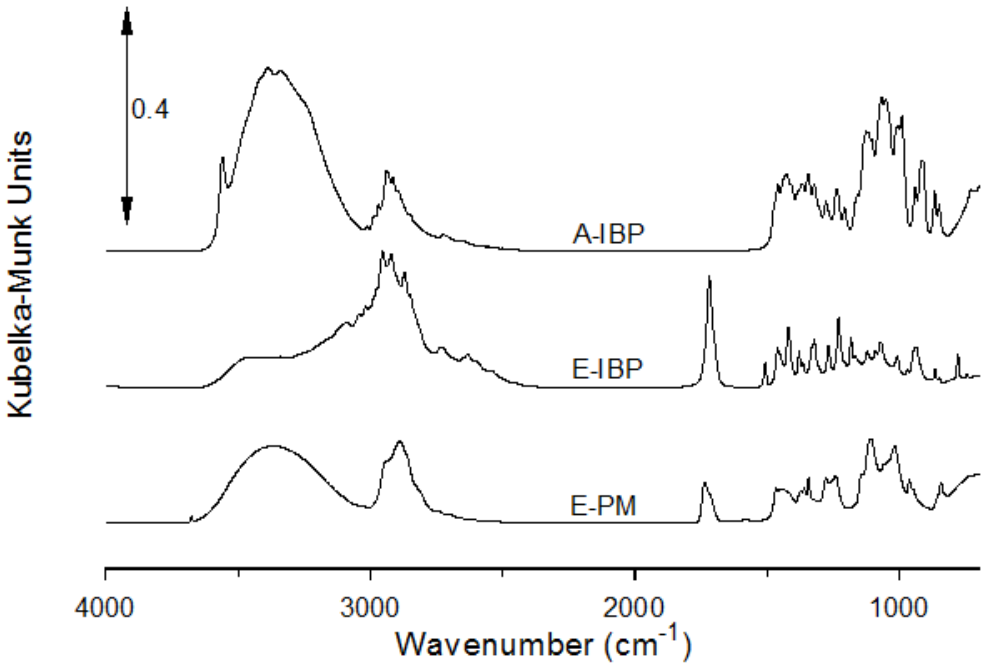

Figure 2.16 - Tablet coating infrared spectra.

spectra for the three exterior coatings differed substantially. The A-IBP coating spectrum exhibits a broad OH stretching vibration band that is likely due to excipients in the formulation, including hydroxypropyl methylcellulose[70-72] and croscarmellose sodium.[73-75] The shoulder at 3560 cm^{-1} may indicate the presence of polysorbate 80.[76-78] The E-IBP coating spectrum contains a sharp band near 1700 cm^{-1} characteristic of the C=O stretching vibration of ibuprofen that is not present in the A-IBP spectrum.[79-81] This band may be due to incorporation of ibuprofen in the coating, or because a thinner coating was used to make the E-IBP tablets, resulting in part of the interior being sampled when the coating surface was removed for analysis. Like the E-IBP spectrum, the E-PM spectrum contains a band near 1700 cm^{-1}, indicating the presence of ibuprofen. However, the E-PM spectrum differs substantially from the E-IBP spectrum above 2800 cm^{-1}, indicating that the E-PM and E-IBP coatings had different compositions. The three tablet coating infrared spectra are substantially different, suggesting that they could be distinguished based on infrared spectroscopy measurements.

Spectra shown in Figures 2.15 and 2.16 can be grouped into six categories, defined by the tablet manufacturer and the location (coating or interior) of the sampled material. In order to identify counterfeit pharmaceutical formulations by infrared spectroscopy, spectrum measurements must provide sufficient sensitivity to detect differences between valid and counterfeit formulations. Furthermore, the reproducibility of infrared spectra obtained for samples with the same composition should reflect the repeatability of the tablet manufacturing process. Therefore, to identify counterfeit formulations, infrared spectrum measurements must be reproducible, so that samples from the same category yield similar results. Also, spectrum measurements must exhibit adequate sensitivity, so that spectra representing different sample categories can be differentiated. Principal component analysis (PCA) can be used to characterize the reproducibility and sensitivity of tablet spectrum measurements obtained by using the button sample holder. PCA is an unsupervised statistical learning technique that reduces data set dimensionality based on variance considerations and reveals cluster patterns. Although direct comparisons of spectra allows for identification of features unique to each group and can be used to differentiate groups, PCA plots provide visualizations of the sensitivity and reproducibility of categorized spectral data.

Because PCA is primarily a shape discrimination technique, spectra are typically baseline corrected and normalized to reduce sample composition independent variability before applying this statistical method. For example, the effects of data pre-processing steps on the 30 infrared spectra obtained from material sampled from A-IBP tablet interiors are depicted in Figure 2.17. Figure 2.17a shows overlaid plots of the 30 spectra. Baseline slopes are evident in all of these spectra, along with reflectance values that exceed 100% at higher wavenumbers. These features can be attributed to greater diffuse reflection when sample

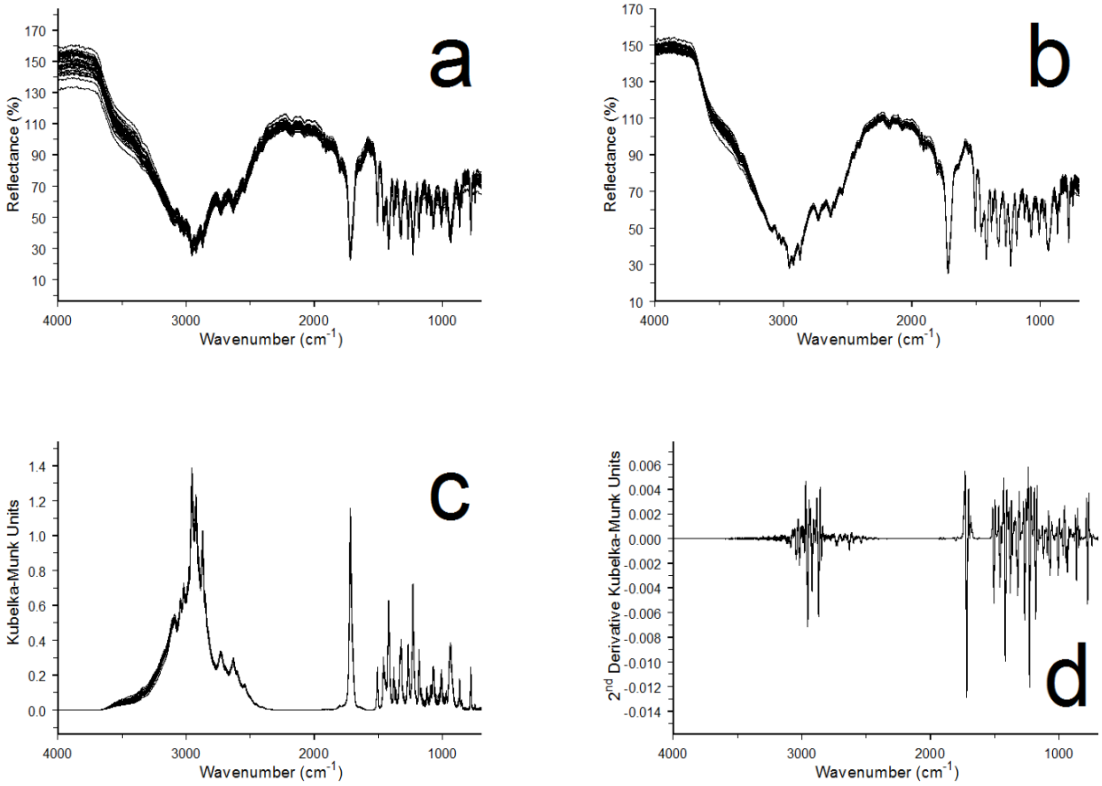

Figure 2.17 - Effects of pre-processing for the A-IBP samples: (a) measured spectra; (b) after multiplicative scatter correction; (c) Kubelka-Munk format; (d) second derivative.

particles are present within button mesh void spaces. The effect is more pronounced at higher wavenumbers, causing baseline reflectance to exceed 100% near 4000 cm^{-1}.[23] The spectra shown in Figure 2.17a overlap better at lower wavenumbers, which may be due to differences in the sizes of tablet fragments that were removed by the button. To compensate for spectrum variabilities that were unrelated to sample composition, multiplicative scattering corrections (MSC) were applied to the spectra within each group. MSC is a commonly used normalization technique that adjusts individual spectra to better match a reference, which is typically the data set mean, by adjusting offsets and scaling.[36] As shown in Figure 2.17b, overlaps between the 30 spectra improved after applying MSC. Figure 2.17c shows the results obtained after removing baseline slopes from the spectra in Figure 2.17b and then converting to the Kubelka-

Munk format, which is proportional to solid sample analyte concentrations. The overlaid spectra in Figure 2.17c exhibit better reproducibility at lower wavenumbers, with the greatest variations evident above 3000 cm^{-1}. Similar reproducibility trends are apparent in Figure

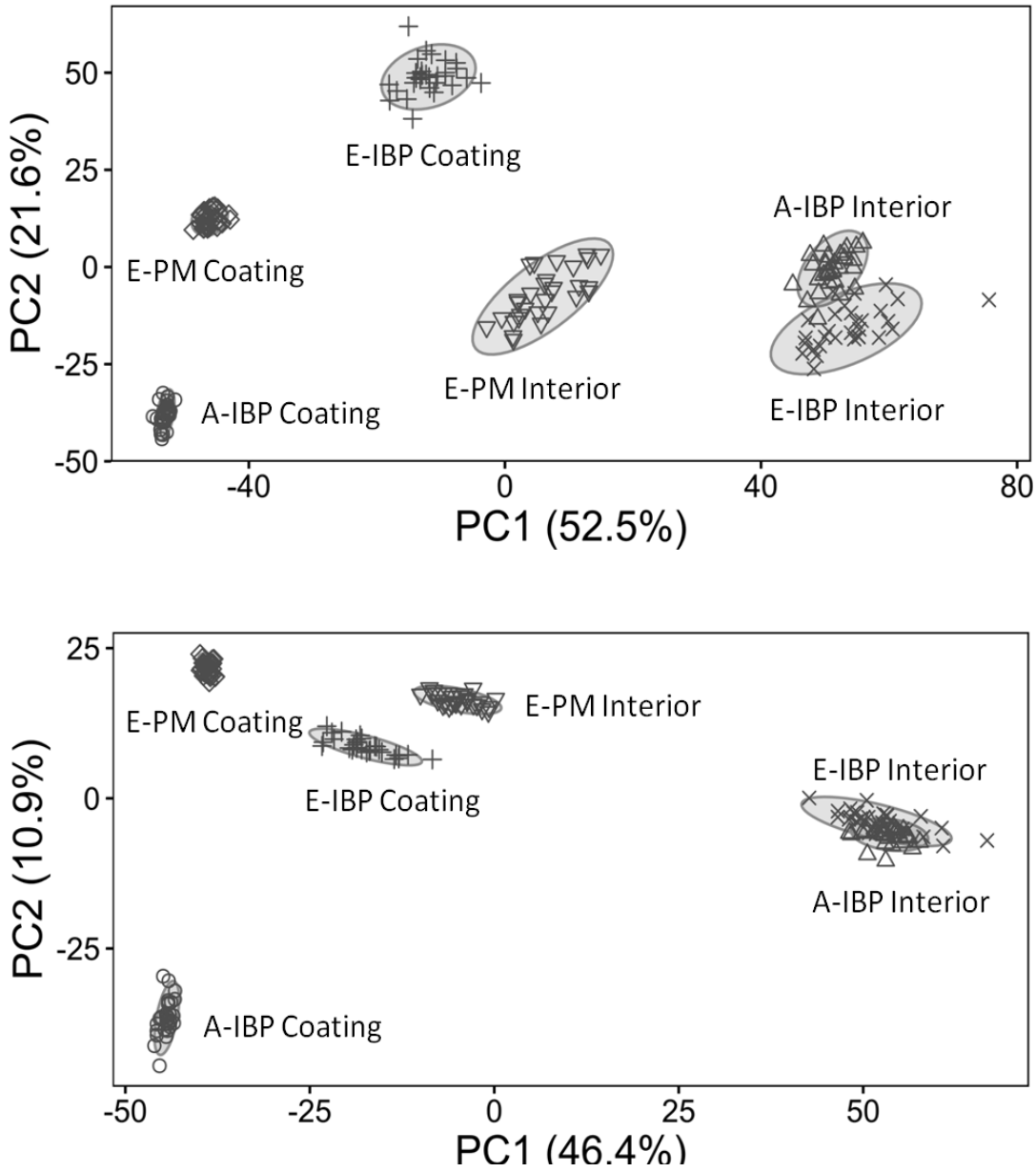

Figure 2.18 - Top: PCA results derived from Kubelka-Munk spectra. Bottom: PCA results derived from second derivative spectra. Full spectrum range (4000–700 cm^{-1}) was employed.

2.17d, which shows overlaid second derivatives that were derived from the Kubelka-Munk spectra in Figure 2.17c.

Figure 2.18 shows the PCA classification results obtained from the 180 tablet spectra. The ellipses around different groups represent a 95% confidence interval. For each category,

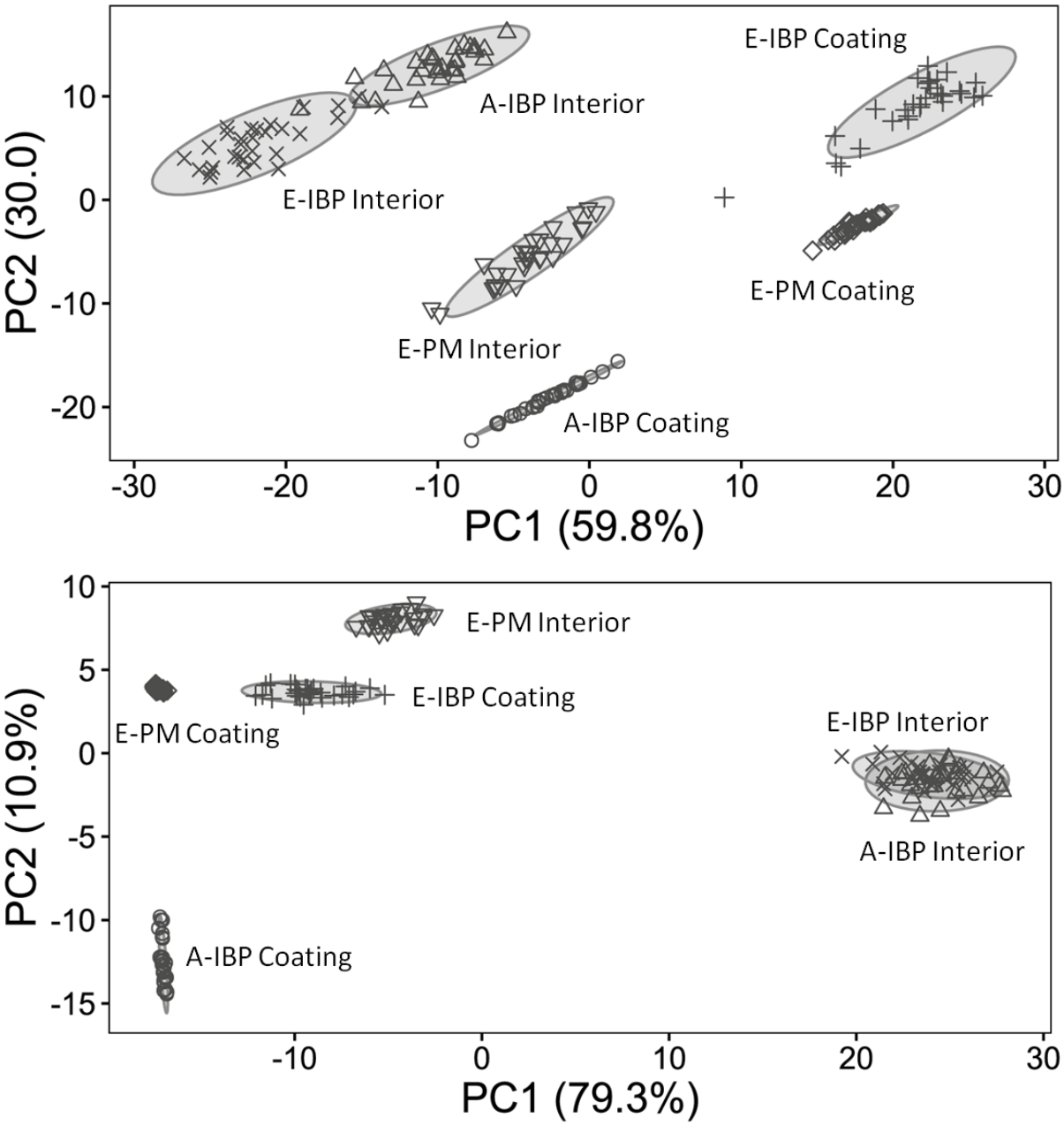

Figure 2.19 - Top: PCA results derived from Kubelka-Munk spectra. Bottom: PCA results derived from second derivative spectra. Fingerprint region (1530–1150 cm^{-1}) was employed.

spectra obtained from material removed from tablet coatings and interiors were pre-processed in the same manner as described for the A-IBP interior spectra, yielding trends similar to those depicted in Figure 2.17. The top graph in Figure 2.18 was obtained from pre-processed Kubelka-Munk spectra representing each category (e.g. Figure 2.17c). PCA clustering shows that the three tablet coatings could be distinguished and that the E-PM interior spectra were statistically different from the A-IBP and E-IBP spectra. The A-IBP and E-IBP interior spectra were the most similar, resulting in category overlaps.

The bottom graph in Figure 2.18 shows the results of applying PCA to the second derivative of the pre-processed Kubelka-Munk spectra (e.g. Figure 2.17d). Calculating the second derivative minimizes effects from baseline fluctuations.[82-84] Compared to the PCA results derived from the Kubelka-Munk spectra (top), the second derivative PCA results exhibit less variation within categories. The overlap of the A-IBP and E-IBP interior spectra groups was greater when second derivatives were used for PCA. This discrepancy suggests that the partial separation of these groups in the top graph was due to subtle baseline differences, which were effectively eliminated in the second derivatives. These differences, which are not readily apparent in measured spectra (Figure 2.15), may be caused by texture differences in Advil and Equate tablet interiors. These differences could affect the sizes and shapes of the tablet fragments removed by using the button mesh, which may affect spectra, especially their baselines.

The spectral region employed to create the vectors defining the PCA multidimensional space can affect group clustering patterns. Figure 2.19 shows PCA results that were calculated by using only those absorbance bands contained within the 1530-1150 cm^{-1} fingerprint region of acquired spectra. The top PCA plot in Figure 2.19 was derived from Kubelka-Munk spectra

that had been pre-processed by MSC and baseline correction. The bottom PCA graph shows results obtained by using the second derivatives in the 1530–1150 cm^{-1} regions of Kubelka-Munk spectra. When compared to the Figure 2.18 PCA plots, the first two principal components associated with the Figure 2.19 results accounted for a larger fraction of the data set variance. Whereas the Figure 2.18 top and bottom PCA graphs represented 74 and 57 percent of the total variance, each of the plots in Figure 2.19 accounted for 90 percent of the variance. Like the top PCA graph in Figure 2.18, the Kubelka-Munk PCA results shown at the top of Figure 2.19 show substantial separation of the A-IBP and E-IBP interior groups. Interestingly, the bottom PCA graphs in Figures 2.18 and 2.19 are very similar. The lack of A-IBP and E-IBP interior group separation in these graphs suggests that subtle baseline differences in the 1530–1150 cm^{-1} region of the infrared spectra measured for these materials were responsible for discrimination of these groups in the Figure 2.18 and 2.19 top spectra. Apparently, these differences were lost after second derivative calculations.

Infrared spectra that are representative of pharmaceutical formulations can be quickly and easily obtained by using the exposed wire mesh of a button sample holder to remove small quantities from tablet surfaces. Unlike ATR and KBr pellet methodologies, grinding is not required prior to analyses because the wire mesh selectively retains small particles removed by abrasion, excluding those that are too large to fit within mesh void spaces. Material removed from tablets can be quickly and easily analyzed by placing loaded mesh buttons on a sample introduction slide which permits sample insertion into the FTIR. The process of tablet sampling and subsequent infrared spectrum measurement can be completed in a matter of seconds. PCA results indicate that abrasive sampling with a button sample holder provides adequate measurement reproducibility and sensitivity to distinguish between different tablet

coatings and to confirm that API compositions are the same or different. The ease of use, fast analysis times, and sensitivity demonstrated by the feasibility study described here suggests that this method should be applicable to detection of counterfeit pharmaceuticals.

This methodology can be fine-tuned by using different mesh sizes to optimize sample surface abrasion and trapping material with desired particle size distributions. In addition, the technique is compatible with handheld infrared spectrophotometers, which would facilitate on-site pharmaceutical product testing.

2.5.1.3 Quantitative Analysis

Solid sample quantitative analysis capabilities were evaluated for both powders and liquid-to-solid depositions by measuring spectra for mixtures containing benzoic acid and ammonium chloride. The 1685 cm^{-1} carbonyl stretching vibration band was used to quantify benzoic acid standard mixtures, which ranged in concentration from 1.25 to 10% (w/w) in potassium bromide. Figure 2.20A shows the calibration curve generated by plotting integrated band area between 1629–1737 cm^{-1} versus benzoic acid concentration. Averages of 3 replicate measurements are plotted and error bars represent ± 1 standard deviation. Linear functions (R^2 > 0.98) were obtained. For ammonium chloride, two bands, 1440 and 1764 cm^{-1}, were used

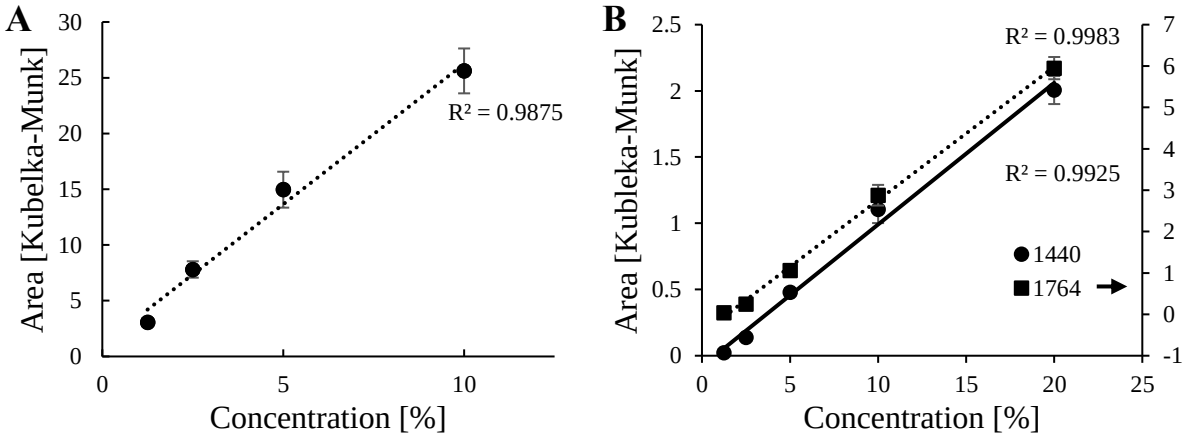

Figure 2.20 - Standard curve for a) benzoic acid and b) liquid-to-solid deposition ammonium chloride.

for quantification of standard mixtures deposited from liquid, ranging in concentration from 1.25 to 20% (w/v). Figure 2.20B shows the calibration curves generated by plotting integrated band area between 1408–1490 cm^{-1} and 1580–1900 cm^{-1} versus ammonium chloride concentration. Averages of 3 replicate measurements are plotted and error bars represent ± 1 standard deviation. Linear functions ($R^2 > 0.98$) were obtained.

2.5.2 Liquids

2.5.2.1 Analysis using Recessed Button

The properties of a recessed button sample holder when used for infrared spectroscopy studies of liquids were characterized by measuring paraffin oil spectra. This high boiling point liquid was selected to minimize sample thickness changes from evaporation. Because the process by which liquid samples interacted with infrared radiation involved both transmission and reflectance, it was categorized as a "transflectance" technique.[85-87] The diagrams in Figure 2.5 (section 2.4) shows button reflectivity with different sample types loaded. The drawing on the right side of Figure 2.5 depicts three incident rays when a homogeneous liquid is present. The horizontal dashed line represents the liquid surface. Radiation that passes through the air/liquid boundary can be absorbed, but also refracts, causing ray paths to be altered when compared to the empty button. The center ray, which reflects from the button backing, leaves the liquid surface at a slightly different location, but at the same angle that it reflects from the empty button. Rays contributing to diffuse reflectance spectra must penetrate the liquid and also reflect from a wire. In contrast, specular reflectance absorbance contributions result from rays that reflect from the backing but do not strike a wire surface.

Figure 2.21 shows paraffin oil infrared spectra obtained by using a transmittance cell and those obtained when the oil was loaded into a button and then oriented to collect specular

and diffuse reflectance spectra. Spectrum baselines are offset to prevent curve overlaps. The most intense paraffin oil spectral features in Figure 2.21 are consistent with those previously reported by using transmittance spectroscopy.[88-89] Overlapping bands near 2900 cm^{-1} can be assigned to C-H stretching vibrations and the two bands below 1500 cm^{-1} are indicative of hydrocarbon bending vibrations.[90]. The spectrum denoted "film" in Figure 2.21a was obtained by placing a few drops of paraffin oil between two NaCl windows and then compressing them to remove excess, creating a thin layer between the windows. This spectrum exhibits overlapping C-H stretching vibration bands near 2950, 2920, and 2850 cm^{-1} and bending vibration bands near 1460 and 1380 cm^{-1}. A 0.012 mm thick Teflon spacer was inserted between the NaCl windows to prepare a fixed path length paraffin oil sample. The transmittance spectrum for this sample is shown below the thin film spectrum in Figure 2.21a. Compared to the film spectrum, the overlapping C-H stretching vibration peaks are missing, bands are broader, and relative intensities of lower absorptivity bands (in particular at 720 cm^{-1}) are enhanced.

Although the modified wire mesh button could be used to obtain specular reflectance infrared spectra, employing a blank button (i.e. without mesh) to hold the liquid sample was preferred for two reasons. First, about 50% of specularly reflected radiation was not collected when the wire mesh was present. Thus, measurement signal-to-noise ratios were higher without the mesh. Second, radiation specularly reflecting from the tops of the mesh wires did not penetrate the liquid and therefore did not contribute to infrared spectrum features. Because a detector signal derived from this radiation was always present, the full 0–100% transflectance intensity range could not be accessed. This limited the range of band intensities that could be obtained and degraded measurement sensitivity.

To make thin film specular reflectance measurements, the paraffin oil was placed inside a blank button reservoir (i.e. containing no wire mesh) by adding a small drop and then using a stream of nitrogen gas to distribute it evenly and remove excess. As expected, the spectrum of this film (Figure 2.21b) contains the same features as the corresponding Figure 2.21a transmittance spectrum. The lower spectrum in Figure 2.21b was obtained by specular reflectance after adding 1 µL of oil to the blank button reservoir. Based on the dimensions of the reservoir indentation, this volume should have created a 0.032 mm thick layer. However, the sample thickness was less than this at the infrared beam focal point because tilting the button at 31^{o} relative to vertical caused the oil to flow towards the low end of the reservoir, resulting in an uneven distribution that was thinner at the center of the reservoir. The Figure 2.21b lower spectrum is similar to the 0.012 mm transmittance spectrum. Both Figure 2.21b spectra were derived from infrared radiation passing through the paraffin oil layer twice. Therefore, these spectra should resemble transmittance spectra obtained by using a cell path length of about twice the liquid layer thickness.

The top spectrum in Figure 2.21c was obtained for a thin layer of oil contained in a modified wire mesh button (Figure 2.2) by using the diffuse reflectance measurement mode. The same procedure used to prepare the paraffin oil thin film in the blank button reservoir was used to make the sample for diffuse reflectance measurements. In addition to the dominant C-H stretching and bending vibration bands also found in the transmittance and specular reflectance spectra, small peaks appear below 1200 cm^{-1} that are not visible in the other film spectra. Like the Figure 2.21b 1 µL specular reflectance spectrum, the Figure 2.21c 1 µL diffuse reflectance spectrum contains peaks for lower absorptivity vibration bands. However, unlike the Figure 2.21b 1 µL specular reflectance spectrum, the three overlapping C-H

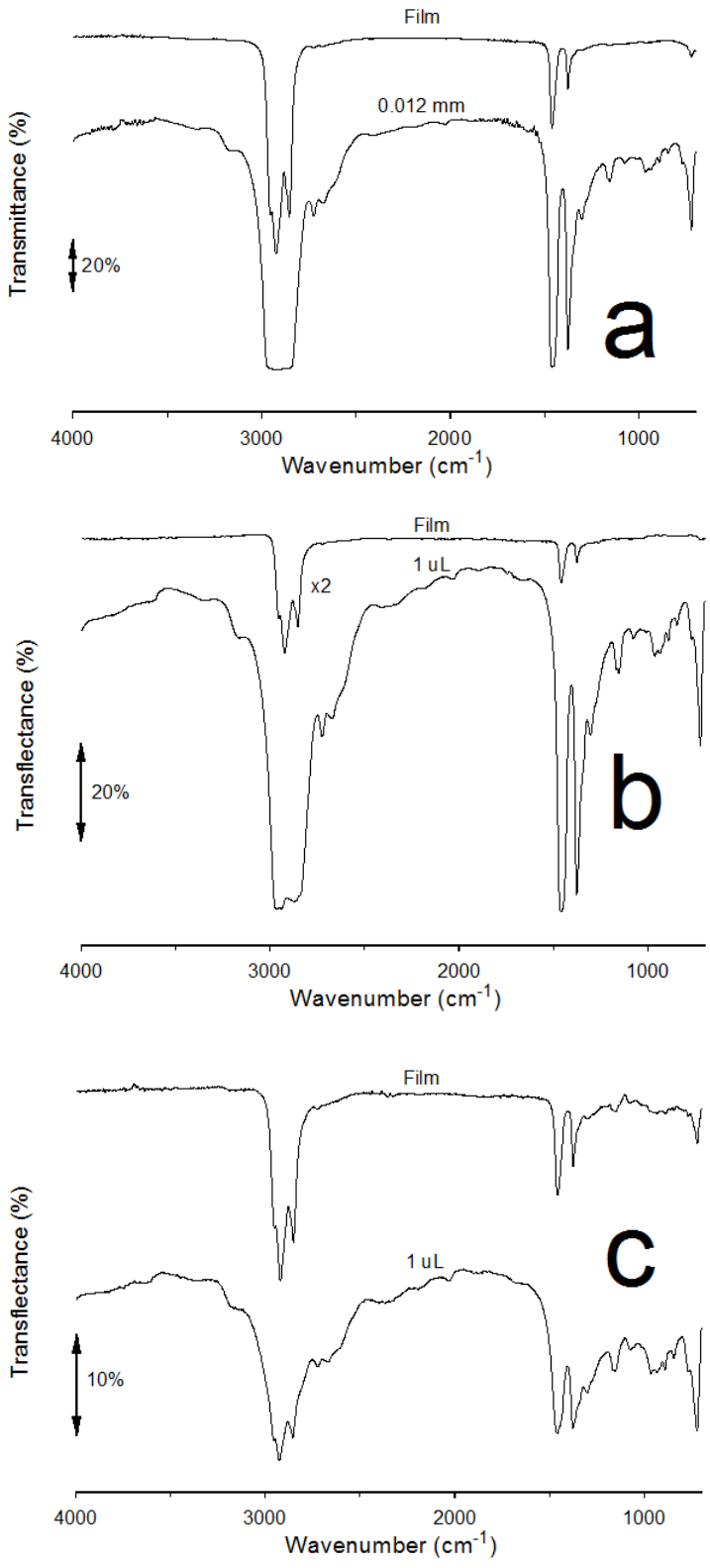

Figure 2.21 – Paraffin oil infrared spectra measured by using (a) transmittance, (b) button specular reflectance, and (c) button diffuse reflectance.

stretching vibration peaks near 2900 cm^{-1} remain in the diffuse reflectance spectrum. The persistence of these overlapping peaks may be explained by the impact of disparate radiation penetration distances through the oil layer.

2.5.2.2 Multiple Pathlengths in Liquids

The effects of multiple radiation path lengths on diffuse reflectance button spectra are exemplified by the paraffin oil spectra in Figure 2.22. The dashed line was measured by diffuse reflectance after placing 3.75 µL of the oil into the modified button reservoir. The dotted line spectrum was obtained with a 0.17 mm fixed path length transmission cell. The 0.17 mm path length was selected because it provided spectra with intensities similar to those obtained by

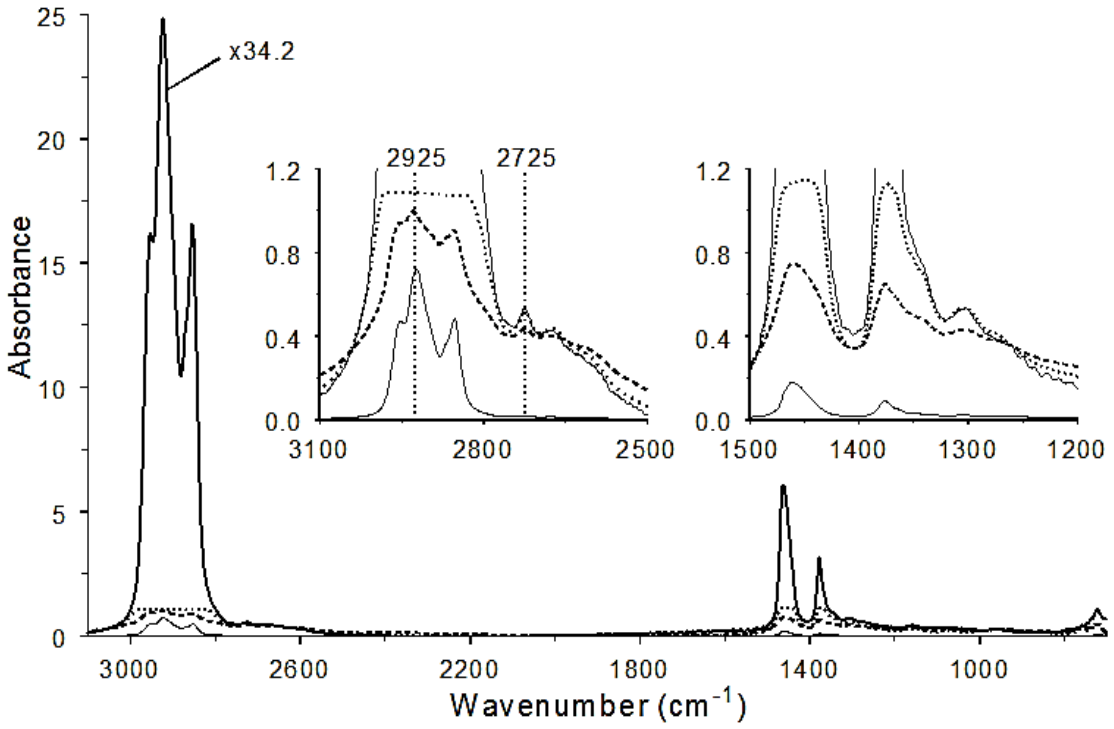

Figure 2.22 - Paraffin oil infrared spectra obtained by diffuse reflection (dashed line) and by using transmission cells containing a thin film (solid lines) and incorporating a 0.17 mm spacer (dotted line).

using the diffuse reflection optics and the button sample holder. The characteristic overlapping C-H stretching vibration band profile in the thin film spectrum is absent in the 0.17 mm path length spectrum. This can be attributed to insufficient measurement sensitivity, which is a well-known limitation of spectrophotometers.[91] The absorbance at which the spectrum flattens is determined by the ability of the detector to distinguish between similar low intensity radiation fluxes, which depends on the spectrophotometer design. The thin film plot that spans 25 absorbance units was calculated by multiplying the measured spectrum by a factor of 34.2. This scaling was implemented to increase the thin film spectrum intensities to better match the button and 0.17 mm transmission cell spectrum intensities below 0.5 absorbance units. Thus, the scaled spectrum represents what the 0.17 mm absorbance spectrum would have been if the FTIR measurement sensitivity was unlimited. Interestingly, the diffuse reflection button spectrum (dashed line) retains the 2980–2820 cm^{-1} overlapping peak profile that is missing from the 0.17 mm path length transmission cell spectrum. Like the thin film spectrum, the intensities of the bending vibration bands at 1460 and 1376 cm^{-1} are lower than the C-H stretching vibration band maximum at 2925 cm^{-1}. In contrast, absorbance values at 2925, 1460 and 1376 cm^{-1} are similar in the 0.17 mm transmission cell absorbance spectrum and the 1460 cm^{-1} band appears flattened when compared to the thin film transmission cell and button diffuse reflection spectra.

Assuming that transmission cell spectrum intensities obey Beer's law ($A_\lambda = a_\lambda bc$) and that concentration (c) and sample absorptivities (a_λ) were constants, absorbance should be directly proportional to path length (b) at all wavenumbers. The expanded plots in Figure 2.22 show that the scaled thin layer and 0.17 mm path length transmission cell paraffin oil spectra were similar below 0.5 absorbance units, which is consistent with Beer's law. However, large

discrepancies are apparent between 2980 and 2820 cm^{-1}. The scaled thin film spectrum maximized at ca. 25 absorbance units over this wavenumber range, but the 0.17 mm path length spectrum absorbance never exceeded 1.2.

Differences between the transmission cell and the diffuse reflection paraffin oil spectra in Figure 2.22 can be explained by considering the disparate paths of radiation passing through the button liquid sample. Because path length is not constant, a modified Beer's law expression incorporating an "effective" path length can be employed. Effective path length (b_{eff}) is defined as the transmission cell window spacing that yields an absorbance equal to that obtained when there are multiple radiation paths through the sample:[92]

$$b_{eff} = A_{mp}/ac \qquad (\mathbf{2.2})$$

where $A_{\lambda(mp)}$ is the absorbance measured by employing multiple path lengths. By summing over all possible radiation path lengths, an expression for b_{eff} can be obtained:[93]

$$b_{eff} = -\log(\Sigma f_i 10^{-ab_ic})/ac \qquad (\mathbf{2.3})$$

where f_i is the fraction of incident radiation passing through the sample with a b_i path length. Because b_{eff} is a function of sample absorptivity, it varies throughout the spectrum. For small values of $a_\lambda c$, b_{eff} approaches a maximum corresponding to the weighted average path length (i.e. $\Sigma f_i b_i$).[93-94] When f_i, b_i, and c are constants, which is true for absorbance bands in the same spectrum, equation 2.3 yields shorter b_{eff} values when a_λ is larger. Consequently, diffuse reflection button spectrum absorbance ratios for bands with different absorptivities are less than those derived from transmission cell measurements. For example, the 2925 to 2725 cm^{-1} intensity ratio is 2.3 in the Figure 2.22 paraffin oil diffuse reflection button spectrum, which differs substantially from the ca. 46 absorbance ratio at these wavenumbers in the thin film transmission cell spectrum.

Figure 2.23 shows ray tracings depicting hypothetical short and long paths through the paraffin oil sample. The horizontal dashed line represents the upper boundary of the oil layer contained in the button reservoir. The ray on the right side strikes a round wire of the mesh near the top of the oil layer and reflects after traversing a path length comparable to twice the thickness of the oil coating at the point of reflection. The detector signal produced by this radiation would yield a spectrum that is similar to the solid line (i.e. thin film) spectrum in Figure 2.22. The left ray enters the oil layer, refracts, and then reflects three times before exiting, resulting in a total path length that would exceed twice the distance between the mesh wires. Detector sensitivity for radiation emerging after travelling a path of this length (i.e. > 0.28 mm) would be insufficient to discriminate between intensities in the in the 2980–2820 cm^{-1} range, resulting in a spectrum similar to the dotted line in Figure 2.22. If the radiation that followed these two paths were combined at the detector, the resulting spectrum would retain the overlapping peak shapes in the C-H stretching vibration region. When incident radiation passes through a range of sample path lengths, the number of distinct path lengths (b_i) and their associated weighting factors (f_i) determines the relative band intensities in measured spectra. The path length distribution function will depend on the button mesh and reservoir dimensions and the liquid sample refractive index and layer thickness.

Although deriving a path length distribution function based on the modified button dimensions and liquid sample properties would be difficult, the dependence of b_{eff} on specific path length distributions can be investigated. For example, Figure 2.24b compares b_{eff} versus $a\lambda c$ plots derived from equation 2.3 for the four path length weighting functions in Figure 2.24a. To be consistent with the hypothetical extreme rays depicted in Figure 2.23, the shortest path

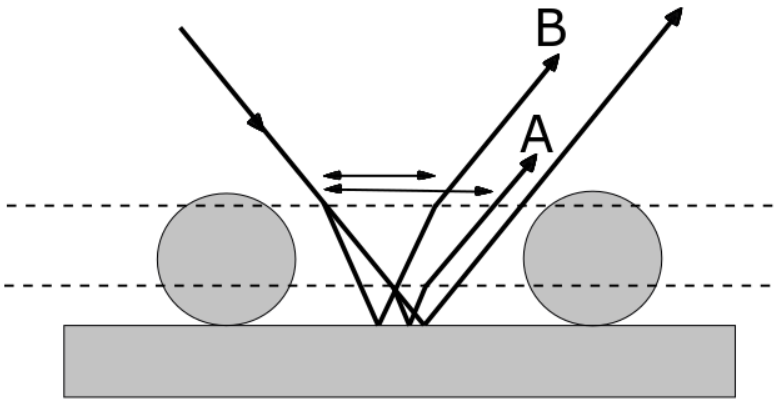

Figure 2.23 – Rays passing through different thicknesses of liquid.

length was chosen to be comparable to the expected thickness of a thin layer of paraffin oil and the longest path length was selected to be slightly longer than twice the 0.14 mm distance between mesh wires. The 100 path lengths (b_i) employed for these calculations ranged from 0.001 to 0.30 mm. The horizontal line in Figure 2.24a depicts equal weighting factors (f_i) for the 100 equally spaced path lengths. The other plots in Figure 2.24a show a Gaussian weighting function maximizing at 0.15 mm and functions that increase and decrease exponentially with increasing path length. The Gaussian function was used to model a nominal 0.15 mm absorption path length with contributions from shorter and longer distances. The other functions represent path length distributions that gradually increase or decrease from shorter to longer distances. The $a_\lambda c$ values employed to calculate the curves in Figure 2.24b ranged from 1 to 150 mm^{-1}, which includes estimated values for the 2725 cm^{-1} (3 mm^{-1}) and 2925 cm^{-1} (138 mm^{-1}) paraffin oil absorbances (vide infra).

The Gaussian weighting function yielded a b_{eff} versus $a_\lambda c$ profile with significantly less curvature than the others. This can be attributed to the narrower path length range for this function. The shape of the Gaussian weighting profile effectively reduced the range from ~0.3

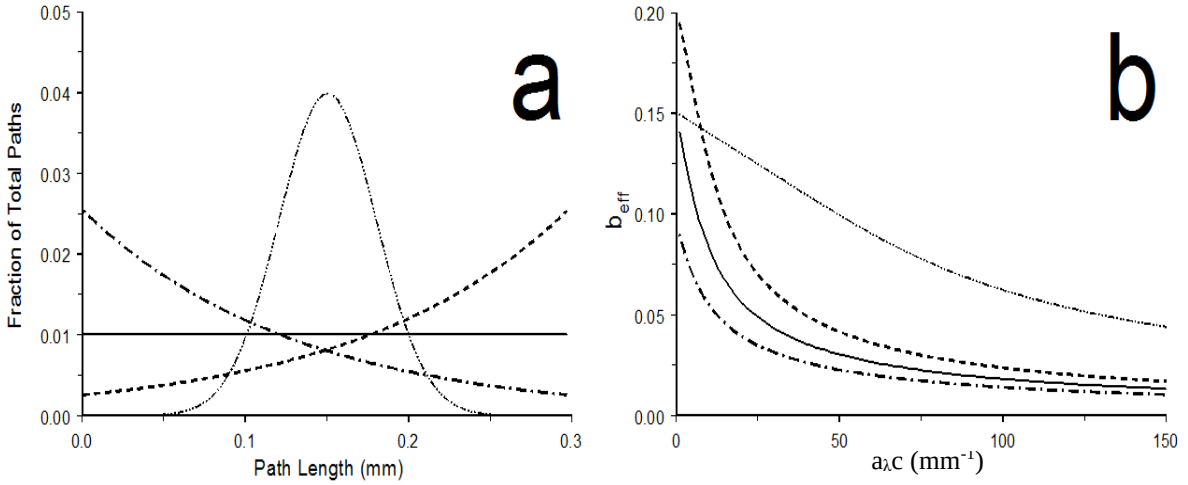

Figure 2.24 – Path length weighting functions (a) and resulting effective path length versus $a_\lambda c$ profiles calculated by using these functions (b).

to ~0.2 mm (i.e. between 0.05 and 0.25 mm). When the Gaussian width was reduced (not shown), the b_{eff} versus $a_\lambda c$ slope diminished and b_{eff} values approached 0.15 mm. Despite significant differences among the shapes of the other path length weighting profiles, the resulting b_{eff} versus $a_\lambda c$ plots in Figure 2.24b exhibited similar trends, with b_{eff} values decreasing exponentially with increasing $a_\lambda c$. Initial b_{eff} values (i.e. for $a_\lambda c = 1$) were more sensitive to changes in the path length weighting factor function than those derived from larger $a_\lambda c$ values. Initial values approached a maximum limit corresponding to the weighted average path length.[93] For the profiles in Figure 2.24a, these weighted averages were 0.10 mm for the decreasing exponential function, 0.20 mm for the increasing exponential function, and 0.15 mm for the equally weighted function and the Gaussian distribution.

The decreasing b_{eff} with increasing $a_\lambda c$ trends exhibited in the Figure 2.24b curves are responsible for the persistence of the overlapping C-H stretching vibration bands in the Figure 2.22 diffuse reflectance button spectrum. Because the absorbance at 2725 cm^{-1} was about the same as that for the 0.17 mm path length transmission cell spectrum, b_{eff} was approximately 0.17 mm at this wavenumber. After multiplying the thin film spectrum by 34.2 to match the

0.17 mm spectrum absorbance at 2725 cm^{-1}, the Figure 2.22 scaled spectrum increased to about 25 absorbance units at 2925 cm^{-1}, which is the absorbance expected for a 0.17 mm path length transmission cell measurement by a spectrophotometer with unlimited sensitivity. Because the diffuse reflection button spectrum absorbance at 2925 cm^{-1} was only about 1.0, b_{eff} at this wavenumber was 0.007 mm (i.e. 1.0/25 x 0.17 mm). Thus, despite the relatively high absorptivity of the 2925 cm^{-1} band ($a_\lambda c \sim 138\ mm^{-1}$), the diffuse reflection button absorbance at this wavenumber was only slightly greater than the thin film transmission cell measurement. Thus, when compared to the ca. 0.17 mm b_{eff} at 2725 cm^{-1}, the multiple path length b_{eff} value at 2925 cm^{-1} was about 28 times shorter.

Plots of b_{eff} versus $a_\lambda c$ can be generated from paraffin oil diffuse reflectance button spectra if $a_\lambda c$ values are available. Transmission cell measurements were employed to estimate these constants. Infrared spectra were measured with 0.04, 0.06, 0.08, and 0.10 mm path

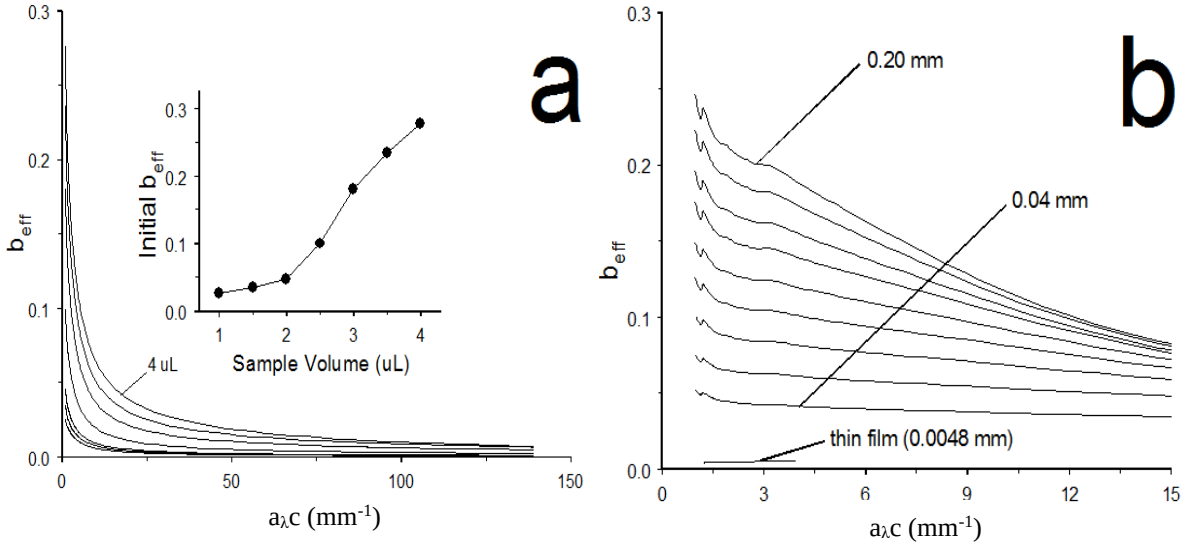

Figure 2.25 - Effective path length versus $a_\lambda c$ plots derived from diffuse reflectance button measurements (a) and transmission cell measurements (b). The seven plots in (a) were derived from spectra obtained with paraffin oil sample volumes ranging from 1 to 4 µL in 0.5 µL intervals. The nine plots in (b) were derived from transmission cell paraffin oil measurements by using path lengths ranging from 0.04 to 0.20 mm in 0.02 mm intervals.

lengths. These spectra had shapes that were similar to the 0.17 mm path length spectrum shown in Figure 2.22. By dividing these absorbance spectra by the cell path length, which was calculated by using the interference fringe method,[67] $a_\lambda c$ constants were obtained (i.e. $a_\lambda c = A_\lambda / b$). Because absorbances were truncated in the 2980–2820 cm^{-1} regions of all four transmission cell spectra, $a_\lambda c$ values for this wavenumber range could not be obtained by this approach. However, $a_\lambda c$ values calculated using the 3075–3010 cm^{-1} and 2780 and 2600 cm^{-1} regions of these spectra yielded relative standard deviations (RSD) that were below 1%. Average $a_\lambda c$ values within these wavenumber ranges were used to calculate the thickness of the film employed to obtain the solid line spectrum in Figure 2.22 (i.e. $b = A_\lambda / a_\lambda c$). Dividing the paraffin oil thin film transmission cell spectrum absorbances in the 3075–3010 cm^{-1} and 2780 and 2600 cm^{-1} regions by the $a_\lambda c$ value averages yielded a 0.0048 ± 0.0003 mm path length, which represents the film thickness. By dividing the thin film transmission cell absorbance spectrum by 0.0048 mm, paraffin oil $a_\lambda c$ estimates were obtained, including the 2980–2820 cm^{-1} range, where absorbance was truncated in all of the fixed path length transmission cell spectra.

The paraffin oil thin film absorbance spectrum varied relatively smoothly from near the baseline at 3075 cm^{-1} to the maximum intensity at 2925 cm^{-1} (Figure 2.22). This wavenumber range was characterized by $a_\lambda c$ constants ranging from 1.5 to 138 mm^{-1} and was employed to generate diffuse reflectance button spectrum b_{eff} versus $a_\lambda c$ plots. Figure 2.25a shows these curves for diffuse reflectance button sample volumes that increased from 1.0 to 4.0 µL in 0.5 µL increments. The curves exhibit exponentially decreasing trends that are similar to the plots in Figure 2.24b. The overall increase in b_{eff} with increasing sample volume in Figure 2.25a can be attributed to increasing oil layer thickness. As shown by the inset plot,

initial b_{eff} values, which approximated weighted average path lengths, increased non-linearly with increasing sample volume, suggesting that path length changes were not proportional to oil volume increments. This can be attributed to the fact that the amount of oil displaced by the round mesh wires depended on the oil depth. Because volumes below 2.0 µL were insufficient to completely cover the reservoir bottom, the two oil increments required to increase the volume to 2.0 µL were spread across the bottom of the reservoir but provided little increase in layer thickness. Because the incident infrared beam diameter was about 3 mm, the wire mesh surface area exceeded the sample illumination area by about a factor of four. Consequently, much of the first two 0.5 µL increments filled portions of the mesh that were not exposed to infrared radiation. The largest b_{eff} changes occurred between 2.0 and 3.5 µL. The maximum increase in layer thickness occurred when the oil level rose to the midpoint of the round wire, where the metal was thickest and displaced the most oil. The slope of the Figure 2.25a inset plot maximized between 2.5 and 3.0 µL, suggesting that about half of the mesh wire was immersed between these sample volumes. The wire mesh was completely immersed in the oil above 3.5 µL. Because the mesh wires provided no oil displacement for the last volume increment, the b_{eff} change when the volume increased to 4.0 µL, which was the button capacity, was somewhat smaller than previous increments. Figure 2.25a shows that although b_{eff} increased for all $a_{\lambda}c$ values with incremental addition of oil, it increased more when $a_{\lambda}c$ values were lower. Thus, all paraffin oil absorbances increased with increasing oil volume, but the increase was greater at wavenumbers corresponding to lower sample absorptivity. Consequently, relative band intensities were dependent on the volume of oil in the button reservoir.

The b_{eff} versus $a_{\lambda}c$ plots in Figure 2.25b were derived from transmission cell measurements and differ substantially from the Figure 2.25a profiles. Ideally, calculated b_{eff} values should be constant when detected radiation penetrates the same distance through the sample (i.e. Beer's law is valid). The short horizontal line near the bottom of Figure 2.25b was derived from the paraffin oil thin film transmission cell spectrum in Figure 2.21. The b_{eff} values for this plot were calculated by dividing the 3075–3010 cm^{-1} spectrum absorbance values by the average $a_{\lambda}c$ values, which were calculated from the four (i.e. 0.04, 0.06, 0.08, and 0.10 mm path length) paraffin oil transmission cell spectra. These calculations yielded 69 b_{eff} values that ranged between 0.004 and 0.005 mm. The b_{eff} versus $a_{\lambda}c$ profiles above the thin film plot in Figure 2.25b were derived from transmission cell measurements with path lengths that increased from 0.04 to 0.20 mm in 0.02 mm increments. Because calculations

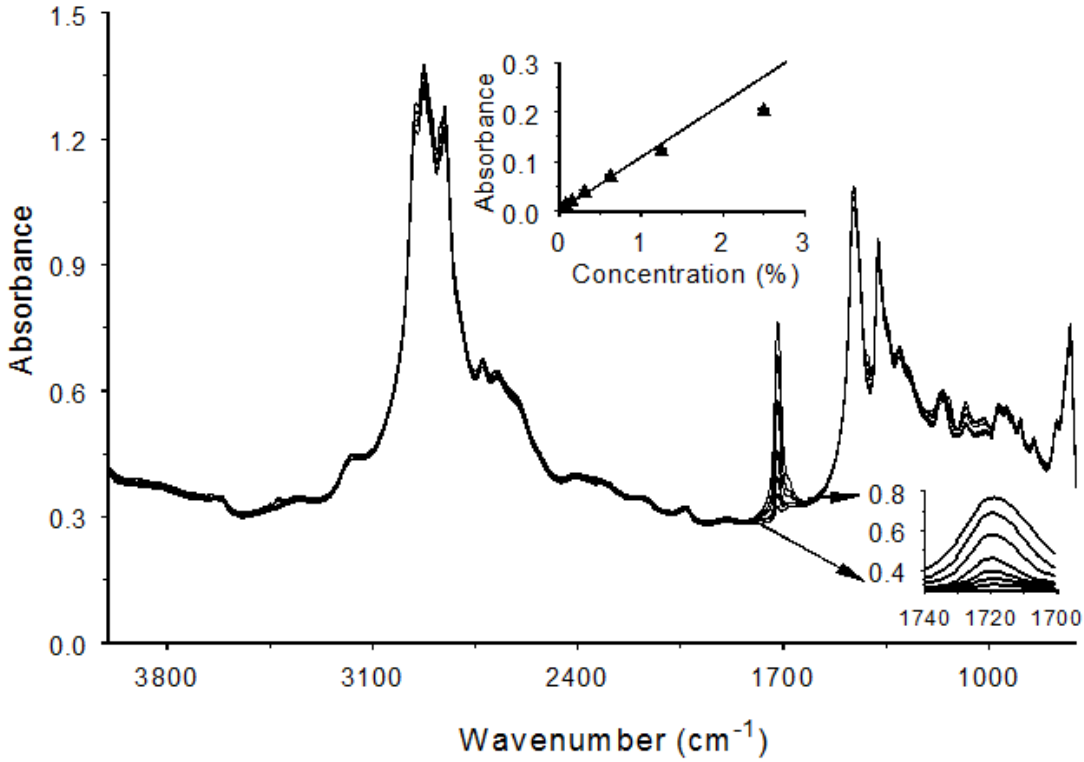

Figure 2.26 - Overlay of six diffuse reflectance button spectra for paraffin oil with different amounts of 10-nonadecanone. Inset plot shows ketone carbonyl band shapes and 1720 cm^{-1} calibration function.

were based on absorbance values spanning the 3075–2970 cm^{-1} range, $a_\lambda c$ values ranged from 1.5 to 38.1. Like the thin film results, b_{eff} values were relatively constant for plots corresponding to the 0.04 and 0.06 transmission cell path length measurements. For path lengths longer than 0.06 mm, initial b_{eff} values exceeded the specified cell path length and b_{eff} versus $a_\lambda c$ plots exhibited negative slopes that became more negative with increasing cell path length. These trends are indicative of Beer's law deviations. In fact, the sloping b_{eff} versus $a_\lambda c$ plots resemble the Gaussian weighting function curve in Figure 2.23b, suggesting that path lengths were more variable for these measurements. The path length distribution was likely

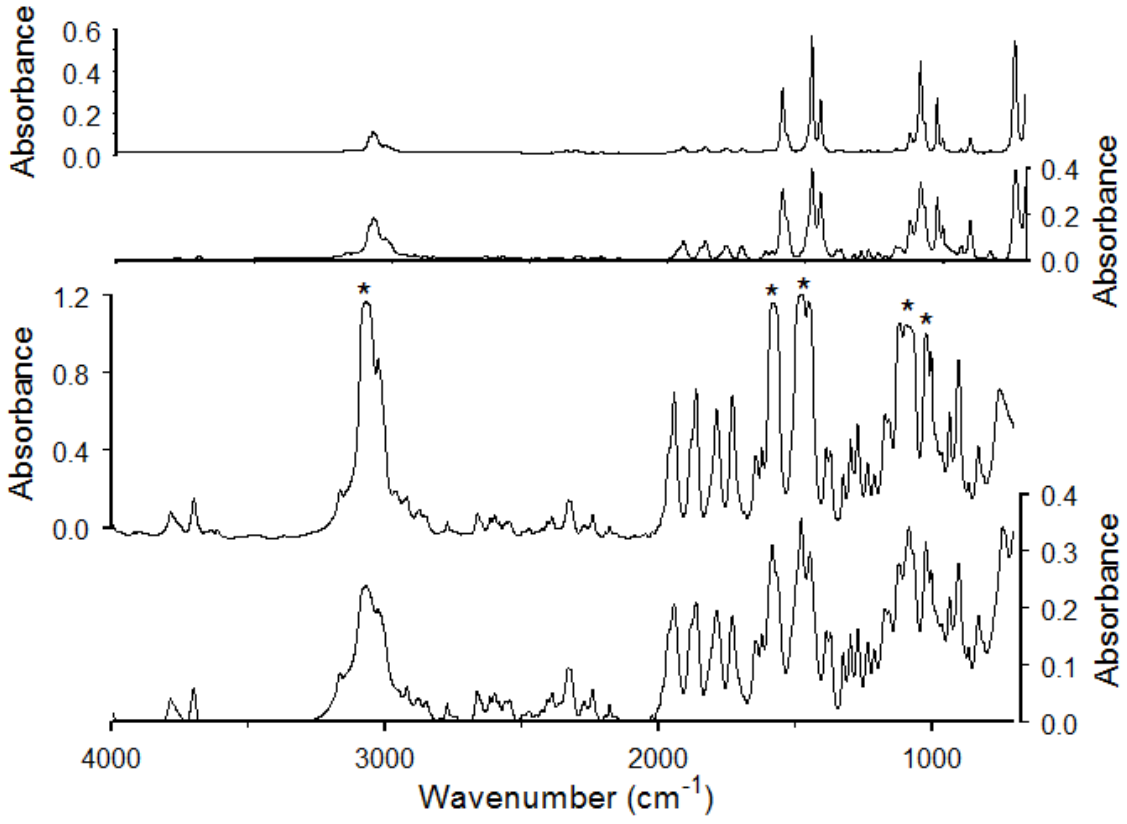

Figure 2.27 - Chlorobenzene transmission cell (left ordinates) and mesh button (right ordinates) infrared spectra. Transmission cell measurements were made by using a thin film (top) and with a 0.25 mm path length (bottom). Button spectra were obtained by using a mesh with 5 µm openings (top) and with 140 µm openings (bottom). Asterisks above some 0.25 mm transmission cell peaks highlight bands with truncated intensities.

caused by cell windows that were not parallel. In fact, absorbance spectrum errors caused by lack of window parallelism would be largest for longer path length measurements.

Although the curves in Figure 2.25a indicate that relative b_{eff} values, and consequently relative band intensities, changed with the volume of sample placed in the button, b_{eff} profiles were consistent when the same sample volume was used for measurements, resulting in reproducible relative band intensities. This is confirmed by Figure 2.26, which shows an overlay of six paraffin oil spectra obtained for 3.7 µL samples spiked with 0.08–2.5% 10-nonadecanone (w/v). Whereas the paraffin oil solvent absorbance bands overlap in these five spectra, the ketone band intensities were proportional to the 10-nonadecanone concentration.

Figure 2.27 compares chlorobenzene liquid spectra obtained by the diffuse reflection button method and by transmission cell measurements. Spectra with right side ordinate labels were measured by using the button sampling method and spectra with left side ordinate labels were obtained by using a transmission cell. The top two spectra were obtained by using a transmission cell containing a thin film of chlorobenzene and by placing 2.0 µL of the liquid into a button containing a mesh with 5 µm openings. The small mesh openings yielded much shorter path lengths than the 100 mesh button, resulting in a spectrum that resembled the thin film transmission cell spectrum. Although these two spectra are similar, relative peak intensities and band widths differed. Because b_{eff} was greater near the baseline than at band maxima, peaks were broader in the button spectrum when compared to the transmission cell spectrum.

The chlorobenzene infrared spectrum contains numerous low intensity absorbance bands that are not evident in thin film spectra. These bands are revealed in the bottom two spectra in Figure 2.27, which were obtained by using longer path length measurements. The

transmission cell spectrum (left ordinate label) was obtained by using a 0.25 mm path length. The button spectrum (right ordinate label) was measured by using the same 100 mesh button with 140 µm openings that was used for paraffin oil measurements. The button and 0.25 mm transmission cell spectra exhibit similar band shapes and spectral features are located at the same wavenumbers. However, unlike the diffuse reflection button spectrum, some of the more intense transmission cell bands (denoted by asterisks) were truncated due to limited instrument sensitivity.

The spectra in Figure 2.28 show that transmittance and diffuse reflectance measurements both exhibited absorbance increases at 2725 cm^{-1} with increasing quantity of liquid. However, unlike the transmittance spectra, all of the diffuse reflectance spectra retain the overlapping C-H stretching vibration peak shapes due to multiple path length effects on b_{eff}. The Figure 2.28a 3300-2500 cm^{-1} portions of paraffin oil absorbance spectra were measured by using transmittance cell path lengths ranging from 0.03 to 0.30 mm. Based on the band maxima absorbance ratio: $A_{2925}/A_{2725} = 46$, derived from the thin film transmittance cell measurement, the 2925 cm^{-1} absorbance should have increased from about 4.6 to about 37 in these spectra. Instead, 2925 cm^{-1} absorbance ranges between 1.0 and 1.2 and the overlapping

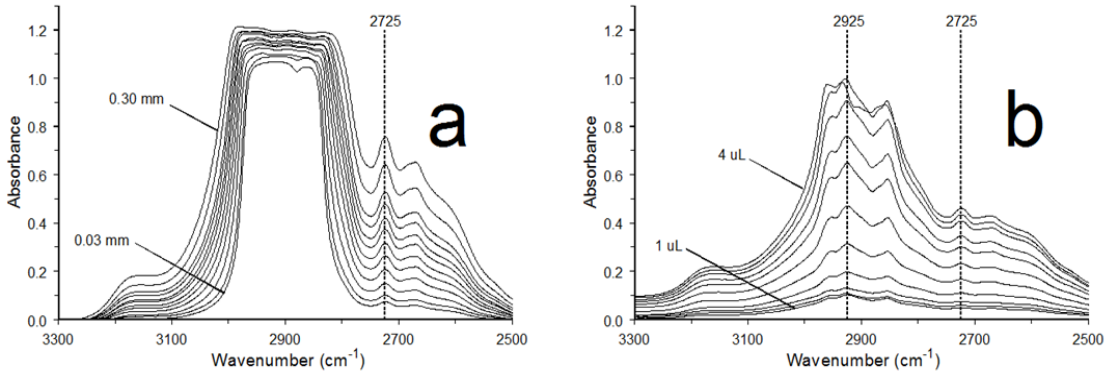

Figure 2.28 – Paraffin oil infrared spectra measured by (a) transmittance and (b) diffuse reflectance with the button sample holder.

C-H stretching vibration bands are absent because detector signals for these highly absorbing bands were indistinguishable from detector noise.

In addition to liquid refractive index and layer thickness, diffuse reflectance path lengths may be influenced by: the reflectivity's of the mesh and backing metal surfaces, the mesh wire diameter and void space dimensions, and the orientation of the woven wire mesh pattern with respect to the diffuse reflection optical system mirrors. Consequently, a linear relationship between absorbance and sample volume would not be expected for liquid diffuse reflectance measurements. The diffuse reflectance spectra in Figure 2.28b were obtained by adding paraffin oil volumes ranging from 1 to 4 µL to the modified button reservoir. The spectra in Figure 2.28b were baseline corrected to remove offsets (vide infra) by subtracting the absorbance at 2000 cm^{-1} from the absorbance measured at each wavenumber. Assuming that the button reservoir was cylindrical, this volume range should produce uniform liquid layer

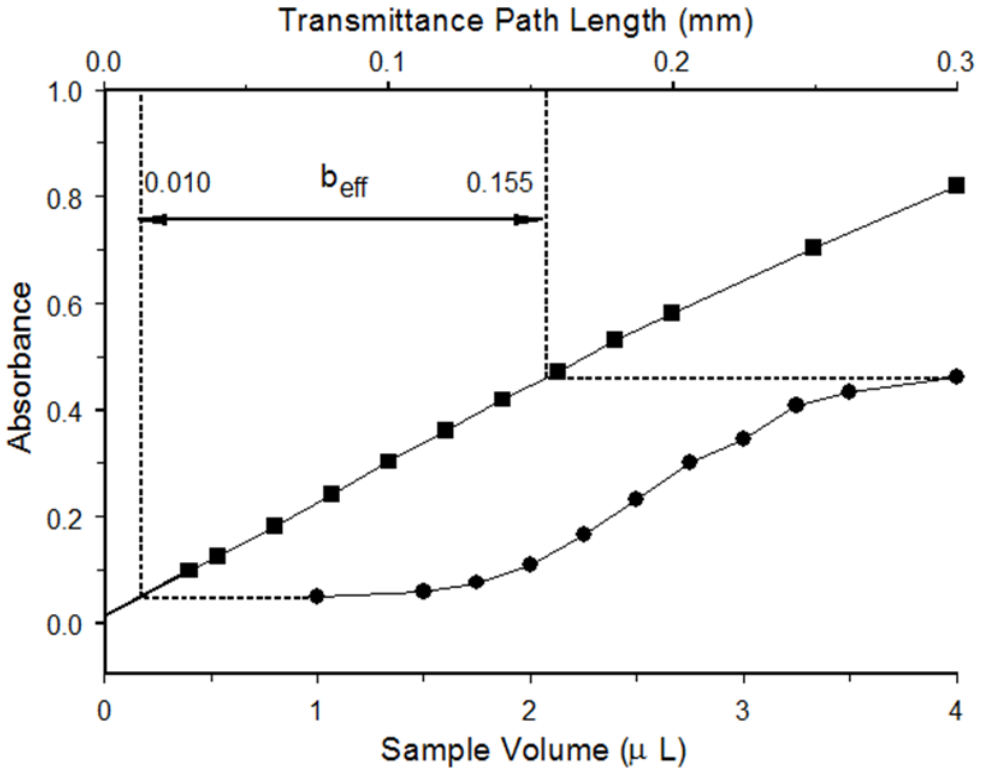

Figure 2.29 – Variation of effective path length as a function of the volume of paraffin oil contained in the modified button reservoir.

thicknesses ranging from 0.032 to 0.127 mm. Actual layer thicknesses should exceed these estimates because the wire mesh displaces liquid in the reservoir. Because the mesh wires are round and woven into a pattern, the amount of liquid displaced, and therefore liquid layer thicknesses, should vary non-linearly with the volume of sample added. The calibration curve shown in Figure 2.29 (squares) was generated by plotting the Figure 2.28 absorbances at 2725 cm^{-1} versus transmittance cell path length (upper abscissa scale). This plot is relatively linear, but the slope does decrease slightly when the path length exceeds 0.2 mm. Using this calibration function and the 2725 cm^{-1} diffuse reflectance absorbance values in Figure 2.28b, multiple path length b_{eff} values were estimated. The circles in Figure 2.29 denote variations in the 2725 cm^{-1} absorbance as a function of sample volume (bottom abscissa scale). As expected, the absorbance versus sample volume plot was non-linear. The 2725 cm^{-1} absorbance measured when 1 µL of oil was placed into the button was about 0.05, which was below the lowest transmittance cell absorbance. By extrapolating the calibration curve, this absorbance could have been attained by using a transmittance cell path length of about 0.010 mm. Diffuse reflectance 2725 cm^{-1} b_{eff} values derived in a similar manner increased with increasing sample volume until reaching 0.155 mm at 4 µL.

The 2925 and 2725 cm^{-1} absorbance versus sample volume plots exhibited similar trends, except that the 2925 cm^{-1} absorbance was about twice that of the 2725 cm^{-1} absorbance. Based on the A_{2925}/A_{2725} ratio obtained from the transmittance thin film spectrum, the 2925 cm^{-1} absorbance for the 4 µL diffuse reflectance spectrum would be 7.13 (i.e. 46 x 0.155) for a 0.155 mm fixed path length transmittance cell measurement. Instead, the Figure 2.28b diffuse reflectance absorbance is only 0.98. Thus, the multiple path length impact on this diffuse reflectance measurement was to reduce the effective path length by about a factor of 7,

resulting in a ~7x detector signal increase when compared to the corresponding 0.155 mm transmittance cell measurement.

Paraffin oil diffuse reflectance spectra exhibited baseline shifts that could be correlated with the volume of oil added to the button reservoir (i.e. layer thickness). Figure 2.30 shows the effect of sample volume variations on diffuse and specular reflectance spectrum baseline offsets. For these comparisons, specular reflectance measurements were made by using the same sample-containing button that was used for the corresponding diffuse reflectance measurement. Baseline was defined as the absorbance at 2000 cm^{-1}. Paraffin oil volumes were varied in 0.5 µL increments between 1.0 and 3.5 µL. When compared to the diffuse reflectance measurement conditions, sample thicknesses at the infrared beam focal point were always less for specular reflectance because vertically tilting the button for these measurements caused the

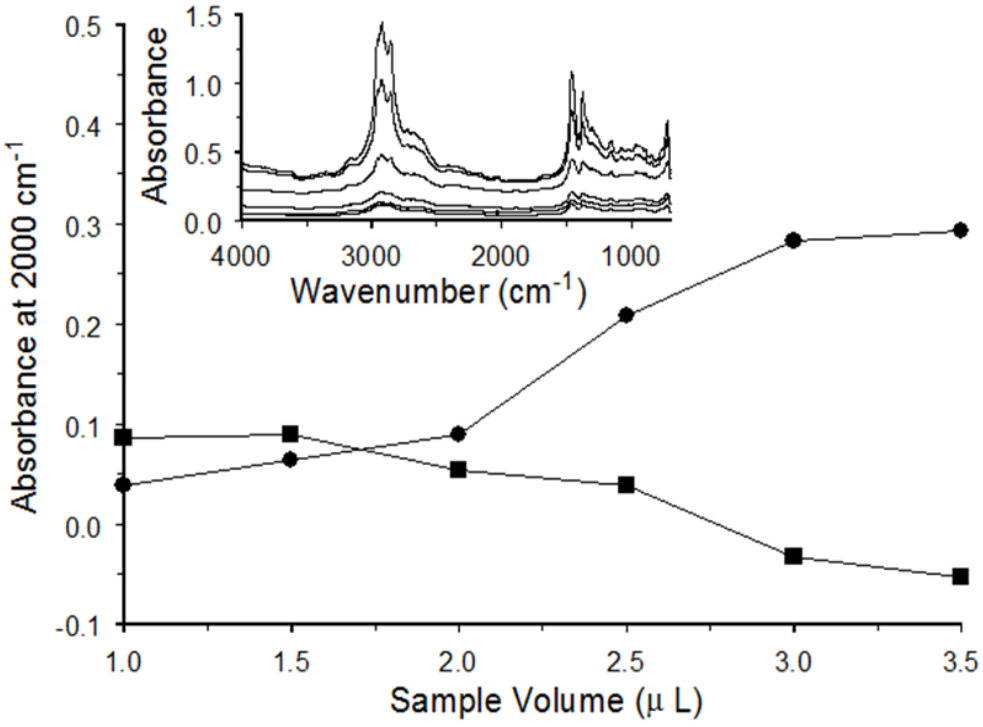

Figure 2.30 – Plots of baseline absorbance as a function of the paraffin oil volume added to the button for diffuse (circles) and specular (squares) reflectance measurements.

oil to collect at the bottom of the reservoir. In fact, specular reflectance measurements for samples greater than 3.5 µL were not included in the plot because the oil leaked from the reservoir. The graph in Figure 2.30 shows increasing baseline absorbance with increasing sample volume for diffuse reflectance measurements (circles) and decreasing baseline absorbance with increasing sample volume for the specular reflectance measurements (squares). These trends can be explained by considering the drawing in Figure 2.5, which shows how the layer thickness affects the path of the center (i.e. specular reflectance) ray as it passes through a homogeneous liquid having a refractive index greater than unity. The two horizontal dashed lines in Figure 2.5 represent different liquid thicknesses. Ray A refracts as it passes through a thin layer of liquid. Compared to the empty button, it emerges from the plane defined by the top of the wire mesh surface slightly closer to the incident ray (represented by the lower horizontal double arrow). Ray B refracts as it passes through a thicker liquid layer. It emerges from the wire mesh surface even closer to the incident ray, which is depicted by the shorter horizontal double arrow. When the distance between incident and exiting beams at the wire mesh surface is reduced due to increased layer thickness, a larger fraction of incident rays reflect from the button backing without striking a wire. Radiation reflecting at this angle is preferentially excluded by the diffuse reflection optics but detected in the specular reflection configuration. The resulting changes in detector signal produce baseline offsets that are dependent on the liquid layer thickness and radiation collection optics. For diffuse reflectance measurements, baselines shift down in transflectance and up in absorbance spectra due to decreasing detector signal. This shifting is evident in the Figure 2.30 inset plots, which show the absorbance spectra from which the diffuse reflectance baseline offsets (circles) were obtained. The opposite trend was observed when the specular reflectance mode was employed

because detector signal increased due to collection of more radiation reflecting only from the button backing. The magnitude of these baseline offsets should be dependent on mesh wire diameter and spacing, so different button configurations would be expected to exhibit different baseline increments.

2.5.2.3 Quantitative Analysis

Liquid sample quantitative analysis capabilities were evaluated by measuring spectra for mixtures containing varying quantities of 10-nonadecanone dissolved in paraffin oil. The 1720 cm^{-1} carbonyl stretching vibration band was used to quantify the ketone content. The effective path length for these measurements was fixed by consistently using 3.5 µL sample volumes. 10-Nonadecanone content in standard mixtures was varied from 0.16 to 2.5% (v/v). Figure 2.31 shows calibration curves generated by plotting absorbances at 1720 cm^{-1} and

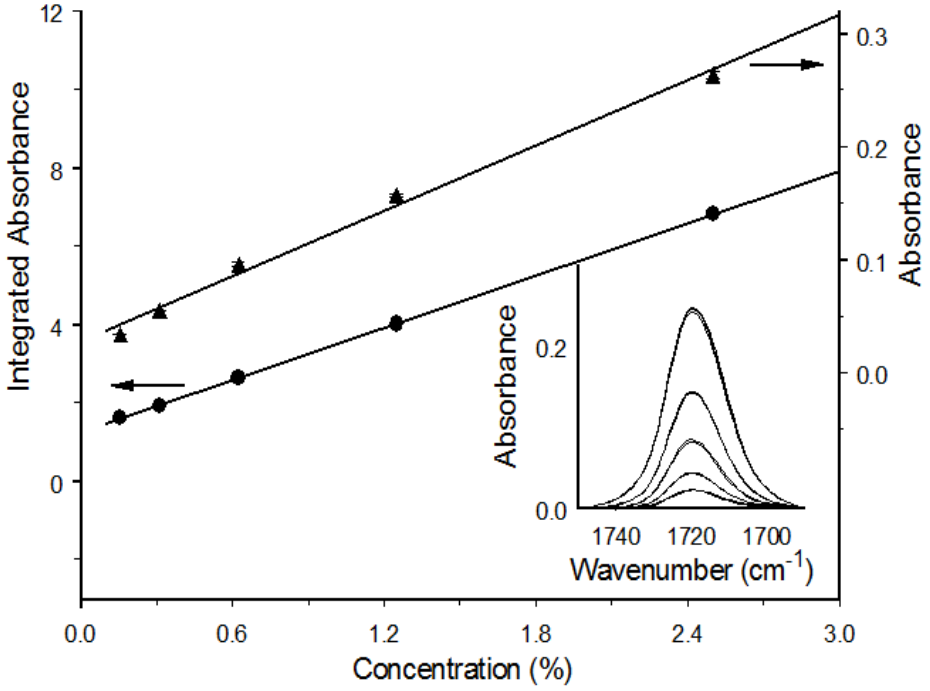

Figure 2.31 – Calibration functions for 10-nonadecanone concentrations in paraffin oil obtained from diffuse reflectance button measurements. Inset plots show overlays of the 15 (3 for each of 5 concentrations) spectra from which band maxima absorbance and integrated absorbance values were obtained.

integrated areas for these bands versus 10-nonadecanone concentration. Averages of 3 replicate measurements are plotted and error bars represent ± 1 standard deviation. Linear functions ($R^2 > 0.99$) were obtained for both 1720 cm^{-1} absorbance and integrated absorbance. The inset plots in Figure 2.31 show overlays of the 15 (i.e. 3 for each concentration) baseline corrected bands used to make the calibration plots.

2.5.3 Reproducibility and Sensitivity

The reproducibility and sensitivity of diffuse reflectance liquid measurements were characterized by measuring automotive engine oil infrared spectra. Diffuse reflectance measurements were made by adding 3.5 µL volumes of each oil to the same wire mesh button reservoir. The spectra plotted in Figure 2.32a were obtained for fresh (solid line) and used (dashed line) motor oil samples. These overlapping spectra are shown without baseline correction or any other post measurement modifications. Spectra were derived by dividing the oil single beam spectra by the same background single beam spectrum, which was obtained by using the clean empty button prior to adding the first (i.e. fresh oil) sample. The fact that the two spectra in Figure 2.32a closely match in regions where no spectrum changes were detected is indicative of high measurement reproducibility. Due to their high hydrocarbon contents, the most intense oil absorbance bands are found at the same wavenumbers as the most intense paraffin oil bands (Figure 2.21). Paraffin oil contributions to the motor oil were effectively removed by subtracting a previously measured 3.5 µL paraffin oil spectrum from the fresh oil spectrum. The result is shown in Figure 2.32b. After removing paraffin oil contributions, the residual difference spectrum absorbance bands in Figure 2.32b can be attributed to oil additives.[95] Figure 2.32c shows the result of subtracting the fresh oil spectrum from the used oil spectrum. Positive intensities represent spectral features that appeared in the used oil

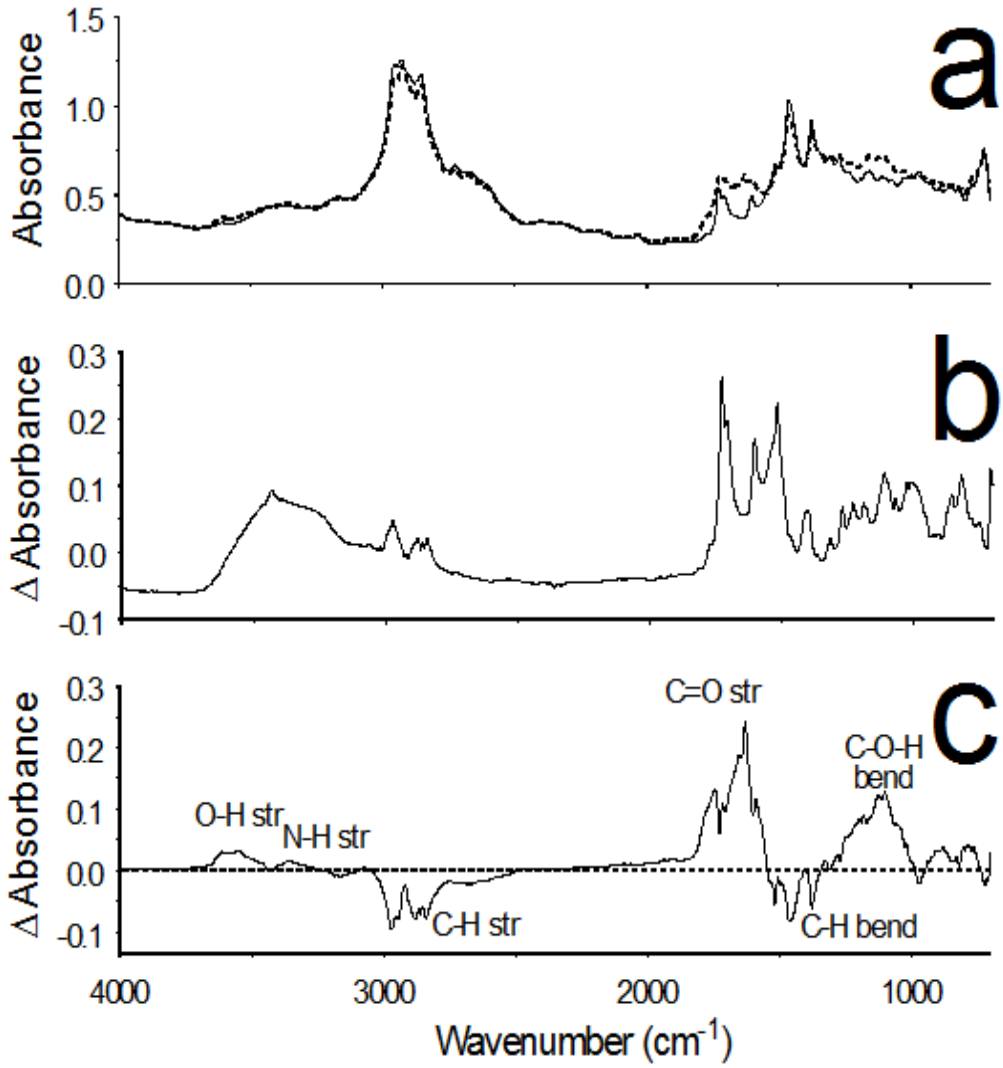

Figure 2.32 – (a) Button diffuse reflectance Infrared spectra for fresh (solid line) and used (dashed line) motor oil. (b) Difference spectrum calculated by subtracting a 3.5 µL paraffin oil spectrum from the fresh oil spectrum. (c) Difference spectrum calculated by subtracting the fresh oil spectrum from the used oil spectrum.

spectrum that were not present in the fresh oil spectrum. Negative difference spectrum bands represent fresh oil functional groups that were lost when the oil was employed for engine lubrication. As expected, the primary oil degradation process was oxidation, primarily yielding infrared absorbance bands associated with oxygen containing functionalities.[96-97] Oil degradation processes also resulted in loss of C-H stretching and bending vibration bands in the infrared spectrum. Even by using a 0.012 mm path length, which was the shortest employed

for fixed path length transmittance measurements in this study, it would have been impossible to detect the C-H stretching vibration band absorbance losses shown in the Figure 2.32c difference spectrum due to the complete loss of peak shapes in this spectral region (Figure 2.27a). Furthermore, transmittance cell or ATR path lengths that would be short enough to retain the C-H stretching vibration band shapes would yield significantly lower intensities for the oxygen containing degradation product bands.[98]

2.6 Conclusion

Buttons have a variety of features that make them an attractive infrared sampling tool. Made with durable stainless-steel, buttons are simple, inexpensive, easily cleaned, and reusable. They have no window to maintain and require minimal to no sample preparation. The button-IR sampling devices are applicable to a wide range of sample types, including substances such as greases, waxes, and pastes. With typical sample sizes around 1 mg, very small quantities are required for analysis. Samples are retained within the mesh void, allowing samples to be preserved for subsequent or later re-analysis. The slide-based operation is user friendly and maintains instrument purge. Results acquired with buttons are similar to transmittance measurements. Sampling by abrasion allows buttons to be a versatile sampling tool. Nanogram detection limits have been demonstrated with buttons, and microanalysis can also be achieved. The small button size makes them potentially compatible with autosamplers as well as portable FTIRs. Buttons are also suited for variable temperature measurements.

With the button feature set outlined here, comparisons can be made with the currently preferred method of ATR. Both buttons and ATR are capable of measuring spectra for solids and liquids. Like buttons, ATR is also applicable to greases, waxes, and pastes. The optical throughput is the major determining factor for spectrum signal to noise ratio. Buttons have an

optical throughput of about 20 percent when using the praying mantis diffuse reflection optics. Literature values for typical ATR optical systems list throughput between 15 and 30%. For ATR, the throughput is impacted by the high refractive index crystal, the refractive index of the sample, and the optics. Compared to ATR, path lengths are more variable with buttons, ranging from thin films up to 200 micrometers. Button path lengths are determined by the amount of liquid deposited in the reservoir. Liquid to solid deposition creates thin, even layers with thicknesses that can be adjusted by the amount of solution added. ATR path lengths are more restricted, typically ranging between 2 and 15 micrometers. The path length represents the penetration depth of the evanescent wave, which varies with wavenumber. Spectra acquired by using buttons can be either in absorbance format for non-scattering liquid samples or in Kubelka-Munk format for diffusely scattering solids. Finally, buttons are cheap, costing only a few dollars due to the inexpensive stainless-steel construction. In contrast, ATR crystals can cost hundreds of dollars.

The increase in signal afforded by the window-free design can be exploited for variable temperature analysis for in situ analysis of complex systems. Thin layers of solid powders can be perturbed by heating while monitoring sample changes by infrared spectroscopy. The increased signal-to-noise ratio for thin neat sample layers allow for reproducible VT-DRIFTS results which can be used to identify subtle temperature-dependent changes. Applications of VT-DRIFTS to temperature-dependent studies of zeolites will be described in detail in chapters 4 and 5.

Chapter 3: Button-IR Accessories

3.1 Introduction

Some properties of the button sample holder make it suitable for applications that would be difficult or impossible to achieve with conventional infrared measurement systems. For example, the high thermal conductivity and low thermal mass of stainless-steel buttons is particularly advantageous for rapidly heating and cooling samples. The minimal cost and reusability of buttons makes them applicable when severe measurement conditions might damage infrared windows or ATR crystals. The simple design and small size of buttons, along with the fact that they can be inserted and removed from the infrared spectrophotometer by using a simple slide mechanism, suggest that they could be incorporated into a computer controlled autosampler, allowing for unsupervised sample analyses and increasing the time available for sample preparation.

Figure 3.1 – 3D printed 8-position button carousel.

3.2 Accessories

3.2.1 Multiple Sample Carousel

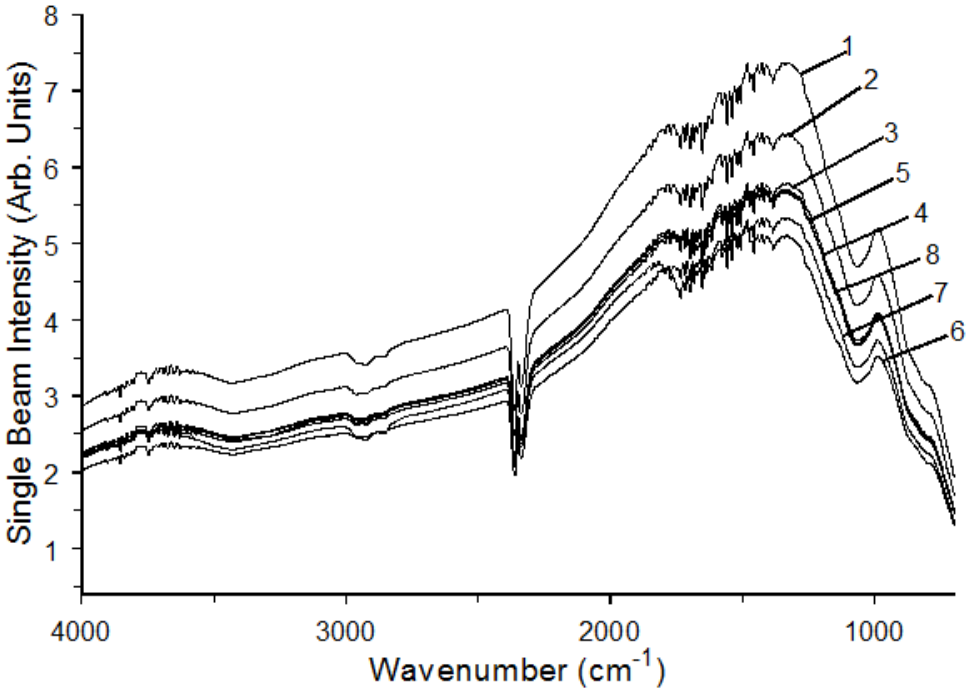

Figure 3.2 – Carousel button single beam spectra. Numbers indicate the location of the button on the carousel in Figure 3.1.

A prototype multiple sample carousel was designed and constructed to permit analysis of up to 8 different samples without opening the infrared spectrophotometer sample compartment. The plastic carousel shown in Figure 3.1 was fabricated by 3D printing. It has an 8-sample capacity. Individual button sample holders are held in place by magnets affixed to the recessed centers at each of the 8 numbered sample locations. A bearing pressed into the center of the plastic carousel allowed for rotation of the sample wheel by hand. A screw through the center of the bearing was used to attach the carousel to a slide. The slide mounted 8 position carousel was inserted into the spectrophotometer by using the same track employed for inserting the specular and diffuse reflection buttons. A metal pin that remained outside the infrared spectrophotometer sample compartment was inserted into holes along the outside

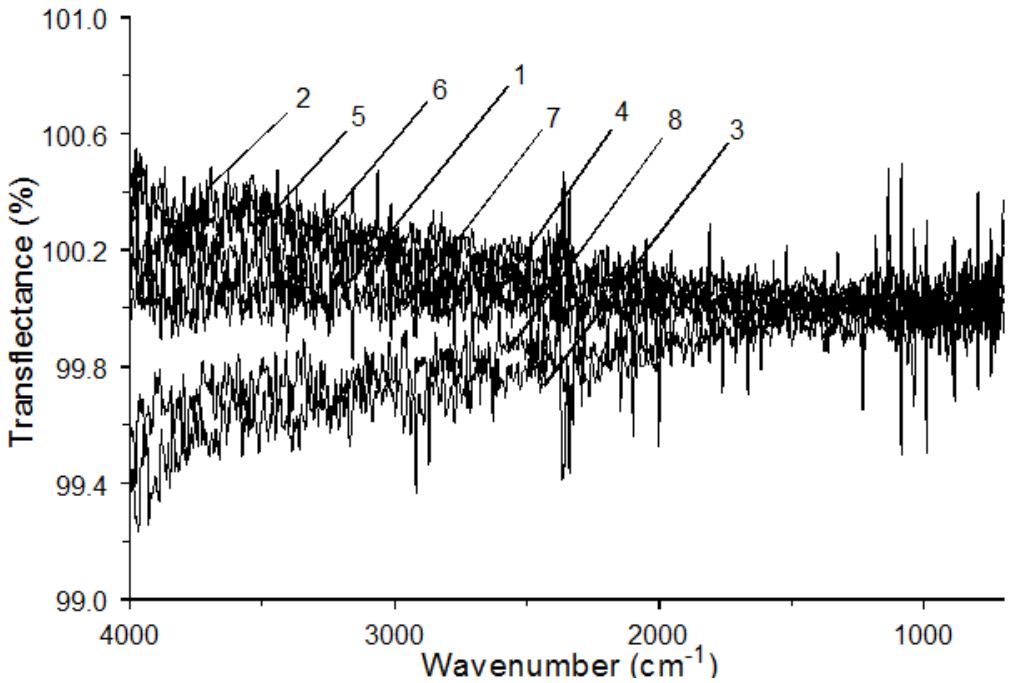

Figure 3.3 – Empty button transflectance spectra. Numbers indicate the location of the button on the carousel in Figure 3.1.

circumference of the carousel to align individual buttons with the diffuse reflection optical system. By rotating the carousel from one alignment hole to the next, samples that were loaded outside of the instrument were sequentially moved into the purged sample compartment for spectrum measurements. Prior to analyses, individual buttons were aligned by positioning them at the diffuse reflection optics focal point and then rotating them until the maximum detector signal was obtained. Figure 3.2 shows an overlay of the background (i.e. empty button) single beam spectra obtained for the 8 buttons. Although the shapes of the single beam spectra are similar, some buttons provided more detector signal than others. The numbers in Figure 3.2 denote the carousel sample locations for each button. When transflectance spectra were obtained for each empty button, variations in background single beam intensities were effectively compensated. Empty button infrared spectra were similar for all 8 buttons and consisted of horizontal lines near 100% (± 0.6%) transflectance (Figure 3.3). The effects of

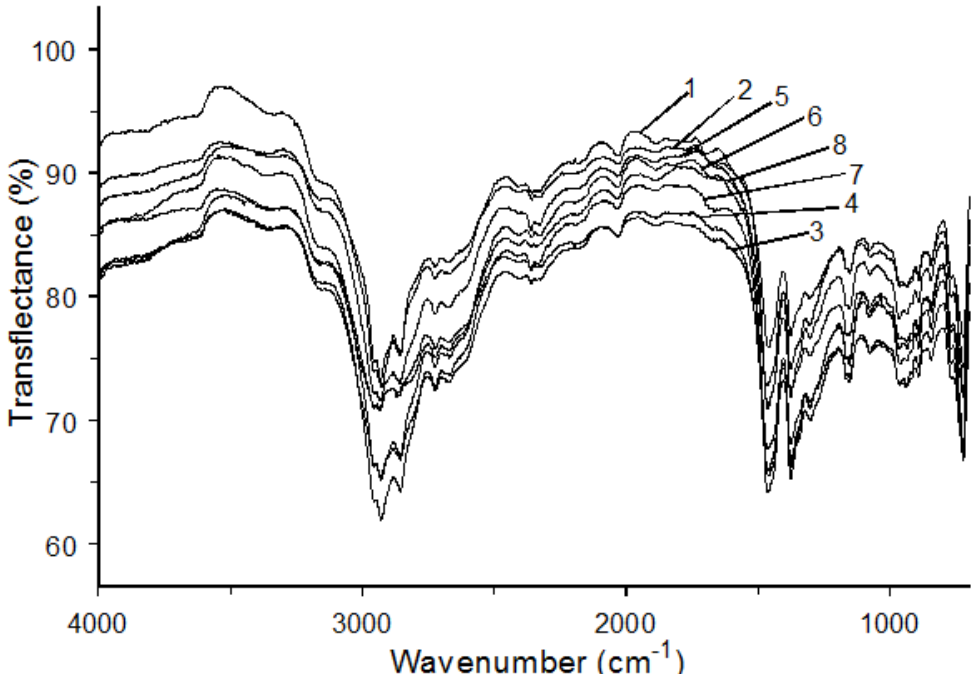

Figure 3.4 – Overlay of paraffin oil spectra measured by using the carousel buttons. Numbers indicate the location of the button on the carousel in Figure 3.1.

sample were tested by adding 2 µl of paraffin oil to each button by using a 10 µl syringe. The infrared spectra obtained for the 8 buttons when they contained paraffin oil are shown in Figure 3.4. Baseline offsets and band intensity variations in Figure 3.4 are indicative of differences in path length. It is noteworthy that these baseline offsets are not correlated with single beam intensities. The paraffin oil spectrum variations in Figure 3.4 [illegible] different reservoir dimensions. Thus, the 2 µl paraffin oil volumes rose to different levels in each reservoir, which would produce path length variations (Chapter 2). Although buttons manufactured by automated machining processes would likely improve button to button spectrum measurement reproducibility, the most consistent path lengths would be obtained by using the same button.

3.2.1.1 Conclusions

This successful sample carousel proof of concept test suggests that a computer-controlled button autosampler is feasible. In contrast, autosamplers incorporating multiple

transmission cells or ATR crystals would not be cost effective, due to the necessary complexity of autosampler robotics and the expense of multiple transmission cells or ATR crystals. In addition, results obtained by using transmission cell and ATR autosamplers would also exhibit reduced measurement reproducibility when spectra obtained by using different transmission cells or ATR crystals are compared.

3.2.2 Low-Temperature Thermoelectric Cooler

Like attenuated total reflectance (ATR), the button is an "open" sample holder because the material being analyzed is not confined within a sealed container. This can be an issue when analyzing volatile liquids because material can be lost by evaporation during measurements. Affixing windows to the button surface could slow evaporation, but this would also diminish measurement signal-to-noise ratios. Alternatively, evaporation can be slowed by cooling samples to reduce vapor pressures. This can be accomplished quickly and easily by employing a thermoelectric cooler (TEC).

Peltier devices can be heated as well as cooled. Therefore, by mounting a button on a TEC, a variety of temperature-dependent infrared spectroscopy studies can be conducted. In the benchmarking studies described here, reproducible linear heating and cooling ramps were employed to elucidate subtle temperature-dependent spectrum changes in kaolinite. Notably, infrared spectra collected during temperature ramps are not isothermal measurements. Instead, they represent the average of interferogram scans obtained over a narrow (~2 °C) temperature range. However, infrared spectra can be measured isothermally at selected temperatures by employing a temperature step program. In this mode, measurements are made while the sample temperature is held constant (i.e. ± 0.2 °C). After each temperature step spectrum measurement, rapid heating or cooling to reach the next programmed temperature and short

equilibration periods at these set points are desired to minimize total analysis times. The effects of heating a montmorillonite clay containing acetylsalicylic acid were elucidated by isothermal infrared spectrum measurements at selected temperature steps. Spectral subtractions reveal subtle differences and provide high sensitivity detection of temperature-dependent sample changes.

3.2.2.1 Experimental

Acetone (CAS: 67-64-1), ethyl acetate (CAS: 141-78-6), and chloroform (CAS: 67-66-3) were obtained from Fisher Scientific (Waltham, MA); kaolinite (CAS: 1318-74-7) was obtained from Ward's Natural Science (Rochester, NY); montmorillonite (CAS: 1318-93-0) and acetylsalicylic acid (CAS: 50-78-2) were obtained from Sigma-Aldrich (St. Louis, MO). Montmorillonite (CaMMT) was subjected to an ion exchange treatment to maximize the concentration of calcium ions. A 100 mesh stainless-steel screen with 140 µm square openings was used for montmorillonite and kaolinite measurements and a 1400 mesh stainless-steel

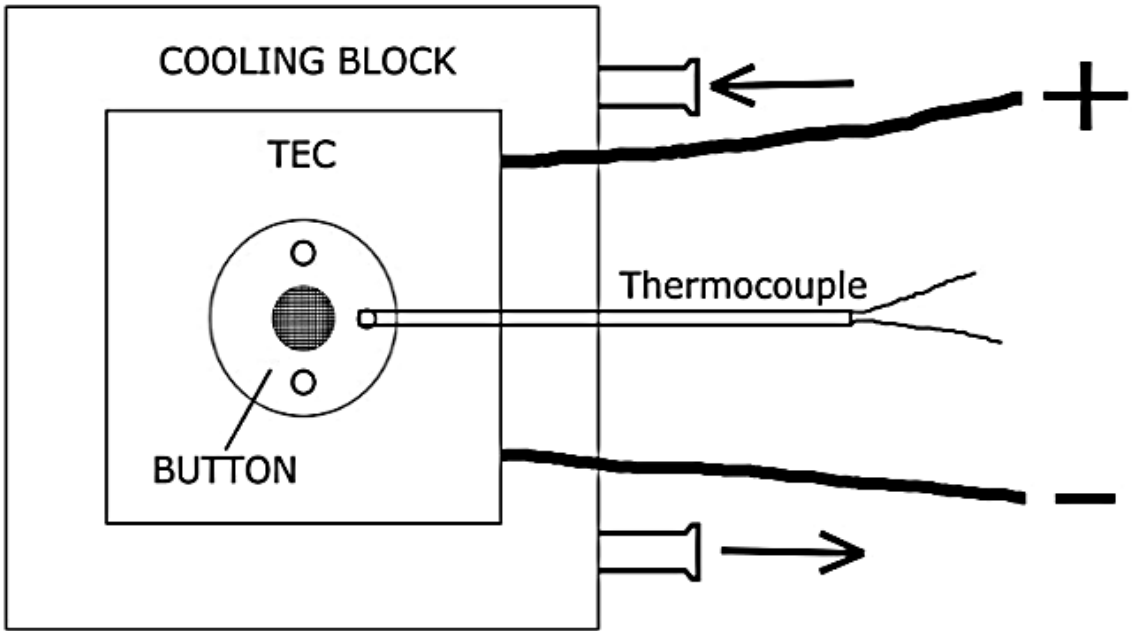

Figure 3.5– Schematic of button heating/cooling apparatus.

screen with 5 µm openings was employed for liquid sample measurements. Figure 3.5 is a

schematic representation of the button heating/cooling apparatus. To enhance heat conduction between the sample and the thermoelectric cooler (TEC), the button bottom surface was sanded flat and polished to maximize smoothness. The heat generated by the CUI Devices (Lake Oswego, OR) CP6030395 TEC chip was removed by an aluminum cooling block. The TEC and cooling block surfaces were coated with a thin layer of Artic Silver 5 (Visalia, CA) to maximize thermal conductivity. A continuous flow of a 50:50 water/ethylene glycol mixture through the cooling block was used to remove heat generated by the TEC. Liquid coolant temperatures were adjusted and regulated by using an RTE-4 ThermoFisher Scientific (Waltham, MA) Neslab recirculating chiller, which provided a 13 L/min flow rate. The button-TEC-cooling block stack depicted in Figure 3.5 was clamped in an aluminum fixture to promote contact between surfaces and restrict component movements. The assembly was mounted on a slide so that samples could be introduced to and removed from the FTIR spectrophotometer through a slot opening cut in the front of the instrument.

Button sample temperatures were measured by using a K-type thermocouple. Temperatures were varied by changing the power to the TEC. An Accuthermo (Fremont, CA) model ATEC302 temperature controller and FTX700DX H-bridge amplifier were used to provide DC power (12 V, 6 A max) to the TEC, using the thermocouple voltage for feedback control. With the H-bridge amplifier, the temperature controller could heat and cool the TEC surface in small increments, preventing large set point overshoots and providing reproducible heating and cooling rates and ± 0.2 °C isothermal temperatures.

A Mattson Instruments Inc. (Madison, WI) Nova Cygni 120 Fourier transform infrared spectrophotometer (FTIR) and a Harrick Scientific Inc. (Pleasantville, NY) praying mantis diffuse reflection accessory[63] were used for infrared spectrum measurements. Liquid sample

spectra were obtained for 1.5 µL volumes over the 4000-700 cm^{-1} range by signal averaging 16 interferograms for both sample and background single beam measurements. Interferogram collections required about 7 seconds. Montmorillonite spectra were measured isothermally by signal averaging 64 interferograms, which required approximately 30 seconds. Successive kaolinite spectra were obtained at about 1 minute intervals by signal averaging 175 interferograms. Although all infrared spectra were measured at 8 cm^{-1} resolution, interferogram zero filling prior to processing yielded a 0.97 cm^{-1} digitization interval. This was found to provide reproducible absorbance band shapes and yielded superior signal-to-noise ratio compared to measurements made at 4 cm^{-1} resolution.[64] Kaolinite and montmorillonite reflectance measurements were converted to Kubelka-Munk units.

3.2.2.2 Results and Discussion

When the apparatus shown in Figure 3.5 was positioned at the diffuse reflectance accessory focal point, button temperatures depended on the spectrophotometer purge gas and thermoelectric cooler (TEC) temperatures and the radiant heat provided by the infrared source. Sample temperatures could be varied by changing the voltage applied to the TEC, which operated as a heat pump.[99] When cooling, temperatures depended on the amount of heat pumped from the button by the TEC. This heat and the heat generated by device operation was transferred to the cooling block.[100] Alternatively, sample heating could be achieved by pumping energy from the TEC into the button. This was accomplished by reversing the TEC power supply polarity. However, because excessive heat could damage piezoelectric components, button temperatures were restricted to a maximum of 100 °C.

To maintain constant button temperatures, the heat pumped by the TEC must be continually removed by the cooling block, which contained a 50:50 water/ethylene glycol mixture flowing from a constant temperature bath. The button ambient temperature (i.e. without TEC power) was determined by the cooling block recirculating fluid temperature. The heating and cooling properties of the apparatus were dependent on this ambient temperature.

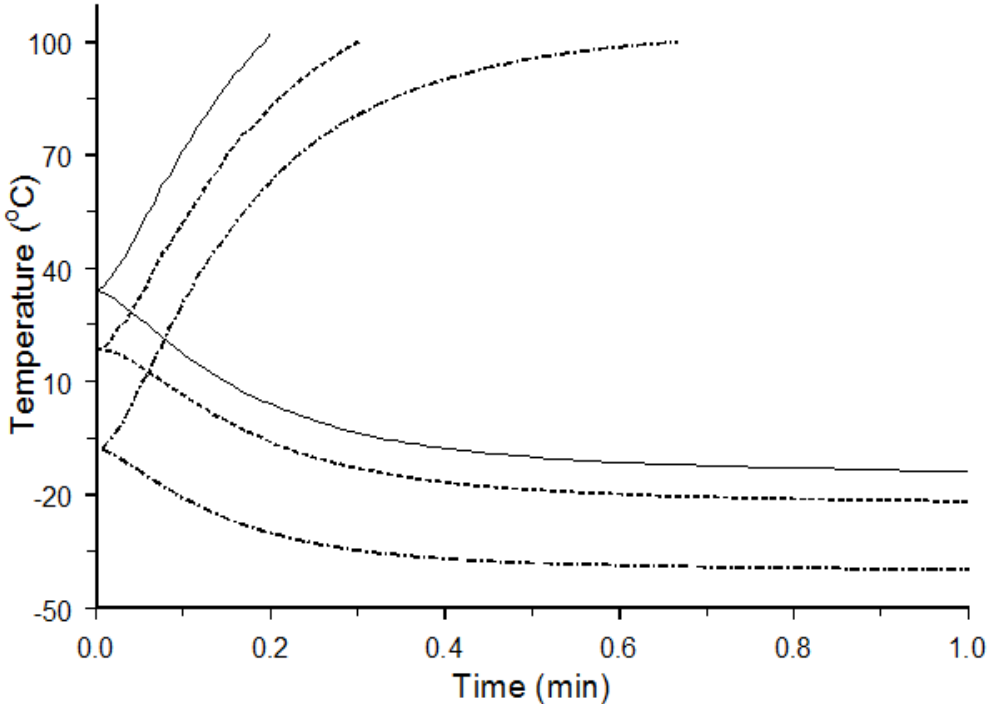

Figure 3.6 – Button maximum heating and cooling temperature profiles beginning from different starting temperatures.

For example, plots in Figure 3.6 depict button heating and cooling properties for the apparatus shown in Figure 3.5 beginning at different ambient temperatures by applying full power (12 V, 6 A) to the TEC. When heating buttons, TEC power was disconnected when the temperature exceeded 100 °C to prevent damage to internal components. A 34 °C ambient button temperature was attained when the recirculating fluid was 37 °C. Reducing the reservoir fluid temperature to 12 °C and -18 °C resulted in ambient button temperatures of 19 °C and -8 °C, respectively. Figure 3.6 shows that, whether heating or cooling, temperatures varied

exponentially with time. The heating and cooling profiles in Figure 3.6 changed significantly when the recirculating fluid temperature was varied. In general, lowering the recirculating fluid temperature provided lower button temperatures at the expense of reduced maximum heating rates. By using the temperature controller and an ambient button temperature of -8 °C, sample temperatures between -40 and 100 °C could be reached in a matter of seconds. When maximum TEC cooling conditions were maintained for more than 10 min, sample temperatures below -50 °C were obtained.

Samples were loaded onto the button outside the spectrophotometer and then isothermally positioned at the infrared beam focal point by using a slide mechanism. For volatile liquids, the time elapsed between placing the sample at the infrared beam focal point and the start of data acquisition had a significant impact on measurement reproducibility. Spectral features were noticeably weaker for slightly longer delays. This was likely caused by radiant heating, which evaporated volatile samples more quickly when infrared radiation was directed onto the button. Evaporative sample loss was qualitatively monitored by observing absorbance band intensities in successively acquired single beam spectra. After positioning a 25 °C button containing 1.5 µL of acetone at the beam focus, the 1740 cm^{-1} carbonyl stretching vibration band persisted for about 20 seconds in successively measured single beam spectra. When the button was cooled to -20 °C, the acetone carbonyl band remained in spectra for at least 6 minutes. Cooling the button from 25 to 10 °C increased the acetone residence period by more than a factor of 2, allowing sufficient time to obtain reproducible, high quality spectrum measurements. Other volatile liquids exhibited similar evaporation trends. Figure 3.7 shows infrared spectra derived from 16 interferogram scans, requiring a total time of about 7 s

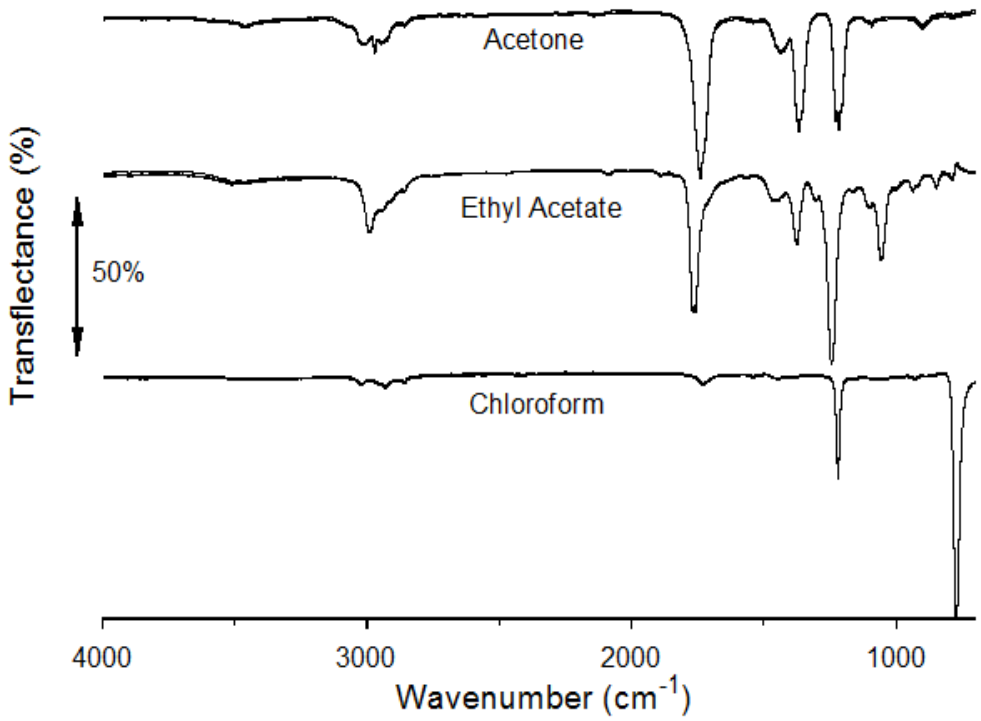

Figure 3.7– Overlays of three replicate infrared spectra for acetone, ethyl acetate, and chloroform measured at 10 ºC.

per spectrum, for acetone, ethyl acetate, and chloroform when the button temperature was maintained at 10 °C. Three spectra obtained by loading separate 1.5 µL aliquots to the same button and computed by using the same background single beam spectrum are superimposed for each liquid. These high signal-to-noise ratio transflectance spectra are similar to thin film transmission cell spectra, except that peak widths are slightly wider and relative band intensities differ due to effects from multiple path length absorbance (Chapter 2).[101] Spectra representing the same substance overlap over the entire wavenumber range, indicating excellent reproducibility. In fact, calculated relative standard deviations (RSD) as a function of wavenumber never exceeded 1% for the three acetone spectra. The largest RSD was found at 1743 cm^{-1}, where absorbance maximized.

The TEC temperature controller could be programmed to provide a variety of heating/cooling sample temperature profiles. The variable temperature analysis capabilities of the apparatus and methodology were evaluated by measuring infrared spectra while applying linear heating/cooling and temperature step profiles to solid samples. To test linear heating/cooling temperature ramps, kaolinite powder infrared spectra were measured at ca. 1 min intervals while cooling a neat sample from 100 to -20 °C at a programmed rate of -2 ° C/min, holding at -20 °C for five minutes, then heating to 100 °C at a programmed rate of 2 ° C/min. Thermocouple measurements were made at 0.5 s intervals throughout these temperature variations. Temperature-dependent trends in acquired spectra were found to be similar to those previously reported for the same material when hot air heating was used to increase sample temperatures from 30 to 150 °C at a rate of 2 °C/min.[102] Because temperature ramps were generated based on thermocouple measurement feedback, button temperatures consistently lagged set point temperatures by 0.1–0.3 °C during heating and cooling ramps. Cooling and heating rates calculated by linear regressions of temperature versus time measurements were found to be -2.01 and +1.98 °C/min, respectively, which were within 1% of the 2 °C/min programmed rates.

Figure 3.8 shows an overlay of five kaolinite infrared spectra obtained at 30 °C intervals while cooling the sample from 100 to -20 °C. This graph is indistinguishable from one obtained by plotting spectra measured at the same temperatures, but while heating to 100 °C after a 5 minute -20 °C isothermal period, suggesting that spectrum changes were mostly reversible. The Figure 3.8 overlaid spectra are similar except for small differences in the O-H stretching vibration and fingerprint regions. The inset plot in Figure 3.8 compares the kaolinite O-H

stretching vibration regions in spectra obtained at 100 and -20 °C. The overlapping hydroxyl stretching vibration band locations are consistent with those reported in several previous studies.[103-106] The 3700 cm^{-1} band shifted to higher wavenumber and the 3620 cm^{-1} band shifted to lower wavenumber with decreasing temperature. In addition, two bands located between 3700 and 3620 cm^{-1} are better resolved at the lower temperature. These trends are consistent with a previous study that employed Raman microprobe measurements to monitor kaolinite hydroxyl group vibrations as a function of temperature. Frost et al. reported a blue shift of the inner hydroxyl band (3700 cm^{-1}) and a red shift of the inner surface hydroxyl band (3620 cm^{-1}) along with a general peak narrowing for O-H stretching vibration bands with decreasing temperature between 400 and 25 °C.[107] By using KBr pellet infrared

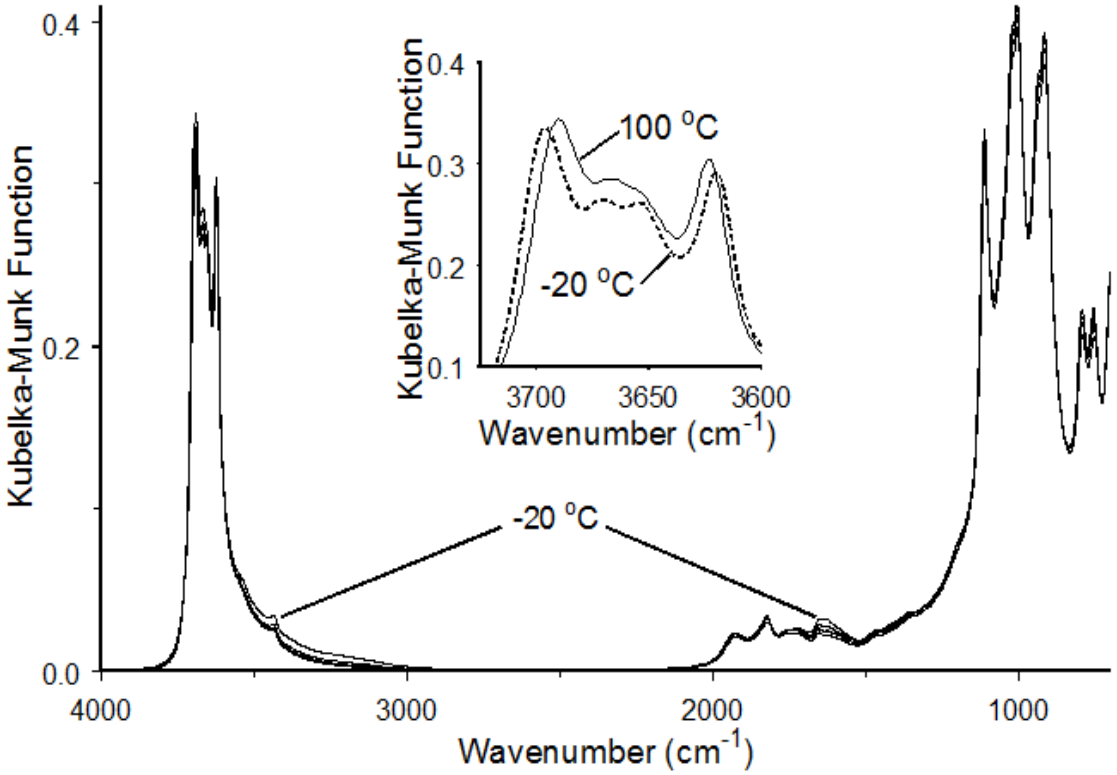

Figure 3.8 – Overlay of kaolinite diffuse reflectance spectra obtained at 100, 70, 40, 10, and -20 ºC. The inset plot shows an expansion of the 100 and -20 °C spectra over the O-H stretching vibration region.

transmission measurements, Balan et al. reported linear 3700 and 3620 cm^{-1} band center shifts in kaolinite spectra between -3 and -173 °C.[108] Similar trends are evident in the top graph in Figure 3.9, which shows peak maxima wavenumber measurements made at ca. 2 °C increments for the 3700 and 3620 cm^{-1} bands when the kaolinite sample was cooled and then

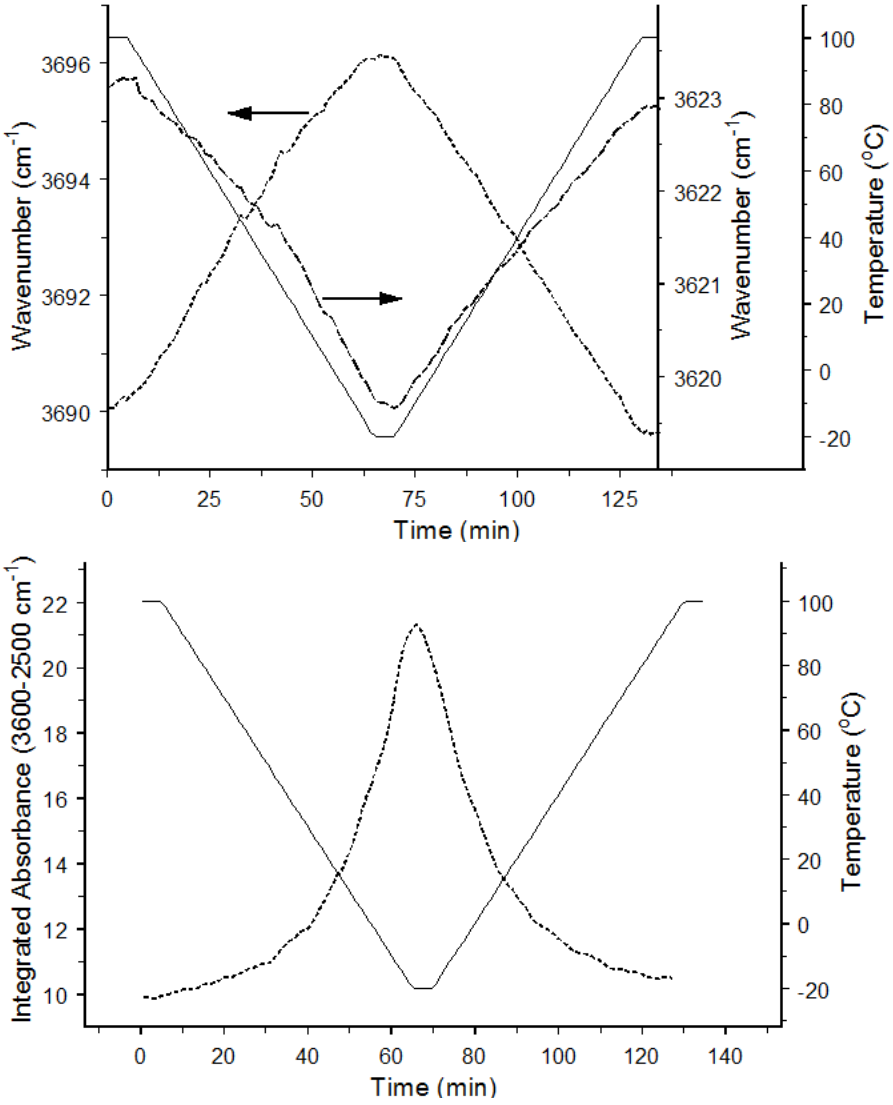

Figure 3.9 – Top – Hydroxyl stretching vibration wavenumber changes with temperature. The solid line denotes sample temperature measurements. Peak center wavenumbers as a function of time are provided for bands nominally located at 3700 cm^{-1} (dotted line) and 3620 cm^{-1} (dashed line). (b) Adsorbed water content (3600–2500 cm^{-1} integrated area) as a function of time (dotted line). The solid line denotes sample temperatures.

heated. Linear regression slopes calculated between 75 and 125 min were: -0.0537 ± 0.0001 (R^2 = 0.999) and +0.0269 ± 0.0002 (R^2 = 0.998) $cm^{-1}/°C$ for the 3700 and 3620 cm^{-1} bands, respectively. These slopes are consistent with the trends reported by Balan et al.[108] Based on their data, slopes derived from band center wavenumber as a function of temperature plots between -173 and -3 °C were estimated to be -0.067 and +0.021 $cm^{-1}/°C$ for the 3700 and 3620 cm^{-1} bands, respectively.

Figure 3.8 shows that kaolinite infrared spectrum intensities over the 3600-2500 cm^{-1} range and near 1620 cm^{-1} increased with decreasing temperature. This can be attributed to water adsorption, leading to increased spectral intensities for hydrogen-bonded O-H stretching vibrations and H-O-H bending vibration bands. Although the spectrophotometer was purged with dry air, some water vapor remained. This was confirmed by the presence of characteristic water vapor absorbance in single beam spectra. Apparently, residual water vapor adsorbed on kaolinite surfaces, and the quantity of adsorbed water increased with decreasing temperature. The plot of the 3600-2500 cm^{-1} integrated area as a function of temperature at the bottom of Figure 3.9 depicts the growth and subsequent loss of adsorbed water while cooling and then heating the sample. The integrated intensity maximized at 72 minutes, which corresponded to the end of the five minute -20 °C isothermal period and the beginning of sample heating, indicating that water adsorption continued throughout the entire cooling period. The symmetrical nature of the graph indicates that the water adsorption process was reversible.

In addition to linear heating ramps, button temperatures were programmed to follow an increasing temperature step function. Infrared spectra were obtained isothermally by using this approach. For example, the top graph in Figure 3.10 shows button temperatures measured at 0.5 s intervals during a step heating/cooling profile employed to study the thermal properties

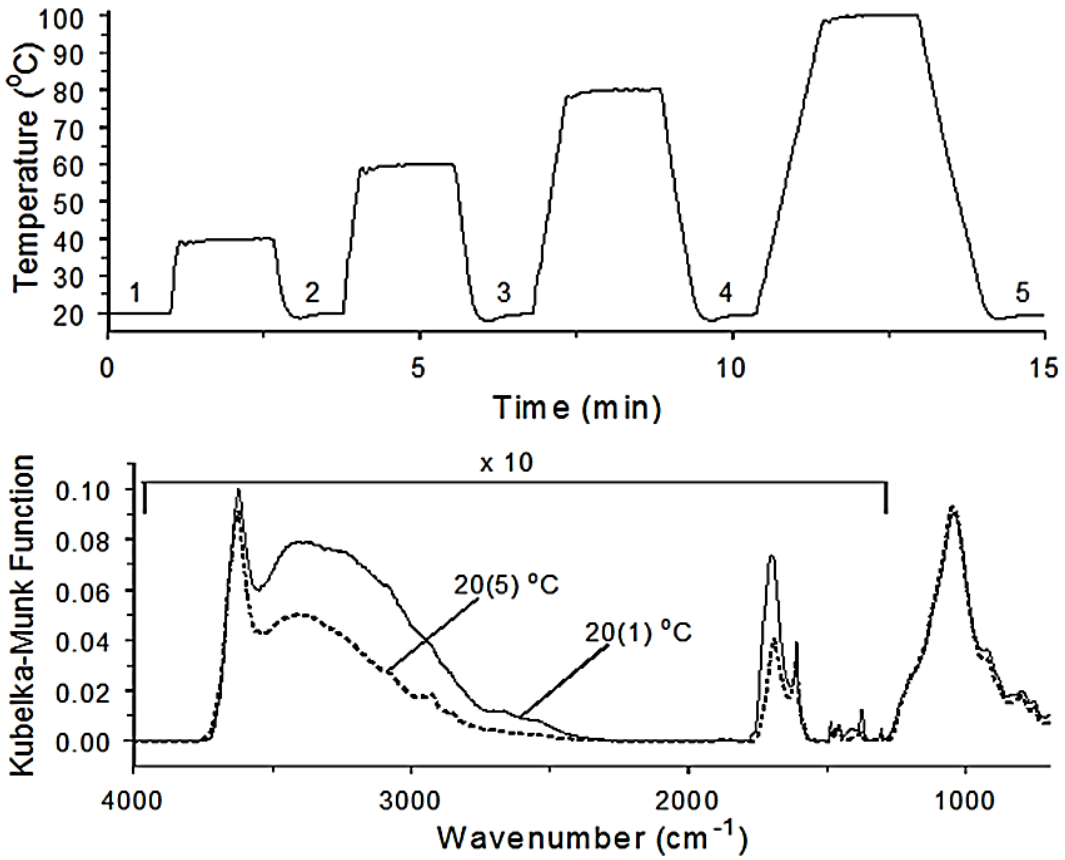

Figure 3.10– Top - Stepped heating profile and Bottom - 15% Acetylsalicylic acid/calcium montmorillonite infrared spectra obtained initially (solid line) and during the final 20 °C isothermal period (dashed line). The 4000-1300 cm^{-1} intensities are magnified by a factor of 10.

of montmorillonite clay containing 15% by weight acetylsalicylic acid. Sample temperatures increased by 20 °C per step from 20 to 100 °C. After a 1 min isothermal period at 20 °C, the temperature was increased to 40 °C at a rate of 1.25 °C/s. After a 1.5 min 40 °C isothermal period, the temperature was returned to 20 °C by cooling at a rate of -1.20 °C/s. This cycle was repeated, sequentially heating the sample to 60, 80, and 100 °C. Infrared spectra were collected during the last 30 s of each isothermal period, when measured temperature standard deviations were ca. ± 0.2 °C.

Heating the montmorillonite/acetylsalicylic acid sample disrupts the hydrogen bonding network, which affects vibrations for the adsorbate and inorganic clay constituents in addition to the water molecules primarily responsible for these interactions.[111] Acetylsalicylic acid vibrations involving the carboxylic acid group were primarily affected by these interactions. Temperature-dependent interlayer water loss, which reduced the spacing between inorganic oxide sheets, affected montmorillonite vibrations. Infrared spectra acquired during the first and final 20 °C isothermal periods are overlaid at the bottom of Figure 3.10. The most intense band in these spectra appeared near 1000 cm^{-1} and was assigned to montmorillonite inorganic oxide vibrations. Ordinate scales were expanded by a factor of 10 over the 4000-1300 cm^{-1} range in these plots to emphasize low absorptivity bands. The main differences in these spectra can be attributed to effects from water loss, which was directly responsible for the broad decrease in the 3700-2500 cm^{-1} O-H stretching vibration band intensity and the H-O-H bending vibration band intensity near 1630 cm^{-1}. Several acetylsalicylic absorption bands appear in the 1800–1300 cm^{-1} spectrum region. Table 3.1 lists peak locations for these bands along with those previously reported for pure acetylsalicylic acid and salicylic acid.[111-112] The second column lists band locations in the initial 20 °C

Table 3. 1 - Initial and final band center locations obtained by increasing temperature step heating compared to pure acetylsalicylic and salicylic acids

Assignment	Initial (20(1) °C)	Acetylsalicylic acid[109]	Final (20(5) °C)	Salicylic acid[110]
C=O	1701	1706	1690	1659
Ring	1609	1606	1611	1611
Ring	1486	1486	1485	1483
Ring	1458	1454	1457/1465	1466
Ring	1374	1370	1377	1383

spectrum. Acetylsalicylic acid interactions with montmorillonite primarily involved hydrogen bonding to interlayer water molecules that bridged between cations and aromatic acid groups.[111] Compared to pure acetylsalicylic acid, these interactions resulted in peak intensity variations as well as band shifting and broadening, causing the ester functionality C=O stretching vibration band, found near 1750 cm^{-1} in the neat acetylsalicylic acid spectrum, to merge with the acid C=O band. These interactions were responsible for the differences between vibration band wavenumbers for acetylsalicylic acid adsorbed on montmorillonite and the neat acid. Table 3.1 also shows that the broadened C=O stretching vibration band maximum shifted from 1701 to 1690 cm^{-1} after the sample was heated. Comparing band locations found in the 20(5) °C spectrum with those in the pure salicylic acid spectrum reveals that this red shift was consistent with the formation of salicylic acid, which is the primary thermal decomposition product of acetylsalicylic acid.[110] Wavenumber shifts for the other peaks listed in Table 3.1, which primarily arise from aromatic ring vibrations, are also consistent with salicylic acid formation. Interestingly, the 1458 cm^{-1} ring vibration band in the first spectrum split into two peaks, located at 1457 and 1465 cm^{-1}, in the final spectrum, indicating the presence of both acetylsalicylic and salicylic acids at the end of the heating profile.

By subtracting infrared spectra obtained during selected segments of the sample temperature step heating/cooling profile, changes associated with heating were elucidated. Differences calculated by subtracting spectra collected at 40, 60, 80, and 100 °C from the 20 ° C spectrum obtained prior to heating the sample to these temperatures contained information characterizing both reversible and irreversible sample changes. Residuals remaining after subtracting the spectrum collected at 20 °C after cooling the sample from the spectrum obtained at 20 °C before heating revealed irreversible changes. Similarly, subtracting the spectrum

collected at elevated temperature from the one measured after cooling provided information for reversible spectrum changes.

The difference spectra in Figure 3.11 contain features that provide insight into subtle sample structure variations associated with each temperature step. For example, Figure 3.11a difference spectra characterize changes caused by heating the sample from 20 to 40 °C. The "total" changes difference spectrum was obtained by the 40-20(1) °C spectrum subtraction, "reversible" changes were identified by the 40-20(2) °C spectrum subtraction, and the

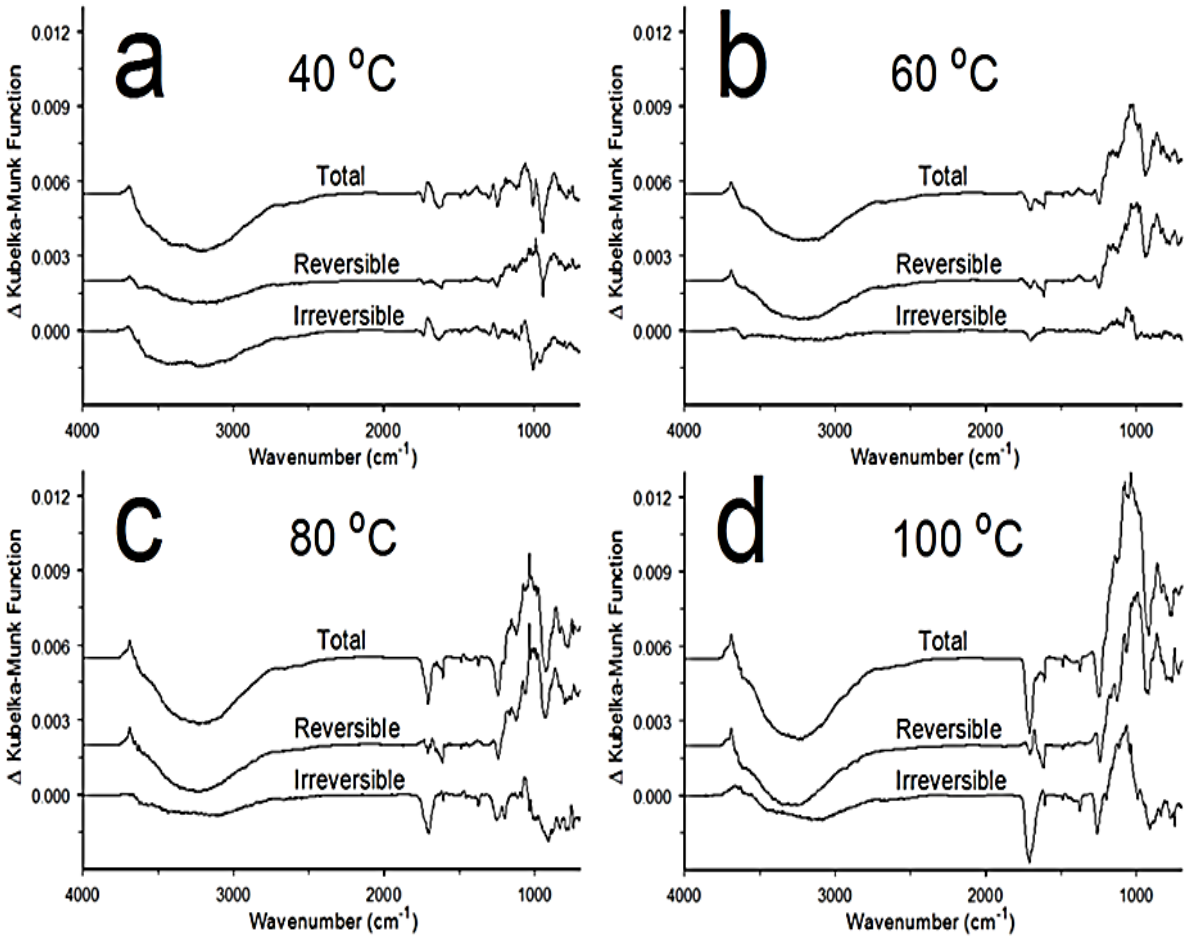

Figure 3.11 – Difference spectra characterizing changes induced by successively heating the 15% acetylsalicylic acid/montmorillonite sample to (a) 40 ºC, (b) 60 ºC, (c) 80 ºC, and (d) 100 ºC.

"irreversible" change difference spectrum was obtained by the 20(2)–20(1) °C spectrum subtraction. Numbers in parentheses correlate with the designations in the temperature step profile at the top of Figure 3.10 and specify which 20 °C isothermal period spectra were employed for subtractions. For each difference spectrum, positive bands denote features gained and negative bands represent features that were lost by heating the sample.

Previous thermogravimetry-mass spectrometry (TG-MS) analyses of calcium montmorillonite (CaMMT) containing acetylsalicylic acid revealed that the adsorbate decomposed above 60 °C, forming salicylic acid and evolving acetic acid.[112] Below 60 °C, TG-MS results indicated that sample mass loss was exclusively caused by water desorption.[113] Therefore, the spectrum changes depicted in Figure 3.11a, which resulted from heating the sample from 20 to 40 °C, may be attributed to effects from clay interlayer water loss. Negative features in the 3670–2500 cm^{-1} range and near 1630 cm^{-1} denote loss of water O-H stretching vibration and H-O-H bending vibration band intensities. Small positive bands in difference spectra at 3690 cm^{-1} can be assigned to inorganic oxide hydroxyl groups (Si-OH and/or Al-OH) that lost hydrogen bonding partners as a result of sample heating. Based on Figure 3.11a difference spectra intensity trends, most of the water loss was irreversible. Difference spectra also indicate changes to montmorillonite inorganic oxide sheet and acetylsalicylic acid vibrations caused by water desorption. Reversible changes in the 1100–900 cm^{-1} region include intensity increases below and above 1000 cm^{-1} but little change near the 1000 cm^{-1} inorganic oxide vibration band maximum. In contrast, irreversible changes included loss of intensity near 1000 cm^{-1}. These two effects combined to yield a total difference spectrum intensity loss near 1000 cm^{-1} and increases above and below 1000 cm^{-1}, which resulted in inorganic oxide vibration band broadening when the sample temperature was

increased. The irreversible difference spectrum in Figure 3.11a exhibits intensity loss at 1733 cm^{-1} and gain at 1708 cm^{-1} that is indicative of acetylsalicylic acid ester C=O loss and an increase in the carboxylic acid C=O stretching vibration band intensity. These changes denote -8% and +6% intensity variations to the initial spectrum intensities at these wavenumbers, respectively. This was likely due to the hydrolysis of some acetylsalicylic acid to form acetic and salicylic acids. The increased intensity at 1708 cm^{-1} indicated that the acetic acid remained in the clay, which was consistent with the previously reported TG-MS result that only water was lost below 60 °C.[112]

A slight irreversible water loss was evident in differences calculated from spectra derived from heating the heating to 60 °C (Figure 3.11b). The small negative band between 1750 and 1670 cm^{-1} was most likely caused by acetic acid desorption. The reversible montmorillonite water loss at this temperature caused inorganic oxide vibration band shape changes that were similar to those observed after heating the sample to 40 °C (Figure 3.11a). Above 60 °C, negative intensity losses between 1750 and 1670 cm^{-1} appeared in difference spectra, which were indicative of continued acetylsalicylic acid decompositions and evolution of acetic acid (Figures 3.11c and 3.11d). The 80 and 100 °C irreversible change difference spectra also contain negative features near 1250 cm^{-1}, which can be assigned to C-OH acetic acid stretching vibrations. Interestingly, this intensity loss was not readily apparent in measured spectra because of the overlapping strong absorbance from montmorillonite inorganic oxide vibrations (Figure 3.10). Small negative peaks at 1611 and 1487 cm^{-1} in the 80 and 100 °C difference spectra are associated with aromatic rings (Table 3.1) and are indicative of salicylic acid desorption, which has been detected at temperatures below 100 °

C.[112] Like the 60 °C temperature step, inorganic oxide vibration band shape variations were mainly associated with reversible water losses when the sample was heated to 80 and 100 °C.

3.2.2.3 Conclusions

The button sample holder consists of a flat, thin piece of high thermal conductivity stainless-steel and can be effectively heated and cooled by using a thermoelectric device. This permits variable temperature infrared spectroscopic studies of neat solid powders and liquid samples. Because samples can be rapidly heated and cooled, various heating/cooling profiles can be employed, including temperature step and linear heating ramps. Linear temperature ramp measurements can be used to monitor infrared band wavenumber and intensities variations over a wide sample temperature range. Alternatively, when investigating the effects of heating samples to specific temperatures, a heating step profile, which provides isothermal spectrum measurements and requires less time, is preferred.

Sample heating was restricted to temperatures below 100 °C for the studies described here. By employing a more robust TEC internal architecture, temperatures approaching 200 ° C should be possible, which will significantly enhance the applicability of the technique.[100] Lower temperatures may be attained by using TEC stacking. By using this approach, the heat generated by the top TEC is removed by one beneath it. Ambient sample temperatures would be determined by the lower TEC temperature, which could be adjusted more quickly than the recirculating temperature bath employed for the studies described here.

Chapter 4: Button-IR Variable Temperature Diffuse Reflection Infrared Spectroscopy of Ion Exchanged Linde Type A Zeolites

4.1 Introduction

Zeolites are crystalline aluminosilicates with commercial applications in petroleum refining,[114] gas separation,[115-117] environmental remediation,[118-119] and agriculture.[120] There are over 40 naturally occurring and over 150 synthetic zeolite frameworks. These frameworks are comprised of 4-coordinate atoms arranged in tetrahedra that link together to form channels and pores. When Al is substituted for Si, frameworks acquire a negative charge, necessitating the presence of counterions. Pore and channel dimensions restrict the size of molecules that can be accommodated within zeolites. Linde type A (LTA) is a synthetic zeolite first reported by Breck et al. in 1956.[121]. The intrinsic properties of this material make it useful for a wide range of applications involving: adsorption,[116, 122] ion-exchange,[123-125] and catalysis.[126] LTA is a molecular sieve that can be used to selectively remove small molecule contaminants from process streams.[127-128] When LTA pores are filled with salts, it can be used as a soil amendment to provide slow release fertilization.[129-130] Water nanoclusters play a significant role in transport processes inherent in these applications. For this reason, LTA water molecule properties have been the focus of numerous research efforts.[131] LTA water nanoclusters have been characterized by x-ray diffraction,[132] thermal analysis,[133-135] neutron scattering,[136-137] and infrared spectroscopy.[137-141] In addition, water molecule interactions have been modeled and LTA bulk properties have been predicted based on computational methods.[125, 128, 131, 141-144]. Properties of LTA can be modified by cation

exchange. For example, nominal pore openings depend on the counterion, with potassium (KA) yielding 3 Å, sodium (NaA) yielding 4 Å, and calcium (CaA) yielding 5 Å.

The LTA zeolite structure consists of two connected aluminosilicate cages with different sizes.[132] It is hydrophilic because of the high framework aluminum content (Si/Al = 1). When sodium ions constitute counterions, the empirical formula for the NaA unit cell is $Na_{96}[Al_{96}Si_{96}O_{384}] \cdot 216\ H_2O$.[132]. The NaA unit cell is comprised of eight interconnected α and β cages. The β-cage can accommodate 4 water molecules. The larger α-cage can hold up to 20 water molecules, and 3 additional water molecules can occupy sites located in eight member ring "windows", for a total capacity of 27 water molecules for the cage system.[132]

Variable temperature infrared spectroscopy measurements provide a means for characterizing zeolite water molecule interactions because water O-H stretching and H-O-H bending vibrations are sensitive to hydrogen bonding and electrostatic interactions. NaA water molecule vibrations have been characterized by monitoring changes in infrared spectra measured while heating samples.[137-140] By using transmission infrared spectroscopy with NaA dispersed in CsI pellets, Crupi et al. described the spectrum changes that occurred between -20 and 55 °C.[137-138] By applying curve fitting to absorbance bands measured at different temperatures, three overlapping constituent bands were identified for the O-H stretching vibration and two overlapping components were found for the H-O-H bending vibration. The O-H stretching vibration components were characterized as: (1) water molecules linked to three or four neighbors (i.e. connective water); (2) water molecules involved in two hydrogen bonds (i.e. intermediate water); and (3) water present as monomers and dimers (i.e. multimeric water).[138] The H-O-H bending vibration absorbance was decomposed into bands at 1648 and 1678 cm^{-1}. The relative absorbance band area contribution

from the 1648 cm^{-1} constituent reportedly increased with increasing temperature. The 1648 cm^{-1} band was assigned to "intermediate water" and the 1678 cm^{-1} band was assigned to "connective water".[137] By using attenuated total reflectance (ATR), infrared spectra for NaA and NaMgA zeolites were measured between -10 and 80 °C.[139] The ATR technique was considered to be more sensitive than the previous CsI pellet transmission measurements and four overlapping constituents were required to fully characterize temperature-dependent O-H stretching vibration band shape changes.[139] The four constituents were described as: (1) water molecules coordinated to a cation; (2) water clusters incorporating linear hydrogen bonding; (3) water molecules involved in weak, bifurcated hydrogen bonds; and (4) water molecules involved in very weak hydrogen bonding.[139-140]

Molecular modeling studies have been used to characterize LTA bulk properties based on molecular interactions. Several studies have focused on the impact of the zeolite cation. For instance, Jensen et al. determined that the larger size of potassium compared to sodium cations decreased water diffusivity by a factor of ten.[128] The cation charge was found to affect the structures of initially formed water clusters but had little impact on saturated water molecule configurations.[125] Studies have suggested that strong water-cation interactions reduce the number of water-water hydrogen bonds, resulting in an average of less than two hydrogen bonds per water molecule in hydrated LTA compared to 3-3.5 hydrogen bonds per molecule in bulk water at a similar density.[142] Demontis, et al. reported that the water-Na^+ interaction energy for molecules in the NaA α-cage is about half that in the β-cage and that each water molecule in the β-cage interacts with two Na^+ ions, significantly reducing water-water hydrogen bond interactions.[143]

In addition to alteration of pore size, exchanging the charge balancing cation within LTA results in different molecular interactions, resulting in different behavior by the zeolite. Several studies have focused on exploiting the unique properties of CaA, particularly for CO_2 capture.[145-149] CaA has been suggested as a suitable material for separating CO_2 from CH_4[146] and for selective removal of SO_2, NO and CO_2 from flue gases.[147] CaA has a high affinity for moisture, and the presence of water reduces its CO_2 adsorption effectiveness.[146] In addition, carbonate species can form inside zeolite pores by reactions between H_2O and CO_2, which complicates small molecule adsorption mechanisms.[146]

To further explore the effects of temperature on LTA and the impact that cation exchange has on interactions, button-IR was employed with variable temperature diffuse reflection infrared Fourier transform spectroscopy (VT-DRIFTS) to monitor dehydration processes. In previous studies, VT-DRIFTS provided a sensitive means for discerning subtle temperature-dependent structural changes in solid materials.[150-152] In contrast to CsI pellet transmission spectroscopy, VT-DRIFTS measurements can be made without diluting the sample. Compared to the previously employed ATR sampling technique, the VT-DRIFTS powder sample is not compressed during measurements and samples can be heated to higher temperatures. Rather than applying curve fitting methods to deconvolve absorbance curves into constituent bands, subtle changes are elucidated from VT-DRIFTS measurements by using spectral subtraction techniques.

4.2 Experimental

4.2.1 Materials. NaA (CAS: 70955-01-0) was obtained from Fisher Scientific. The molecular sieve powder was comprised of particles smaller than 50 μm. To attain maximum NaA hydration, about 1 g of the powder was suspended in 50 mL of deionized water and stirred

overnight. The powder was recovered by filtration and allowed to dry under ambient conditions before analysis.

Calcium ions were substituted for Na^+ in the LTA zeolite by an ion exchange procedure similar to those previously published that yield at least 90% Na^+ replacement.[153-155] About 5g of pretreated NaA was dispersed in 100 mL of 1M $CaCl_2$ solution. This suspension was heated at 50 °C for 48 h with stirring to facilitate substitution of Ca^{2+} for Na^+. Calcium enriched A zeolite (i.e. CaA) was removed by filtration, placed in 500 mL of deionized water, and heated at 50 °C for 48 h with constant stirring. The CaA solid was then removed by filtration, repeatedly washed with deionized water (~500 mL total), and allowed to dry at room temperature prior to thermogravimetric and infrared studies.

4.2.2 Instrumentation. Sample heating was accomplished by using the apparatus shown in Figure 4.1. About 1 mg of powder was loaded into a 6 x 6 mm (0.25" x 0.25") square opening in a 100 mesh button, which was mounted on top of a quartz tube. Dry air purge gas flowing at 100 mL/min entered the bottom of the quartz tube and flowed around a cartridge heater, transferring heated air to the bottom of the button. The button sample holder consisted of a thin stainless-steel disk to which a stainless-steel wire mesh was welded. This sample holder was attached to an alignment ring by three screws. The alignment ring outer diameter was slightly smaller than the inner diameter of the quartz tube. The three attaching screws passed through stainless-steel washers placed between the alignment ring and button to create gaps, which served as vents for heated air to escape after the alignment ring was inserted into the quartz tube. This prevented pressure increases within the tube and improved heated gas flow rate stability. Sample temperatures were measured by using a K-type thermocouple pressed to the

wire mesh button front surface. The sample heating profile was generated by using a Eurotherm Controls Inc. (Reston, VA) model 818p temperature controller.

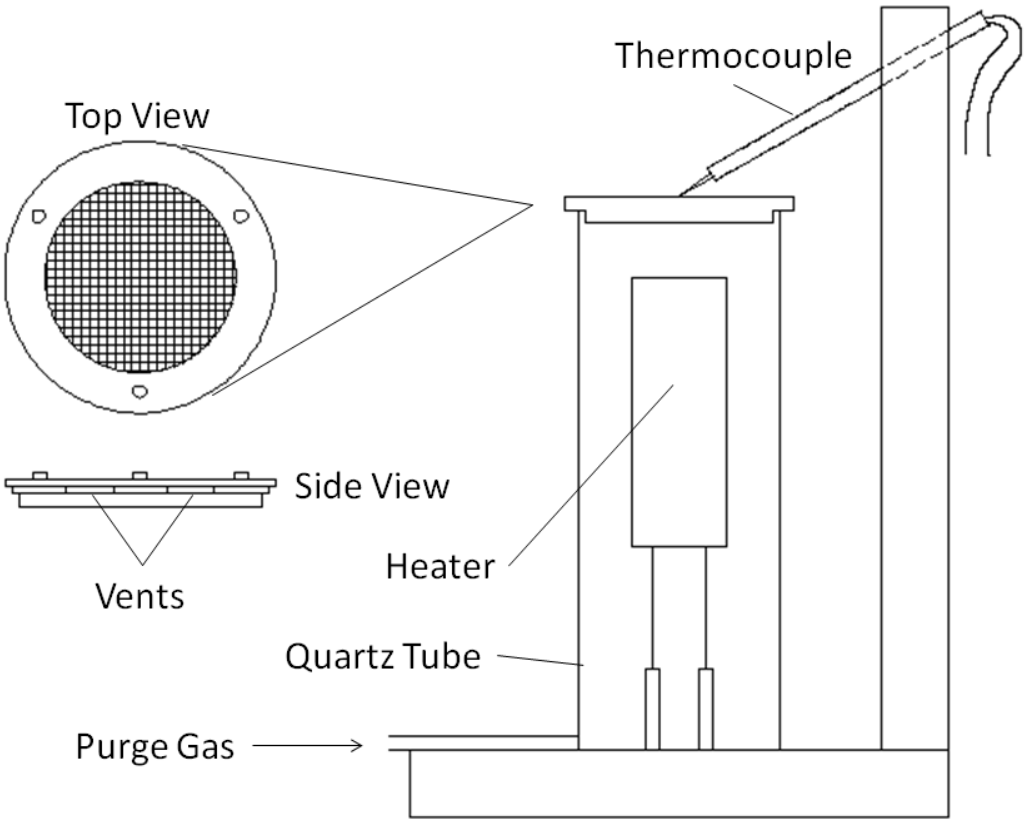

Figure 4.1 - Diagram of the variable temperature diffuse reflection infrared spectroscopy apparatus.

Thermogravimetry (TG) measurements were made by using a Du Pont Instruments model 951 Thermogravimetric Analyzer (TGA) controlled by an IBM Personal System/2 Model 55 SX with Thermal Analyst software. Approximately 10 mg samples of pretreated NaA and CaA were placed on the TG sample pan. Mass loss was monitored while each sample was heated from ambient temperature to 500 °C at a rate of 2 °C/min. Samples were purged with 50.0 mL/min helium during TG measurements.

A Mattson Instruments Nova Cygni 120 Fourier transform infrared spectrophotometer (FTIR) and a Harrick Scientific Inc. praying mantis diffuse reflection accessory[63] were used for infrared spectroscopy measurements. The optical system and the VT-DRIFTS methodology are described in chapter 2, section 2.2 and elsewhere.[156] A sealed environmental chamber was not employed for measurements described here. Instead, a thin layer of ion-exchange LTA powder was placed in the sample holder at the infrared focal point, which was directly exposed to the FTIR dry air purge. Because the sample holder was heated in atmospheric oxygen, temperatures were restricted to 150 °C to avoid metal oxidation. Infrared spectra were obtained at 1.07 min intervals while the sample was heated from ambient temperature to 150 °C at a rate of 2.0 °C/min. Spectrum collection continued at this rate during a 5 min isothermal period at 150 °C and throughout cooling (2.0 °C/min) to ambient temperature. While heating and cooling the sample, successive infrared spectra were acquired at 2.14 °C intervals.

4.3 Results and Discussion

4.3.1 Sodium-LTA (NaA)

The TG mass loss curve for neat NaA is shown in Figure 4.2. The shape of this curve is similar to previously published NaA results for the zeolite heated at 3 °C/min in nitrogen.[133] Mass loss was detected as soon as sample heating began. The sample mass measured at 500 °C was 80.8% of the initial mass, so a total of 19.2% of the sample was lost, presumably as water. This value is slightly less than the maximum NaA water content based on its empirical formula (22.2%), suggesting that the zeolite cage system was not completely filled. The mass loss curve in Figure 4.2 consists of two steps. A sharp decline in sample mass

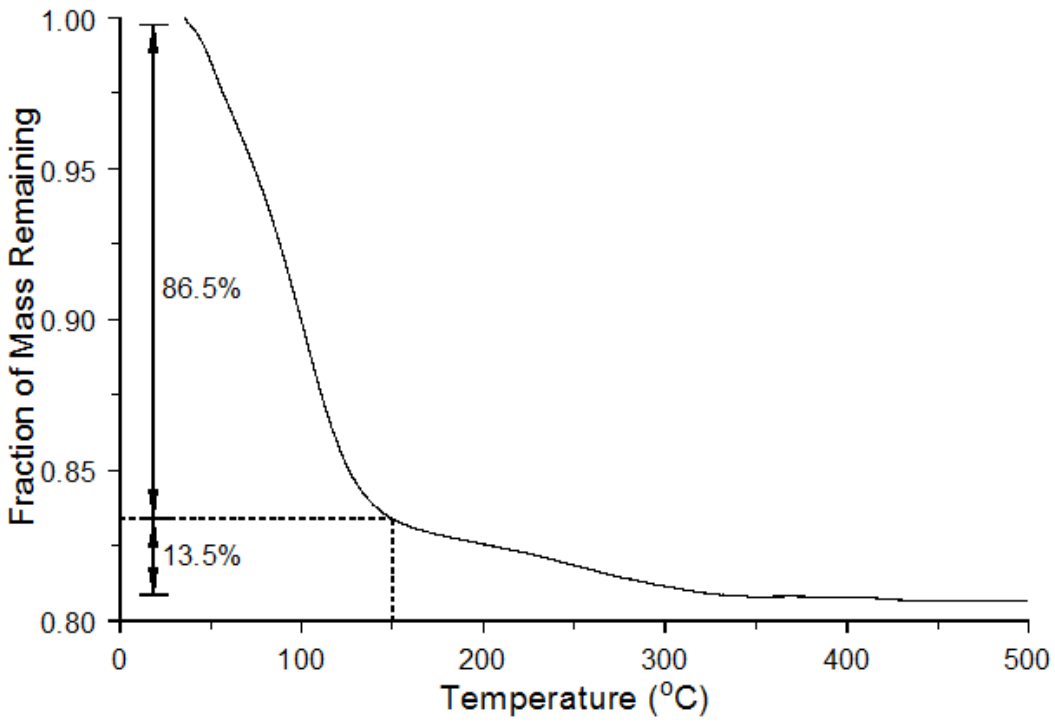

Figure 4.2 - Mass loss curve for NaA heated at 2 °C/min in 50.0 mL/min helium

between ambient temperature and 150 °C was followed by a smaller and more gradual mass loss between 150 and 350 °C. Above 350 °C, sample mass remained fairly constant, suggesting that the sample was fully dehydrated. Based on interaction energy calculations, water molecules located within α-cages should be more easily removed than those in β-cages.[143] Therefore, the sequential mass loss steps in Figure 4.2 can be assigned to loss of water from α-cages followed by loss of water from β-cages. Assuming that the β-cage capacity was 4 water molecules and that the total number of water molecules in the aluminosilicate cage system was 27, the first mass loss step should correspond to 85.2% of the total loss and the second step should correspond to 14.8%. As indicated in Figure 4.2, calculated values were 86.5 and 13.5% when 150 °C was assumed to be the transition temperature between the α-cage and β-cage dehydration steps. The differences between calculated and expected values may be due

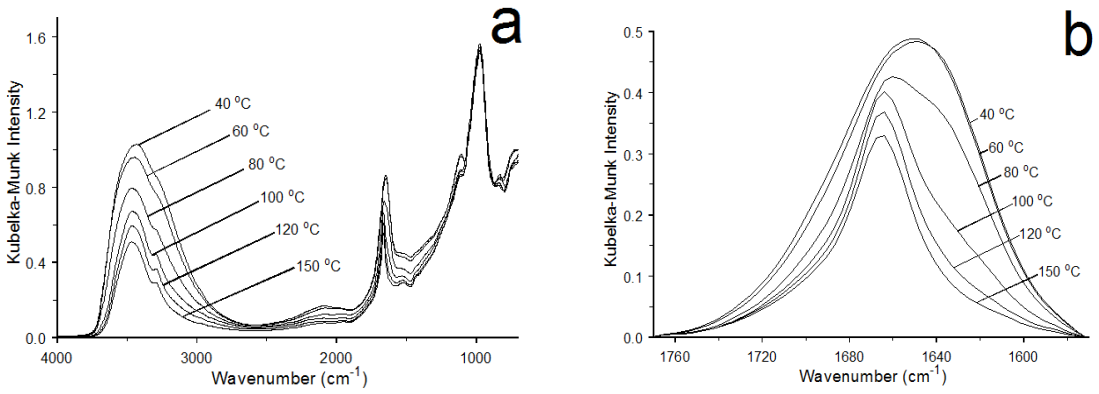

Figure 4.3 – VT-DRIFTS infrared spectra for NaA: (a) full spectrum and (b) water bending vibration band expansion.

to overlap in α-cage and β-cage dehydration processes and/or that a smaller fraction of β-cages were filled with water.

4.3.1.1 Broad loss in OH stretching and bending upon heating

VT-DRIFTS spectra obtained for neat NaA heated from ambient temperature to 150 ° C are shown in Figure 4.3. Decreased intensity in the O-H stretching (2800-3800 cm^{-1}) and H-O-H bending (1550-1750 cm^{-1}) spectral regions with increasing sample temperature are apparent (Figure 4.3a). The most intense band, located at 970 cm^{-1}, does not exhibit a significant intensity change with temperature. This band is assigned to aluminosilicate framework vibrations and should be invariant as long as the zeolite structure remains intact. The O-H stretching vibration absorbance maximum shifts from 3430 cm^{-1} at ambient temperature to 3470 cm^{-1} at 150 °C, which is indicative of a loss in hydrogen bonding. Figure 4.3b shows an expansion of the H-O-H bending vibration band region. For clarity, sloping baselines in this spectral region were removed by subtracting straight lines passing through the 1570 and 1770 cm^{-1} data points. The water bending vibration band becomes sharper and the peak maximum shifts from 1640 cm^{-1} at ambient temperature to 1665 cm^{-1} at 150 °C. Figure

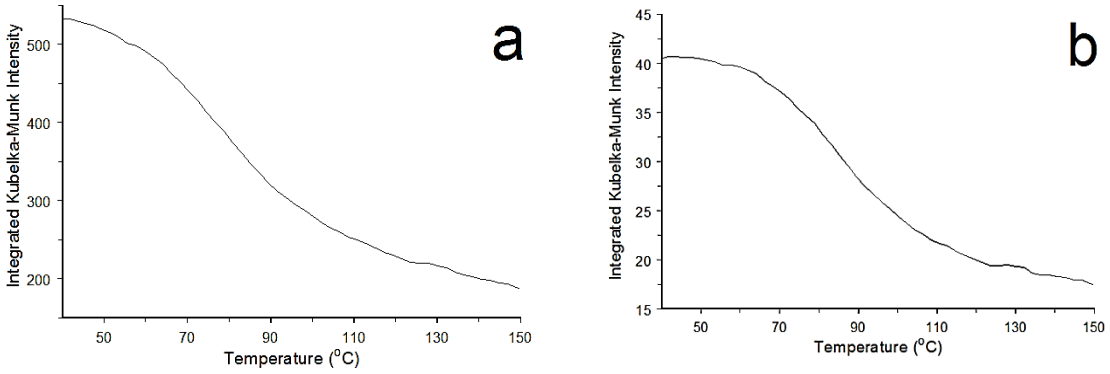

Figure 4.4 – Integrated intensity temperature profiles for the (a) O-H stretching vibration band and (b) H-O-H bending vibration band.

4.4 shows integrated band intensity versus temperature profiles for the O-H stretching (Figure 4.4a) and the H-O-H bending (Figure 4.4b) vibrations. The shapes of these curves are qualitatively like the first step in the mass loss curve (Figure 4.2). However, the initial decrease in integrated band area is greater for the stretching vibration (Figure 4.4a).

4.3.1.2 Water loss from 40-60°C

Infrared difference spectra, calculated by subtracting infrared spectra measured at different temperatures, contain only those features that changed during the temperature increment. As a result, difference spectroscopy permits sensitive detection of small temperature-dependent sample changes. Figure 4.5 shows differences between spectra measured at selected temperatures near the beginning of the heating ramp. Difference spectra contain negative bands that represent intensities that decreased while heating and positive bands that represent features that became more intense while heating. Figure 4.5a difference spectra reveal spectral changes that occurred to the O-H stretching vibration band when the sample temperature increased from 40 to 50 °C and from 50 to 60 °C. The sample mass loss (Figure 4.2) was 1% between 40 and 50 °C and 1.5% between 50 and 60 °C. Figure 4.5a shows

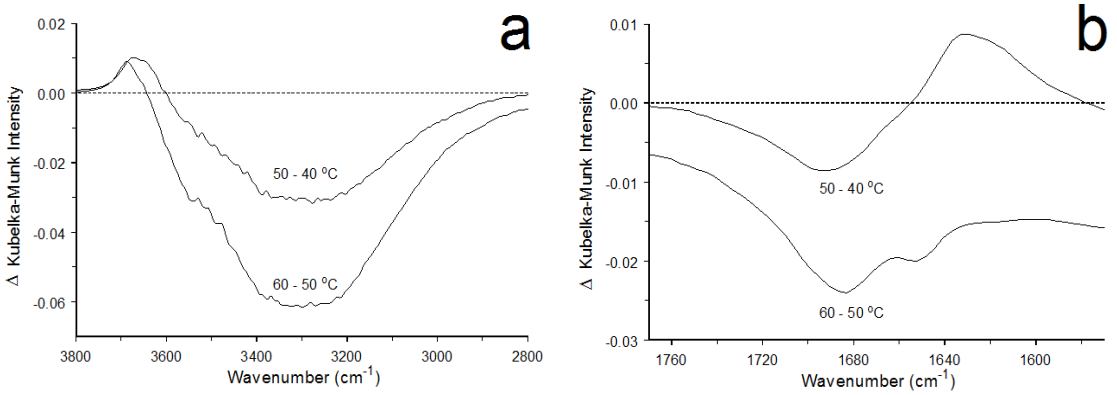

Figure 4.5 – VT-DRIFTS difference spectrum regions representing (a) O-H stretching vibrations and (b) H-O-H bending vibrations.

that the loss of O-H stretching vibration band intensity over these two temperature ranges was broad and exhibited minima near 3300 cm^{-1}. The widths of these bands are similar to the bulk water absorbance band width in this spectral range, but the band maximum for bulk water occurs about 100 cm^{-1} higher, near 3400 cm^{-1}.[157] The lower O-H stretching vibration wavenumber compared to bulk water suggests that water molecules responsible for difference spectra intensity losses had been involved in stronger interactions than the average bulk water molecule. The widths of the difference spectra negative bands indicate the loss of water molecules from a range of hydrogen bonding environments. Positive difference spectrum bands in the 3630-3690 cm^{-1} range can be attributed to framework hydroxyl groups.[158] These bands appear because water molecules that had been hydrogen bonded to framework hydroxyl functionalities were removed, resulting in framework O-H stretching vibration blue shifts. Both difference spectra in Figure 4.5a exhibit asymmetry between 3400 and 3600 cm^{-1}. The slight increase in intensity over this wavenumber range may be caused by NaA water cluster reorganization after partial dehydration, resulting in higher O-H stretching vibration

wavenumbers associated with water molecules having weaker interactions after loss of hydrogen bonding partners.

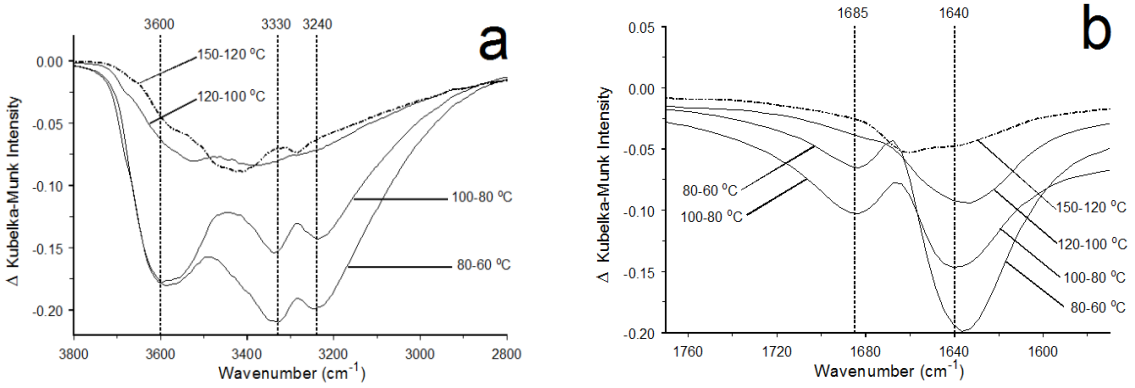

Figure 4.6 - VT-DRIFTS difference spectrum regions representing (a) O-H stretching vibrations and (b) H-O-H bending vibrations.

Figure 4.5b shows the same difference spectra as in Figure 4.5a, but expanded over the H-O-H bending vibration spectral region. The shape of the 50–40 °C curve is consistent with a red shift of the water bending vibration from 1690 to 1630 cm^{-1}. Although the areas under the positive and negative difference spectrum bands are similar, suggesting no net change in water content, thermogravimetry and O-H stretching vibration band measurements confirm that water loss occurred over this temperature range. Based on previously reported water bending vibration trends, this red shift is consistent with a decrease in interaction strength for the water molecules responsible for the 1690 cm^{-1} band.[159-160]

4.3.1.3 Unique water interactions are observed between 60-100°C

Figure 4.6 shows VT-DRIFTS difference spectra corresponding to incremental temperature steps between 60 and 150 °C. All spectra exhibit only negative features. The largest intensity changes occur between 60 and 100 °C, which is consistent with the mass loss curve and integrated band area versus temperature profiles (Figures 4.2 and 4.4). The negative

O-H stretching vibration bands in the 80–60 °C and 100–80 °C difference spectra (Figure 4.5a) exhibit minima near 3240, 3330, and 3600 cm^{-1}. These wavenumbers are similar to the band center locations employed by Crupi et al. for curve fitting NaA O-H stretching vibration bands.[137] In addition, the strong 3330 and 3600 cm^{-1} negative bands are located near the intense water O-H symmetric (3327 cm^{-1}) and asymmetric (3539 cm^{-1}) stretching vibration absorptions in the infrared spectrum of natrolite, a fibrous zeolite.[143, 161] The natrolite cavity size and structure inhibits water-water hydrogen bonding. Instead, water oxygens interact with two Na^+ cations and hydrogen bonds link each water hydrogen to a framework oxygen.[161] Thus, the 3330 and 3600 cm^{-1} negative bands in Figure 4.6a are likely indicative of water-Na^+ cation interaction disruption.

Figure 4.6b shows H-O-H bending vibration difference bands derived from VT-DRIFTS measurements between 60 and 150 °C. Band intensity losses maximized near 1685 and 1640 cm^{-1}. Most of the H-O-H bending vibration band intensity loss occurred near 1640 cm^{-1}, representing water molecules involved in weaker interactions compared to those responsible for the 1685 cm^{-1} vibration. Water molecules involved in weaker interactions would be expected to desorb first. Loss of the weakly interacting water molecules would also affect those remaining due to reduced hydrogen bonding opportunities. Consequently, the negative difference spectrum feature at 1685 cm^{-1} may reflect the loss of hydrogen bonding interactions for water molecules that remained, resulting in a red shift like that observed for the 40 to 50 °C temperature increment (Figure 4.5b). However, the positive band associated with this red shift would be masked by the large negative 1640 cm^{-1} band attributed to water desorption.

4.3.1.4 Water-NA^+ interactions are revealed through OH stretching and bending

Based on thermogravimetric mass loss results, the negative difference spectrum features shown in Figures 4.5 and 4.6 can be assigned to water molecules removed from NaA α-cages. Molecular dynamics studies suggest that most α-cage water molecules interact with one Na^+ cation and form intermolecular hydrogen bonds with other water molecules and framework oxygens. Demontis, et al. proposed that about 4 of the α-cage waters are not involved in interactions with Na^+ cations.[143] Instead, these water molecules form hydrogen bonds to other waters and attain a "bulk" water environment. The negative O-H stretching vibration difference spectra in Figure 4.5a are consistent with the loss of this type of water. The negative bands would represent net intensity losses due to water desorption combined with the effects of wavenumber shifting resulting from vibrational changes for those water molecules that lost hydrogen bonding interactions with the desorbed water. The 50–40 °C H-O-H bending vibration difference spectrum in Figure 4.5b exhibits a positive band maximizing at 1630 cm^{-1} and a negative band with a minimum at 1690 cm^{-1}. Based on reported trends in H-O-H bending vibrations for hydrated crystals,[160] the 1690 cm^{-1} band likely represents water molecules involved in Na^+ cation interactions that also participate in significant intermolecular hydrogen bonding, whereas the 1630 cm^{-1} positive band can be assigned to waters involved with Na^+ cation interactions, but with fewer hydrogen bonding partners. In fact, natrolite waters, which interact with two Na^+ cations and also form two hydrogen bonds with framework oxygens, exhibit an H-O-H bending vibration band that maximizes at about the same wavenumber (i.e. 1636 cm^{-1}).[161] Thus, the red shift likely denotes a reduction in hydrogen bonding for some of the water-Na^+ associations within α-cages. If the initially desorbing water molecules were like "bulk" water, the H-O-H bending vibration band loss

should occur near 1640 cm^{-1}. This loss would be obscured by the positive band resulting from the red shift if the number of waters that desorbed was substantially less than the number of water-Na^+ hydrogen bond disruptions. Thus, the derivative shape exhibited by the 50–40 °C difference spectrum in Figure 4.5b is consistent with a shift of the water-Na^+ bending vibration from ~1690 to ~1630 cm^{-1} combined with the formation of "bulk" type waters that absorb at ~1640 cm^{-1} and were mostly retained by the zeolite. Between 50 and 60 °C, water loss was 50% greater than for the 40 to 50 °C temperature increment, so the red shift positive band was offset by the negative band representing loss of "bulk" waters. Water desorption dramatically increased between 60 and 100 °C, which was reflected by the increased band intensity loss near 1640 cm^{-1} (Figure 4.6b).

Figure 4.6a difference spectra reveal negative O-H stretching vibration band fine structure. These peaks represent the loss of water-Na^+ interactions. The NaA difference bands contain three peaks, whereas the natrolite spectrum exhibits only two strong peaks. The NaA absorbance near 3240 cm^{-1}, which is weak in the natrolite spectrum, has been attributed to a splitting of the O-H symmetric stretching vibration.[143] When compared to the natrolite spectrum, the NaA peaks are significantly broader, likely because of the increased flexibility of hydrogen bonding interactions that can occur within NaA β-cages. Although clearly evident in the 80–60 °C and 100–80 °C difference spectra, minima at 3240, 3330, and 3600 cm^{-1} were not present in the 100–120 °C and 120–150 °C curves (Figure 4.6a). The much smaller negative O-H stretching vibration band differences exhibited over these temperature ranges suggests that α-cage dehydration was nearly complete by 150 °C. This assumption is supported by the thermogravimetric mass loss curve shown in Figure 4.2.

4.3.1.5 Waters remain in NaA β-cages at 150°C

The VT-DRIFTS spectrum overlays shown in Figure 4.3 indicate that a significant amount of NaA water remained at 150 °C. Thermogravimetric results and trends in the difference spectra in Figure 4.6 suggest that water molecules remaining in the zeolite at 150 ° C were primarily those confined to β-cages. Therefore, the VT-DRIFTS spectrum measured at 150 °C should be representative of β-cage water molecule vibrations. The O-H stretching vibration band exhibits a maximum at 3470 cm^{-1} with a shoulder at about 3285 cm^{-1}. These overlapping bands likely represent asymmetric and symmetric O-H stretching vibrations, respectively. Molecular dynamics modeling results suggest that, on average, β-cage water molecules interact with 2 Na^{+} cations and can be involved in hydrogen bonds with other waters or a framework oxygen. Energetically, the β-cage water molecule environment should be like that of natrolite. However, water molecules in natrolite would be expected to adopt more regular configurations because interactions primarily involve specific framework sites. In contrast, the larger β-cage volume allows for greater hydrogen bond interaction flexibility, yielding broader absorption bands. Thus, the β-cage O-H stretching vibration bands are broader (Figure 4.3a) when compared to the natrolite infrared spectrum peaks.[161] Also, water-water hydrogen bonding, which is not possible in natrolite, is likely responsible for the shift of the H-O-H bending vibration from 1636 cm^{-1} in natrolite, to 1665 cm^{-1} for NaA β-cage water molecules.

4.3.2 Calcium-LTA (CaA)

Thermogravimetric mass loss profiles for NaA and CaA samples are shown in Figure 4.7. In contrast to NaA dehydration, CaA mass loss steps are not as well defined[162-163] and

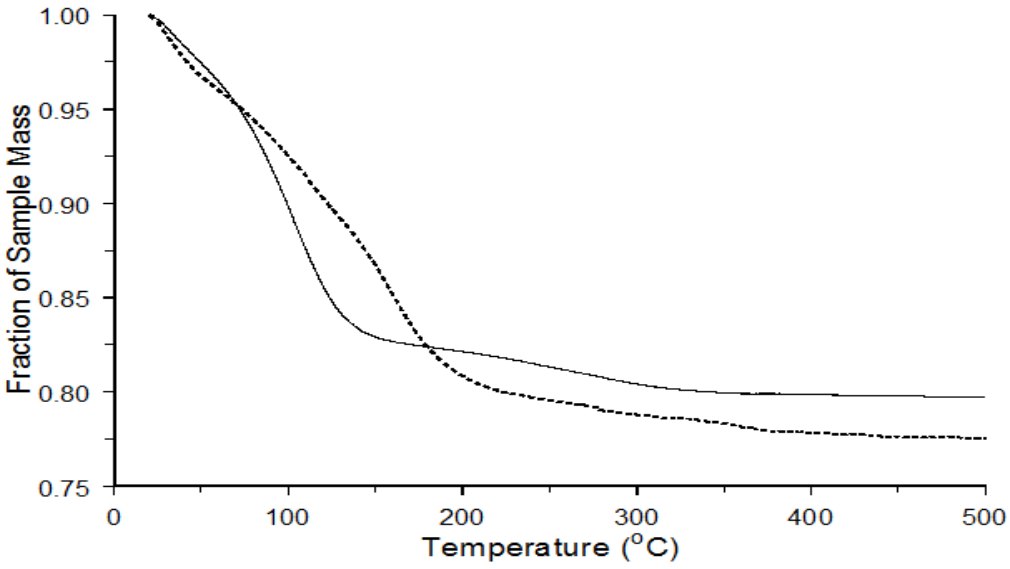

Figure 4.7 – Mass loss versus temperature profiles for NaA (solid line) and CaA (dashed line).

the mass lost at 500 °C was greater (22.7%). In a similar thermogravimetry study (94.5% Na^+ replacement), CaA was found to contain 23.92% water, which was 1.37% more than the precursor NaA material.[164] Based on the fact that zeolite A water content is directly proportional to the degree of Ca^{2+} exchange[165], the 22.7% mass loss depicted in Figure 4.6 is consistent with a high degree of Na^+ replacement. Substitution of Ca^{2+} for Na^+ reduces the number of cations in zeolite cages, leaving more space for water molecules. Because alkaline earth and alkali metals occupy different zeolite A sites, CaA has larger pore openings than NaA.[166] Consequently, weakly bound water molecules were more easily removed from CaA, yielding a greater negative slope in the Figure 4.7 mass loss profile below 75 °C. At higher temperatures, mass loss was slower from CaA due to stronger interactions between water molecules and Ca^{2+}.[162]

4.3.2.1 Water and carbonate are present in CaA after heating

CaA temperature-dependent infrared spectrum changes during sample heating are illustrated in Figure 4.8. Figure 4.8 is an overlay plot of VT-DRIFTS spectra obtained at 25 ° C intervals, beginning at 50 °C. Changes in spectra with increasing sample temperature are primarily caused by loss of water, which is responsible for the substantial intensity losses in the O-H stretching (2800-3800 cm^{-1}) and H-O-H bending (1600-1700 cm^{-1}) vibration spectral regions. Sample dehydration was incomplete at 150 °C, as evidenced by the persistence of an H-O-H bending vibration band. In addition, the significant 2800-3800 cm^{-1} intensity remaining in the spectrum obtained at 150 °C indicates that the sample still contained O-H

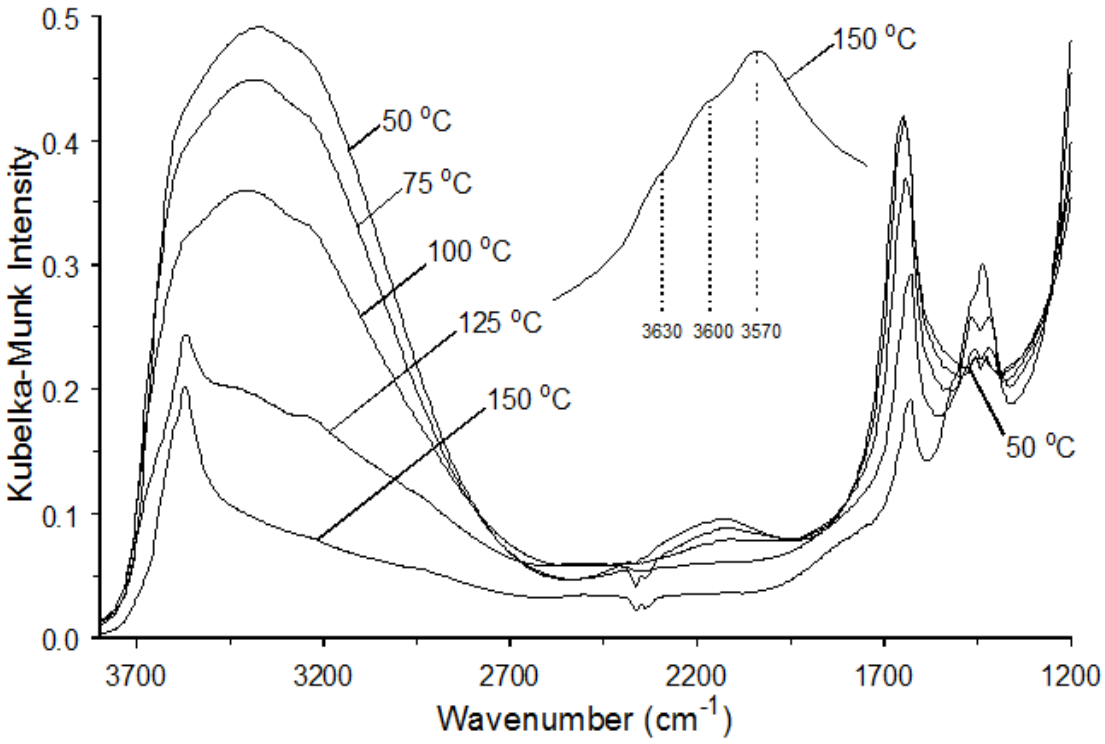

Figure 4.8 – Overlay of VT-DRIFTS spectra obtained while heating CaA.

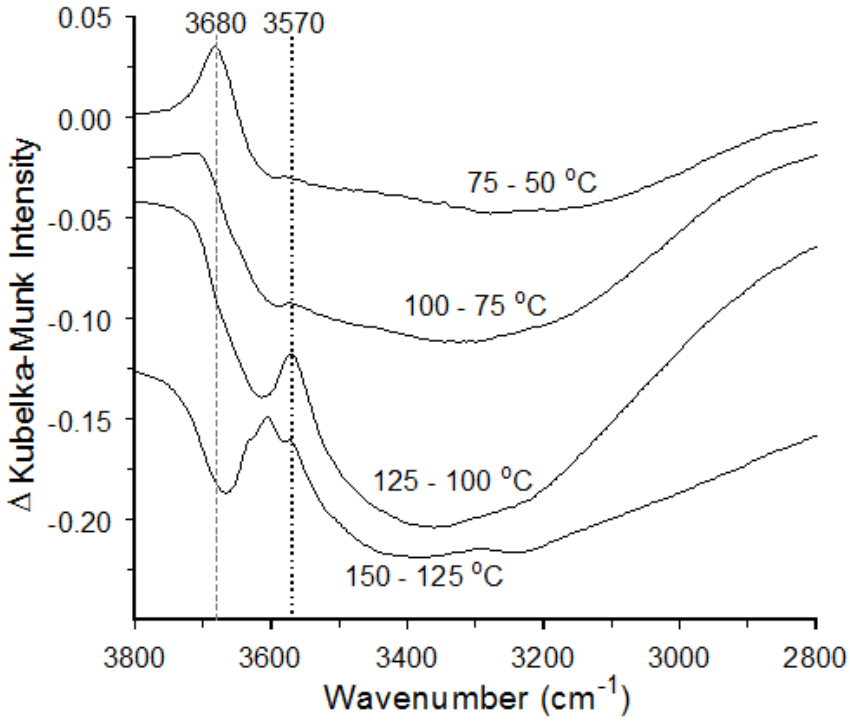

Figure 4.9 - Results of subtracting the spectra in Figure 4.8 in the O-H stretching vibration region

functionalities. The 150 °C plot expansion (inset) reveals that this O-H stretching vibration band was comprised of at least 3 overlapping components. A 1400-1500 cm^{-1} intensity gain with increasing sample temperature was attributed to carbonate formed by reactions between carbon dioxide and water in zeolite pores.[167] Trends in Figure 4.8 VT-DRIFTS spectra show that the carbonate infrared absorption initially comprised two closely spaced bands that grew larger at higher temperatures and then merged into a single, broad absorption band.

4.3.2.2 Water loss and change in framework-OH interactions

More specific details of VT-DRIFTS temperature-dependent band intensity and shape variations are revealed by the spectral subtraction results shown in Figures 4.9 and 4.10. Difference spectra contain positive and negative features that represent sample changes occurring during successive 25 °C heating increments. The spectra in Figure 4.9 show

temperature-dependent variations in the O-H stretching vibration region. The 75-50 °C difference spectrum contains a broad negative feature extending from 3600 to 2900 cm^{-1} caused by the loss of hydrogen bonded O-H moieties. A positive peak at about 3680 cm^{-1} can be assigned to zeolite O-H functionalities that lost hydrogen bonding partners when the sample temperature increased from 50 to 75 °C. A similar band at 3685 cm^{-1} reportedly appeared after heating NaX and was assigned to extra-framework Al-OH functionalities.[168] Jiang and Karge postulated that bands between 3675 and 3685 cm^{-1} may represent mordenite Al-OH species for which the aliuminum is also connected to the zeolite framework (i.e. partially extra-framework).[169] The 3680 cm^{-1} positive feature is absent from the 100-75 °C difference spectrum, which is dominated by a broad negative feature with a shape similar to that of the

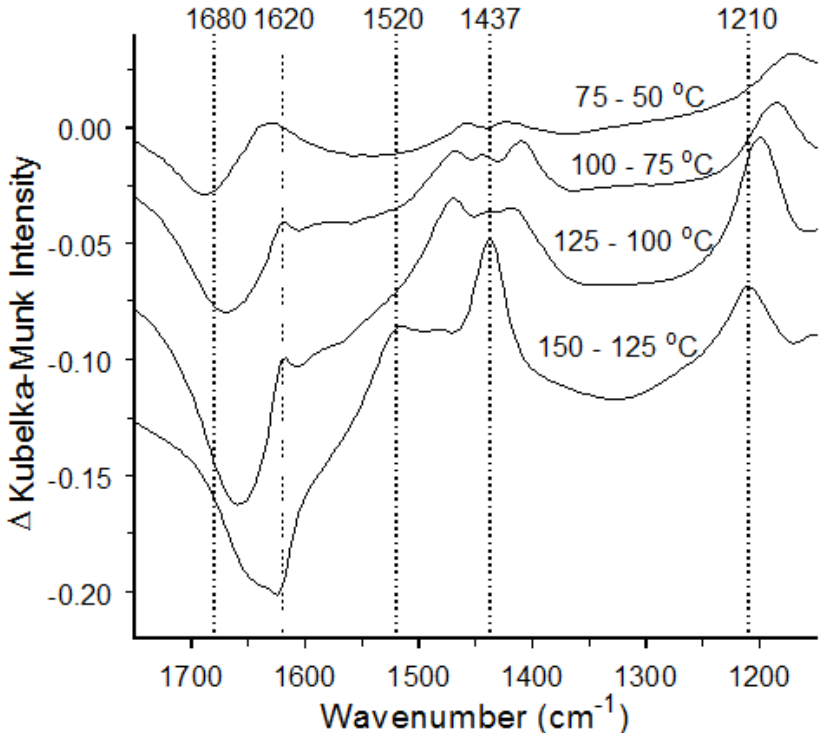

Figure 4.10 - Results of subtracting the spectra in Figure 4.8 in the fingerprint vibration region.

75-50 ^{o}C difference spectrum. However, the intensity of the 100-75 ^{o}C difference spectrum band is greater than the 75-50 ^{o}C band, suggesting that the sample water loss rate increased above 75 ^{o}C. The 75-50 and 100-75 ^{o}C difference spectra exhibit positive anomalys in the broad negative band at about 3570 cm^{-1} that result from intensity increases superimposed on the broad negative band. The positive feature is more evident in the 125-100 ^{o}C difference spectrum and denotes infrared absorption for O-H moieties that are involved in minimal hydrogen bonding. Compared to the top two difference spectra, the broad negative band intensity is greater in the 125-100 ^{o}C spectrum, which is consistent with a continued increase in water desorption rate above 100 ^{o}C. In contrast, the 150-125 ^{o}C difference spectrum features are consistent with slower water loss rates above 125 ^{o}C along with continued 3570 cm^{-1} intensity increases. In addition, two positive overlapping O-H stretching vibration bands appear above 3600 cm^{-1}. Maxima for these positive features occur at about the same wavenumbers as the overlapping band positions in the 150 ^{o}C VT-DRIFTS spectrum (Figure 4.8 inset plot).

Figure 4.10 contains portions of the same difference spectra shown in Figure 4.9, but in the fingerprint region (1150-1750 cm^{-1}). The H-O-H bending vibration in the 75-50 ^{o}C difference spectrum consists of a negative band near 1680 cm^{-1} and a positive band slightly above 1620 cm^{-1}. This “derivative” shape is characteristic of a red shift in the H-O-H bending vibration from 1680 to 1620 cm^{-1}. Although the areas under the positive and negative regions are similar, thermogravimetry results (Figure 4.7) confirm that significant water was lost (~4% of total mass) over this temperature range. This suggests that the absorptivity for the band near 1620 cm^{-1} was greater than for the 1680 cm^{-1} band. The positive H-O-H bending vibration band in the 100-75 ^{o}C difference spectrum is smaller than in the 75-50 ^{o}C spectrum, and the

negative band is shifted to a slightly lower wavenumber (~ 1670 cm^{-1}). The predominately negative intensities between 1600 and 1700 cm^{-1} in difference spectra above 75 ^{o}C are consistent with water loss over these temperature ranges. The H-O-H bending vibration band in the 150-125 ^{o}C spectrum is red shifted relative to the other difference spectra bands and does not exhibit an overlapping positive contribution near 1620 cm^{-1}. The 1600-1700 cm^{-1} trends

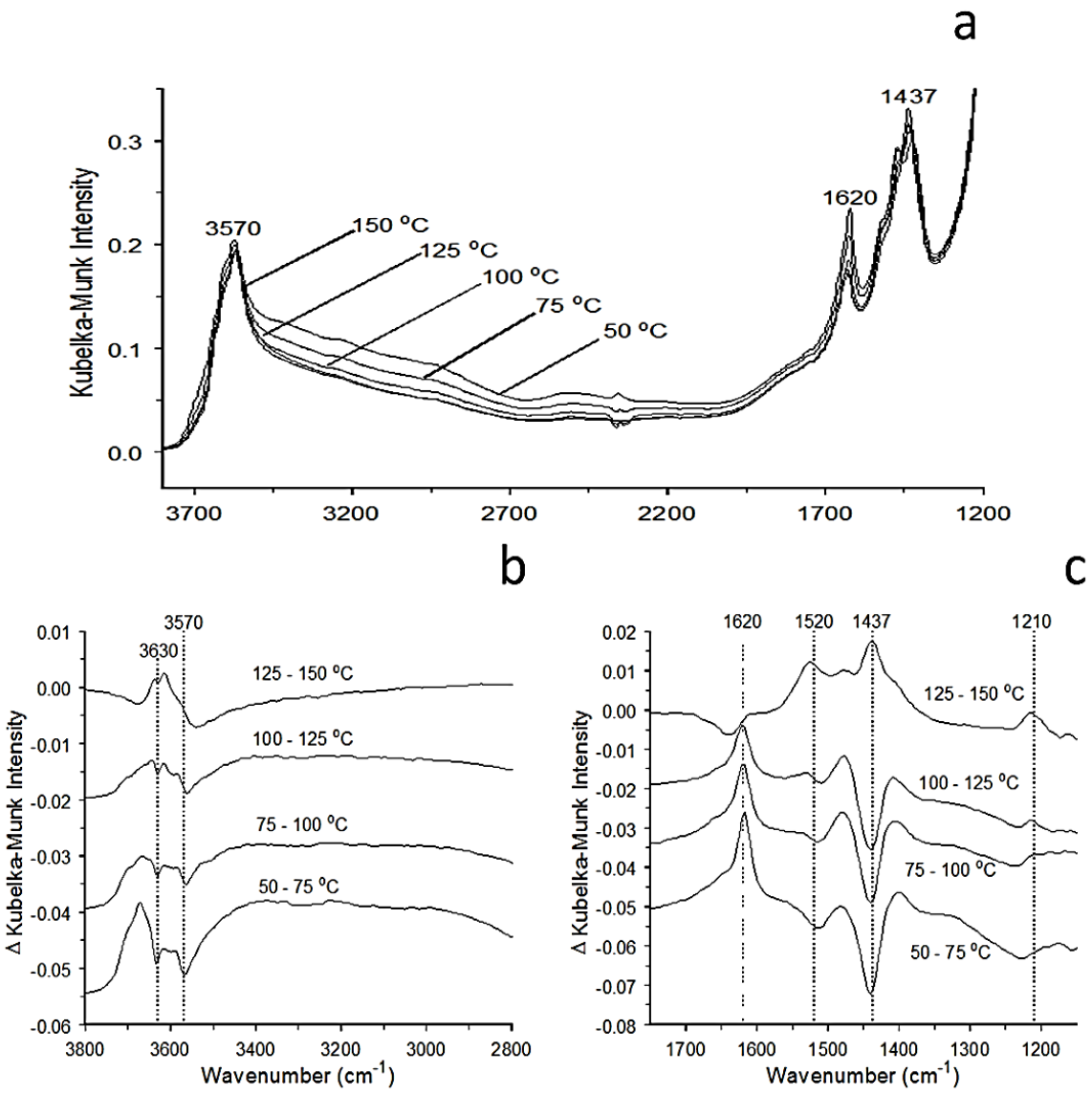

Figure 4.11 – (a) Overlay of VT-DRIFTS spectra obtained during CaA sample cooling, (b) results of subtracting the spectra in (a) in the O-H stretching vibration region, (c) results of subtracting the spectra in (a) in the fingerprint vibration region.

in Figure 4.10 indicate that water molecules with H-O-H bending vibrations near 1680 cm^{-1} were initially affected by sample heating. Water loss resulted in rearrangment of the remaining water molecules so that H-O-H bending vibrations near 1620 cm^{-1} were enhanced. Above 75 ^{o}C, spectral changes can be attributed to loss of more strongly bound water molecules and to a progressive decrease in hydrogen bonding interactions for remaining water molecules.[170]

4.3.2.3 Carbonate species

In addition to H-O-H bending vibration features, the 75-50 ^{o}C difference spectrum exhibits two small positive peaks above and below 1437 cm^{-1} and another below 1200 cm^{-1}. Positive intensity near 1437 cm^{-1} can be attributed to carbonate species and a similar absorbance near 1200 cm^{-1} was previously assigned to CaA framework Si-O-Al vibrations.[116] Three distinct positive bands appear in the 100-75 ^{o}C difference spectrum near 1437 cm^{-1} and the band near 1200 cm^{-1} is sharper and shifted to higher wavenumber. These trends continue in the 125-100 ^{o}C spectrum, but with larger intensity changes. The band structure near 1437 cm^{-1} in the 150-125 ^{o}C difference specturm consists of a single positive feature at 1437 cm^{-1}. The lowest wavenumber band in this spectrum is blue shifted to 1210 cm^{-1} relative to the other difference spectra, and a weak positive absorbance near 1520 cm^{-1} represents new carbonate species formed above 125 ^{o}C.[171]

4.3.2.4 OH stretch and bend upon cooling

Figure 4.11 shows VT-DRIFTS spectra acquired while the sample cooled. Figure 4.11a contains overlay plots of spectra obtained at 25 ^{o}C increments during cooling. Compared to spectra obtained while heating the sample (Figure 4.8), changes were much smaller due to the low water vapor concentration within the purged FTIR. The O-H stretching vibration band at 3570 cm^{-1} was a dominant feature in all spectra. Intensity throughout the O-H stretching

vibration region (2800-3800 cm^{-1}) increased as sample temperature decreased due to water adsorption. In addition, the 1620 cm^{-1} H-O-H bending vibration band intensity increased with decreasing sample temperatures. Intensities associated with carbonate species (i.e. 1400-1550 cm^{-1}) changed slightly, indicating that carbonate formation processes were mostly irreversible.

Figure 4.11b shows VT-DRIFTS difference spectra (O-H stretching vibration region) generated by subtracting Figure 4.11a spectra. When cooling from 150 to 125 ^{o}C, intensity loss was detected at about 3550 cm^{-1} whereas gains occurred at 3613 and 3637 cm^{-1}. The broad negative O-H stretching vibration band extending to 2800 cm^{-1} is consistent with diminished hydrogen bonding due to continued water loss at early stages of sample cooling. The overlapping bands at 3613 and 3637 cm^{-1} likely represent framework hydroxyl functionalities that lost hydrogen bonding partners. In contrast to the 125-150 ^{o}C difference spectrum, the 100-125 ^{o}C subtraction yielded a broad positive O-H stretching vibration band due to water adsorption. The positive 3613 and 3637 cm^{-1} bands are also present, but have lower intensities. The negative 3560 cm^{-1} band may be indicative of a $Ca(OH)^{+}$ vibration band wavenumber shift caused by hydrogen bonding interactions with newly adsorbed water molecules. Similar trends are found in the 75-100 and 50-75 ^{o}C difference spectra. In these spectra, a negative band also appears near 3630 cm^{-1}, and the 3560 cm^{-1} negative band shifts to 3568 cm^{-1} in the 50-75 ^{o}C subtraction.

4.3.2.5 Carbonate interactions upon cooling

Changes to infrared fingerprint region bands during sample cooling are depicted in Figure 4.11c. The 125-150 ^{o}C difference spectrum contains a negative band at 1640 cm^{-1} indicative of loss of H-O-H bending vibration intensity, which, like the Figure 4.11b 125-150 ^{o}C difference spectrum, confirms continued water loss over this temperature interval. Positive

bands at 1437 and 1520 cm^{-1} indicate that carbonate was formed during this initial sample cooling period. Like Figure 4.10, the positive 1210 cm^{-1} band is consistent with framework Si-O-Al vibration perturbations. Further sample cooling led to increased H-O-H bending vibration intensity at 1620 cm^{-1}, associated with water molecule adsorption. The 1620 cm^{-1} positive bands in the lower three Figure 4.11c spectra are more narrow than the negative 1640 cm^{-1} band in the 125-150 ^{o}C subtraction, suggesting that adsorbed water molecules were involved in weaker but more selective interactions than those that were lost at the beginning of the cooling period. Compared to the 125-150 ^{o}C spectrum, the spectral feature near 1520 cm^{-1} is red-shifted and negative, indicating significant perturbation or loss of these carbonate moieties after water adsorption. The distinct negative difference spectra bands at 1437 cm^{-1} represent loss of carbonate anions characterized by minimal interactions with their surroundings.[116] The 1210 cm^{-1} spectral feature is smaller or absent in the lower three

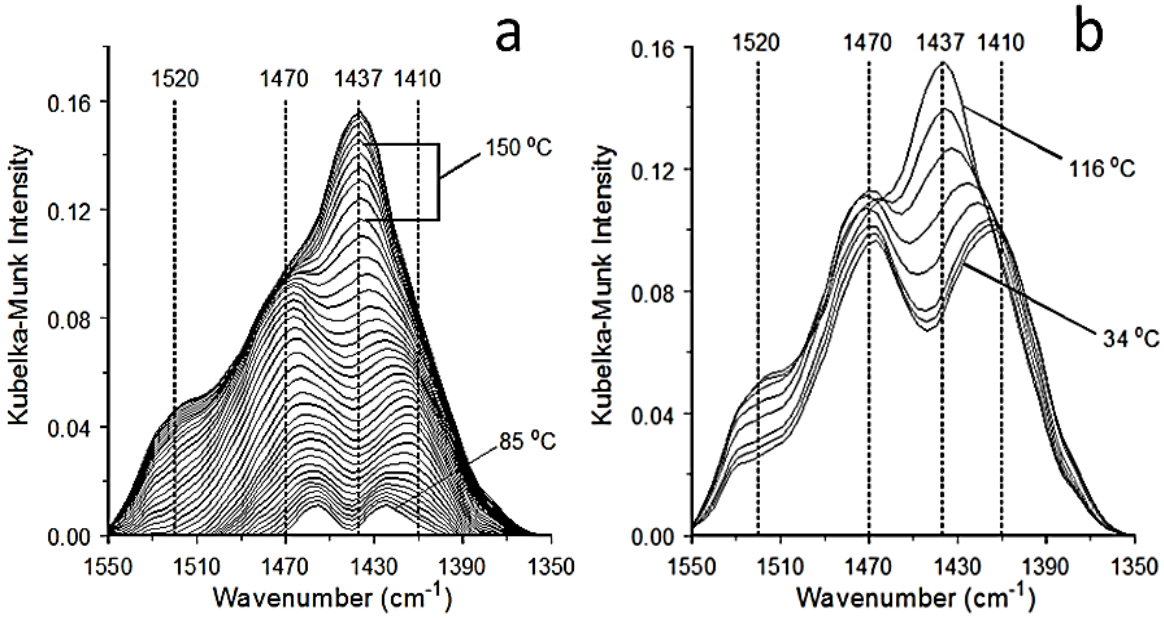

Figure 4.12 – (a) Overlay of VT-DRIFTS spectral bands associated with carbonate formation during CaA sample heating and (b) overlay of spectral bands associated with carbonate during CaA sample cooling.

Figure 4.11c difference spectra, indicating that changes to the zeolite framework during sample heating were mostly irreversible. Broad intensity increases are evident on both sides of 1437 cm^{-1} in the 50-75 ^{o}C spectrum, which could denote a shift in vibration band wavenumber from 1437 cm^{-1} to these regions. The relatively broad nature of these positive features suggests that carbonate moieties were involved in a wide range of interaction strengths.

4.3.2.6 Carboante trends during heating and cooling

General trends in carbonate vibration band properties during sample heating and cooling are revealed by the overlay plots in Figure 4.12. Figure 4.12a shows spectra acquired at about 1 min (~ 2 °C) intervals between 30 and 80 min, which encompasses sample heating and the start of cooling. Two small peaks at 1426 and 1455 cm^{-1} are initially apparent. These peaks, which likely result from splitting of the degenerate ν_3 CO_3^{2-} asymmetric stretching vibration when one of the anion oxygen atoms is involved in interactions (i.e. a monodentate ligand configuration) [6, 153, 172-173], initially had baseline widths of about 35 cm^{-1}. The

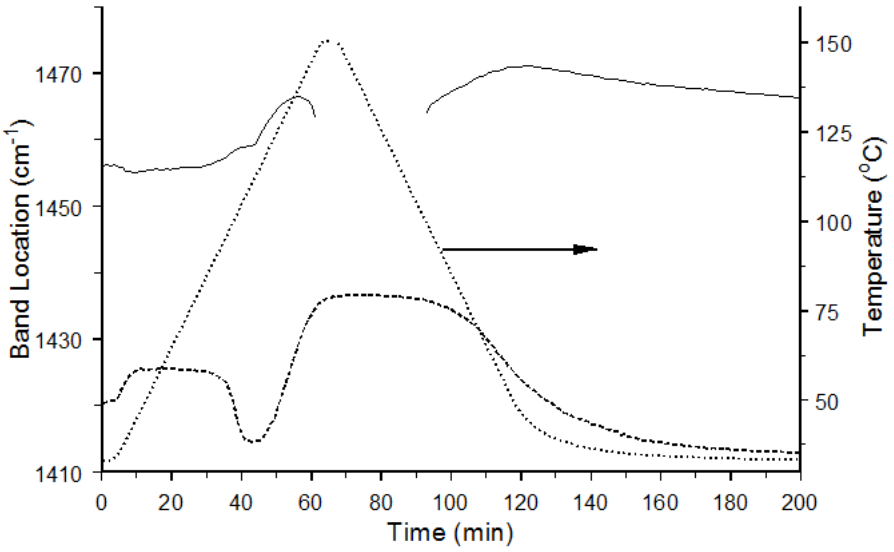

Figure 4.13 – Band location versus elapsed time plots for the split bands representing monodentate carbonate species. The dotted line represents measured sample temperatures as a function of time.

intensities and widths of these overlapping absorption bands increased with increasing sample temperature. The 1437 cm^{-1} intensity continued to increase even after the sample began to cool. An unresolved shoulder appearing above 1500 cm^{-1} when temperatures exceeded 115 ° C is assigned to a low symmetry carbonate species that was not involved in monodentate interactions.

Figure 4.12b shows VT-DRIFTS spectra acquired in ~10 min intervals while the sample cooled from 116 °C. The most prominent changes were intensity losses at 1437 and 1520 cm^{-1}, leaving the split ν_3 carbonate bands that were evident during sample heating. This indicates that carbonate species responsible for the 1437 and 1520 cm^{-1} bands were lost during sample cooling, likely because of interactions with adsorbed water.

Figure 4.13 shows trends in the split ν_3 carbonate band positions derived from Figure 4.12 spectra as a function of sample temperature. Band maxima locations remained relatively constant until about 35 min (~100 °C). Between 35 and 45 min (~100-115 °C), band maxima separations increased from 34 to 46 cm^{-1}, primarily due to red shifts in the low wavenumber band. After 60 min (145 °C), the low wavenumber band was obscured by 1437 cm^{-1} absorbance and the high wavenumber band was a shoulder for which a reliable band maximum could not be determined (Figure 4.12a). After 100 min (cooling to ~85 °C), separate band maxima reappeared (Figure 4.12b), with a 33 cm^{-1} separation. Gradual shifting resulted in a 53 cm^{-1} separation of these bands after 200 min (33 °C).

4.3.2.7 OH and carbonate species band location shifts indicate functional group local environment variations

The spectral subtractions depicted in Figures 4.8, 4.9, 4.10 and 4.11 provide information regarding the creation, loss, and change in CaA functionalities over successive 25 °C intervals. More subtle temperature-dependent spectrum changes can be elucidated by subtracting spectra acquired at smaller temperature increments. In general, difference spectrum intensities reflect the rate of change in absorbing species concentrations, whereas band location shifts indicate functional group local environment variations. Therefore, plots of difference spectrum band intensity and location as a function of sample temperature can be used to compare the time/temperature dependencies of functional group properties. However, when plotting difference spectrum information versus sample temperature, signal-to-noise ratio must be considered. Temperature-dependent profile fine structures can be lost when subtracted spectra represent large temperature increments. Alternatively, signal-to-noise ratios are reduced when subtracted spectra represent small temperature changes. Thus, the temperature interval employed for spectral subtractions must be small enough to preserve profile shapes but large enough to provide adequate signal-to-noise ratios. After considering profile shape versus signal-to-noise tradeoffs, an acceptable compromise was found by subtracting spectra obtained at ~8 °C intervals. Because VT-DRIFTS measurements were acquired at ~2 °C increments, differences were calculated between each measured spectrum and the fourth subsequently acquired spectrum. Figure 4.14a represents intensity changes over ~8 °C temperature increments ($\Delta I/\Delta T$) plotted as a function of elapsed time for O-H stretching vibration bands at 3570, 3610, and 3630 cm^{-1}. For reference, the dotted line in Figure 4.14a denotes measured sample temperatures. The overlay plots in Figure 4.14a show that the 3610 and 3630 cm^{-1} intensity changes maximized at similar times and temperatures

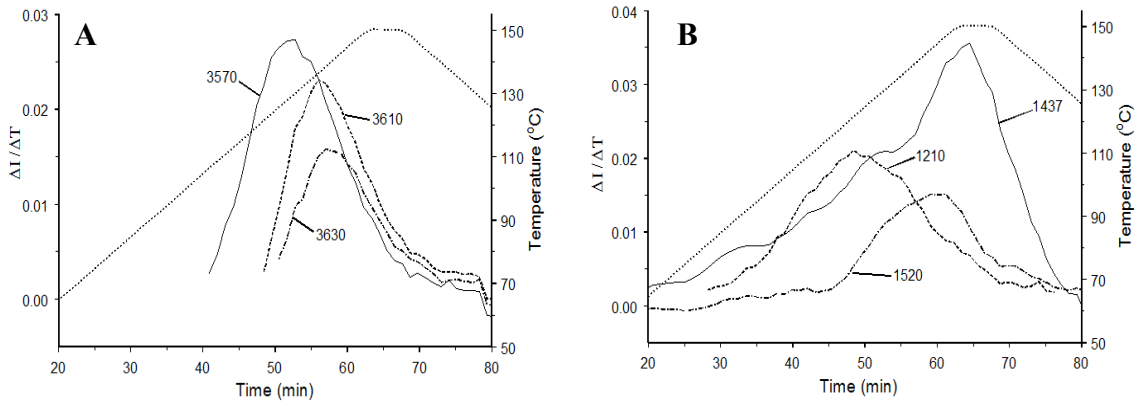

Figure 4.14 – Difference spectra derived intensity changes (ΔT = 8 °C) versus elapsed time for (a) O-H vibration bands and (b) carbonate and framework vibration bands.

(ca. 57 min, 138 °C) but that the maximum ΔI/ΔT increase for 3570 cm^{-1} occurred earlier, at a lower temperature (ca. 50 min, 125 °C).

Figure 4.14b shows ΔI/ΔT versus time plots for carbonate (1437 and 1520 cm^{-1}) and framework (1210 cm^{-1}) vibration bands. The 1437 and 1520 cm^{-1} band changes were derived by subtracting spectrum intensities at these wavenumbers. However, because the ~1210 cm^{-1} band shifted with temperature, the Figure 4.14b plot was derived from difference spectrum values corresponding to peak maxima locations. The ΔI/ΔT values for 1437 cm^{-1} gradually increased from ambient temperature to 50 min (125 °C) followed by a steeper increase to a maximum at 60 min (145 °C). During the temperature range corresponding to the most rapid ΔI/ΔT rise in Figure 4.14b, the ν_3 carbonate split bands merged into a single 1437 cm^{-1} absorption band (Figure 4.12a). The ~1210 cm^{-1} band intensity maximized at about 48 min (120 °C), which was near the temperature above which the 1437 cm^{-1} ΔI/ΔT versus time slope increased. This suggests that carbonate species responsible for the sharp 1437 cm^{-1} ΔI/ΔT increase did not significantly contribute to Si-O-Al perturbations. Figure 4.14b also shows that 1520 cm^{-1} ΔI/ΔT values began to increase after 42 min (110 °C) and maximized at about

58 min (140 °C). Thus, the behaviors of this band and the 1437 cm^{-1} intensity were uncorrelated.

Figure 4.15 shows difference spectrum peak maximum location variations throughout the sample heating and cooling temperature profile for bicarbonate, carbonate and framework stretching vibrations. Solid lines denote positive difference spectrum peaks (increasing intensity) and dash lines denote negative difference spectrum peaks (decreasing intensity). Difference spectrum peaks representing bicarbonate species increased from about 1510 cm^{-1} at 55 min (134 °C) to about 1520 cm^{-1} after 90 min (cooling to 105 °C). After 95 min the bicarbonate difference spectrum feature was represented by a negative peak centered near 1510 cm^{-1}. The high wavenumber component of the split carbonate ν_3 vibration increased from 1465

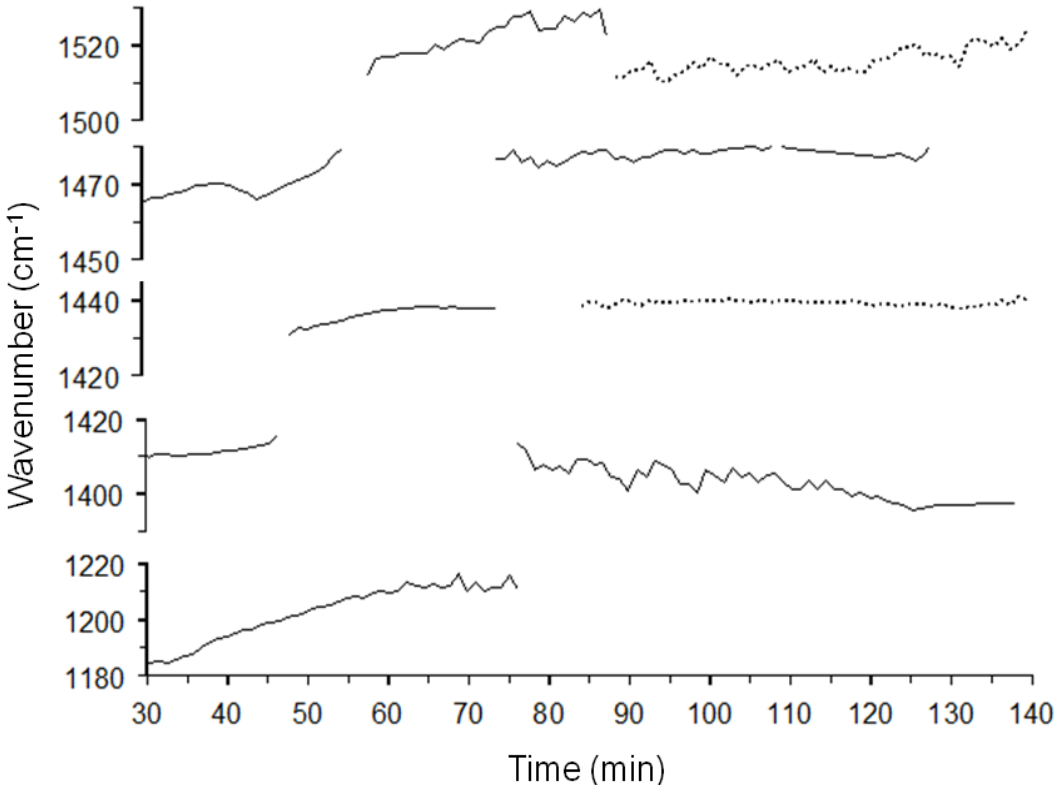

Figure 4.15 - Difference spectrum peak maximum variation for bicarbonate, carbonate, and framework stretching.

cm^{-1} at the start of sample heating to about 1475 cm^{-1} after 50 min (125 °C). This peak remained positive in difference spectra derived from spectra obtained during sample cooling and appeared nearly constant at 1480 cm^{-1}. A merged ν_3 positive peak appeared after 50 min at 1433 $cm^{-1}$and gradually shifted to 1437 cm^{-1} after 60 min. Difference spectrum features corresponding to this vibration were not apparent over the 75-80 min time interval. After 80 min, a negative peak was detected at 1437 cm^{-1}. The low wavenumber component of the split carbonate ν_3 vibration was located near 1410 cm^{-1} initially and remained fairly constant until it merged into the 1437 cm^{-1} peak near 48 min (120°C). After 75 min, this positive peak reappeared near 1410 cm^{-1} and gradually shifted to 1405 cm^{-1} as the sample cooled. A peak associated with perturbed framework vibrations was discerned at low sample temperatures (e.g. 30 min) as a positive peak at about 1185 cm^{-1}. With increasing sample temperature, this peak gradually shifted to higher wavenumbers, eventually reaching 1215 cm^{-1} after 75 min. The peak was not observed in difference spectra after 75 min.

4.3.2.8 Framework hydroxyls and $Ca(OH)^+$ formation during CaA heating

Structural analysis of dehydrated CaA single crystals have indicated that Ca^{2+} cations are located near the centers of hexagonal windows and coordinated to at least 3 different framework oxygen atoms.[155, 174] When present, water molecules occupy the Ca^{2+} hydration shell, weakening cation-framework interactions. Fully hydrated CaA contains 4-5 water molecules per Ca^{2+}.[154, 166] Molecular modeling suggests that two of these waters form hydrogen bonds to framework oxygens while coordinating with Ca^{2+}, but are sterically restricted from hydrogen bonding to other hydration shell water molecules.[175] Other CaA water molecules may form hydrogen bonds to each other and to framework oxygens not contained in Ca^{2+} coordinated hexagonal rings.[165] VT-DRIFTS spectrum variations reflect

temperature-dependent changes to CaA water molecule configurations. Negative difference bands in Figure 4.8 spectra can be attributed to a combination of water loss caused by dehydration and a reduction in available hydrogen bonding partners resulting from this loss. The initial H-O-H bending vibration band shift from 1680 to 1620 cm^{-1} may signify disruption of framework oxygen hydrogen bonding for water molecules interacting with Ca^{2+}.

Montanari et al. reported that infrared spectra of NaA, KA, and CaA samples obtained after heating them to 450 °C under vacuum contained interesting differences.[116] Absorption bands due to O-H stretching and H-O-H bending vibrations were absent in the KA spectrum, suggesting near complete water removal. Small bands attributed to O-H stretching and H-O-H bending vibrations persisted in the NaA spectrum, indicative of incomplete dehydration. The CaA sample spectrum contained significant intensity between 3514 and 3555 cm^{-1}, but the H-O-H bending vibration band was very small. The O-H stretching vibration band intensity was attributed to $Ca(OH)^{+}$ moieties. The 150 °C spectrum in Figure 4.8 exhibits a band maximum near 3570 cm^{-1} that likely represents $Ca(OH)^{+}$ absorbance. Difference spectra representing sample changes that occurred above 100 °C (Figure 4.9) exhibit positive peaks at 3570 cm^{-1} likely associated with new $Ca(OH)^{+}$ species formed during sample heating. In addition, the 150-125 °C difference spectrum exhibits increased infrared absorption above 3600 cm^{-1}, most likely associated with new framework hydroxyls. The formation of $Ca(OH)^{+}$ and framework hydroxyls by heating the CaA sample can be explained by the Hirschler-Plank dissociative water adsorption model:[176-178]

$$H_2O + [Si\text{-}O\text{-}Al]^{-}Ca^{2+} \leftrightarrow Si\text{-}OH\text{-}Al + Ca(OH)^{+} \qquad (\mathbf{4.1})$$

In addition to $Ca(OH)^{+}$, framework Si-OH-Al acid sites are produced by this mechanism. These acid sites are likely responsible for infrared absorption above 3600 cm^{-1}.[116, 176-177,

179] Although the reaction scheme suggests that Si-OH-Al and $Ca(OH)^+$ should be generated concurrently, temperature profiles for band intensity changes associated with these functionalities differed (Figure 4.14a). Thus, if these species were concurrently formed, they participated in subsequent reactions that accounted for their different temperature-dependent vibration band intensity behaviors. For example, initially formed $Ca(OH)^+$ and Si-OH-Al hydroxyls may participate in hydrogen bonding interactions, which would broaden O-H stretching vibration bands and shift them to lower wavenumbers. As shown by Figure 4.13a, the positive 3570 cm^{-1} feature appears after 40 min (~105 °C), which is before the appearance of the two overlapping bands above 3600 cm^{-1}. If the acid sites responsible for the 3610 and 3630 cm^{-1} bands were involved in stronger hydrogen bonding than $Ca(OH)^+$, higher temperatures would be required to disrupt these interactions, causing a delay in the appearance of Si-OH-Al bands. This behavior is consistent with acidic Si-OH-Al and basic $Ca(OH)^+$ hydroxyl moieties.

4.3.2.9 Carbonate formation through carbonic acid dissociation

Because an air dryer/CO_2 remover was employed to generate FTIR purge gas, ambient carbon dioxide concentrations were well below atmospheric levels. Consequently, infrared bands associated with adsorbed CO_2, which are typically found near gas phase absorbance bands,[153] were not detected. However, infrared absorptions below 1600 cm^{-1} were attributed to carbonate species inside CaA pores, which were formed from ambient CO_2.[180-181] Carbonates derive from carbonic acid, which is produced by reactions between carbon dioxide and water.[182] Initially formed carbonic acid can dissociate yielding protons, bicarbonate, and carbonate.[183] Carbonate absorbance bands near 1437 cm^{-1} were previously reported for CaA studies conducted in carbon dioxide atmospheres.[116, 171] In addition, intensity

changes near 1200 cm^{-1} were found to correlate with the amount of carbonate detected, and were assigned to zeolite framework vibrations perturbed by newly formed carbonate species.[116] Previous studies have shown that substituting Ca^{2+} for Na^{+} in zeolite A results in measurable crystal structure changes.[154] Therefore, adding carbonate ligands, which screen Ca^{2+} from framework interactions, may be expected to impact framework vibrations.[184] Mono- and bi-dentate CO_3^{2-} interactions typically cause splitting of the otherwise degenerate ν_3 vibration characteristic of symmetric CO_3^{2-}.[173, 185] The wavenumber difference between split band maxima can be correlated to the degree of anion distortion, with stronger ligand interactions yielding larger band separations.[6] As shown in Figure 4.13, the initial band maximum separation of about 35 cm^{-1} increased to about 45 cm^{-1} at 115 °C. With continued sample heating, band maxima moved closer together and the split bands eventually merged into the single 1437 cm^{-1} band. Upon cooling, band maxima separations increased to 53 cm^{-1}, suggesting stronger monodentate carbonate interactions were formed after water molecules returned to zeolite pores. The 1520 cm^{-1} band, which is likely associated with carbonate species, does not have a low wavenumber partner characteristic of a split ν_3 vibration. The appearance of this band is delayed relative to the other carbonate bands (Figure 4.14b), indicating that it is formed by a different mechanism. Like the 1437 cm^{-1} band, the 1520 cm^{-1} band intensity decreased when water was re-adsorbed (Figure 4.12b). Clearly, the 1520 cm^{-1} band represents a lower symmetry CO_3^{2-} species that is more reactive with water than monodentate carbonate. Based on these properties, the 1520 cm^{-1} absorbance might be associated with a distorted carbonate species involved in simultaneous interactions with Ca^{2+} and hydroxyl functionalities, adopting a “bicarbonate-like” configuration. Although aqueous bicarbonate species do not typically have absorptions in this spectral region,[186] bands near

1520 cm^{-1} have previously been assigned to surface bicarbonate species. For example, Al-Hosney et al. reported a band at 1552 cm^{-1} that they assigned to bicarbonate formed by reactions between water and a $CaCO_3$ surface.[187] During cyclic voltammetry measurements of Cu films coated with CO_2 saturated $NaHCO_3$ electrolyte, Wuttig et al. reported infrared bleaching at 1524 cm^{-1}, which they associated with surface bicarbonate desorption.[188] The delayed appearance of the 1520 cm^{-1} absorption might be due to a requirement for Si-OH-Al hydrogen bonding partners, which would be formed gradually by dissociative water adsorption reactions when the sample was heated. Loss of 1520 cm^{-1} intensity during cooling may be attributed to reactions of the "bicarbonate-like" structure with re-adsorbed water to form carbonic acid.

Because carbonate formation was a consequence of carbonic acid dissociation, detection of infrared bands attributed to carbonate species was indirect evidence of H^+ formation inside CaA pores. The two small bands in Figure 4.12a detected at 85 °C are indicative of carbonate species involved in monodentate interactions with Ca^{2+}, but absorption bands associated with H_2CO_3 and HCO_3^- species were not apparent at this temperature. This suggests that stabilizing interactions between carbonate and Ca^{2+} had the effect of shifting carbonic acid equilibria towards complete dissociation. Protons released from carbonic acid could attach to framework negative charge centers to create acid sites or react with hydroxyl groups (e.g. $Ca(OH)^+$) to produce water. Framework negative charge center protonation would result in increased infrared absorption for acid site infrared bands (3610 and 3630 cm^{-1}) whereas reactions with hydroxide would reduce the $Ca(OH)^+$ (3570 cm^{-1}) band intensity. These predictions are not supported by the $\Delta I/\Delta T$ profiles shown in Figure 4.14a, which indicate that the bands attributed to acid sites appeared only after the $Ca(OH)^+$ band intensity

had significantly increased. The absence of acid site band intensity before 48 min (~120 °C) may be a consequence of hydrogen bonding between Si-OH-Al protons and water molecules, which would shift O-H stretching vibrations to lower wavenumbers and broaden the bands. After 55 min (~135 °C), $\Delta I/\Delta T$ for the $Ca(OH)^+$ O-H stretching vibration band diminished more rapidly than for the acid site bands, which would be consistent with reactions between protons derived from carbonic acid and hydroxyl groups coordinated with Ca^{2+}. In fact, Figure 4.14b indicates that the rate of carbonate formation, and therefore proton production from carbonic acid dissociations, maximized at about 60 min (145 °C).

4.3.2.10 Reaction sequence during CaA heating and cooling

Based on VT-DRIFTS infrared band position and intensity variations, a reaction sequence describing the temperature-dependent processes occurring during CaA sample heating and cooling can be proposed. The presence of small carbonate absorbance bands prior to sample heating suggests that some carbonate was formed while heating the zeolite during the Ca^{2+} ion exchange procedure. Throughout VT-DRIFTS measurements, the quantity of carbonate detected within CaA pores steadily increased with increasing temperature, which is consistent with carbonic acid production and dissociation. Protons derived from carbonic acid attached to framework negative charge centers to form Si-OH-Al acid sites, weakening interactions between cations and the zeolite framework. A positive difference spectrum band at 1210 cm^{-1}, attributed to framework perturbation, was detected after about 30 min (~85 °C). The temperature-dependence of this difference spectrum feature was correlated with the increase in the split ν_3 carbonate band intensities (Figure 4.14b). This correlation could be explained by framework negative charge center protonation or by the formation of monodentate Ca^{2+}- CO_3^{2-} configurations that weakened interactions between cations and

framework. Both mechanisms would result in perturbed Si-O-Al vibrations that would correlate with the amount of carbonate detected. The appearance of the 3570 cm^{-1} band associated with $Ca(OH)^+$ is consistent with dissociative water adsorption reactions. The acid sites formed by this process may not have initially been detected because of hydrogen bonding effects on O-H stretching vibrations. After 45 min (~115 °C), infrared bands at 1520 cm^{-1} appeared in difference spectra, and were attributed to carbonate anions with lower symmetry than the monodentate ligands responsible for the split ν_3 CO_3^{2-} bands. These carbonate species may be simultaneously interacting with Ca^{2+} and Si-OH-Al functionalities. After 48 min (~120 °C), loss of water from zeolite pores was sufficient to disrupt hydrogen bonding for some Si-OH-Al sites, revealing peaks at 3610 and 3630 cm^{-1} in difference spectra. After 50 min (125 °C), the steady increase in the split ν_3 carbonate band intensities was replaced by growth of intensity at 1437 cm^{-1}, superimposed on the split ν_3 carbonate bands. The lack of splitting for the 1437 cm^{-1} absorbance indicates that carbonate anions that formed after 50 min had higher symmetry than monodentate anions, suggesting that these carbonates may be loosely associated with Ca^{2+} cations.

Water desorption continued immediately following the 150 °C isothermal period as the sample cooled, which was confirmed by the broad negative feature in the top difference spectrum of Figure 4.11b. During this period, the 3610 and 3630 cm^{-1} intensities increased, but the 3570 cm^{-1} intensity was relatively unchanged. High symmetry carbonate anions continued to be formed during this initial sample cooling stage, indicating that H^+ (via carbonic acid) was also formed. Consequently, the 3610 and 3630 cm^{-1} intensity increases may be attributed to the combined effects of framework negative charge center protonation and loss of hydrogen bonding between previously formed acid sites and desorbing water molecules.

VT-DRIFTS spectra confirm that water began to re-adsorb when the sample cooled below 125 °C. Comparing difference spectra in Figures 4.8 and 4.11 reveals that the amount of water adsorbed during sample cooling was much less than the quantity desorbed during heating. In fact, the increase in O-H stretching vibration and H-O-H bending vibration band areas after cooling were 35 and 33 percent of the band area losses detected during sample heating, respectively. This suggests that about one-third of the water originally present in the sample was restored by the end of VT-DRIFTS measurements. Water adsorption during sample cooling resulted in the appearance of broad O-H stretching vibration band absorbances (Figure 4.11b) with intensity distributions like the broad negative bands in Figure 4.9. The increase in the H-O-H bending vibration band near 1620 cm^{-1} during sample cooling can be attributed to new water molecules, likely interacting with Ca^{2+}, but involved in minimal hydrogen bonding. Continued water adsorption while cooling below 50 °C (not shown in Figure 4.10) led to increased intensity near 1640 cm^{-1}, which may be attributed to water molecules involved in hydrogen bonding. In addition, water adsorption during sample cooling led to loss of band intensity for Si-OH-Al and $Ca(OH)^{+}$ species, likely due to hydrogen bonding interactions, which shifted and broadened these absorption bands.

After 85 min (cooling below 115 °C), difference spectra contained negative bands at 1510 and 1437 cm^{-1}, indicating the loss of carbonate species not involved in monodentate interactions with Ca^{2+}. Adsorbed water molecules may react with these carbonate species to form bicarbonate and carbonic acid, which may be responsible for increased positive difference spectrum intensity between 1300 and 1375 cm^{-1} as the sample cooled below 125 °C (Figure 4.11c). Carbonic acid may also dissociate to produce CO_2, which could escape zeolite pores, and H_2O. The separation between split ν_3 carbonate bands (Figures 4.12) increased during

sample cooling (Figure 4.13), indicating that interactions between carbonate ligands and Ca^{2+} cations became stronger. Increased Ca^{2+} and carbonate coordination would consequently weaken interactions between cations and framework, facilitating cation migration. If Ca^{2+} cations move far enough from the zeolite framework, hydration shell water molecules would no longer be able to form hydrogen bonds with framework oxygens, which would explain the lack of 1680 cm^{-1} H-O-H bending vibration band intensity during the water re-adsorption process.

4.4 Conclusions

Thermogravimetric and VT-DRIFTS results indicate that NaA dehydration occurs by a step-wise mechanism involving loss of water from the α-cages followed by water desorption from the β-cages. When water evaporates from the heated zeolite, remaining water molecules rearrange and establish new interactions to minimize potential energy. This process results in broad absorption bands and difference spectrum complexity due to the overlap of positive and negative bands. NaA dehydration mechanisms depend heavily on the nature of water-Na^{+} interactions, resulting in infrared spectral similarities with natrolite, for which water-water hydrogen bonding is not possible.

Additionally, a complex sequence of overlapping events characterizing CaA dehydration can be postulated, based on VT-DRIFTS temperature-dependent infrared band variations and correlations with previously published reports. Analysis results indicate that water desorption was only one of several processes that occurred while heating the CaA sample. Water molecules were also involved in temperature-dependent reactions that produced Si-OH-Al acid sites and $Ca(OH)^{+}$. Reactions between water and carbon dioxide formed carbonic acid, which subsequently dissociated into protons and carbonate anions.

Three types of carbonate were detected. Initially, monodentate carbonate formed in which one oxygen atom was coordinated to a Ca^{2+}. At higher temperatures, a less symmetric carbonate species appeared, possibly involved in simultaneous interactions with Si-OH-Al and Ca^{2+}. At the highest sample temperatures investigated, loosely bound, highly symmetric carbonate was detected. Upon cooling, infrared bands for loosely bound carbonate species disappeared, likely because of reactions with re-adsorbing water. Results described here highlight the importance of temperature and residual water on CaA carbon dioxide adsorption processes. At lower temperatures, the high affinity of CaA for moisture allows water molecules to effectively compete with carbon dioxide for adsorption sites. At higher temperatures, water molecule reactions with carbon dioxide and framework negative charge centers produce carbonate, which affects reversible carbon dioxide adsorption processes by permanently reducing void volume and altering cation–framework interactions. Therefore, to maximize carbon dioxide adsorption capacities, CaA should be pretreated to remove water and gas streams should be dried before exposure to the absorbent. Furthermore, when using thermal swing adsorption methodologies, care must be taken to exclude water when releasing adsorbent by heating.

Chapter 5: Button-IR Variable Temperature Diffuse Reflection Infrared Spectroscopy of Faujasite Y Zeolite

5.1 Introduction

Introduced by Breck et al. in 1964 [189], zeolite Y is a synthetic faujasite used in petroleum refining [114, 190-191], for gas adsorption [192-194], and in green chemistry applications [195-196]. Composed of $(Si,Al)O_4$ tetrahedra, zeolite Y has a structure characterized by sodalite cages and supercages connected by hexagonal prisms. Void spaces are filled by water and charge balancing cations, which play important roles in determining zeolite properties [197-198]. Water is a particularly important guest molecule that affects zeolite structure [199-201] and catalytic and adsorption properties [202-203]. Cation substitution [192, 204], position [205-207], and migration as a function of temperature [208-209] also impact zeolite properties.

Fully hydrated NaY has a unit cell consisting of 8 sodalite cages and 8 supercages containing between 240-260 water molecules [210]. Of these, a maximum of 4 waters occupy each sodalite cage, with 26-28 water molecules typically found in supercages. During hydration, water first partially fills the supercages, enabling Na^+ mobility that facilitates continued filling of supercages and sodalite cages [211-213]. Water molecules in sodalite cages are very stable, and remain at temperatures as high as 400 °C [212]. Within the zeolite, water can interact with other water molecules, charge-balancing cations, and framework oxygens. Supercage waters are stabilized by framework oxygen interactions and can form layers resembling spherical shells [206, 214]. In the 12-member ring windows between supercages, water molecules form 6-member rings and interact with Na^+ [206]. Water molecules in sodalite cages strongly interact with Na^+, and cation mobility is linked to water

content. Cations preferentially reside within the larger supercages, where cation-cation repulsions are minimized, and tend to move out of sodalite cages when the zeolite is dehydrated [205, 214].

Hu et al. [215] recently reported the use of synchrotron-based, time-resolved X-ray diffraction (TR-XRD), to monitor NaY cation and water molecule movements during thermal dehydration under vacuum. They identified three unique water configurations within the zeolite: $(H_2O)_4$ clusters in sodalite cages (W1), ice-like hexagonal $(H_2O)_6$ structures near the 12-member rings of supercages (W2), and disordered triangle arrangements associated with Na^+ cations in supercages (W3). When heated, water molecules were found to be involved in a complex sequence of events. For instance, sodalite cage (W1) water-water distances decreased with increasing temperature, suggesting that stronger intermolecular hydrogen bonds were formed, whereas Na^+-water interactions diminished. A new sodalite cage Na^+-water interaction was detected at 68 °C, which disappeared with subsequent heating. The hexagonal W2 water cluster radius increased with increasing temperature, as evidenced by greater water-water distances. Simultaneously, distances between W2 waters and framework oxygens decreased, suggesting that stronger water-framework interactions were formed. W3 water molecules were postulated to exist in Na^+-water-Na^+ bridges and their occupancy was found to be lower than W1 and W2 waters due to steric restrictions. At 120 °C, residual water molecules were primarily located in sodalite cages, and Na^+ cations were found at three distinct zeolite sites.

Hu et al. concluded that the three types of water molecules existed in unique environments, and that these environments changed in distinctly different ways when NaY was heated [215]. Consequently, the vibrational characteristics of these waters should differ, as

should changes in their characteristic vibration absorbance bands as a function of temperature. As shown here, variable temperature infrared spectroscopic analysis of NaY can be used to characterize zeolite water molecule vibrations and study the influence of temperature on their local molecular environments. Thus, variable temperature infrared spectrum band changes provide further insight into the complicated temperature-dependent behaviors of NaY water molecules, which can be correlated with the Na^+ and water molecule movements previously elucidated by TR-XRD [215].

5.2 Experimental

5.2.1 Materials. NaY zeolite with a Si/Al ratio of 5.30 was obtained from Universal Oil Products (Danbury, CT). Sample heating was accomplished by using the apparatus described in Chapter 4. Diffuse reflection infrared spectra were obtained by using a stainless-steel "button" sample holder to obtain thin layers of neat NaY powder.[62] NaY powder was loaded into a 100 mesh button, which was mounted on top of a quartz tube. Sample layer thicknesses were varied by placing different amounts of NaY powder into the wire mesh voids of the button.

5.2.2 Instrumentation. A Mattson Instruments Inc. (Madison, WI) Nova Cygni 120 Fourier transform infrared spectrophotometer (FTIR) was used for infrared spectroscopy measurements. Spectra were obtained over the 4000-700 cm^{-1} range by signal averaging 175 scans at 8 cm^{-1} resolution for both sample and background measurements. Infrared spectra were obtained at 1.07 min intervals while the sample was heated from ambient temperature to 150 °C at a rate of 2.0 °C /min. Spectrum collection continued at this rate during a 5 min isothermal period at 150 °C and throughout cooling (2.0 °C /min) to ambient temperature.

While heating and cooling the sample, successive infrared spectra were acquired at 2.14 °C intervals.

5.2.3 Data Processing. Spectra representing the O-H stretching vibration region were baseline corrected prior to Kubelka-Munk transformation by subtracting straight lines passing through 4200 and 2500 cm^{-1} in reflectance spectra. In the H-O-H bending vibration region, baselines were corrected by subtracting lines passing through 1830 and 1530 cm^{-1}. For framework vibrations, spectra were baseline corrected by subtracting lines passing through 1400 and 850 cm^{-1}. Difference spectra are designated by the temperatures at which the subtracted spectra were acquired. Subtractions were performed in the order specified (i.e. the second spectrum was subtracted from the first).

5.3 Results and Discussion

Variable temperature diffuse reflection infrared spectroscopy (VT-DRIFTS) was employed to monitor the effects of heating on NaY water molecules and zeolite framework. Figure 5.1 shows the diffuse reflectance spectrum obtained from a thin layer (< 200 μm) of NaY powder measured at ambient temperature. The band locations and relative intensities in the Figure 5.1 spectrum are consistent with previously published spectra [216]. This spectrum contains a broad absorption band between 2800 and 3800 cm^{-1}, with a slight shoulder near 3200 cm^{-1}. This broad band can be attributed to overlapping O-H stretching vibrations associated with water and zeolite framework hydroxyl groups [217]. The sharper band between 1600 and 1700 cm^{-1} primarily results from H- O-H bending vibrations and is therefore indicative of water molecules [179]. Absorption bands below 1400 cm^{-1} correspond to overlapping zeolite framework vibrations [218-219].

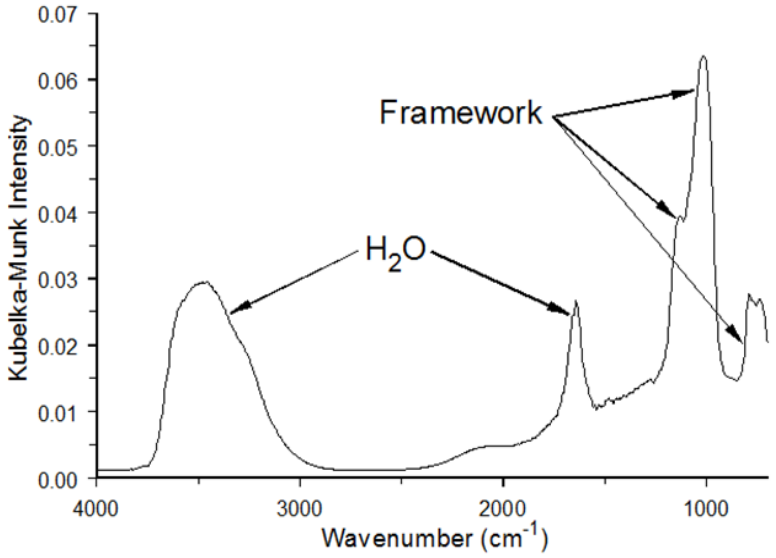

Figure 5.1 – Ambient temperature NaY infrared spectrum.

5.3.1 OH stretch and bend during NaY heating

VT-DRIFTS sample layer thicknesses were adjusted to maximize infrared spectrum sensitivity without introducing spectral artifacts. Consequently, O-H stretching and H-O-H bending vibration band measurements were made by employing a ca. 200 µm thick sample layer and spectra for the more intense framework vibration bands were measured by using a thinner layer. When the NaY sample was heated, water desorption resulted in significantly diminished infrared absorbance in the 2800-3800 and 1600-1700 cm^{-1} spectral ranges. Figure 5.2 is an overlay of VT-DRIFTS spectra obtained at 20°Cintervals. Kubelka-Munk intensities for O-H stretching and H-O-H bending vibrations are larger in Figure 5.2 compared to Figure 5.1 because the NaY layer exposed to infrared radiation for these measurements was thicker. Dehydration resulted in intensity losses in both the O-H stretching (3000-3800 cm^{-1}) and H-O-H bending (1550-1750 cm^{-1}) vibration band regions. Incomplete dehydration at 150 °C resulted in the persistence of band intensity associated with the O-H stretching and H-O-H

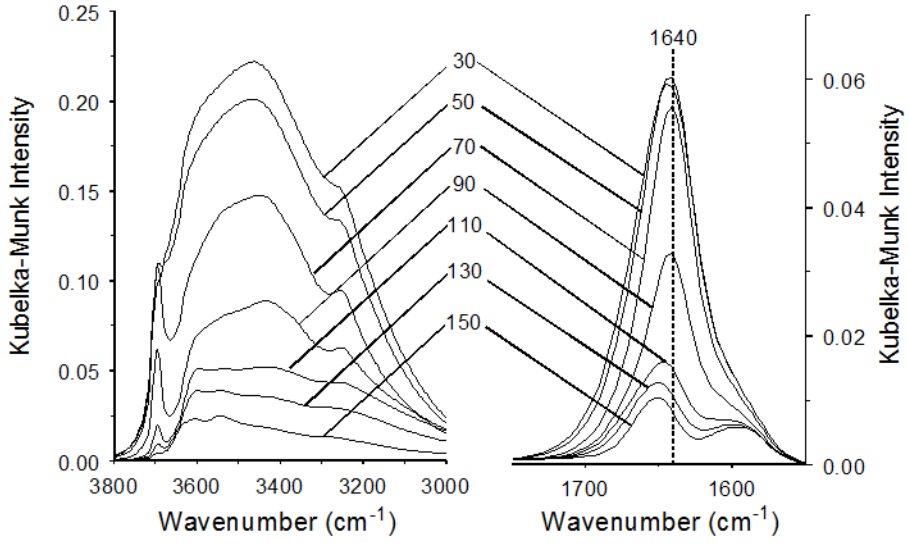

Figure 5.2 – Variable temperature infrared spectra collected at 20 °C increments during sample heating in the O-H stretching (left) and H-O-H bending (right) vibration regions.

bending vibrations of water. Between 30 and 50 °C, intensity loss in the O-H stretching vibration region below 3600 cm^{-1} could be attributed to loss of water molecules. Continued heating to 70 °C resulted in the appearance of a sharp band near 3700 cm^{-1}. This band was previously attributed to faujasite isolated O-H moieties that were not involved in hydrogen bonding interactions [220] and was also associated with strong cation–water interactions, based on infrared spectroscopy studies of sodium poisoned de-aluminated samples [179, 221-222]. Below 3700 cm^{-1}, the O-H stretching vibration band consisted of at least two overlapping bands with maxima located near 3450 and 3250 cm^{-1}. Figure 5.2 also shows that the ambient temperature H-O-H bending vibration band was comprised of two overlapping components. Sample heating primarily resulted in loss of intensity near 1640 cm^{-1}. A smaller band at 1600 cm^{-1}, likely associated with framework vibrations, was revealed above 110 °C.

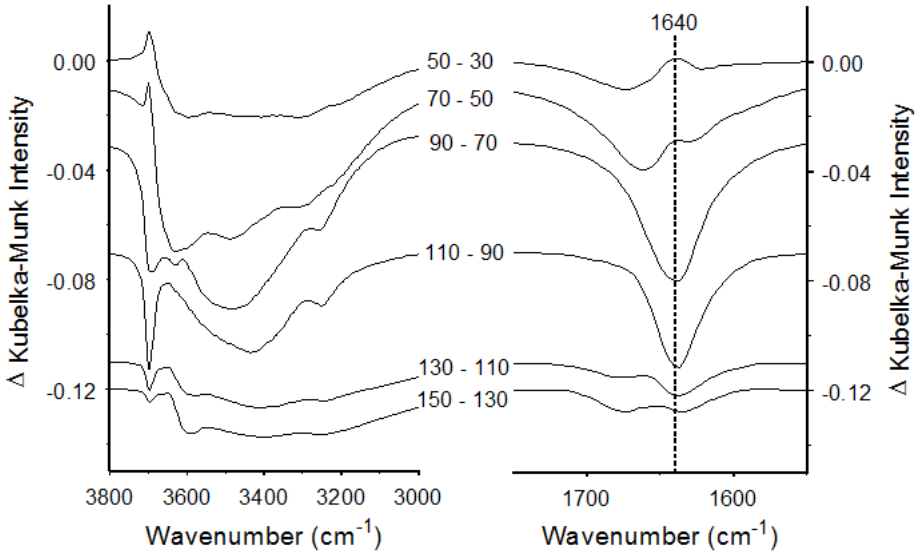

Figure 5.3 – Variable temperature infrared difference spectra representing 20 °C increment changes during sample heating in the O-H stretching (left) and H-O-H bending (right) vibration regions.

The subtle changes in infrared spectra caused by sample heating are more evident in the difference spectra shown in Figure 5.3. These spectra were obtained by subtracting the spectra in Figure 5.2. Spectral baselines are offset in Figure 5.3 plots to better reveal temperature-dependent shape changes. In the O-H stretching vibration region, the 50-30 and 70-50 °C difference spectra exhibit sharp positive bands near 3700 cm^{-1}. Above 70 °C, the 3700 cm^{-1} difference band becomes negative, indicating a net loss of these O-H functionalities. The broad negative O-H stretching vibration band below 3700 cm^{-1} represents loss of water molecules, water - Na^{+} cation interactions, and hydrogen bonds of varying strengths. Below 70 °C, this band consisted of broad, overlapping features, whereas the 90-70 °C and 110-90 °C negative band components were better defined. The 90-70 °C difference spectrum exhibits negative minima at 3700, 3630, 3480, and 3250 cm^{-1}. The 3630 cm^{-1} band is absent in the 110-

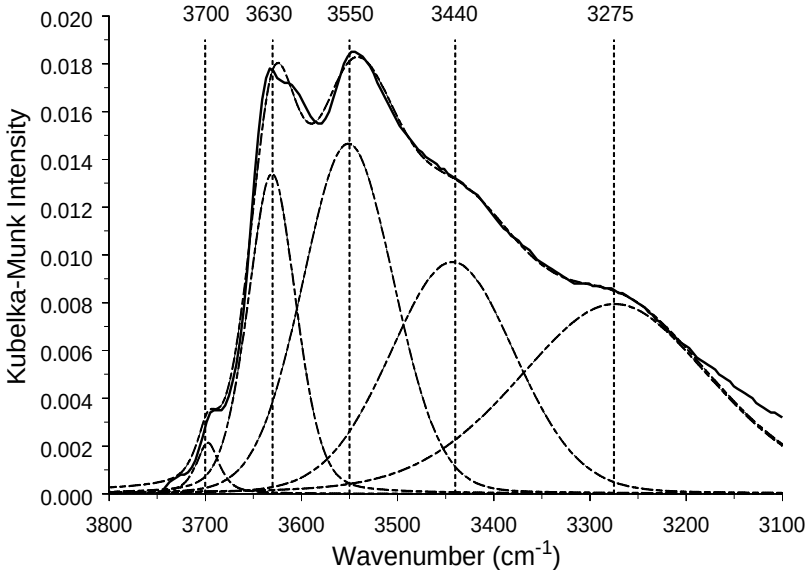

Figure 5.4 – NaY infrared spectrum obtained at 150 °C (solid line) and component bands obtained by curve fitting (dashed lines).

90 °C difference spectrum, whereas the 3700 and 3250 cm^{-1} negative bands remain and the band at 3480 is shifted to 3430 cm^{-1}. Difference spectra above 110 °C exhibit broad band losses in the O-H stretching vibration region and contain distinct negative peaks near 3600 cm^{-1}.

The H-O-H bending vibration range (1550-1750 cm^{-1}) in the Figure 5.3 50-30 °C difference spectrum exhibits an intensity loss near 1660 cm^{-1} and a gain near 1640 cm^{-1}. Apparently, initially lost water molecules disturbed interactions of remaining waters, causing H-O-H bending vibrations to shift from 1660 to 1640 cm^{-1}. This trend is similar to that observed for NaA over a similar temperature range [170]. Between 70 and 110 °C, intensity losses were detected near 1640 cm^{-1}. Above 110 °C, difference spectra revealed intensity losses near 1670 and 1640 cm^{-1}, but overall intensity changes were much less than those occurring at lower temperatures.

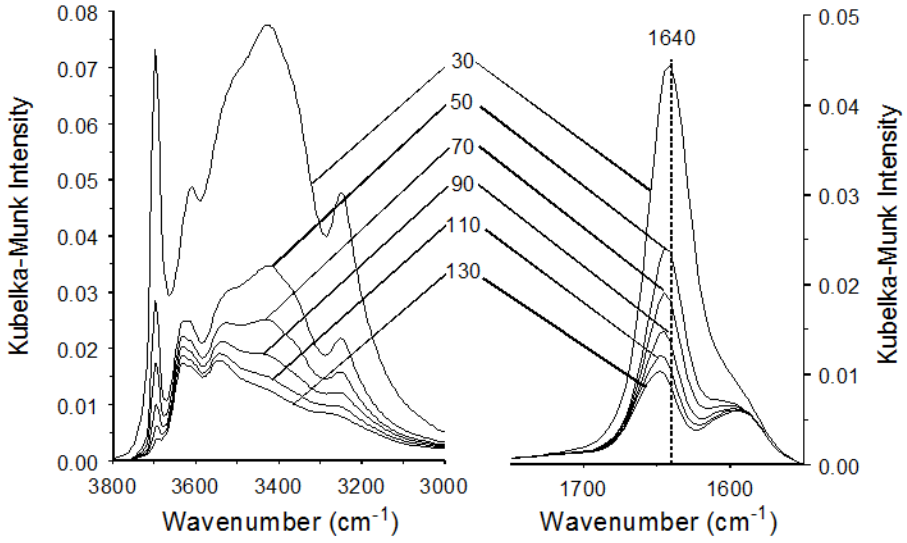

Figure 5.5 – Variable temperature infrared spectra collected at 20 °C increments during sample cooling in the O-H stretching (left) and H-O-H bending (right) vibration regions.

Figure 5.4 shows the NaY VT-DRIFTS spectrum obtained when the sample temperature had reached 150 °C. Dotted lines denote potential constituent bands derived by curve fitting. The O-H stretching vibration region was effectively fit by five overlapping bands at 3700, 3630, 3550, 3440 and 3275 cm^{-1}. After a 5 minute isothermal period at 150 °C, the NaY sample was cooled to 30 °C at a rate of 2 °C /min. During this cooling period, the zeolite re-adsorbed water molecules, resulting in increased absorbance for O-H stretching and H-O-H bending vibration bands. Because the sample was continually exposed to the FTIR spectrophotometer dry air purge, the atmospheric water vapor concentration was much lower than ambient room humidity. Consequently, water re-adsorption was slow and incomplete.

5.3.2 OH stretch and bend during NaY cooling

VT-DRIFTS infrared spectra obtained during sample cooling are shown in Figure 5.5. In general, the intensity of the O-H stretching and H-O-H bending vibration bands increased with sample cooling. However, the rates of intensity increase for these bands were greatest

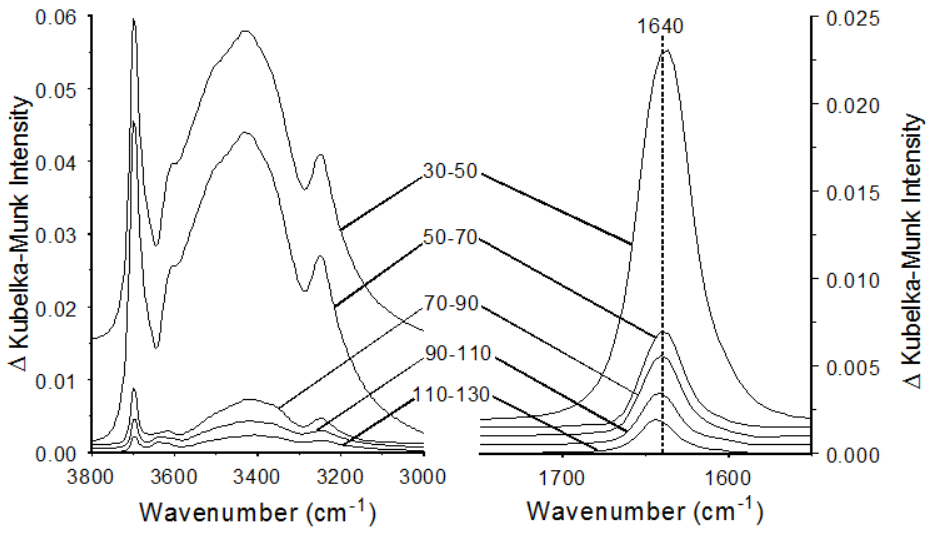

Figure 5.6 – Variable temperature infrared difference spectra representing 20 °C increment changes during sample cooling in the O-H stretching (left) and H-O-H bending (right) vibration regions.

when temperatures dropped below 50 °C. Intensities for the sharp 3700 cm^{-1} band and the broad overlapping bands at lower wavenumbers steadily increased during sample cooling. Figure 5.6 shows difference spectra derived from the VT-DRIFTS spectra in Figure 5.5. Overlapping O-H stretching vibration bands exhibit maxima near 3700, 3620, 3430, and 3250 cm^{-1} in all difference spectra, whereas the H-O-H bending vibration band consisted of a single peak that shifted slightly from 1643 cm^{-1} (110-130 °C) to 1637 cm^{-1} (30-50 °C).

5.3.3 Temperature-dependent changes to the NaY framework

In addition to the complex O-H stretching and H-O-H bending vibration band structures evident in Figures 5.2-5.6, VT-DRIFTS spectra revealed systematic temperature-dependent changes to the NaY framework. Figure 5.7 shows difference spectra in the framework vibration wavenumber range (800-1300 cm^{-1}) obtained by subtracting the initially acquired spectrum from the one measured at 150 °C (i.e. 30–150 °C) and by subtracting the spectrum

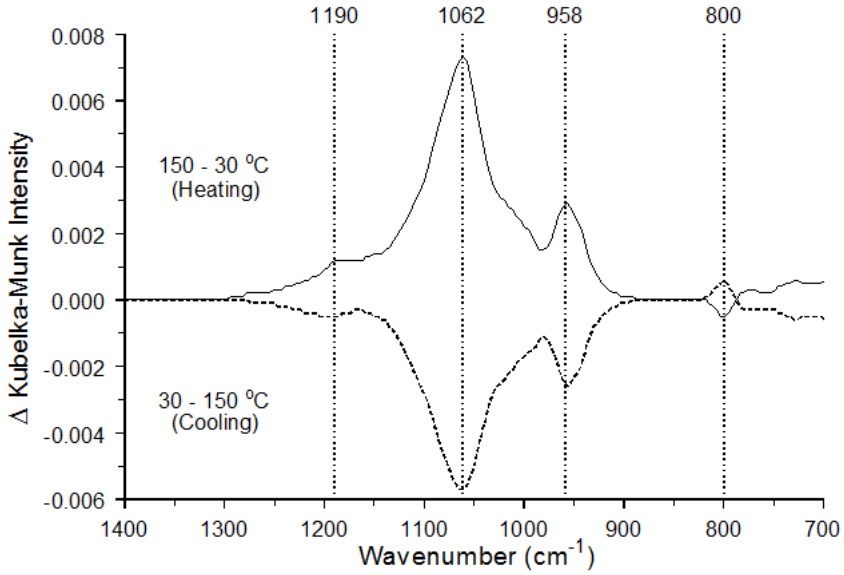

Figure 5.7 – Infrared difference spectra representing framework vibration band changes that occurred during sample heating (solid line) and sample cooling (dashed line).

obtained at 150 °C from the spectrum measured after the sample had cooled (i.e. 30–150 °C). During heating, band intensity increases were detected at 1190, 1062, and 958 cm^{-1}, and a slight intensity decrease near 800 cm^{-1} was detected. These changes were mostly reversible, as evidenced by the "mirror image" dotted line plot in Figure 5.7, which represents the 30-150 °C difference spectrum derived from measurements made during sample cooling. Framework band intensities did not return to their initial values after cooling, probably because the re-hydration process was incomplete. This suggests that these band intensity variations were primarily caused by changes in interactions between zeolite framework and water molecules.

Temperature-dependent band intensity profiles obtained by VT-DRIFTS revealed that most of the changes apparent in Figure 5.7 occurred at low temperatures. As shown in Figure 5.8, significant intensity increases were detected near 1060 and 960 cm^{-1} after heating the sample by only 10 °C. The 800 cm^{-1} band intensity also increased during this 10 °C increment,

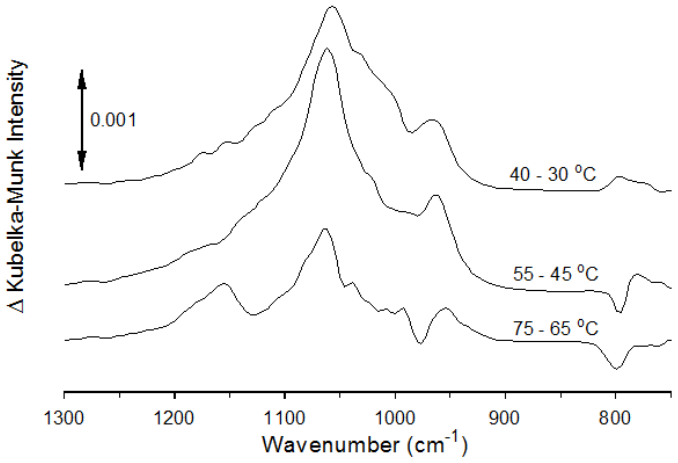

Figure 5.8 – Infrared difference spectra representing framework vibration band changes that occurred during the specified temperature increments while heating the sample.

but only slightly. Between 45 and 55 °C, difference spectra bands near 1060 and 960 cm^{-1} became narrower and the 800 cm^{-1} intensity change was negative. The 75-65 °C difference spectrum exhibits a positive peak at 1190 cm^{-1} that was not apparent at lower temperatures. Figure 5.9 shows the temperature-dependent 1190, 1060, 960 and 800 cm^{-1} intensity profiles. The 1190, 1060, and 960 cm^{-1} band intensities all maximized above 75 °C, but the 800 cm^{-1} band intensity continued to decrease, reaching a minimum near 150 °C.

5.3.4 Interactions between unique water arrangements and charge-balancing Na^+

The TR-XRD study by Hu, et al. elucidated temperature-dependent cation and water molecule movements while heating NaY. At room temperature, sodium ions were found in the sodalite cage (I' site) and at two locations within the supercage (II and III' sites) with unit cell populations of 21, 14, and 19 respectively. Water molecules were arranged in distinct cluster arrangements within the sodalite cage (W1) and supercages (W2 and W3) with unit cell populations of 32, 96, and 26 respectively. After heating NaY, sodium ions migrated from III' sites to the II and II' sites. Concurrently, water cluster disruptions and water molecule losses were detected [215].

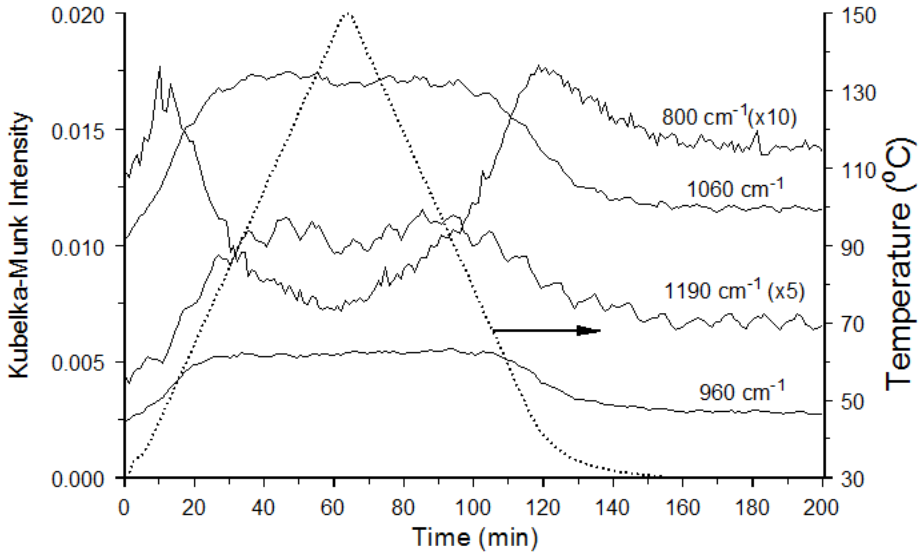

Figure 5.9 – Infrared band intensity versus temperature profiles for selected framework vibration wavenumbers.

VT-DRIFTS results indicate that when NaY was heated, absorbance band intensity at 3700 cm^{-1} gradually increased to a maximum at about 70 °C. The initial 3700 cm^{-1} band intensity (i.e. at 30 °C) was 84% of this maximum. Above 70 °C, the intensity of this band decreased until reaching a minimum (2.5% of maximum) at 144 °C. Subsequently, as the sample cooled, the 3700 cm^{-1} band intensity gradually increased, reaching 65% of maximum after 200 min (30 °C). For reference, a similar TiO_2 band near 3700 cm^{-1} was previously assigned to an isolated O-H stretching vibration and theoretical water cluster analyses have suggested that stretching vibrations for O-H functionalities that are not involved in hydrogen bonding should occur near 3700 cm^{-1} [223-224]. Carion, et al. [225-226] investigated the properties of the 3700 cm^{-1} NaY band and determined that it could not be attributed to molecular water because it was present when water bending vibration bands were absent from infrared spectra. Based on basic probe molecule adsorption studies, this NaY band was assigned to framework hydroxyl groups that were less acidic (H_o = -5) than HY acid sites (H_o = -9) [227].

The correlation between the previously reported temperature-dependent Na^+ occupancy at the II' site and the 3700 cm^{-1} band intensity indicates a possible link between these framework O-H functionalities and Na^+ distribution. This may be explained by the mechanism shown in (5.1), in which water molecules that are hydrogen bonded to framework oxygens while simultaneously interacting with Na^+ cations dissociate, resulting in protons that

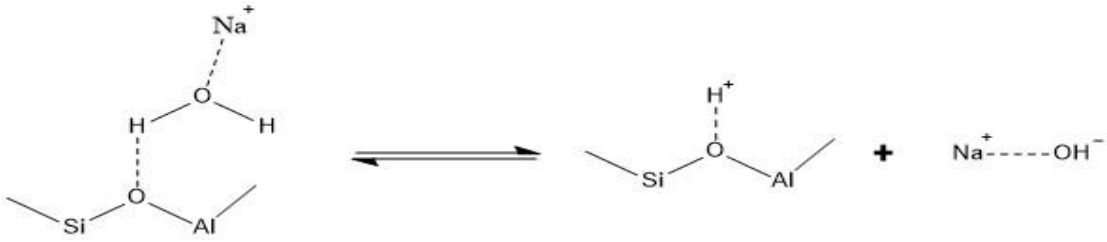

(5.1)

remain with framework oxygens to form acidic OH groups and hydroxyl anions that are electrostatically bound to Na^+ cations. This is similar to the Hirschler-Plank water dissociation model for multivalent cations [177-178, 228], except that the driving force for water dissociation would involve opposing interactions between negatively polarized framework oxygen atoms and positive Na^+ cations. The framework oxygens involved in this process were likely those located near III' supercage sites. Thus, W3 water molecules that were hydrogen bonded to these oxygens and simultaneously attracted to Na^+ cations could dissociate, producing the acid sites and hydroxyl anions. The resulting Na^+OH^- ion pairs could then migrate from III' to II' sites. Based on this mechanism, the number of framework OH groups responsible for the 3700 cm^{-1} band should depend on both the zeolite water content and Na^+ cation distribution. This mechanism is supported by the fact that Hu et al. measured relatively short Na^+ (III')–W3 distances at 25 and 51 °C [215], indicating the presence of strong interactions between these cations and water molecules over the temperature range for which the 3700 cm^{-1} band intensity steadily increased. The reverse of this mechanism, in which hydroxyl anions and acidic protons recombine to form water, would result in diminished 3700

cm^{-1} band intensity. This may occur above 70 °C, when extensive dehydration limited stabilizing hydrogen bonding opportunities for OH^- moieties. The number of W3 waters and Na^+ cations in III' sites reportedly dropped to zero by 80 °C [215], which is consistent with the proposed mechanism and the observed loss in 3700 cm^{-1} band intensity above 70 °C. Because of temperature-dependent Na^+ cation migration [215] and acid site mobility by proton hopping [229-232], H^+ and OH^- recombination's could occur at locations that differed from the original dissociation sites.

5.3.5 Loss of unique water arrangements during NaY heating

Below 3700 cm^{-1}, Figure 5.3 difference spectra exhibit broad overlapping negative bands attributed to a net loss of OH functionalities. This decrease in intensity is due to an overall loss of hydrogen bonding interactions resulting from the combined effects of water cluster disruptions and water molecule evaporation. Results from Hu, et al. indicated that 64% of the water lost by heating NaY from 25 to 50 °C came from W2 clusters, with 19% associated with W3 and 17% attributed to W1 [215]. Thus, the broad negative band in the O-H stretching vibration region of the 50-30 °C difference spectrum represents loss from all three water molecule environments, but mostly the loss of hydrogen bonding interactions associated with supercage $(H_2O)_6$ hexagonal clusters.

Between 60 and 80 °C, Hu et al. reported that the number of W2 and W3 water molecules decreased but the number of W1 waters remained nearly constant [215]. Thus, some of the negative band intensity in the O-H stretching vibration region of the 70-50°C difference spectrum can be attributed to loss of W3 (~10 molecules/unit cell), but most of this band arises from W2 water loss (~45 molecules/unit cell). Unlike the W3 configuration, W2 water molecules do not significantly interact with Na^+ cations, and instead hydrogen bond to other

W2 waters and to framework oxygens. Inspection of the 70-50°C difference spectrum reveals component bands near 3630, 3480, and 3300 cm^{-1}. Similar bands at 3600 and 3300 cm^{-1} were previously assigned to Na^+ - H_2O interactions [170]. Thus, these features likely represent W3 water molecule loss. The 3480 cm^{-1} minimum occurs near the O-H stretching vibration band maxima in the 30 and 50 °C spectra (Figure 5.2), and thus represents loss of W2 clusters, the most abundant ambient temperature water configuration.

Between 80 and 100 °C, most disrupted water clusters were the W2 type, with some W1 also lost [215]. The O-H stretching vibration regions of the 90-70 and 110-90 °C difference spectra are consistent with this trend and contain negative bands near 3480 and 3430 cm^{-1}, respectively, which can be assigned to W2 loss. The O-H stretching vibration difference band minimum shifted from 3480 to 3430 cm^{-1} because water molecules lost at higher temperatures were involved in stronger hydrogen bonding. Above 110 °C, difference spectra indicate that fewer water molecules were lost, which were primarily W1 type. These water molecules interacted with Na^+ cations, and their loss resulted in negative bands near 3600 and 3250 cm^{-1} in the O-H stretching vibration region of difference spectra.

Like the OH stretching vibration band, intensity variations in the H-O-H bending vibration region of the 50-30 °C difference spectrum can be attributed to all three water cluster types, but mostly to loss of W2 configurations. The derivative shape of the H-O-H bending vibration 50-30 °C difference spectrum is characteristic of a shift from 1660 to 1640 cm^{-1}. Based on previously reported water bending vibration trends, this red shift can be interpreted as a decrease in interaction strengths for the water molecules responsible for the negative 1660 cm^{-1} band [159-160, 233-234]. This may be explained by disruption of W1 and/or W3 water - Na^+ cation interactions, converting these waters into W2 configurations, or, in the case of

W3, dissociation (i.e. by reaction 5.1). The 1640 cm^{-1} bending vibration band absorptivity must be greater than the 1660 cm^{-1} vibration because the difference spectrum integrated area was near zero, even though a substantial number of water molecules were lost over this temperature range. In the 70-50 °C difference spectrum, intensity loss was detected as a broad negative band with a small positive deviation near 1640 cm^{-1}, suggesting that the process responsible for the red shift continued over this temperature increment. Between 90 and 110 °C, the single negative band near 1640 cm^{-1} indicated that most loss could be attributed to W2 type water molecules. Above 110 °C, little water remained, so difference spectrum bands were less intense. However, the negative bands near 1670 cm^{-1} that appeared in both the 130-110 and 150-130 °C difference spectra suggest that some of the lost water molecules had been involved in Na^+ cation interactions. According to Hu, et al., only sodalite W1 water configurations remained above 120 °C [215]. In fact, the H-O-H bending vibration band in the 150 °C spectrum (Figure 5.2) maximized near 1660 cm^{-1}, confirming that most residual water molecules were involved in Na^+ cation interactions.

According to results from Hu, et al., Na^+ cations were located at II, I', and I sites at 150 °C, with unit cell populations of about 32, 17, and 5, respectively [215]. Figure 5.4 shows that O-H stretching vibration band intensity persisted at 150 °C and curve fitting results suggested that the broad envelope was comprised of at least five overlapping components. The 3700 cm^{-1} band intensity is minimal in Figure 5.4, which would be expected if it were contingent on zeolite water molecule content. The component bands at 3630 and 3550 cm^{-1} likely correspond to acid sites associated with HY impurities in the NaY sample [235]. HY exhibits characteristic infrared absorbance bands at 3627 and 3562 cm^{-1} assigned to high frequency (HF) hydroxyls in supercages and low frequency (LF) hydroxyls in sodalite cages, respectively [236]. The

presence of an H-O-H bending vibration band maximum at 1650 cm^{-1} in the 150 °C spectrum (Figure 5.2) confirmed that water remained. Thus, the Figure 5.4 bands at 3440 and 3275 cm^{-1} may be attributed to residual water. An additional band at 3600 cm^{-1}, characteristic of W1 type waters, may be present, but would be obscured by the HF and LF bands from HY impurities.

5.3.6 Increase of unique water arrangements during NaY cooling

Based on integrated band areas, about 30% of the water initially present within NaY pores returned after sample cooling. In contrast to the changing shapes of the VT-DRIFTS difference spectra derived from measurements made during sample heating (Figure 5.3), those representing cooling (Figure 5.6) had similar shapes. In the O-H stretching vibration region, positive peaks were detected at 3700, 3610, 3430, and 3250 cm^{-1}. Interestingly, the consistent O-H stretching vibration band difference spectrum shapes can be approximated by inverting the 90-70 °C difference spectrum (Figure 5.3). This suggests that the water molecules returning to the zeolite tended to adopt W2 (i.e. without Na^+ interactions) and W3 (i.e. with Na^+ interactions) configurations. In addition, the gradual shift in the H-O-H bending vibration band maximum during cooling from about 1650 cm^{-1} at 130 °C to about 1640 cm^{-1} at 30 °C (Figure 5.5) suggests that a larger fraction of the water molecules returning at 130 °C adopted configurations that involved interactions with Na^+ cations compared to those added at lower temperatures. The W3-type configuration may have been preferred because it represented lower potential energy due to limited hydrogen bonding opportunities. The W2 and W3 configuration types formed during sample cooling were most likely located within the supercages. Apparently, the mechanism by which sodalite cage W1 clusters were formed,

which required Na^+ migration, was not initially favored, causing a delay in their appearance relative to the W2 and W3 configurations.

5.3.7 Framework vibrations during Nay heating and cooling

Based on previous studies, the 1190 cm^{-1} framework band can be assigned to Si-O-Si asymmetric stretching [237], the 1060 and 960 cm^{-1} bands can be assigned to both Si-O-Si and Si-O-Al asymmetric stretching [237-238], and the 800 cm^{-1} band can be assigned to Si-O-Si symmetric stretching [237]. The maximum temperature-dependent vibration band intensity changes detected during heating (Figure 5.8) were small when compared to the initial 30 °C spectrum (Figure 5.1), representing 8, 20, 13, and 3% of the initial values measured at 1190, 1062, 958, and 800 cm^{-1}, respectively. VT-DRIFTS trends suggest that the 1190, 1060, and 960 cm^{-1} framework band intensities were sensitive to zeolite water content. In contrast, above 40 °C, the 800 cm^{-1} band intensity decreased steadily and was inversely correlated with unit cell volume changes [215]. Framework vibrational mode dipole moment changes responsible for these stretching vibration band intensity trends likely resulted from variations in sodium ion and water molecule interactions with the framework. For example, Hu, et al. postulated that cation migration during NaY heating resulted in stronger interactions between Na^+ cations and framework oxygens, leading to an overall disruption of unit cell stabilizing interactions linking the framework, Na^+ cations, and water molecules and resulting in unit cell expansion [215]. Hannus, et al. reported that a weak 792 cm^{-1} NaY band shifted to lower wavenumbers when larger cations were incorporated into the zeolite by ion exchange [239], indicating that this vibration was affected by nearby cations. Thus, whereas the asymmetric stretching vibration band intensities at 1190, 1060, and 960 cm^{-1} could be correlated with zeolite water content, the 800 cm^{-1} Si-O-Si symmetric stretching vibration band intensity variations may

depend on Na^+ cation distribution. These intensity variations likely result from changes at specific framework sites, and not to an overall change in the framework structure.

5.4 Conclusion

VT-DRIFTS is a sensitive method for monitoring zeolite water molecule and framework changes that occur during thermal dehydration. Overlapping O-H stretching vibration bands provide a means for tracking hydroxyl functionalities, which includes both water molecules and framework acid sites. The H-O-H bending vibration is unique to water, so variations in this band are indicative of water molecule local environment changes**.** Temperature-dependent molecular vibrations for water molecules and NaY framework entities provided insight into complex dehydration mechanisms. In particular, the 3700 cm^{-1} absorbance band intensity exhibited a significant correlation with the Na^+ occupation of II' sites. This implies that the formation of acidic framework hydroxyl functionalities responsible for the 3700 cm^{-1} band was linked to Na^+ migration within NaY supercages. Loss of water molecules involved in significant interactions with Na^+ cations (W1 and W3) can be identified by diminished absorbance near 3600 and between 1650 and 1670 cm^{-1}. The influence of water molecule hydrogen bonding with framework oxygens was reflected by intensity changes for Si-O-Si and Si-O-Al asymmetric stretching vibration bands. Results described here are consistent with previous findings obtained by TR-XRD monitoring of temperature-dependent Na^+ cation and water molecule movements in NaY. Despite the facts that X-ray results were obtained under vacuum for a sample with a different Si/Al ratio (~2.6), and by heating at a slightly higher rate (3 °C), infrared spectral changes indicated that water molecules occupying unique environments were lost in the same order and at about the same temperatures.

Chapter 6: Future Outlook

The work described here includes the design, characterization, theory of operation, and applications of the button-IR sampling method for mid-IR spectroscopy. Button-IR represents the first major development in IR sampling methods for routine analyses since the 1960's. The button-IR technique is compatible with solids, liquids, and pastes, and is capable of both qualitative and quantitative analysis. The button-IR sampling method is user friendly. Robust construction and low fabrication costs alleviate concerns about chemically reactive samples and harsh cleaning methods. In addition to routine applications, button-IR can be exploited to separate samples by particle size during sample loading, which cannot be accomplished by other infrared sampling methods. Button-IR can also be incorporated into a unique apparatus designed to facilitate VT-DRIFTS studies.

Although mid-infrared spectroscopy button-IR was the focus of this dissertation, the basic concepts should be applicable to other wavelength regions. Results obtained when using the low-temperature TEC accessory were limited by the cooling capacity afforded by a single chip. It should be possible to attain lower temperatures by employing multiple chips in a stacked configuration. In fact, dual- and multi-stage TEC chip systems are commercially available that can significantly lower sample temperatures. However, significant design changes to the apparatus, likely including a sealed chamber with infrared transparent windows, would be necessary to avoid water adsorption and ice formation. Similarly, the high temperature limits for the two variable temperature sample analysis approaches described here were restricted by a desire to avoid damage (i.e. button oxidation or TEC chip internal component failure) to the apparatus components. This upper temperature limit could be

moderately extended by changing the composition of the metal button and/or by selecting a TEC chip containing more robust internal components.

Spectral intensities obtained by button-IR analysis of solid powders were represented in Kubelka-Munk units. The Kubelka-Munk function is derived starting from the assumption that the sample consists of an infinitely thick layer, which is not true for the thin-layer samples employed for button-IR measurements. A method for converting transflectance spectra into a more appropriate format (i.e. proportional to analyte concentration) may be necessary. This can be investigated by repeating the mathematical modeling process, but starting with a sample model consisting of a finite, thin layer of material.

The small size of a button and its ability to trap and hold samples suggests that it should be compatible with compact portable infrared spectrometers, particularly those already designed to implement diffuse reflection measurements. Compact and portable spectrometers are invaluable instruments for field-based measurements. Button-IR sampling would facilitate on-site decisions based on rapid analyses that would otherwise not be possible. For example, the identities of suspicious powders could be determined in real-time during a forensic investigation, which would dictate investigators' next steps. In addition, unlike ATR, materials placed on a button sample holder can be stored for additional future assays. Because buttons are comprised of stainless-steel, they can be thoroughly cleaned and sterilized before use. Rather than collecting forensic samples by using swabs, suspicious materials could be loaded into the wire mesh reservoirs of buttons, making them easy to catalog and transport.

The windowless design of the button-IR technique allows for greater experimental flexibility. For example, a variety of different sample perturbations could be implemented to investigate sample properties, such as exposing materials to UV light to monitor resin curing

reactions. The windowless design also facilitates potential new hyphenated analysis possibilities, such as sampling the gases released during a variable temperature study or a laser ablation experiment to add mass spectrometric detection and identification of the volatile products. Finally, there is potential in applying buttons to high throughput applications. Each void in the mesh of a button can be considered a unique sample, with the container clearly defined by the region bounded by the base and four sides of a single mesh void space. By using a microscope, button-IR could be used to provide two-dimensional, structure-dependent information regarding samples. Rather than rubbing the wire mesh across a surface to collect sample material, a button would be pressed into the sample, preserving analyte spatial distributions.

In conclusion, the button-IR sampling method represents an attractive alternative to commercially available methods. Its low cost, ease-of-use, and rugged design allows it to be used for both routine and unique analyses. Based on ease of use, the button-IR methodology should be competitive with the currently preferred ATR method for sampling solids and liquids. In addition, because of its unique properties, button-IR may be the best choice for characterizing some materials. In fact, it may represent the only option.

References

1. Ingle, J. D.; Crouch, S. R., *Spectrochemical Analysis*. Prentice Hall: Englewood Cliffs, NJ 07632, 1988; p 614.

2. Shapaval, V.; Walczak, B.; Gognies, S.; Møretrø, T.; P. Suso, H.; Åsli, A. W.; Belarbi, A.; Kohler, A., FTIR spectroscopic characterization of differently cultivated food related yeasts. *Analyst* **2013,** *138* (14), 4129-4138.

3. Anjos, O.; Campos, M. G.; Ruiz, P. C.; Antunes, P., Application of FTIR-ATR spectroscopy to the quantification of sugar in honey. *Food Chem.* **2015,** *169*, 218-223.

4. Balan, B.; Dhaulaniya, A. S.; Jamwal, R.; Amit; Sodhi, K. K.; Kelly, S.; Cannavan, A.; Singh, D. K., Application of Attenuated Total Reflectance-Fourier Transform Infrared (ATR-FTIR) spectroscopy coupled with chemometrics for detection and quantification of formalin in cow milk. *Vib. Spectrosc.* **2020,** *107*, 103033.

5. Amorim, T. L.; Fuente, M. A. d. l.; Oliveira, M. A. L. d.; Gómez-Cortés, P., ATR-FTIR and Raman Spectroscopies Associated with Chemometrics for Lipid Form Evaluation of Fish Oil Supplements: A Comparative Study. *ACS Food Sci. Technol.* **2021**.

6. Stevens, R. W.; Siriwardane, R. V.; Logan, J., In Situ Fourier Transform Infrared (FTIR) Investigation of CO2 Adsorption onto Zeolite Materials. *Energy & Fuels* **2008,** *22* (5), 3070-3079.

7. Ioakeimidis, C.; Fotopoulou, K. N.; Karapanagioti, H. K.; Geraga, M.; Zeri, C.; Papathanassiou, E.; Galgani, F.; Papatheodorou, G., The degradation potential of PET bottles in the marine environment: An ATR-FTIR based approach. *Sci. Rep.-UK* **2016,** *6* (1), 23501.

8. Renner, G.; Sauerbier, P.; Schmidt, T. C.; Schram, J., Robust Automatic Identification of Microplastics in Environmental Samples Using FTIR Microscopy. *Anal. Chem.* **2019,** *91* (15), 9656-9664.

9. Moss, D. A.; Keese, M.; Pepperkok, R., IR microspectroscopy of live cells. *Vib. Spectrosc.* **2005,** *38* (1), 185-191.

10. Derenne, A.; Gasper, R.; Goormaghtigh, E., The FTIR spectrum of prostate cancer cells allows the classification of anticancer drugs according to their mode of action. *Analyst* **2011,** *136* (6), 1134-1141.

11. Jiang, W.; Saxena, A.; Song, B.; Ward, B. B.; Beveridge, T. J.; Myneni, S. C. B., Elucidation of Functional Groups on Gram-Positive and Gram-Negative Bacterial Surfaces Using Infrared Spectroscopy. *Langmuir* **2004,** *20* (26), 11433-11442.

12. Singh, J. S., FTIR and Raman spectra and fundamental frequencies of biomolecule: 5-Methyluracil (thymine). *J. Mol. Struct.* **2008,** *876* (1), 127-133.

13. Chen, Y.; Mastalerz, M.; Schimmelmann, A., Characterization of chemical functional groups in macerals across different coal ranks via micro-FTIR spectroscopy. *International Journal of Coal Geology* **2012,** *104*, 22-33.

14. Smidt, E.; Schwanninger, M., Characterization of Waste Materials Using FTIR Spectroscopy: Process Monitoring and Quality Assessment. *Spectrosc. Lett.* **2005,** *38* (3), 247-270.

15. Herschel, W., XIV. Experiments on the refrangibility of the invisible rays of the sun. *Philosophical Transactions of the Royal Society of London* **1800,** *90*, 284-292.

16. Abney William De, W.; Festing, L. c., XX, On the influence of the atomic grouping in the molecules of organic bodies on their absorption in the infra-red region of the spectrum. *Philosophical Transactions of the Royal Society of London* **1881,** *172*, 887-918.

17. Coblentz, W. W., Investigations of infra-red spectra. **1905**.

18. Michelson, A. A.; Morley, E. W., On the relative motion of the Earth and the luminiferous ether. *Am. J. Sci.* **1887,** *Series 3 Vol. 34* (203), 333-345.

19. Chen, Y.; Furmann, A.; Mastalerz, M.; Schimmelmann, A., Quantitative analysis of shales by KBr-FTIR and micro-FTIR. *Fuel* **2014,** *116*, 538-549.

20. Forato, L. A.; Bernardes-Filho, R.; Colnago, L. A., Protein Structure in KBr Pellets by Infrared Spectroscopy. *Anal. Biochem.* **1998,** *259* (1), 136-141.

21. Benramdane, L.; Bouatia, M.; Idrissi, M. O. B.; Draoui, M., Infrared Analysis of Urinary Stones, Using a Single Reflection Accessory and a KBr Pellet Transmission. *Spectrosc. Lett.* **2008,** *41* (2), 72-80.

22. Namli, H.; Turhan, O., Simultaneous observation of reagent consumption and product formation with the kinetics of benzaldehyde and aniline reaction in FTIR liquid cell. *Vib. Spectrosc.* **2007,** *43* (2), 274-283.

23. Litvak, I.; Anker, Y.; Cohen, H., On-line in situ determination of deuterium content in water via FTIR spectroscopy. *RSC Adv.* **2018,** *8* (50), 28472-28479.

24. Flejszar-Olszewska, J. Z.; Muszyński, A. S.; Hawranek, J. P., Thin film FTIR transmission spectra of liquid 2,4,6-trimethylpyridine. *J. Mol. Struct.* **1997,** *404* (1), 247-256.

25. Onori, G.; Santucci, A., IR investigations of water structure in Aerosol OT reverse micellar aggregates. *The Journal of Physical Chemistry* **1993,** *97* (20), 5430-5434.

26. Bak, J.; Clausen, S., FTIR transmission–emission spectrometry of gases at high temperatures: demonstration of Kirchhoff's law for a gas in an enclosure. *J. Quant. Spectrosc. Radiat. Transfer* **1999,** *61* (5), 687-694.

27. Bartlome, R.; Baer, M.; Sigrist, M. W., High-temperature multipass cell for infrared spectroscopy of heated gases and vapors. *Rev. Sci. Instrum.* **2007,** *78* (1), 013110.

28. Madarász, J.; Székely, E.; Halász, J.; Bánsághi, G.; Varga, D.; Simándi, B.; Pokol, G., Ammonium carbamate type self-derivative salts of (R-)- and racemic α-methylbenzylamine. *J. Therm. Anal. Calorim.* **2013,** *111* (1), 567-574.

29. Stallard, B. R.; Espinoza, L. H.; Rowe, R. K.; Garcia, M. J.; Niemczyk, T. M., Trace Water Vapor Detection in Nitrogen and Corrosive Gases by FTIR Spectroscopy. *J. Electrochem. Soc.* **1995,** *142* (8), 2777-2782.

30. Evseev, V.; Fateev, A.; Clausen, S., High-resolution transmission measurements of CO2 at high temperatures for industrial applications. *J. Quant. Spectrosc. Radiat. Transfer* **2012,** *113* (17), 2222-2233.

31. Fathy, A.; Sabry, Y. M.; Gnambodoe-Capochichi, M.; Marty, F.; Khalil, D.; Bourouina, T., Silicon Multi-Pass Gas Cell for Chip-Scale Gas Analysis by Absorption Spectroscopy. *Micromachines* **2020,** *11* (5), 463.

32. Chalmers, J. M.; Everall, N. J.; Ellison, S., Specular reflectance: A convenient tool for polymer characterization by FTIR-microscopy? *Micron* **1996,** *27* (5), 315-328.

33. Voyiatzis, G. A.; Andrikopoulos, K. S.; Papatheodorou, G. N.; Kamitsos, E. I.; Chryssikos, G. D.; Kapoutsis, J. A.; Anastasiadis, S. H.; Fytas, G., Polarized Resonance Raman and FTIR Reflectance Spectroscopic Investigation of the Molecular Orientation in Industrial Poly(vinyl chloride) Specimens. *Macromolecules* **2000,** *33* (15), 5613-5623.

34. Mancini, D.; Percot, A.; Bellot-Gurlet, L.; Colomban, P.; Carnazza, P., On-site contactless surface analysis of modern paintings from Galleria Nazionale (Rome) by reflectance FTIR and Raman spectroscopies. *Talanta* **2021,** *227*, 122159.

35. Machefert, J. M.; Le Calvar, M.; Lenglet, M., FTIR study of nickel and copper oxidation: Theoretical approach and experience. *Surf. Interface Anal.* **1991,** *17* (3), 137-142.

36. Sirita, J.; Phanichphant, S.; Meunier, F. C., Quantitative Analysis of Adsorbate Concentrations by Diffuse Reflectance FT-IR. *Anal. Chem.* **2007,** *79* (10), 3912-3918.

37. Masserschmidt, I.; Cuelbas, C. J.; Poppi, R. J.; de Andrade, J. C.; de Abreu, C. A.; Davanzo, C. U., Determination of organic matter in soils by FTIR/diffuse reflectance and multivariate calibration. *J. Chemom.* **1999,** *13* (3-4), 265-273.

38. Souillac, P. O.; Middaugh, C. R.; Rytting, J. H., Investigation of protein/carbohydrate interactions in the dried state. 2. Diffuse reflectance FTIR studies. *Int. J. Pharm.* **2002,** *235* (1), 207-218.

39. Lopez, T.; Sanchez, E.; Bosch, P.; Meas, Y.; Gomez, R., FTIR and UV-Vis (diffuse reflectance) spectroscopic characterization of TiO2 sol-gel. *Mater. Chem. Phys.* **1992,** *32* (2), 141-152.

40. Navas, N.; Romero-Pastor, J.; Manzano, E.; Cardell, C., Benefits of applying combined diffuse reflectance FTIR spectroscopy and principal component analysis for the study of blue tempera historical painting. *Anal. Chim. Acta* **2008,** *630* (2), 141-149.

41. Arai, Y.; Sparks, D. L., ATR–FTIR Spectroscopic Investigation on Phosphate Adsorption Mechanisms at the Ferrihydrite–Water Interface. *J. Colloid Interface Sci.* **2001,** *241* (2), 317-326.

42. Giamougiannis, P.; Morais, C. L. M.; Rodriguez, B.; Wood, N. J.; Martin-Hirsch, P. L.; Martin, F. L., Detection of ovarian cancer (± neo-adjuvant chemotherapy effects) via ATR-FTIR spectroscopy: comparative analysis of blood and urine biofluids in a large patient cohort. *Anal. Bioanal. Chem.* **2021,** *413* (20), 5095-5107.

43. Guiliano, M.; Asia, L.; Onoratini, G.; Mille, G., Applications of diamond crystal ATR FTIR spectroscopy to the characterization of ambers. *Spectrochimica Acta Part A: Molecular and Biomolecular Spectroscopy* **2007,** *67* (5), 1407-1411.

44. Beattie, J. W.; Rowland-Jones, R. C.; Farys, M.; Tran, R.; Kazarian, S. G.; Byrne, B., Insight into purification of monoclonal antibodies in industrial columns via studies of Protein A binding capacity by in situ ATR-FTIR spectroscopy. *Analyst* **2021,** *146* (16), 5177-5185.

45. Kazarian, S. G.; Chan, K. L. A., ATR-FTIR spectroscopic imaging: recent advances and applications to biological systems. *Analyst* **2013,** *138* (7), 1940-1951.

46. Banerjee, A.; Gokhale, A.; Bankar, R.; Palanivel, V.; Salkar, A.; Robinson, H.; Shastri, J. S.; Agrawal, S.; Hartel, G.; Hill, M. M.; Srivastava, S., Rapid Classification of COVID-19 Severity by ATR-FTIR Spectroscopy of Plasma Samples. *Anal. Chem.* **2021,** *93* (30), 10391-10396.

47. Possenti, E.; Colombo, C.; Realini, M.; Song, C. L.; Kazarian, S. G., Time-Resolved ATR–FTIR Spectroscopy and Macro ATR–FTIR Spectroscopic Imaging of Inorganic Treatments for Stone Conservation. *Anal. Chem.* **2021**.

48. Zhang, G.; Ranjith, P. G.; Li, Z.; Vongsvivut, J.; Gao, M., Application of synchrotron ATR-FTIR microspectroscopy for chemical characterization of bituminous coals treated with supercritical CO2. *Fuel* **2021,** *296*, 120639.

49. Mohammadi, M.; Khanmohammadi Khorrami, M.; Vatani, A.; Ghasemzadeh, H.; Vatanparast, H.; Bahramian, A.; Fallah, A., Genetic algorithm based support vector machine regression for prediction of SARA analysis in crude oil samples using ATR-FTIR spectroscopy. *Spectrochimica Acta Part A: Molecular and Biomolecular Spectroscopy* **2021,** *245*, 118945.

50. Brunn, J.; Grosse, P.; Wynands, R., Quantitative analysis of photoacoustic IR spectra. *Appl. Phys. B* **1988,** *47* (4), 343-348.

51. Kuusela, T.; Peura, J.; Matveev, B. A.; Remennyy, M. A.; Stus', N. M., Photoacoustic gas detection using a cantilever microphone and III–V mid-IR LEDs. *Vib. Spectrosc.* **2009,** *51* (2), 289-293.

52. Mikkonen, T.; Amiot, C.; Aalto, A.; Patokoski, K.; Genty, G.; Toivonen, J., Broadband cantilever-enhanced photoacoustic spectroscopy in the mid-IR using a supercontinuum. *Opt. Lett.* **2018,** *43* (20), 5094-5097.

53. Cervantes-Uc, J. M.; Cauich-Rodríguez, J. V.; Vázquez-Torres, H.; Garfias-Mesías, L. F.; Paul, D. R., Thermal degradation of commercially available organoclays studied by TGA–FTIR. *Thermochim. Acta* **2007,** *457* (1), 92-102.

54. Singh, S.; Wu, C.; Williams, P. T., Pyrolysis of waste materials using TGA-MS and TGA-FTIR as complementary characterisation techniques. *J. Anal. Appl. Pyrolysis* **2012,** *94*, 99-107.

55. Gosav, S.; Dinica, R.; Praisler, M., Choosing between GC–FTIR and GC–MS spectra for an efficient intelligent identification of illicit amphetamines. *J. Mol. Struct.* **2008,** *887* (1), 269-278.

56. Berdeaux, O.; Fontagné, S.; Sémon, E.; Velasco, J.; Sébédio, J. L.; Dobarganes, C., A detailed identification study on high-temperature degradation products of oleic and linoleic acid methyl esters by GC–MS and GC–FTIR. *Chem. Phys. Lipids* **2012,** *165* (3), 338-347.

57. Kuligowski, J.; Quintás, G.; Garrigues, S.; Lendl, B.; de la Guardia, M.; Lendl, B., Recent advances in on-line liquid chromatography - infrared spectrometry (LC-IR). *TrAC, Trends Anal. Chem.* **2010,** *29* (6), 544-552.

58. Jordan, S. L.; Taylor, L. T., HPLC Separation with Solvent Elimination FTIR Detection of Polymer Additives. *J. Chromatogr. Sci.* **1997,** *35* (1), 7-13.

59. Jansen, J. A. J., On-line liquid chromatography — Fourier transform infrared spectroscopy for the analysis of polymers and additives. *Fresenius J. Anal. Chem.* **1990,** *337* (4), 398-402.

60. Harrick, N. J., Surface Chemistry Ffrom Spectral Analysis Of Totally Internally Reflected Radiation*. *The Journal of Physical Chemistry* **1960,** *64* (9), 1110-1114.

61. Fahrenfort, J., Attenuated total reflection: A new principle for the production of useful infra-red reflection spectra of organic compounds. *Spectrochim. Acta* **1961,** *17* (7), 698-709.

62. White, R. L., Diffuse reflection mid-infrared spectroscopy of neat powders by using a wire mesh “Button” sample holder. *Anal. Chim. Acta* **2020,** *1098*, 110-116.

63. Milosevic, M.; Berets, S. L., A review of FT-IR diffuse reflection sampling considerations. *Appl. Spectrosc. Rev.* **2002,** *37* (4), 347-364.

64. Maraoulaite, D.; White, R. L., Optical efficiency effects on infrared diffuse reflection spectroscopy signal-to-noise ratio. *Am. Lab.* **2018,** *50* (4), 14-17.

65. Menges, F. *Spectragryph - optical spectroscopy software*, 1.2.15; 2020.

66. Team, R. C. *R: A language and environment for statistical compouting*, R Foundation for Statistical Computing: Vienna, Austria, 2021.

67. Miles, A. J.; Wien, F.; Lees, J. G.; Wallace, B. A., Calibration and standardisation of synchrotron radiation and conventional circular dichroism spectrometers. Part 2: Factors affecting magnitude and wavelength. *Spectroscopy* **2005,** *19* (1), 43-51.

68. Liang, C. Y.; Krimm, S., Infrared spectra of high polymers. VI. Polystyrene. *Journal of Polymer Science* **1958,** *27* (115), 241-254.

69. Custers, D.; Cauwenbergh, T.; Bothy, J. L.; Courselle, P.; De Beer, J. O.; Apers, S.; Deconinck, E., ATR-FTIR spectroscopy and chemometrics: An interesting tool to discriminate and characterize counterfeit medicines. *J. Pharm. Biomed. Anal.* **2015,** *112*, 181-189.

70. Bajwa, G. S.; Sammon, C.; Timmins, P.; Melia, C. D., Molecular and mechanical properties of hydroxypropyl methylcellulose solutions during the sol:gel transition. *Polymer* **2009,** *50* (19), 4571-4576.

71. Mahdavinia, G. R.; Ettehadi, S.; Amini, M.; Sabzi, M., Synthesis and characterization of hydroxypropyl methylcellulose-g-poly(acrylamide)/LAPONITE® RD nanocomposites as novel magnetic- and pH-sensitive carriers for controlled drug release. *RSC Adv.* **2015,** *5* (55), 44516-44523.

72. Oh, C. M.; Heng, P. W. S.; Chan, L. W., Influence of Hydroxypropyl Methylcellulose on Metronidazole Crystallinity in Spray-Congealed Polyethylene Glycol Microparticles and Its Impact with Various Additives on Metronidazole Release. *AAPS PharmSciTech* **2015,** *16* (6), 1357-1367.

73. Coelho Neto, J.; Lisboa, F. L. C., ATR-FTIR characterization of generic brand-named and counterfeit sildenafil- and tadalafil-based tablets found on the Brazilian market. *Science & Justice* **2017,** *57* (4), 283-295.

74. Sarfraz, R. M.; Ahmad, M.; Mahmood, A.; Khan, H. U.; Bashir, S.; Minhas, M. U.; Sher, M., Comparative Study of Various Polymeric Superdisintegrants on the Design and Evaluation of Novel Antihypertensive Orodispersible Tablets. *Adv. Polym. Tech.* **2016,** *35* (4), 378-385.

75. Szakonyi, G.; Zelkó, R., Water content determination of superdisintegrants by means of ATR-FTIR spectroscopy. *J. Pharm. Biomed. Anal.* **2012,** *63*, 106-111.

76. Badria, F. A.; Abdelaziz, A. E.; Hassan, A. H.; Elgazar, A. A.; Mazyed, E. A., Development of Provesicular Nanodelivery System of Curcumin as a Safe and Effective Antiviral Agent: Statistical Optimization, In Vitro Characterization, and Antiviral Effectiveness. *Molecules* **2020,** *25* (23), 5668.

77. Kim, B.; Yang, J.; Hwang, M.; Choi, J.; Kim, H.-O.; Jang, E.; Lee, J. H.; Ryu, S.-H.; Suh, J.-S.; Huh, Y.-M.; Haam, S., Aptamer-modified magnetic nanoprobe for molecular MR imaging of VEGFR2 on angiogenic vasculature. *Nanoscale Research Letters* **2013,** *8* (1), 399.

78. Sinha, N.; Joshi, A. S.; Thakur, A. K., Analytical validation of an ATR-FTIR based method for quantifying the amount of polysorbate 80 adsorbed on PLGA nanoparticles. *Anal. Methods* **2020,** *12* (44), 5360-5366.

79. Andrew Chan, K. L.; G. Kazarian, S., Detection of trace materials with Fourier transform infrared spectroscopy using a multi-channel detector. *Analyst* **2006,** *131* (1), 126-131.

80. Chan, K. L. A.; Kazarian, S. G., High-Throughput Study of Poly(ethylene glycol)/Ibuprofen Formulations under Controlled Environment Using FTIR Imaging. *J. Comb. Chem.* **2006,** *8* (1), 26-31.

81. Janus, E.; Ossowicz, P.; Klebeko, J.; Nowak, A.; Duchnik, W.; Kucharski, Ł.; Klimowicz, A., Enhancement of ibuprofen solubility and skin permeation by conjugation with l -valine alkyl esters. *RSC Adv.* **2020,** *10* (13), 7570-7584.

82. Kher, A.; Udabage, P.; McKinnon, I.; McNaughton, D.; Augustin, M. A., FTIR investigation of spray-dried milk protein concentrate powders. *Vib. Spectrosc.* **2007,** *44* (2), 375-381.

83. Wu, J.; Wang, M.-J.; Stark, J. P. W., Evaluation of band structure and concentration of ionic liquid BMImBF4 in molecular mixtures by using second derivatives of FTIR spectra. *J. Quant. Spectrosc. Radiat. Transfer* **2006,** *102* (2), 228-235.

84. Zhang, J.; Yan, Y.-B., Probing conformational changes of proteins by quantitative second-derivative infrared spectroscopy. *Anal. Biochem.* **2005,** *340* (1), 89-98.

85. Bassan, P.; Lee, J.; Sachdeva, A.; Pissardini, J.; Dorling, K. M.; Fletcher, J. S.; Henderson, A.; Gardner, P., The inherent problem of transflection-mode infrared spectroscopic microscopy and the ramifications for biomedical single point and imaging applications. *Analyst* **2013,** *138*, 144-157.

86. Mayerhofer, T. G.; Paholo, S.; Hubner, U.; Popp, J., Removing interference-based effects from the infrared transflectance spectra of thin films on metallic substrates: a fast and wave optics conform solution. *Analyst* **2018,** *143*, 3164-3175.

87. Dannenbert, H.; Forbes, J. W.; Jones, A. C., Infrared spectroscopy of surface coatings in reflected light. *Anal. Chem.* **1960,** *32* (3), 365-370.

88. Cann, P. M.; Spikes, H. A., In-contact IR spectroscopy of hydrocarbon lubricants. *Tribol. Lett.* **2005,** *19* (4), 289-297.

89. Guillen, M. D.; Cabo, N., Characterization of edible oils and lard by Fourier transform infrared spectroscopy. Relationships between composition and frequency of concrete bands. *J. Am. Oil Chem. Soc.* **1997,** *74* (10), 1281-1286.

90. Pfister, M. K. H.; Horn, B.; Riedi, J., Vibrational spectroscopy in practice: Detection of mineral oil in sunflower oil with near- and mid-infrared spectroscopy. *NIR News* **2018,** *29*, 6-11.

91. Zorin, I.; Kilgus, J.; Duswald, K.; Lendl, B.; Heise, B.; Brandstetter, M., Sensitivity-enhanced Fourier transform mid-infrared spectroscopy using a supercontinuum laser source. *Appl. Spectrosc.* **2020,** *74* (4), 485-493.

92. Mayerhofer, T. G.; Pahlow, S.; Popp, J., The Bouguer-Beer-Lambert law: shining light on the obscure. *Chemphyschem.* **2020,** *21*, 1-19.

93. Dasgupta, P. K., Multipath cells for extending dynamic range of optical absorbance measurements. *Anal. Chem.* **1984,** *56*, 1401-1403.

94. Li, Y. H.; Shelor, C. P.; Dasgupta, P. K., Nonlinear absorbance amplification using a diffuse reflectance cell: total organic carbon monitoring at 214 nm. *Anal. Chem.* **2015,** *87*, 1111-1117.

95. Zieba-Palus, J.; Koscielniak, P., Differentation of motor oils by infrared spectroscopy and elemental analysis for criminalistic purposes. *J. Mol. Struct.* **1999,** *482-483*, 533-538.

96. Jin, Y.; Duan, H.; Wei, L.; Chen, S.; Qian, X.; Jia, D.; Li, J., Online infrared spectra detection of lubricating oil during friction process at high temperature. *Ind. Lubr. Tribol.* **2018,** *70* (7), 1294-1302.

97. Kupareva, A.; Maki-Arvela, P.; Grenman, H.; Eranen, K.; Sjoholm, R.; Reunanen, M.; Murzin, D. Y., Chemical characterization of lube oils. *Energ. Fuel.* **2013,** *27*, 27-34.

98. Mihalcova, J., Study of degradation of mineral oils products by FTIR method. *Chem. Pap.* **2003,** *57* (3), 211-215.

99. Zebarjadi, M., Electronic cooling using thermoelectric devices. *Appl. Phys. Lett.* **2015,** *106*.

100. He, R.; Schierning, G.; Nielsch, K., Thermoelectric devices: a review of devices, architectures, and contact optimization. *Adv. Mater. Technol* **2018,** *3*.

101. Singh, J.; White, R. L., Multiple path length mid-infrared spectra of liquids obtained by using a modified button sample holder. *Appl. Spectrosc.* **submitted**.

102. Noneman, H. F.; Hollingsworth, M. E.; Singh, J.; White, R. L., A high sensitivity variable temperature infrared spectroscopy investigation of kaolinite structure changes. *Spectrochimica Acta Part A: Molecular and Biomolecular Spectroscopy* **2021,** *247*, 119113.

103. White, C. E.; Provis, J. L.; Riley, D. P.; Kearley, G. J.; Deventer, J. S. J. v., What Is the structure of kaolinite? reconciling theory and experiment. *J. Phys. Chem. B* **2009,** *113*, 6756-6765.

104. Balan, E.; Lazzeri, M.; Saitta, A. M.; Allard, T.; Y. Fuchs; Mauri, F., First-principles study of OH-stretching modes in kaolinite, dickite, and nacrite. *Am. Mineral.* **2005,** *90*, 50-60.

105. Frost, R. L., Hydroxyl deformation in kaolins. *Clay Clay Miner.* **1998,** *46* (3), 280-289.

106. Aroke, U. O.; Abdulkarim, A.; Ogubunka, R. O., Fourier-transfrom infrared characterization of kaolin, granite, betonite, and barite. *J. Environ, Tech*, **2013,** *6* (1), 42-53.

107. Frost, R. L.; Kloprogge, J. T., Raman spectroscopy of kaolinite hydroxyls between 25 C and 500 C. *J. Raman Spectrosc.* **2000,** *31*, 415-420.

108. Balan, E.; Delattre, S.; Guillaumet, M.; Salje, E. K. H., Low-temperature infrared spectroscopic study of OH-stretching modes in kaolinite and dickite. *Am. Mineral.* **2010,** *95*, 1257-1266.

109. Binev, I. G.; Stamboliyska, B. A.; Binev, Y. I., The infrared spectra and structure of acetylsalicylic acid (aspirin) and its oxyanion: an ab initio force field treatment. *J. Mol. Struct.* **1996,** *378*, 189-197.

110. Green, J. H. S.; Kynaston, W.; Lindsey, A. S., The vibrational spectra of benzene derivatives - I nitrobenzene, the benzoate ion, alkali metal benzoates and salicylates. *Spectrochim. Acta* **1961,** *17*, 486-502.

111. Ingram, A. L.; Nickels, T. M.; Maraoulaite, D. K.; White, R. L., Variable temperature infraredsSpectroscopy studies of aromatic acid adsorbate effects on montmorillonite dehydration. *Appl. Spectrosc.* **2017,** *71* (2), 238-249.

112. Ingram, A.; Nickels, T.; Maraoulaite, D.; White, R., Thermogravimetry-mass spectrometry investigations of salicylic acid and acetylsalicylic acid desorption from montmorillonites. *Thermochim. Acta* **2016,** *639* (10), 120-129.

113. Ingram, A. L.; Nickels, T. M.; Maraoulaite, D. K.; White, R. L., Thermogravimetry-mass spectrometry investigations of montorillonite interlayer water perturbations caused by aromatic acid adsorbates. *J. Therm. Anal. Calorim.* **2016,** *126*, 1157-1166.

114. Degnan, T. F., Applications of zeolites in petroleum refining. *Top. Catal.* **2000,** *13* (4), 349-356.

115. Nibou, D.; Mekatel, H.; Amokrane, S.; Barkat, M.; Trari, M., Adsorption of Zn2+ ions onto NaA and NaX Zeolites: Kinetic, Equilibrium and Thermodynamic Studies. *J. Haz. Mat.* **2010,** *173* (1), 637-646.

116. Montanari, T.; Busca, G., On the Mechanism of Adsorption and Separation of CO2 on LTA Zeolites: An IR Investigation. *Vib. Spectrosc.* **2008,** *46* (1), 45-51.

117. Pillai, R. S.; Peter, S. A.; Jasra, R. V., Correlation of Sorption Behavior of Nitrogen, Oxygen, and Argon with Ca2+ Locations in Zeolite A: A Grand Canonical Monte Carlo Simulation Study. *Langmuir* **2007,** *23* (17), 8899-8908.

118. Wang, S.; Peng, Y., Natural Zeolites as Effective Adsorbents in Water and Wastewater Treatment. *Chem. Eng. J.* **2010,** *156* (1), 11-24.

119. Erdem, E.; Karapinar, N.; Donat, R., The Removal of Heavy Metal Cations by Natural Zeolites. *J. Colloid Int. Sci.* **2004,** *280* (2), 309-314.

120. Eroglu, N.; Emekci, M.; Athanassiou, C. G., Applications of Natural Zeolites on Agriculture and Food Production. *J. Sci. Food Agr.* **2017,** *97* (11), 3487-3499.

121. Breck, D. W.; Eversole, W. G.; Milton, R. M.; Reed, T. B.; Thomas, T. L., Crystalline Zeolites I. The Properties of a New Synthetic Zeolite. *J. Am. Chem. Soc.* **1956,** *78* (23), 5963-5972.

122. Hashemian, S.; Hosseini, S. H.; Salehifar, H.; Salari, K., Adsorption of Fe(III) from Aqueous Solutiion by Linde Type A Zeolite. *Am. J. Anal. Chem.* **2013,** *4*, 123-126.

123. Pena, Y. P. d.; Rondon, W., Linde Type A Zeolite and Type Y Faujasite as a Solid-Phase for Lead, Cadmium, Nickel and Cobalt Preconcentration and Determination using a Flow Injection System Coupled to Flame Atomic Absorption Spectrometry. *Am. J. Anal. Chem.* **2013,** *4*, 387-397.

124. Sherry, H. S.; Walton, H. F., The Ion-Exchange Properties of Zeolites. II. Ion Exchange in the Synthetic Zeolite Linde 4A. *J. Phys. Chem.* **1967,** *71* (5), 1457-1465.

125. Gomez-Alvarez, P.; Carbajo, J. P.; Balestra, S. R. G.; Calero, S., Impact of the Nature of Exchangeable Cations on LTA Type Zeolite Hydration. *J. Phys. Chem. C* **2016,** *120*, 23254-23261.

126. Huang, Z. Y.; Xu, C. H.; Meng, J.; Zheng, C. F.; Xiao, H. W.; Chen, J.; Zhang, Y. X., Glycerol Steam Reforming to Syngas over Ni-Based Catalysts on Commercial Linde Type 5A Zeolite Modified by Metal Oxides. *J. Environ. Chem. Eng.* **2014,** *2* (1), 598-604.

127. Li, Y.; Zhou, H.; Zhu, G.; Liu, J.; Yang, W., Hydrothermal Stability of LTA Zeolite Membranes in Pervaporation. *J. Membrane Sci.* **2007,** *297*, 10-15.

128. Jensen, B.; Kuznetsova, T.; Kvamme, B.; Olsen, R., The Impact of Electrostatics in Bulk Linde Type A Zeolites. *Micropor. Mesopor. Mat.* **2015,** *201*, 105-115.

129. Petfield, A. T.; Cooney, R. P., Infrared Spectroscopic Studies of Melt-Deposited Salt Occlusion by Zeolites. *Aust. J. Chem.* **1980,** *33*, 659-664.

130. Park, M.; Shin, S. C.; Choi, C. L.; Lee, D. H.; Lim, W. T.; Komarneni, S.; Kim, M. C.; Choi, J.; Heo, N. H., Role of Framework on NH4NO3 Occlusion in Zeolite Pores. *Micropor. Mesopor. Mat.* **2001,** *50*, 91-99.

131. Gren, W.; Parker, S. C.; Slater, B.; Lewis, D. W., Structure of Zeolite A (LTA) Surfaces and the Zeolite A/Water Interface. *J. Phys. Chem. C* **2010,** *114*, 9739-9747.

132. Gramlich, V.; Meier, W. M., Crystal Structure of Hydrated NaA - Detailed Refinement of a Pseudosymmetric Zeolite Structure. *Z. Kristallogr. Krist.* **1971,** *133*, 134-149.

133. Muller, J. C. M.; Hakvoort, G.; Jansen, J. C., DSC and TG Study of Water Adsorption and Desorption on Zeolite NaA. *J. Therm. Anal.* **1998,** *53*, 449-466.

134. Sanchez, J. R.; Palermo, A.; Aldao, C. M., Monte Carlo Study of Thermal Desorption Curves of Water from Zeolite Type A. *Langmuir* **1996,** *12*, 36-39.

135. Palermo, A.; Aldao, C. M., Readsorption and Diffusion-Limited TPD of Water from Zeolite Linde 4A. *Thermochim. Acta* **1998,** *319*, 177-184.

136. Corsaro, C.; Crupi, V.; Longo, F.; Majolino, D.; Venuti, V.; Wanderlingh, U., Mobility of Water in Linde Type A Synthetic Zeolites: an Inelastic Neutron Scattering Study. *J. Phys. Condens. Mat.* **2005,** *17*, 7925-7934.

137. Crupi, V.; Majolino, D.; Venuti, V., Diffusional and Vibrational Dynamics of Water in NaA Zeolites by Neutron and Fourier Transform Infrared Spectroscopy. *J. Phys.: Condens. Matter.* **2004,** *16*, S5297-S5316.

138. Crupi, V.; Majolino, D.; Migliardo, P.; Venuti, V.; Wanderlingh, U., A FT-IR Absorption Analysis of Vibrational Properties of Water Encaged in NaA Zeolites: Evidence of a "Structure Maker" Role of Zeolitic Surface. *Eur. Phys. J. E* **2003,** *12*, S55-S58.

139. Crupi, V.; Longo, F.; Majolino, D.; Venuti, V., T Dependence of Vibrational Dynamics of Water in Ion-Exchanged Zeolites A: A Detailed Fourier Transform Infrarerd Attenuated Total Reflection Study. *J. Chem. Phys.* **2005,** *123*, 154702-1 - 154702-11.

140. Crupi, V.; Longo, F.; Majolino, D.; Venuti, V., Vibrational Properties of Water Molecules Adsorbed in Different Zeolitic Frameworks. *J. Phys. Condens. Mat.* **2006,** *18*, 3563-3580.

141. Coudert, F. X.; Vuilleumier, R.; Boutin, A., Dipole Moment, Hydrogen Bonding and IR Spectrum of Confined Water. *ChemPhysChem* **2006,** *7*, 2464-2467.

142. Calero, S.; Gomez-Alvarez, P., Effect of the Confinement and Presence of Cations on Hydrogen Bonding of Water in LTA-Type Zeolite. *J. Phys. Chem. C* **2014,** *118*, 9056-9065.

143. Demontis, P.; Gonzalez, J. G.; Jobic, H.; Masia, M.; Sale, R.; Suffritti, G. B., Dynamical Properties of Confined Water Nanoclusters: Simulation Study of Hydrated Zeolite NaA: Structural and Vibrational Properties. *ACS Nano* **2008,** *2* (8), 1603-1614.

144. Castillo, J. M.; Silvestre-Albero, J.; Rodriguez-Reinoso, F.; Vlugt, T. J. H.; Calero, S., Water Adsorption in Hydrophilic Zeolites: Experiment and Simulation. *Phys. Chem. Chem. Phys.* **2013,** *15*, 17374-17382.

145. Dirar, Q. H.; Loughlin, K. F., Intrinsic Adsorption Prpoerties of CO2 on 5A and 13X Zeolite. *Adsorption.* **2013,** *19*, 1149-1163.

146. Li, Y.; Yi, H.; Tang, X.; Li, F.; Yuan, Q., Adsorption Separation of CO2/CH4 Gas Mixture on the Commercial Zeolites at Atmospheric Pressure. *Chem. Eng. J.* **2013,** *229*, 50-56.

147. Yi, H.; Deng, H.; Tang, X.; Yu, Q.; Zhou, Z.; Liu, H., Adsorption Equilibrium and Kinetics for SO2, NO, CO2 on Zeolites FAU and LTA. *J. Haz. Mat.* **2012,** *203-204*, 111-117.

148. Merel, J.; Clausse, M.; Meunier, F., Experimental Investigation on CO2 Post-Combustion Capture by Indirect Thermal Swing Adsorption using 13X and 5A Zeolites. *Ind. Eng. Chem. Res.* **2008,** *47*, 209-215.

149. Wang, Y.; LeVan, M. D., Adsorption Equilibrium of Carbon Dioxide and Water Vapor on Zeolites 5A and 13X and Silica Gel: Pure Components. *Journal of Chemical & Engineering Data* **2009,** *54* (10), 2839-2844.

150. Maraoulaite, D. K.; Nickels, T. M.; Ingram, A. L.; White, R. L., VT-DRIFTS Investigations of Interactions between Benzoic Acid and Montmorillonite Clay. *Spectrosc.* **2015,** *30* (10), 32-42.

151. Nickels, T. M.; Ingram, A. L.; Maraoulaite, D. K.; White, R. L., Variable Temperature Infrared Spectroscopy Investigation of Benzoic Acid Interactions with Montmorillonite Clay Interlayer Water. *Appl. Spectrosc.* **2015,** *69* (7), 850-856.

152. Ingram, A. L.; Nickels, T. M.; Maraoulaite, D. K.; White, R. L., Variable Temperature Infrared Spectroscopy Studies of Aromatic Acid Adsorbate Effects on Montmorillonite Dehydration. *Appl. Spectrosc.* **2016,** *71* (2), 238-249.

153. Forster, H.; Schumann, M., Infrared Spectroscopic Studies on Carbon Dioxide Adsorption in Alkali-Metal and Alkaline-Earth-Metal Ion-Exchanged A-Type Zeolites. *J. Chem. Soc. Faraday Trans. 1* **1989,** *85* (5), 1149-1158.

154. Luhrs, H.; Derr, J.; Fischer, R. X., K and Ca Exchange Behavior of Zeolite A. *Microporous and Mesoporous Mater.* **2012,** *151*, 457-465.

155. Pluth, J. J.; Smith, J. V., Crystal Structure of Dehydrated Ca-Exchanged Zeolite A. Absence of Near-Zero-Coordinate Ca2+. Presence of Al Complex. *J. Am. Chem. Soc.* **1983,** *105* (5), 1192-1195.

156. White, D. R., White, R.L., Isoconversion effective activation energies obtained by variable temperature diffuse reflectance infrared spectroscopy. *Appl. Spectrosc.* **2008,** *62* (1), 116-120.

157. Robertson, C. W.; Williams, D., Lambert Absorption Coefficients of Water in the Infrared. *J. Opt. Soc. Am.* **1971,** *61* (10), 1316-1320.

158. McMillan, P. F.; Remmele, R. L., Hydroxyl Sites in SiO2 glass: a Note on Infrared and Raman Spectra. *Am. Mineral.* **1986,** *71*, 772-778.

159. Shen, Y.; Wu, P., Two-dimensional ATR-FTIR spectroscopic investigation on water diffusion in polypropylene film: water bending vibrration. *J. Phys. Chem. B* **2003,** *107*, 4224-4226.

160. Grodzicki, A.; Piszczek, P., The bending frequencies of water molecules in different crystal surroundings. *Polish J. Chem.* **1996,** *70*, 620-631.

161. Kolesov, B. A.; Geiger, C. A., Behavior of H2O Molecules in the Channels of Natrolite and Scolecite: A Raman and IR Spectroscopic Investigation of Hydrous Microporous Silicates. *Am. Mineral.* **2006,** *91*, 1039-1048.

162. Roy, G. D.; Vansant, E. F.; Hendrickx, M., Sorption in Partially Hydrated NaA and CaA Zeolites. *J.C.S. Faraday I* **1980,** *76*, 1166-1174.

163. Henao-Sierra, W.; Romero-Saez, M.; Gracia, F.; Cacua, K.; Buitrago-Sierra, R., Water Vapor Adsorption Performance of Ag and Ni Modified 5A Zeolite. *Microporous and Mesoporous Mater.* **2018,** *265*, 250-257.

164. Berger, A. S.; Samsonova, T. I.; Yakovlev, L. K., Thermal Decomposition of Cation Exchange Forms of Zeolite A. *Phys. Chem.* **1971**, 2015-2019.

165. Sun, H.; Wu, D.; Guo, X.; Shen, B.; Navrotsky, A., Energetics of Sodium-Calcium Exchanged Zeolite A. *Phys. Chem. Chem. Phys.* **2015,** *17*, 11198-11203.

166. Sun, H.; Wu, D.; Liu, K.; Guo, X.; Navrotsky, A., Energetics of Alkali and Alkaline Earth Ion-Exchanged Zeolite A. *J. Phys. Chem. C* **2016,** *120*, 15251-15256.

167. Gallei, E.; Stumpf, G., Infrared Spectroscopic Studies of the Adsorption of Carbon Dioxide and the Coadsorption of Carbon Dioxide and Water on CaY and NiY Zeolites. *J. Colloid Int. Sci.* **1976,** *55* (2), 415-420.

168. Martra, G.; Coluccia, S.; Davit, P.; Gianotti, E.; Marchese, L.; Tsuji, H.; Hattori, H., Acidic and Basic Sites in NaX and NaY Faujasites Investigated by NH3, CO2 and CO Molecular Probes. *Res. Chem. Intermed.* **1999,** *25* (1), 77-93.

169. Jiang, M.; Karge, H. G., Investigation of Acid Properties of Dealuminated H-Mordenite Zeolites by Low-Temperature Diffuse Reflectance FTIR. *J. Chem. Soc. Faraday Trans.* **1996,** *92* (14), 2641-2649.

170. Singh, J.; White, R. L., A variable temperature infrared spectroscopy study of NaA zeolite dehydration. *Vib. Spectrosc.* **2018,** *94*, 37-42.

171. Masuda, T.; Tsutsumi, K.; Takahashi, H., Infrared and Calorimetric Studies of Adsorbed Carbon Dioxide on NaA and CaNaA Zeolites. *J. Colloid Int. Sci.* **1980,** *77* (1), 232-237.

172. Ucun, F., An Infrared Study of the CaA Zeolite Reacted with CO2. *Z. Naturforsch.* **2002,** *57a*, 283-284.

173. Adler, H. H.; Kerr, P. F., Infrared Spectra, Symmetry and Structure Relations of some Carbonate Minerals. *Am. Mineral.* **1963,** *48*, 839-853.

174. Porcher, F.; Souhassou, M.; Graafsma, H.; Puig-Molina, A.; Dusausoy, Y.; Lecomte, C., Refinement of Framework Disorder in Dehydrated CaA Zeolite from Single-Crystal Synchrotron Data. *Acta Cryst.* **2000,** *B56*, 766-772.

175. Malenkov, G. G.; Frank-Kamenetskii, M. M., Computer Simulation of the Structure of the Hydration Shells of Calcium and Calcium-Water-Zeolite A. *J. Struct. Chem.* **1996,** *37* (1), 76-83.

176. Subbotin, A. N.; Zhidomirov, G. M.; Subbotina, I. R.; Kazansky, V. B., Molecular and Dissociative Adsorption of H2O on Zeolite Zn/ZSM-5 Studied by Diffuse-Reflectance IR Spectroscopy and Quantum Chemical Calculations. *Kin. Catal.* **2013,** *54* (6).

177. Beta, I. A.; Hunger, B.; Bohlmann, W.; Jobic, H., Dissociative Adsorption of Water in CaNaA Zeolites Studied by TG, DRIFTS, and 1H and 27Al MAS NMR Spectroscopy. *Microporous and Mesoporous Mater.* **2005,** *79*, 69-70.

178. Hunger, M., Multinuclear solid-state NMR studies of acidic and non-acidic hydroxyl protons in zeolites. *Solid State Nucl. Magn. Reson.* **1996,** *6* (1), 1-29.

179. Ward, J. W., Spectroscopic study of the surface of zeolite Y. II. Infrared spectra of structural hydroxyl groups and adsorbed water on alkali, alkaline earth, and rare earth ion-exchanged zeolites. *J. Phys. Chem.* **1968,** *72* (12), 4211-4223.

180. Rybakov, A. A.; bryukhanov, I. A.; Larin, A. V.; Zhidomirov, G. M., Carbonates in Zeolites: Formation, Properties, Reactivity. *Int. J. Quant. Chem.* **2015,** *115*, 1709-1717.

181. Larin, A. V.; Bryukhanov, I. A.; Rybakov, A. A.; Kovalev, V. L.; Vercauteren, D. P., Theoretical Identification of Carbonate Geometry in Zeolites from IR Spectra. *Microporous and Mesoporous Mater.* **2013,** *173*, 15-21.

182. Hage, W.; Hallbrucker, A.; Mayer, E., Carbonic Acid: Synthesis by Protonation of Bicarbonate and FTIR Spectroscopic Characterization via a New Cryogenic Technique. *J. Am. Chem. Soc.* **1993,** *115*, 8427-8431.

183. Rudolph, W. W.; Fischer, D.; Irmer, G., Vibrational Spectroscopic Studies and Density Functional Theory Calculations of Speciation in the CO2-Water System. *Appl. Spectrosc.* **2006,** *60* (2), 130-144.

184. Demontis, P.; Suffritti, G. B.; Bordiga, S.; Buzzoni, R., Atom Pair Potential for Molecular Dynamics Simulations of Structural and Dynamical Properties of Aluminosilicates: Test on Silicalite and Anhydrous Na-A and Ca-A Zeolites and Comparison with Experimental Data. *J. Chem. Soc. Faraday Trans.* **1995,** *91* (3), 525-533.

185. Ucun, F.; Atalay, Y.; Ilbasmis, T., Ab Initio Calculation of the Molecular Strucure and Vibration Frequencies of Carbonate Ions Coordinated to Calcium Ions in the Zeolite CaA by Hartree-Fock Methods. *Z. Naturforsch.* **2005,** *60a*, 608-610.

186. Oliver, B. G.; Davis, A. R., Vibrational Spectroscopic Studies of Aqueous Alkali Metal Bicarbonate and Carbonate Solutions. *Can. J. Chem.* **1973,** *51*, 698-702.

187. Al-Hosney, H. A.; Carlos-Cuellar, S.; Baltrusaitis, J.; Grassian, V. H., Heterogeneous Uptake and Reactivity of Formic Acid on Calcium Carbonate Particles: a Knudsen Cell Reactor, FTIR and SEM Study. *Phys. Chem. Chem. Phys.* **2005,** *7*, 3587-3595.

188. Wuttig, A.; Liu, C.; Peng, Q.; Yaguchi, M.; Hendon, C. H.; Motobayashi, K.; Ye, S.; Osawa, M.; Surendranath, Y., Tracking a Common Surface-Bound Intermediate during CO2-to-Fuels Catalysis. *ACS Cent. Sci.* **2016,** *2*, 522-528.

189. Breck, D. W. Crystalline zeolite y. US3130007A, 1964/04/21/, 1964.

190. Babitz, S. M.; Williams, B. A.; Miller, J. T.; Snurr, R. Q.; Haag, W. O.; Kung, H. H., Monomolecular cracking of n-hexane on Y, MOR, and ZSM-5 zeolites. *Appl. Catal. A-Gen.* **1999,** *179* (1), 71-86.

191. C. Vogt, E. T.; M. Weckhuysen, B., Fluid catalytic cracking: recent developments on the grand old lady of zeolite catalysis. *Chem. Soc. Rev.* **2015,** *44* (20), 7342-7370.

192. Djeffal, N.; Benbouzid, M.; Boukoussa, B.; Sekkiou, H.; Bengueddach, A., CO2 adsorption properties of ion-exchanged zeolite Y prepared from natural clays. *Mater. Res. Express* **2017,** *4* (3), 035504.

193. Langmi, H. W.; Walton, A.; Al-Mamouri, M. M.; Johnson, S. R.; Book, D.; Speight, J. D.; Edwards, P. P.; Gameson, I.; Anderson, P. A.; Harris, I. R., Hydrogen adsorption in zeolites A, X, Y and RHO. *J. Alloys Compd.* **2003,** *356-357*, 710-715.

194. Shao, W.; Zhang, L.; Li, L.; Lee, R. L., Adsorption of CO2 and N2 on synthesized NaY zeolite at high temperatures. *Adsorption.* **2009,** *15* (5-6), 497-505.

195. Gomes, G. J.; Dal Pozzo, D. M.; Zalazar, M. F.; Costa, M. B.; Arroyo, P. A.; Bittencourt, P. R. S., Oleic acid esterification catalyzed by zeolite Y-model of the biomass conversion. *Top. Catal.* **2019**.

196. Rizkiana, J.; Guan, G.; Widayatno, W. B.; Yang, J.; Hao, X.; Matsuoka, K.; Abudula, A., Mg-modified ultra-stable Y type zeolite for the rapid catalytic co-pyrolysis of low-rank coal and biomass. *RSC Adv.* **2015,** *6* (3), 2096-2105.

197. Julbe, A.; Drobek, M., Zeolite Y Type. In *Encyclopedia of Membranes*, Drioli, E.; Giorno, L., Eds. Springer Berlin Heidelberg: Berlin, Heidelberg, 2016; pp 2060-2061.

198. Lutz, W., Zeolite Y: synthesis, modification, and properties—a case revisited. *Adv. Mater. Sci. Eng.* **2014,** *2014*, 724248.

199. Bushuev, Y. G.; Sastre, G.; de Julián-Ortiz, J. V., The structural directing role of water and hydroxyl groups in the synthesis of beta zeolite polymorphs. *J. Phys. Chem. C* **2010,** *114* (1), 345-356.

200. Cruciani, G., Zeolites upon heating: Factors governing their thermal stability and structural changes. *J. Phys. Chem. Solids* **2006,** *67* (9), 1973-1994.

201. Huang, Y.; Wang, K.; Dong, D.; Li, D.; Hill, M. R.; Hill, A. J.; Wang, H., Synthesis of hierarchical porous zeolite NaY particles with controllable particle sizes. *Micropor. Mesopor. Mat.* **2010,** *127* (3), 167-175.

202. Farrell, J.; Manspeaker, C.; Luo, J., Understanding competitive adsorption of water and trichloroethylene in a high-silica Y zeolite. *Micropor. Mesopor. Mat.* **2003,** *59* (2), 205-214.

203. Kraus, M.; Trommler, U.; Holzer, F.; Kopinke, F.-D.; Roland, U., Competing adsorption of toluene and water on various zeolites. *Chem. Eng. J.* **2018,** *351*, 356-363.

204. Deng, C.; Zhang, J.; Dong, L.; Huang, M.; Li, B.; Jin, G.; Gao, J.; Zhang, F.; Fan, M.; Zhang, L.; Gong, Y., The effect of positioning cations on acidity and stability of the framework structure of Y zeolite. *Sci. Rep.-UK* **2016,** *6*, 23382.

205. Frising, T.; Leflaive, P., Extraframework cation distributions in X and Y faujasite zeolites: A review. *Micropor. Mesopor. Mat.* **2008,** *114* (1), 27-63.

206. Perez, C. A. C.; de Resende, N. S.; Salim, V. M. M.; Schmal, M., Water interaction in faujasite probed by in situ X-ray powder diffraction. *J. Phys. Chem. C* **2017,** *121* (5), 2755-2761.

207. Lim, K. H.; Grey, C. P., Characterization of extrafFramework cation positions in zeolites NaX and NaY with very fast 23Na MAS and multiple quantum MAS NMR spectroscopy. *J. Am. Chem. Soc.* **2000,** *122* (40), 9768-9780.

208. Norby, P.; Poshni, F. I.; Gualtieri, A. F.; Hanson, J. C.; Grey, C. P., Cation migration in zeolites: an in situ powder diffraction and MAS NMR study of the structure of zeolite Cs(Na)−Y during dehydration. *J. Phys. Chem. B* **1998,** *102* (5), 839-856.

209. Ramsahye, N. A.; Bell, R. G., Cation mobility and the sorption of chloroform in zeolite NaY: molecular dynamics study. *J. Phys. Chem. B* **2005,** *109* (10), 4738-4747.

210. Boddenberg, B.; U. Rakhmatkariev, G.; Hufnagel, S.; Salimov, Z., A calorimetric and statistical mechanics study of water adsorption in zeolite NaY. *Phys Chem Chem Phys* **2002,** *4* (17), 4172-4180.

211. Beauvais, C.; Boutin, A.; Fuchs, A. H., Adsorption of water in zeolite sodium-faujasite: A molecular simulation study. *Comptes Rendus Chimie* **2005,** *8* (3), 485-490.

212. Bellat, J.-P.; Paulin, C.; Jeffroy, M.; Boutin, A.; Paillaud, J.-L.; Patarin, J.; Di Lella, A.; Fuchs, A., Unusual hysteresis loop in the adsorption−desorption of water in NaY zeolite at very low pressure. *J. Phys. Chem. C* **2009,** *113* (19), 8287-8295.

213. Shirono, K.; Endo, A.; Daiguji, H., Molecular dynamics study of hydrated faujasite-type zeolites. *J. Phys. Chem. B* **2005,** *109* (8), 3446-3453.

214. Kirschhock, C. E. A.; Hunger, B.; Martens, J.; Jacobs, P. A., Localization of residual water in alkali-metal cation-exchanged X and Y type zeolites. *J. Phys. Chem. B* **2000,** *104* (3), 439-448.

215. Hu, M.; Hanson, J. C.; Wang, X., Structure and thermal stability of (H2O)4 tetrahedron and (H2O)6 hexagon adsorbed on NaY zeolite studied by synchrotron-based time-resolved X-ray diffraction. *Ind. Eng. Chem. Res.* **2018,** *57* (14), 4988-4995.

216. Wang, N. N.; Wang, Y.; Cheng, H. F.; Tao, Z.; Wang, J.; Wu, W. Z., Impact of cationic lanthanum species on zeolite Y: an infrared, excess infrared and Raman spectroscopic study. *RSC Adv.* **2013,** *3*, 20237-20245.

217. Beta, I. A.; Böhlig, H.; Hunger, B., Structure of adsorption complexes of water in zeolites of different types studied by infrared spectroscopy and inelastic neutron scattering. *Phys Chem Chem Phys* **2004,** *6* (8), 1975-1981.

218. Flanigen, E. M.; Khatami, H.; Szymanski, H. A., Infrared structural studies of zeolite frameworks. *Molecular Sieve Zeolites I* **1974,** *101* (101), 201-229.

219. Król, M.; Mozgawa, W.; Jastrzębski, W.; Barczyk, K., Application of IR spectra in the studies of zeolites from D4R and D6R structural groups. *Micropor. Mesopor. Mat.* **2012,** *156*, 181-188.

220. Angell, C. L.; Schaffer, P. C., Infrared spectroscopic investigations of zeolites and adsorbed molecules. I. structural OH groups[1]. *J. Phys. Chem.* **1965,** *69* (10), 3463-3470.

221. Fritz, P. O.; Lunsford, J. H., The effect of sodium poisoning on dealuminated Y-type zeolites. *J. Catal.* **1989,** *118* (1), 85-98.

222. Halasz, I.; Senderov, E.; Olson, D. H.; Liang, J.-J., Further search for hydroxyl nests in acid dealuminated zeolite Y. *J. Phys. Chem. C* **2015,** *119* (16), 8619-8625.

223. Finnie, K. S.; Cassidy, D. J.; Bartlett, J. R.; Woolfrey, J. L., IR spectroscopy of surface water and hydroxyl species on nanocrystalline TiO2 films. *Langmuir* **2001,** *17* (3), 816-820.

224. Lengyel, J.; Ončák, M.; Herburger, A.; van der Linde, C.; Beyer, M. K., Infrared spectroscopy of O˙− and OH− in water clusters: evidence for fast interconversion between O˙− and OH˙OH−. *Phys Chem Chem Phys* **2017,** *19* (37), 25346-25351.

225. Cairon, O.; Loustaunau, A.; Gautier, M., FTIR studies of unusual OH groups in steamed HNaY zeolites: Influence of Na insertion. *J. Phys. Chem. Solids* **2006,** *67* (5), 994-997.

226. Cairon, O.; Thomas, K.; Chevreau, T., FTIR studies of unusual OH groups in steamed HNaY zeolites: preparation and acid properties. *Micropor. Mesopor. Mat.* **2001,** *46* (2), 327-340.

227. Boréave, A.; Auroux, A.; Guimon, C., Nature and strength of acid sites in HY zeolites: a multitechnical approach. *Microporous Mater.* **1997,** *11* (5), 275-291.

228. Hirschler, A. E., The measurement of catalyst acidity using indicators forming stable surface carbonium ions. *J. Catal.* **1963,** *2* (5), 428-439.

229. Ryder, J. A.; Chakraborty, A. K.; Bell, A. T., Density functional theory study of proton mobility in zeolites: proton migration and hydrogen exchange in ZSM-5. *J. Phys. Chem. B* **2000,** *104* (30), 6998-7011.

230. Viswanathan, U.; Fermann, J. T.; Toy, L. K.; Auerbach, S. M.; Vreven, T.; Frisch, M. J., Modeling proton jumps in HY zeolite: effects of acid site heterogeneity. *J. Phys. Chem. C* **2007,** *111* (49), 18341-18347.

231. Kanellopoulos, J.; Gottert, C.; Schneider, D.; Knorr, B.; Prager, D.; Ernst, H.; Freude, D., NMR investigation of proton mobility in zeolites. *J. Catal.* **2008,** *255* (1), 68-78.

232. Wang, M.; Jaegers, N. R.; Lee, M.-S.; Wan, C.; Hu, J. Z.; Shi, H.; Mei, D.; Burton, S. D.; Camaioni, D. M.; Gutiérrez, O. Y.; Glezakou, V.-A.; Rousseau, R.; Wang, Y.; Lercher, J. A., Genesis and stability of hydronium ions in zeolite channels. *J. Am. Chem. Soc.* **2019,** *141* (8), 3444-3455.

233. Hobza, P.; Havlas, Z., Blue-shifting hydrogen bonds. *Chem. Rev.* **2000,** *100* (11), 4253-4264.

234. Hobza, P.; Špirko, V.; Selzle, H. L.; Schlag, E. W., Anti-hydrogen bond in the benzene dimer and other carbon proton donor complexes. *J. Phys. Chem. A* **1998,** *102* (15), 2501-2504.

235. Datka, J.; Sulikowski, B.; Gil, B., IR spectroscopic studies of dealuminated and realuminated zeolite HY. *J. Phys. Chem.* **1996,** *100*, 11242-11245.

236. Montanari, T.; Finocchio, E.; Busca, G., Infrared spectroscopy of heterogeneous catalysts: acidity and accessibility of acid sites of faujasite-type solid acids. *J. Phys. Chem. C* **2011,** *115*, 937-943.

237. Mofrad, A. M.; Peixoto, C.; J.Blumeyer; Liu, J.; Hunt, H. K.; Hammond, K. D., Vibrational spectroscopy of sodalite: theory and experiments. *J. Phys. Chem.C* **2018,** *122*, 24765-24779.

238. Liu, X.; Zhang, Z.; Xu, Y.; Xu, R., A second-derivative IR study of zeolite Y in the asymmetric stretching region of framework vibration. *J. Chem. Soc., Chem. Commun.* **1990**, 13-14.

239. Hannus, I.; Palinko, I.; Kiricsi, I., Fourier-transform mid and far IR and 23Na MAS NMR analysis of framework vibrations and distribution of cations in alkali-exchanged Y-type zeolites. *Mikrochim. Acta* **1997,** *14*, 701-702.

Appendix 1: Button-IR Accessories 3D Model and Images

3D Model button-IR Carousel

Top

Side

Multiple-sample carousel under diffuse reflection optics

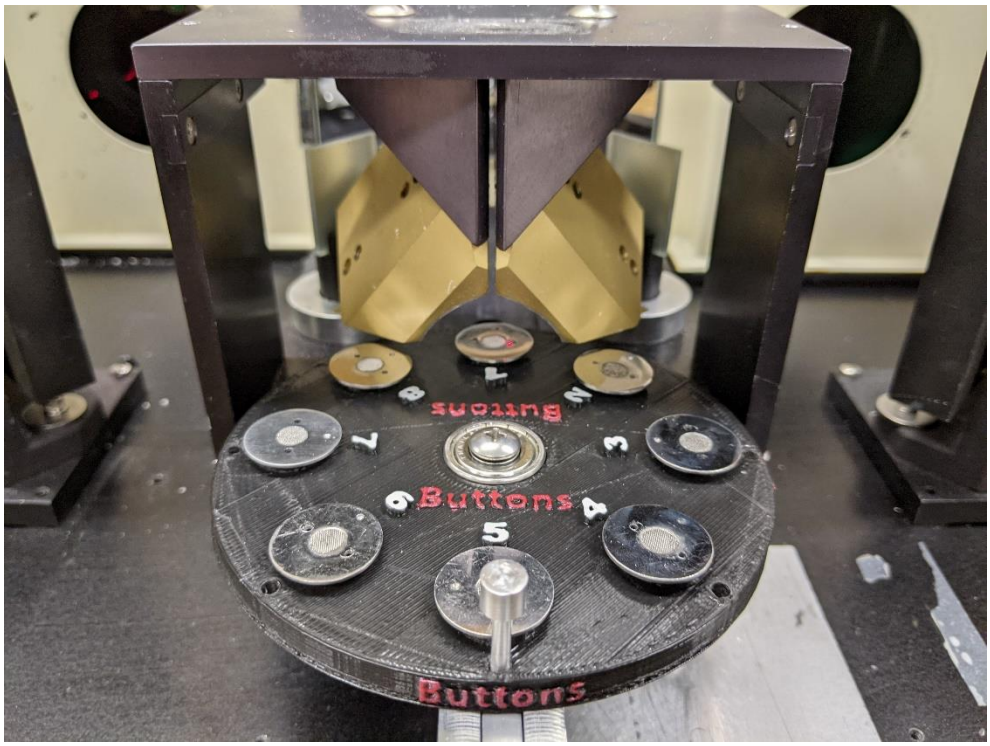

3D Model low-temperature TEC Accessory

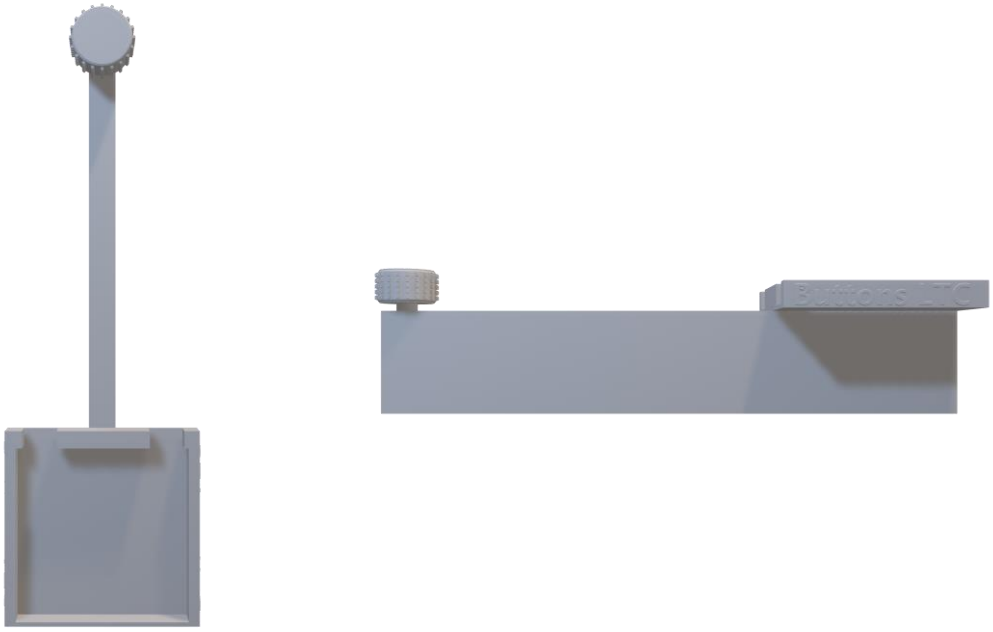

Top Side

Image of low-temperature TEC Accessory using 3D printed design.

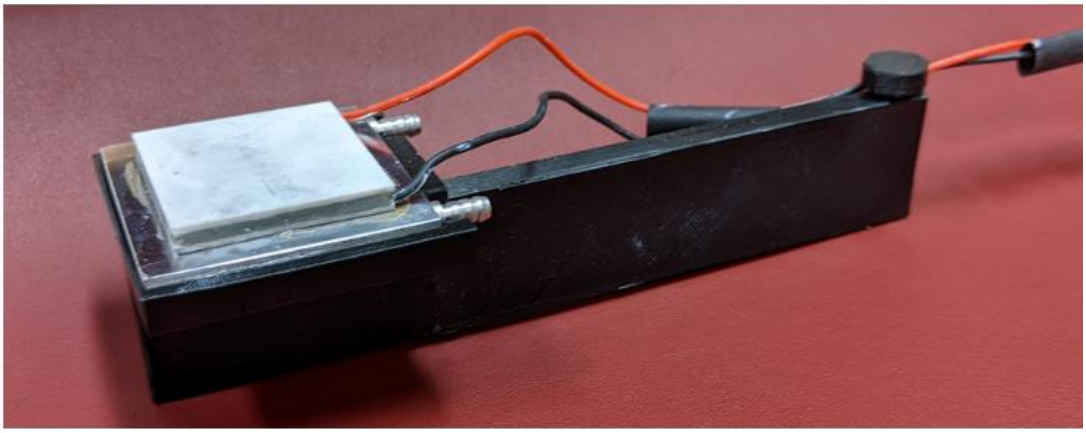

Appendix 2: R Script

Script 1: Data conversion and baseline correction

```
#load all working packages
library(ChemoSpec)

#set working directory to folder containing only files of interest in CSV format
#from the menu bar: session>set working directory> choose directory
setwd(choose.dir())

#convert transmittance(RAS) to absorbance

myfiles <- list.files(pattern = '*.csv')
tools::file_path_sans_ext(myfiles)
dir.create(paste0("Absorbance"), showWarnings = TRUE)

# A=2-log(y)
for (i in myfiles){
  dat <- read.csv(i, header = FALSE) #read in file
  dat <- dat[3:nrow(dat), -3] #remove top two rows and 3rd column
  y <- as.numeric((dat[, 2]), digits = 8)
  y <- 2-log10(y)
  dat[, 2] <- y
  z <- as.numeric(dat[, 1])
  dat[, 1] <- round(z, digits = 6)
  dat <- dat[!dat$V1 > 4000,] #remove rows with wavenumbers above 4000
  write.table(dat, file = paste0("./Absorbance/", gsub(".csv", i, ".csv")), row.names = FALSE,
col.names = FALSE, sep = ",")
}

#convert ABS to Reflectance
setwd("./Absorbance")

myfiles <- list.files(pattern = '*.csv')
tools::file_path_sans_ext(myfiles)
dir.create(paste0("../Reflectance"), showWarnings = TRUE)

for (i in myfiles){
  dat <- read.csv(i, header = FALSE) #read in file
  dat <- dat[1:nrow(dat), -3] #remove top two rows and 3rd column
  y <- as.numeric((dat[, 2]))
  y <- (1/10^y)
  dat[, 2] <- y
  z <- as.numeric(dat[, 1])
  dat[, 1] <- round(z, digits = 6)
```

```
  write.table(dat, file = paste0("../Reflectance/", gsub(".csv", i, ".csv")), row.names = FALSE,
col.names = FALSE, sep = ",")
}

setwd("../Reflectance")
myfiles <- list.files(pattern = '*.csv')
tools::file_path_sans_ext(myfiles)
dir.create(paste0("../Kubelka-Munk"), showWarnings = TRUE)

# KM=((1-r)^2/(2r))
for (i in myfiles){
  dat <- read.csv(i, header = FALSE) #read in file
  dat <- dat[1:nrow(dat), -3] #remove top two rows and 3rd column
  x <- as.numeric((dat[, 2]))
  y <- (((1-x)**2)/(2*x))
  dat[, 2] <- y
  z <- as.numeric(dat[, 1])
  dat[, 1] <- round(z, digits = 6)
  write.table(dat, file = paste0("../Kubelka-Munk/", gsub(".csv", i, ".csv")), row.names =
FALSE, col.names = FALSE, sep = ",")
}

rm(list = ls())
setwd("../Absorbance")

#load spectra sequentially labeled into R
#ex. S-1, S-2, S-3 ,...
S_1 <- files2SpectraObject(
  gr.crit = c("AC"), #use appropriate group labels
  gr.cols = c("auto"),
  freq.unit = "Wavenumber",
  int.unit = "Absorbance",
  descrip = "full import",
  fileExt = "\\.(csv|CSV)$",
  sep = ",",
  dec = ".",
  header = FALSE,
  debug = TRUE,
)

#baseline correct absorbance spectra
S_1.IR <- baselineSpectra(S_1,
                          int = FALSE, #widget to interactively correct
                          lambda =9,
                          p = 0.0001,
                          maxit = 1000,
```

```
                method = "als", #style of fit ex. rfbaseline, modpolyfit...
                retC = TRUE #save corrected spectra into the new Spectra object
)

tmp <- cbind(S_1.IR$freq, t(S_1.IR$data))
colnames(tmp) <- c("freq", S_1.IR$names)
tmp <- as.data.frame(tmp) # it was a matrix

dir.create(paste0("../Absorbance_BaseCorr"), showWarnings = TRUE)

#Output new data as individual csv files
for(i in 2:ncol(tmp)){
  tmp_df = tmp[,c(1,i)]
  write.table(tmp_df, file = paste0("../Absorbance_BaseCorr/", colnames(tmp_df)[2], ".csv"),
sep = ",", row.names = FALSE)
}

rm(list = ls())
#convert absorbance_basecorr to reflectance_basecorr
# R=[1/(10^A)]

setwd("../Absorbance_BaseCorr")

myfiles <- list.files(pattern = '*.csv')
tools::file_path_sans_ext(myfiles)
dir.create(paste0("../ReflectanceBaseCorr"), showWarnings = TRUE)

for (i in myfiles){
  dat <- read.csv(i, header = FALSE) #read in file
  dat <- dat[2:nrow(dat), -3] #remove top row and 3rd column
  y <- as.numeric((dat[, 2]))
  y <- (1/10^y)
  dat[, 2] <- y
  z <- as.numeric(dat[, 1])
  dat[, 1] <- round(z, digits = 6)
  write.table(dat, file = paste0("../ReflectanceBaseCorr/", gsub(".csv", i, ".csv")), row.names =
FALSE, col.names = FALSE, sep = ",")
}

#convert reflectance_basecorr to KM_basecorr
# KM=(((1-x)**2)/(2*x))
rm(list = ls())
setwd("../ReflectanceBaseCorr")

myfiles <- list.files(pattern = '*.csv')
tools::file_path_sans_ext(myfiles)
```

```
dir.create(paste0("../KMBaseCorr"), showWarnings = TRUE)

# KM=((1-r)^2/(2r))
for (i in myfiles){
  dat <- read.csv(i, header = FALSE) #read in file
  dat <- dat[2:nrow(dat), -3] #remove top two rows and 3rd column
  x <- as.numeric((dat[, 2]))
  y <- (((1-x)**2)/(2*x))
  dat[, 2] <- y
  z <- as.numeric(dat[, 1])
  dat[, 1] <- round(z, digits = 6)
  write.table(dat, file = paste0("../KMBaseCorr/", gsub(".csv", i, ".csv")), row.names = FALSE,
col.names = FALSE, sep = ",")
}

rm(list = ls())
```

Script 2: Principal Component Analysis

```
#load all working packages
library(tidyverse)
library(ggplot2)
library(ggfortify)
library(chemometrics)
library(dplyr)

#FOR ALL THE WAVENUMBERS####
#set working directory to folder containing only files of interest in CSV format
#from the menu bar: session>set working directory> choose directory
setwd(choose.dir())
# define the filename, should have all the data compiled into 1 csv
filename <- "filename.csv"
# load the CSV file from the local directory
dataset <- read.csv(filename, header=TRUE)

#FOR A SUBSET OF THE WAVENUMBERS####
setwd(choose.dir())
#load spectra sequentially labeled into R
#ex. S-1, S-2, S-3 ,...
S_1 <- files2SpectraObject(
  gr.crit = c("Names"),
  gr.cols = c("auto"),
  freq.unit = "Wavenumber",
  int.unit = "Absorbance",
  descrip = "full import",
```

```
  fileExt = "\\.(csv|CSV)$",
  sep = ",",
  dec = ".",
  header = TRUE,
  debug = TRUE,
)
S_1.IR <- S_1

#Remove spectra below 2200 (OPTIONAL)
S_2.IR <- removeFreq(S_1.IR,
                     rem.freq = low ~ 2200)
S_1.IR <- S_2.IR

#Remove spectra above 2200(OPTIONAL)
S_2.IR <- removeFreq(S_1.IR,
                     rem.freq = high ~ 2200)
S_1.IR <- S_2.IR

#Dataframe of matrix
tmp <- cbind(S_1.IR$freq, t(S_1.IR$data))
colnames(tmp) <- c("freq", S_1.IR$names)
tmp <- as.data.frame(tmp) # it was a matrix
tmp <- t(tmp)
colnames(tmp) <- tmp[1, ]
tmp <- tmp[-1, ]
tmp <- as.data.frame(tmp)
dataset <- cbind(Drug = S_1$groups, tmp)

#PCA####
myPr <- prcomp(dataset[, -1], scale = TRUE)
summary(myPr)
plot(myPr, type = "l")
var_explained = as.data.frame((myPr$sdev^2 / sum(myPr$sdev^2))*100)
dataset2 <- cbind(GROUP = dataset[,1],Variance = var_explained, myPr$x[, 1:10])

# PLOT
theme<-theme(panel.background = element_blank(),
             panel.border=element_rect(fill=NA),
             panel.grid.major = element_blank(),
             panel.grid.minor = element_blank(),
             strip.background=element_blank(),
             axis.text.x=element_text(colour="black"),
             axis.text.y=element_text(colour="black"),
             axis.ticks=element_line(colour="black"),
             plot.margin=unit(c(1,1,1,1),"line"))
p <- ggplot(dataset2, aes(PC1, PC2, col = GROUP, fill = GROUP)) +
```

```
  stat_ellipse(geom = "polygon", col = "white", alpha = 0.15) +
  geom_point(aes(shape = GROUP, color = GROUP)) + theme
p + ggtitle(bquote('PLOT TITLE')) +
  theme(plot.title = element_text(hjust = 0.5)) +
  labs(x = "PC1 (#%)", y = "PC2 (#%)")

#Diagnostics Plot for PCA####
X <- scale(dataset[,-1])
X_nipals <- nipals(X, a=5, it=160)
X_nipals2 <- list(scores=myPr$x, loadings=myPr$rotation,
                  sdev=myPr$sdev)

res <- pcaDiagplot(X, X.pca=X_nipals, a=5)

#Scree Plot - Alternate Style
myt <- expression(
  bolditalic("TITLE"))
plotScree(myPr, style = "alt", main = myt)

#EXPORT DATA####
#Export Spectral Loading
write.csv(myPr$rotation[,1:3], "SpecLoading.csv", row.names = FALSE)

# Export
#Export PC and Variance
write.csv(dataset2, "PC and Variance2.csv")
```

Appendix 3: Copyright

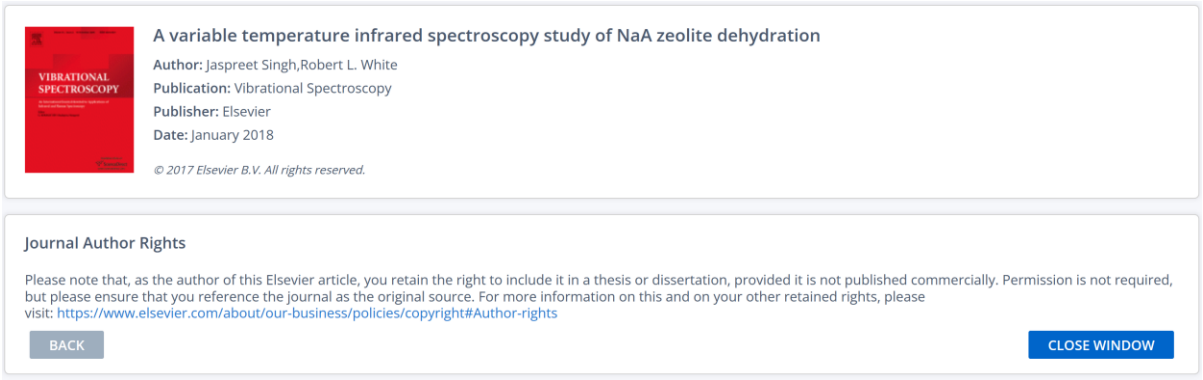

A variable temperature infrared spectroscopy study of NaA zeolite dehydration

Author: Jaspreet Singh,Robert L. White
Publication: Vibrational Spectroscopy
Publisher: Elsevier
Date: January 2018

© 2017 Elsevier B.V. All rights reserved.

Journal Author Rights

Please note that, as the author of this Elsevier article, you retain the right to include it in a thesis or dissertation, provided it is not published commercially. Permission is not required, but please ensure that you reference the journal as the original source. For more information on this and on your other retained rights, please visit: https://www.elsevier.com/about/our-business/policies/copyright#Author-rights

BACK CLOSE WINDOW

Singh, J. & White, R. L. A variable temperature infrared spectroscopy study of NaA zeolite dehydration. *Vibrational Spectroscopy* 94, 37–42 (**2018**).

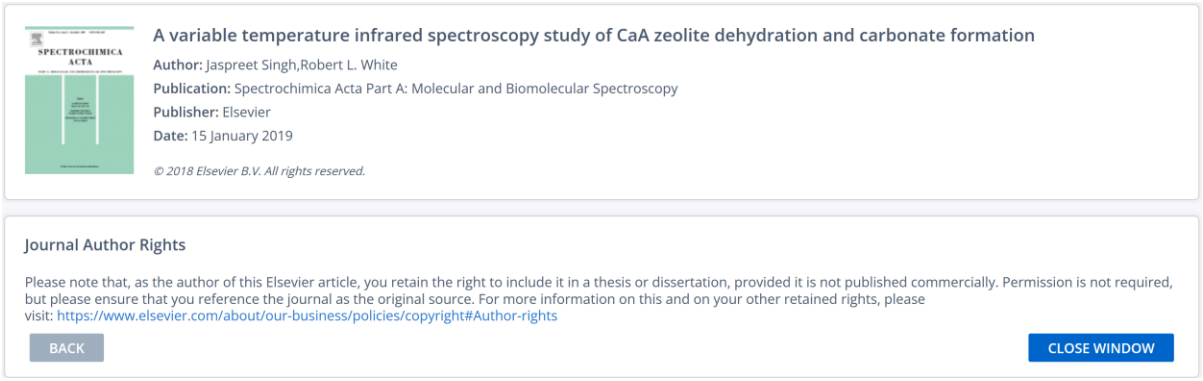

A variable temperature infrared spectroscopy study of CaA zeolite dehydration and carbonate formation

Author: Jaspreet Singh,Robert L. White
Publication: Spectrochimica Acta Part A: Molecular and Biomolecular Spectroscopy
Publisher: Elsevier
Date: 15 January 2019

© 2018 Elsevier B.V. All rights reserved.

Journal Author Rights

Please note that, as the author of this Elsevier article, you retain the right to include it in a thesis or dissertation, provided it is not published commercially. Permission is not required, but please ensure that you reference the journal as the original source. For more information on this and on your other retained rights, please visit: https://www.elsevier.com/about/our-business/policies/copyright#Author-rights

BACK CLOSE WINDOW

Singh, J. & White, R. L. A variable temperature infrared spectroscopy study of CaA zeolite dehydration and carbonate formation. *Spectrochimica Acta Part A: Molecular and Biomolecular Spectroscopy* 207, 189–196 (**2019**).

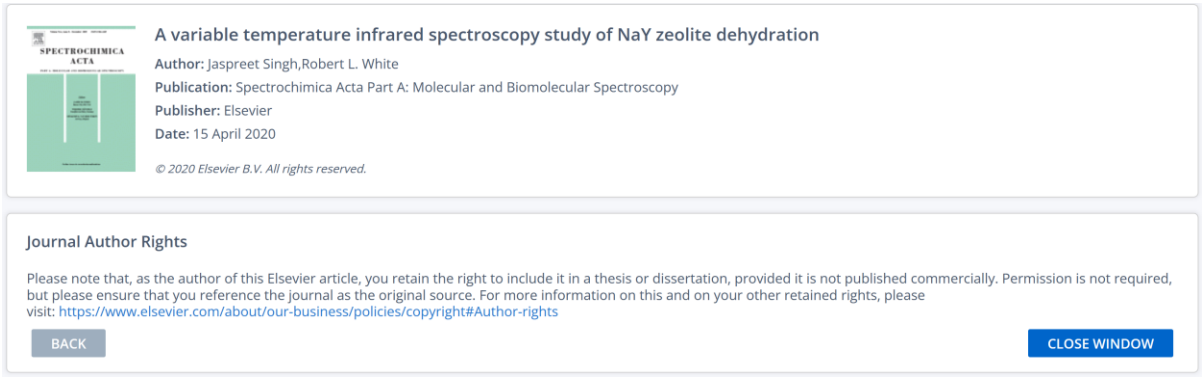

A variable temperature infrared spectroscopy study of NaY zeolite dehydration

Author: Jaspreet Singh,Robert L. White
Publication: Spectrochimica Acta Part A: Molecular and Biomolecular Spectroscopy
Publisher: Elsevier
Date: 15 April 2020

© 2020 Elsevier B.V. All rights reserved.

Journal Author Rights

Please note that, as the author of this Elsevier article, you retain the right to include it in a thesis or dissertation, provided it is not published commercially. Permission is not required, but please ensure that you reference the journal as the original source. For more information on this and on your other retained rights, please visit: https://www.elsevier.com/about/our-business/policies/copyright#Author-rights

BACK CLOSE WINDOW

Singh, J. & White, R. L. A variable temperature infrared spectroscopy study of NaY zeolite dehydration. *Spectrochimica Acta Part A: Molecular and Biomolecular Spectroscopy* 231, 118142 (**2020**).

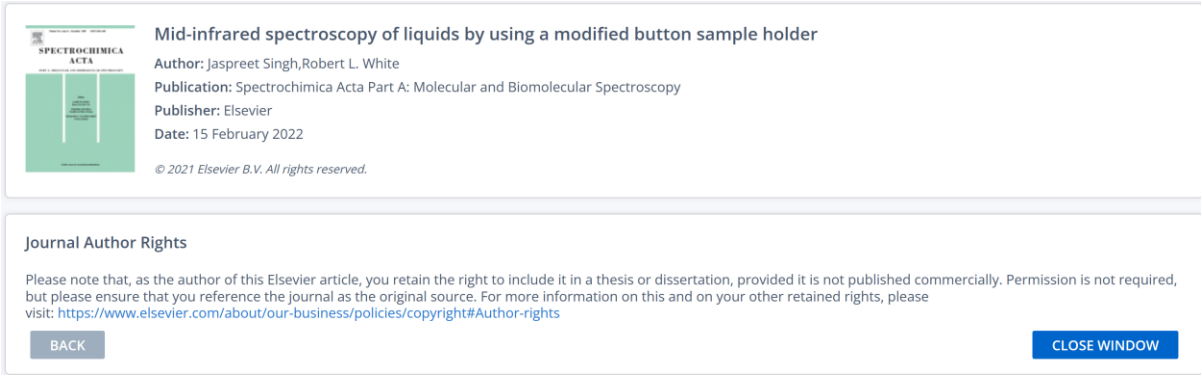

Singh, J. & White, R. L. Mid-infrared spectroscopy of liquids by using a modified button sample holder. *Spectrochimica Acta Part A: Molecular and Biomolecular Spectroscopy* 267, 120526 (**2022**).

Noneman, H. F., Hollingsworth, M. E., Singh, J. & White, R. L. A high sensitivity variable temperature infrared spectroscopy investigation of kaolinite structure changes. *Spectrochimica Acta Part A: Molecular and Biomolecular Spectroscopy* 247, 119113 (**2021**).

ELSEVIER LICENSE
TERMS AND CONDITIONS
Nov 17, 2021

This Agreement between Mr. Jaspreet Singh ("You") and Elsevier ("Elsevier") consists of your license details and the terms and conditions provided by Elsevier and Copyright Clearance Center.

License Number	5191431015229
License date	Nov 17, 2021
Licensed Content Publisher	Elsevier
Licensed Content Publication	Analytica Chimica Acta
Licensed Content Title	Diffuse reflection mid-infrared spectroscopy of neat powders by using a wire mesh “Button” sample holder
Licensed Content Author	Robert L. White
Licensed Content Date	Feb 15, 2020

Licensed Content Volume	1098
Licensed Content Issue	n/a
Licensed Content Pages	7
Start Page	110
End Page	116
Type of Use	reuse in a thesis/dissertation
Portion	figures/tables/illustrations
Number of figures/tables/illustrations	3
Format	both print and electronic
Are you the author of this Elsevier article?	No
Will you be translating?	No
Title	APPLICATIONS OF BUTTON SAMPLE HOLDERS FOR MID-INFRARED SPECTROSCOPY MEASUREMENTS
Institution name	University of Oklahoma
Expected presentation date	Dec 2021
Portions	Figures 2, 6, and 7
Requestor Location	Mr. Jaspreet Singh 101 Stephenson Parkway, Norman, OK, USA 101 Stephenson Parkway NORMAN, OK 73019 United States Attn: University of Oklahoma
Publisher Tax ID	98-0397604
Total	0.00 USD

Terms and Conditions

INTRODUCTION

1. The publisher for this copyrighted material is Elsevier. By clicking "accept" in connection with completing this licensing transaction, you agree that the following terms and conditions apply to this transaction (along with the Billing and Payment terms and conditions established by Copyright Clearance Center, Inc. ("CCC"), at the time that you opened your Rightslink account and that are available at any time at http://myaccount.copyright.com).

GENERAL TERMS

2. Elsevier hereby grants you permission to reproduce the aforementioned material subject to the terms and conditions indicated.

3. Acknowledgement: If any part of the material to be used (for example, figures) has appeared in our publication with credit or acknowledgement to another source, permission must also be sought from that source. If such permission is not obtained then that material may not be included in your publication/copies. Suitable acknowledgement to the source must be made, either as a footnote or in a reference list at the end of your publication, as follows:

"Reprinted from Publication title, Vol /edition number, Author(s), Title of article / title of chapter, Pages No., Copyright (Year), with permission from Elsevier [OR APPLICABLE SOCIETY COPYRIGHT OWNER]." Also Lancet special credit - "Reprinted from The Lancet, Vol. number, Author(s), Title of article, Pages No., Copyright (Year), with permission from Elsevier."
4. Reproduction of this material is confined to the purpose and/or media for which permission is hereby given.
5. Altering/Modifying Material: Not Permitted. However figures and illustrations may be altered/adapted minimally to serve your work. Any other abbreviations, additions, deletions and/or any other alterations shall be made only with prior written authorization of Elsevier Ltd. (Please contact Elsevier's permissions helpdesk here). No modifications can be made to any Lancet figures/tables and they must be reproduced in full.
6. If the permission fee for the requested use of our material is waived in this instance, please be advised that your future requests for Elsevier materials may attract a fee.
7. Reservation of Rights: Publisher reserves all rights not specifically granted in the combination of (i) the license details provided by you and accepted in the course of this licensing transaction, (ii) these terms and conditions and (iii) CCC's Billing and Payment terms and conditions.
8. License Contingent Upon Payment: While you may exercise the rights licensed immediately upon issuance of the license at the end of the licensing process for the transaction, provided that you have disclosed complete and accurate details of your proposed use, no license is finally effective unless and until full payment is received from you (either by publisher or by CCC) as provided in CCC's Billing and Payment terms and conditions. If full payment is not received on a timely basis, then any license preliminarily granted shall be deemed automatically revoked and shall be void as if never granted. Further, in the event that you breach any of these terms and conditions or any of CCC's Billing and Payment terms and conditions, the license is automatically revoked and shall be void as if never granted. Use of materials as described in a revoked license, as well as any use of the materials beyond the scope of an unrevoked license, may constitute copyright infringement and publisher reserves the right to take any and all action to protect its copyright in the materials.
9. Warranties: Publisher makes no representations or warranties with respect to the licensed material.
10. Indemnity: You hereby indemnify and agree to hold harmless publisher and CCC, and their respective officers, directors, employees and agents, from and against any and all claims arising out of your use of the licensed material other than as specifically authorized pursuant to this license.
11. No Transfer of License: This license is personal to you and may not be sublicensed, assigned, or transferred by you to any other person without publisher's written permission.
12. No Amendment Except in Writing: This license may not be amended except in a writing signed by both parties (or, in the case of publisher, by CCC on publisher's behalf).
13. Objection to Contrary Terms: Publisher hereby objects to any terms contained in any purchase order, acknowledgment, check endorsement or other writing prepared by you, which terms are inconsistent with these terms and conditions or CCC's Billing and Payment terms and conditions. These terms and conditions, together with CCC's Billing and Payment terms and conditions (which are incorporated herein), comprise the entire agreement

between you and publisher (and CCC) concerning this licensing transaction. In the event of any conflict between your obligations established by these terms and conditions and those established by CCC's Billing and Payment terms and conditions, these terms and conditions shall control.
14. Revocation: Elsevier or Copyright Clearance Center may deny the permissions described in this License at their sole discretion, for any reason or no reason, with a full refund payable to you. Notice of such denial will be made using the contact information provided by you. Failure to receive such notice will not alter or invalidate the denial. In no event will Elsevier or Copyright Clearance Center be responsible or liable for any costs, expenses or damage incurred by you as a result of a denial of your permission request, other than a refund of the amount(s) paid by you to Elsevier and/or Copyright Clearance Center for denied permissions.

LIMITED LICENSE

The following terms and conditions apply only to specific license types:
15. **Translation**: This permission is granted for non-exclusive world **English** rights only unless your license was granted for translation rights. If you licensed translation rights you may only translate this content into the languages you requested. A professional translator must perform all translations and reproduce the content word for word preserving the integrity of the article.
16. **Posting licensed content on any Website**: The following terms and conditions apply as follows: Licensing material from an Elsevier journal: All content posted to the web site must maintain the copyright information line on the bottom of each image; A hyper-text must be included to the Homepage of the journal from which you are licensing at http://www.sciencedirect.com/science/journal/xxxxx or the Elsevier homepage for books at http://www.elsevier.com; Central Storage: This license does not include permission for a scanned version of the material to be stored in a central repository such as that provided by Heron/XanEdu.
Licensing material from an Elsevier book: A hyper-text link must be included to the Elsevier homepage at http://www.elsevier.com . All content posted to the web site must maintain the copyright information line on the bottom of each image.

Posting licensed content on Electronic reserve: In addition to the above the following clauses are applicable: The web site must be password-protected and made available only to bona fide students registered on a relevant course. This permission is granted for 1 year only. You may obtain a new license for future website posting.
17. **For journal authors:** the following clauses are applicable in addition to the above:
Preprints:
A preprint is an author's own write-up of research results and analysis, it has not been peer-reviewed, nor has it had any other value added to it by a publisher (such as formatting, copyright, technical enhancement etc.).
Authors can share their preprints anywhere at any time. Preprints should not be added to or enhanced in any way in order to appear more like, or to substitute for, the final versions of articles however authors can update their preprints on arXiv or RePEc with their Accepted Author Manuscript (see below).
If accepted for publication, we encourage authors to link from the preprint to their formal publication via its DOI. Millions of researchers have access to the formal publications on

ScienceDirect, and so links will help users to find, access, cite and use the best available version. Please note that Cell Press, The Lancet and some society-owned have different preprint policies. Information on these policies is available on the journal homepage.
Accepted Author Manuscripts: An accepted author manuscript is the manuscript of an article that has been accepted for publication and which typically includes author-incorporated changes suggested during submission, peer review and editor-author communications.
Authors can share their accepted author manuscript:

- immediately
    - via their non-commercial person homepage or blog
    - by updating a preprint in arXiv or RePEc with the accepted manuscript
    - via their research institute or institutional repository for internal institutional uses or as part of an invitation-only research collaboration work-group
    - directly by providing copies to their students or to research collaborators for their personal use
    - for private scholarly sharing as part of an invitation-only work group on commercial sites with which Elsevier has an agreement
- After the embargo period
    - via non-commercial hosting platforms such as their institutional repository
    - via commercial sites with which Elsevier has an agreement

In all cases accepted manuscripts should:

- link to the formal publication via its DOI
- bear a CC-BY-NC-ND license - this is easy to do
- if aggregated with other manuscripts, for example in a repository or other site, be shared in alignment with our hosting policy not be added to or enhanced in any way to appear more like, or to substitute for, the published journal article.

Published journal article (JPA): A published journal article (PJA) is the definitive final record of published research that appears or will appear in the journal and embodies all value-adding publishing activities including peer review co-ordination, copy-editing, formatting, (if relevant) pagination and online enrichment.
Policies for sharing publishing journal articles differ for subscription and gold open access articles:
Subscription Articles: If you are an author, please share a link to your article rather than the full-text. Millions of researchers have access to the formal publications on ScienceDirect, and so links will help your users to find, access, cite, and use the best available version.
Theses and dissertations which contain embedded PJAs as part of the formal submission can be posted publicly by the awarding institution with DOI links back to the formal publications on ScienceDirect.
If you are affiliated with a library that subscribes to ScienceDirect you have additional private sharing rights for others' research accessed under that agreement. This includes use for classroom teaching and internal training at the institution (including use in course packs and courseware programs), and inclusion of the article for grant funding purposes.
Gold Open Access Articles: May be shared according to the author-selected end-user license and should contain a CrossMark logo, the end user license, and a DOI link to the formal publication on ScienceDirect.

Please refer to Elsevier's posting policy for further information.
18. **For book authors** the following clauses are applicable in addition to the above: Authors are permitted to place a brief summary of their work online only. You are not allowed to download and post the published electronic version of your chapter, nor may you scan the printed edition to create an electronic version. **Posting to a repository:** Authors are permitted to post a summary of their chapter only in their institution's repository.
19. **Thesis/Dissertation**: If your license is for use in a thesis/dissertation your thesis may be submitted to your institution in either print or electronic form. Should your thesis be published commercially, please reapply for permission. These requirements include permission for the Library and Archives of Canada to supply single copies, on demand, of the complete thesis and include permission for Proquest/UMI to supply single copies, on demand, of the complete thesis. Should your thesis be published commercially, please reapply for permission. Theses and dissertations which contain embedded PJAs as part of the formal submission can be posted publicly by the awarding institution with DOI links back to the formal publications on ScienceDirect.

Elsevier Open Access Terms and Conditions

You can publish open access with Elsevier in hundreds of open access journals or in nearly 2000 established subscription journals that support open access publishing. Permitted third party re-use of these open access articles is defined by the author's choice of Creative Commons user license. See our open access license policy for more information.

Terms & Conditions applicable to all Open Access articles published with Elsevier:

Any reuse of the article must not represent the author as endorsing the adaptation of the article nor should the article be modified in such a way as to damage the author's honour or reputation. If any changes have been made, such changes must be clearly indicated.

The author(s) must be appropriately credited and we ask that you include the end user license and a DOI link to the formal publication on ScienceDirect.

If any part of the material to be used (for example, figures) has appeared in our publication with credit or acknowledgement to another source it is the responsibility of the user to ensure their reuse complies with the terms and conditions determined by the rights holder.

Additional Terms & Conditions applicable to each Creative Commons user license:

CC BY: The CC-BY license allows users to copy, to create extracts, abstracts and new works from the Article, to alter and revise the Article and to make commercial use of the Article (including reuse and/or resale of the Article by commercial entities), provided the user gives appropriate credit (with a link to the formal publication through the relevant DOI), provides a link to the license, indicates if changes were made and the licensor is not represented as endorsing the use made of the work. The full details of the license are available at http://creativecommons.org/licenses/by/4.0.

CC BY NC SA: The CC BY-NC-SA license allows users to copy, to create extracts, abstracts and new works from the Article, to alter and revise the Article, provided this is not done for commercial purposes, and that the user gives appropriate credit (with a link to the formal publication through the relevant DOI), provides a link to the license, indicates if changes were made and the licensor is not represented as endorsing the use made of the work. Further, any new works must be made available on the same conditions. The full details of the license are available at http://creativecommons.org/licenses/by-nc-sa/4.0.

CC BY NC ND: The CC BY-NC-ND license allows users to copy and distribute the Article, provided this is not done for commercial purposes and further does not permit distribution of the Article if it is changed or edited in any way, and provided the user gives appropriate credit (with a link to the formal publication through the relevant DOI), provides a link to the license, and that the licensor is not represented as endorsing the use made of the work. The full details of the license are available at http://creativecommons.org/licenses/by-nc-nd/4.0. Any commercial reuse of Open Access articles published with a CC BY NC SA or CC BY NC ND license requires permission from Elsevier and will be subject to a fee. Commercial reuse includes:

- Associating advertising with the full text of the Article
- Charging fees for document delivery or access
- Article aggregation
- Systematic distribution via e-mail lists or share buttons

Posting or linking by commercial companies for use by customers of those companies.
20. **Other Conditions**:
v1.10
Questions? customercare@copyright.com or +1-855-239-3415 (toll free in the US) or +1-978-646-2777.